

Hydrogen permeation and hydrogen production by DBD plasma in different type reactors

種々のリアクター形式での
DBD プラズマによる水素透過および水素製造

**Gifu University
Graduate school of Engineering
Environmental and Renewable Energy Systems
Engineering**

Mostafa Ibrahim Elshafie

2021

Preface

The present thesis is submitted as partial fulfillment of the requirements for the degree of Philosophiae Doctor (Ph.D.) at the graduate school of engineering, Gifu University, Japan.

This thesis was performed at the Environmental and Renewable energy Systems Division, Graduate School of Engineering, Gifu University, Japan. This work was carried out from 1st of April 2018 to March 2021 under the supervision of Professor Shinji Kambara.

The PhD was funded by the graduate school of engineering, Gifu University, Japan. Also, the financial support was received from Prof. Shinji Kambara laboratory.

The PhD thesis is written in the form of a monograph and includes all publications produced during the PhD time frame.

Gifu, March 2021

Mostafa El-Shafie



Acknowledgments

Acknowledgments

Foremost, I would like to express my deepest gratitude to my supervisor Professor Shinji Kambara for the continuous support of my PhD study and research, for his patience, motivation, enthusiasm, and immense knowledge. His guidance helped me in all the time of research and completing of this thesis. Also, I am so grateful to my co-supervisor Doctor Yukio Hayakawa for both the productive conversations and the friendly working environment.

It is hard not thank all the people at the university that have directly contributed to the work presented in this thesis. I thank my fellow labmates for the productive discussions.

At last, but not least I want to thank my family. My father Ibrahim, my mother Omhashim, my wife Heba, and my beloved children Mohamed, Hana, Ibrahim for all the support they gave me through these many years.

Abstract

Hydrogen energy became the most significant energy as the current demand gradually starts to increase. Hydrogen energy is an important key solution to tackle the global temperature rise. The key important factor of hydrogen production is the hydrogen economy.

The present thesis will firstly review the hydrogen production technologies from both fossil and non-fossil fuels such as (steam reforming, partial oxidation, auto thermal, pyrolysis, and plasma technology). Water electrolysis can be combined with the renewable energy to get eco-friendly technology. These technologies have different challenges such as the total energy consumption and carbon emissions to the environment are still too high.

The diffusion of hydrogen through palladium and palladium-copper alloys membrane has been provided the highest hydrogen selectivity and permeance. The hydrogen permeation through the Pd_{0.60}-Cu_{0.40}wt% membrane foils with thicknesses of 15 μm , 20 μm are measured under gas driven permeation (GDP) and plasma driven permeation (PDP) in the plate and cylindrical type reactors. The maximum hydrogen flux, hydrogen permeability and Permeation rate of the heating and plasma-heating experiments are found at the highest reactor temperature and plasma voltage. A comparison between both experiments showed the hydrogen permeation flux of the plasma-heating experiment is higher than that obtained from the heating only.

For the water vapour decomposition by the dielectric-barrier discharge (DBD) plasma, the experimental and theoretical analyses are investigated. The simulation analysis showed a good agreement with the experimental results for the model selecting the dissociative attachment reaction.

The energy and exergy efficiencies of three hydrogen production systems from ammonia decomposition using the dielectric barrier discharge plasma (DBD) are comparatively evaluated. The catalyst materials effect on the decomposition process of NH_3 is experimentally investigated. Also, the exergy analysis and entropy generation of ammonia decomposition under heating is investigated.

List of Publications

All publications are peer-reviewed and are divided into journal and conference papers. Part of the work performed during the Ph.D. thesis in the first year is not related to the Ph.D. project and for this reason, are listed under other publications to give the reader a full view of the publications produced during the time frame of the Ph.D. project.

Journal Papers

1. **Mostafa El-Shafie**^{*}, Shinji Kambara, Yukio Hayakawa. Alumina particle size effect on H₂ production from ammonia decomposition by DBD plasma. *Energy Reports*, Accepted.
2. **Mostafa El-Shafie**^{*}, Shinji Kambara, Yukio Hayakawa. Comprehensive assessment of hydrogen production in argon-water vapours plasmolysis, *Energy Science & Engineering (WILEY Library)*, Accepted.
3. **Mostafa El-Shafie**^{*}, Shinji Kambara, Yukio Hayakawa. Performance evaluation of hydrogen permeation through Pd/Cu membrane at different plasma system conditions, *South African Journal of Chemical Engineering (SAJCE)*. In press.
4. **Mostafa El-Shafie**^{*}, Shinji Kambara, Yukio Hayakawa. Comparative study between the simulation and experimental results of H₂ production from water vapour plasmolysis, *AIMS Energy*, 2020, 8(5):835-858.
5. **Mostafa El-Shafie**^{*}, Shinji Kambara, Yukio Hayakawa. Energy and exergy analysis of hydrogen production from ammonia decomposition systems using non-thermal plasma, *Int J of Hydrogen Energy*, 2020. In Press.
6. **Mostafa El-Shafie**^{*}, Shinji Kambara, Yukio Hayakawa. Study of the hydrogen production and heat transfer distributions of ammonia decomposition in atmospheric pressure plasma plate reactor. *J. sustain. dev. energy water environ. syst.*, 1080347.
7. **Mostafa El-Shafie**^{*}, Shinji Kambara, Yukio Hayakawa. One-dimensional simulation of hydrogen production kinetic models by water vapor plasmolysis in a DBD plate reactor. *J Theor Appl Phys* 14, 181–194 (2020).
8. **Mostafa El-Shafie**^{*}, Shinji Kambara, Yukio Hayakawa. A comparative study of hydrogen permeation through Cu/Pd membrane in different reactor types. *J. Appl. Phys.* 59, 056003 (2020).

List of Publications

9. **Mostafa El-Shafie**^{*}, Shinji Kambara, Yukio Hayakawa, Study of the plasma and heating effect on hydrogen permeation through Pd0.60-Cu0.40 membrane in a micro-channel plate reactor, *Int J of Hydrogen Energy*, 2019, In Press.
10. **Mostafa El-Shafie**^{*}, Shinji Kambara, Yukio Hayakawa, A comparison between GDP and PDP experiments of hydrogen permeation through 15 μm Pd60-Cu40% membrane thickness in a micro channel plate type reactor, *Fusion Engineering and Design*, 2019, 149, 11320-27.
11. **Mostafa El-Shafie**^{*}, Shinji Kambara, Yukio Hayakawa, Experimental analysis of plasma and heating effect on H₂ permeation behavior through Pd–Cu40% membranes in 1mm gap length plate reactor, *Int J of Hydrogen Energy*, 2019, In Press.
12. **Mostafa El-Shafie**^{*}, Shinji Kambara, Yukio Hayakawa, Preliminary results of hydrogen production from water vapor decomposition using DBD plasma in a PMCR reactor, *Int J of Hydrogen Energy*, 2019, 44, 20239-48.
13. **Mostafa El-Shafie**^{*}, Shinji Kambara, Yukio Hayakawa, Hydrogen Production Technologies Overview, *Journal of Power and Energy Engineering*, 2019, 7, 107-154.
14. **Mostafa El-Shafie**^{*}, Shinji Kambara, Yukio Hayakawa. Study of Zirconia Material Effect on H₂ Production from Ammonia-argon base Gas in Plasma Plate Type Reactor. *2020 IOP Conf. Ser.: Mater. Sci. Eng.* 908 012002.
15. **Mostafa El-Shafie**^{*}, Shinji Kambara, Yukio Hayakawa, Study of the reactor temperature effect on H production from steam decomposition using DBD plasma, *Energy Reports*, 2019, In Press.

(2) Other Publications

16. **Mostafa El-Shafie**^{*}, A. A. Hussien, Shinji Kambara, Yukio Hayakawa, Performance Evaluation of an Industrial Absorption System, *Energy Procedia*, 2019, 156, 266-272.

Contents

Chapter 1 Introduction.....	1
1.1 Outlook	1
1.1.1 World Energy Consumption	2
1.1.2 Environmental Impact.....	3
1.2 Hydrogen Production Technology	4
1.2.1 Water Electrolysis	4
1.2.2 Thermolysis & Thermochemical water splitting	7
1.2.3 Photonic	8
1.2.4 Biomass	9
1.3 Hydrocarbons reforming technology	11
1.3.1 Steam Reforming	12
1.3.2 Partial oxidation	13
1.3.3 Auto-thermal.....	14
1.3.4 Gasification	15
1.3.5 Pyrolysis	16
1.4 Hydrocarbons reforming assisted by using plasma technology	17
1.4.1 Thermal plasma technology.....	17
1.4.2 Non-thermal plasma technology	20
Conclusion	21
1.5 Objectives of this Study	22
References.....	24
 Chapter 2 Hydrogen permeation through Pd-Cu membranes	51
2.1 Outlook	51
2.1.1 Hydrogen separation techniques.....	53
2.1.2 Hydrogen separation membrane types	54
2.1.3 Pd-based membranes	55
2.1.4 Permeation theory	58
2.2 Introduction.....	63
2.2.1 Experimental.....	65
2.2.2 Results and discussion	67
Conclusion	79
2.3 Introduction.....	80
2.3.1 Experimental	82

Contents

2.3.2 Results and discussion	84
Conclusion	93
2.4 A comparison between GDP and PDP experiments of hydrogen permeation through 15 μ m Pd60-Cu40% membrane thickness	94
2.4.1 Experimental	96
2.4.2 Results and discussion	99
Conclusion	105
2.5 Assessment of H ₂ permeation through Pd-Cu40% membrane cylinder type reactor.....	106
2.5.1 Material and methods	106
2.5.2 H ₂ permeation in (CTR) using DBD plasma	108
2.5.3 The effect of feeding pressure on hydrogen production from syngas of (75%H ₂ /25%N ₂)	111
2.5.4 Catalytic materials effect on H ₂ permeation through Pd-Cu40% membrane.....	112
Conclusion	121
References.....	122
Chapter 3 Hydrogen Production from Water Vapour	138
3.1 Introduction.....	138
3.1.1 Hydrogen formation kinetics	139
3.1.2 Experimental.....	140
Conclusion	151
3.2 The Reactor Temperature Effect on H ₂ Production from Steam Decomposition Using DBD Plasma.....	152
3.2.1 Experimental.....	152
3.2.2 Results& Discussion	153
Conclusion	157
References.....	158
Chapter 4 Water vapour decomposition simulation.....	161
4.1 Introduction.....	161
4.1.1 Water molecular properties	162
4.1.2 Simulation models kinetics	163
4.1.3 Reaction mechanism and cross sectional of Model I.....	167
4.1.4 Reaction mechanism and cross sectional of Model II.....	168
4.1.5 Reaction mechanism and cross sectional of Model III.....	172
4.1.6 Analysis & Simulation Results	173
4.1.7 Comparison and discussions between models	185

Contents

Conclusion	185
4.2 Comprehensive assessment of hydrogen production in argon-water vapours plasmolysis	187
4.2.1 Simulation model description	188
4.2.2 Experimental setup and methods	190
4.2.3 Results & discussions	193
Conclusion	205
4.3 Comparative study between the simulation and experimental results of H ₂ production from water vapour plasmolysis	207
4.3.1 Simulation of hydrogen production	208
4.3.2 Initial boundary conditions	210
4.3.3 Experimental method	211
4.3.4 Results and discussions	212
4.3.5 Simulation model I (without dissociative attachment reaction)	213
4.3.6 Comparison between theoretical and experimental results (Model I)	216
4.3.7 Theoretical analysis of water vapor decomposition using DBD plasma with dissociative attachment reaction	220
4.3.8 Comparison between theoretical and experimental results (Model II)	223
4.3.9 Comparison between both simulation models reaction mechanism results	227
Conclusion	229
References	256
 Chapter 5 H₂ Production from ammonia gas	263
5.1 Introduction	263
5.2 Zirconia material effect on H ₂ production from ammonia-argon base gas in plasma plate type reactor	263
5.2.1 Experimental setup	264
5.2.2 Results & discussions	265
5.3 Ruthenium and Soda glass effect on NH ₃ decomposition	271
5.3.1 Experimental	273
5.3.2 Results & discussions	275
5.3.3 Assessment of the catalyst effect on the hydrogen production from ammonia decomposition by DBD plasma	280
Conclusion	282
5.4 Alumina thickness effect on low concentration ammonia	283
5.4.1 Experimental	283
5.4.2 Results & discussions	285
Conclusion	288

Contents

5.5 Energy and exergy analysis of thermal ammonia decomposition.....	288
5.5.1 Methodology.....	290
5.5.2 System description.....	291
5.5.3 Results & discussion.....	292
Conclusion	296
5.6 Energy and exergy analysis of NH ₃ decomposition by DBD plasma	297
5.6.1 Thermodynamics and exergy analyses	298
5.6.2 Results & discussion.....	301
5.6.3 Exergy analysis of H ₂ production from NH ₃ gas in PMR with zeolite and pre-catalytic reactor.....	307
Conclusion	313
5.7 Hydrogen Production and Heat Transfer Distributions of Ammonia Decomposition in an Atmospheric Pressure Plasma Plate Reactor	314
5.7.1 Introduction	314
5.7.2 Experimental.....	316
5.7.3 Energy distribution.....	318
5.7.4 RESULTS AND DISCUSSION.....	319
Conclusion	327
References.....	328

Nomenclature

Nomenclature

E	Energy (m^2)
\dot{E}	Rate of net energy (kWs^{-1})
h	Specific enthalpy (kJ kg^{-1})
\dot{m}	Mass flow (kg s^{-1})
R	Specific gas constant ($\text{J kg}^{-1}\text{K}^{-1}$)
P	Pressure (atm)
Q	Heat (kW)
\dot{Q}	Heat rate (kW s^{-1})
r	Reaction rate
s	Entropy ($\text{kJ kg}^{-1} \text{K}^{-1}$)
T	Temperature (K)
T_0	Temperature of the environment, 300 K
\dot{W}	Work rate (kJ s^{-1})
EX	Specific exergy (kJ kg^{-1})
$\dot{E}X$	Exergy (kW)

Greeks

η	Efficiency (%)
--------	----------------

Subscripts

0	environment, initial state
ch	chemical
dest	destroyed
ex	exergy
en	energy
in	inlet
kin	kinetics
out	outlet
p	Location p
pot	potential

Chapter 1 Introduction

1.1 Outlook

Energy is the most important needs for the human life and development of the worldwide. So, energy is the world key consideration in all discussions and meetings of the sustainable energy development. The renewable energy sources, such as solar energy, wind energy, waves, and tides energy are considered eco-friendly. It is expected that the hydrogen fuel and its demand will rise rapidly over the next few decades [1, 2]. The hydrogen energy utilization as an energy source and storage methods has been reviewed [3]. The recycling of the waste materials to useful energy sources through waste-to-energy technologies such as hydrogen, biogas, etc., have been reviewed [4]. The importance of hydrogen fuel is known as alternative clean energy and to overcome the fossil fuels depletion due to the high extension usage. In addition, fossil fuels have a bad effect on the environment due to combustion product gases such as carbon oxides, nitrogen, sulfur, etc. which have the main responsibilities of the global warming [5]. Hydrogen fuel is considered the alternative clean energy fuel and it can be produced from eco-friendly sources. In the current state, it is investigated that too little quantity of hydrogen is produced from the renewable energy resources through water electrolysis and the highest quantity is still generated from fossil fuels [6, 7]. Due to the hydrogen fuel advantages and versatility, in the long-term hydrogen will be the alternative of hydrocarbons fuels [8]. Also, hydrogen fuel is considered the highest efficient and clean energy carrier which produced water only as a by-product of its combustion. The worldwide is accepted to use hydrogen fuel as an independent clean energy source and high energy content compared to the fossil fuels, Table (1.1) is shown the energy content of different fuels resources [9]. In different energy applications such as fuel cells, hydrogen energy can be utilized as a clean energy source without CO₂ products emission to the environment which water is the outlet combustion products. It has been investigated that the nitrogen oxides gases are produced in the high temperature hydrogen combustion, but these environmental pollutants can be removed at the low temperature usage such as fuel cells [10]. The power-to-gas pilot plants have been used to generate electricity from hydrogen fuel or feeding the hydrogen gas into the gas distribution system [11]. Currently, this technology is used for storing power in some European countries as a hydrogen gas [13-17]. In most power-to-gas pilot plants in Germany, the wind energy, and solar energy is used to produce electricity [18].

Many studies have been developed to evaluate the challenges of transition of using the hydrogen economy [19-48]. The steps which involved the implementation of a hydrogen economy have been investigated [49-52]. The hydrogen energy prospects have been described to avoid the climate change-related problems [53]. The rationale of the hydrogen energy systems and technology has been studied including the present energy systems and their environmental impact [3, 54-63]. In this article, the hydrogen gas production technologies from the fossil and non-fossil fuels such as steam reforming process, water electrolysis process... etc. are reviewed. A novel hydrogen gas production method using ammonia decomposition by plasma

Chapter 1. Introduction

technology is reviewed. Ammonia decomposition using plasma technology without and with the catalyst to produce pure hydrogen is considered as compared case studies.

Table.1.1 Energy contents of different fuels [9].

Fuel	Energy content (MJ/kg)
Hydrogen	120
Liquefied natural gas	54.4
Propane	49.6
Aviation gasoline	46.8
Automotive gasoline	46.4
Automotive diesel	45.6
Ethanol	29.6
Methanol	19.7
Coke	27
Wood(dry)	16.2
Begasse	9.6

1.1.1 World Energy Consumption

As global population increases and the urbanization trend continues, the energy consumers will become ever more and recently, the International Energy Agency report is predicted that the global energy demand will increase by 2030 to 50% [64]. Due to the fossil fuels limited nature and depletion, research and development have extensively started on generating new alternative sources and study the efficiently use of the current fossil fuels. The percentage of the power consumption of different humanities applications such as the building power consumption is considered the main energy usage and acts 51% of the total energy consumption [65]. The world population is estimated that will be triple by 2030. The common Energy Gases begins with natural gas or methane which have only one carbon and four hydrogen atoms. The world has been started to convert energy from one energy form to another form. The transition of solids to liquids to gases has been illustrated in figure (1.1) by GHK Company [66].

Before the mid of 19th century, the most reliance energy of the world was from wood. Coal has still remained the main reliable of the world energy in the 19th century. The energy usage was growing rapidly due to the high increase in world population, the world is directed toward oil fuel which overcomes the coal energy problems. But oil fuel is now facing environmental problems and the world is directed to use natural gas fuel. It has solved most of the environmental problems due to it is cleaner, lighter and more efficiently. Also, the distribution can be through a pipe network that is less conspicuous and more extensive than oil fuel. Nowadays, natural gas fuel became the first choice for generating electricity. The renewable energy ratio generated the electric energy and the renewable energy development has been compared by Japan energy 2017 [67]. Firstly, the world energy consumption rate is investigated to show

Chapter 1. Introduction

the importance of increasing renewables energy through increasing energy efficiency and switching it to be clean, low carbon resources and economic growth is required. The increasing of fossil fuel usage the increasing of air pollution growing with a possibility of a highly serious economic and negative environmental effect [68, 69].

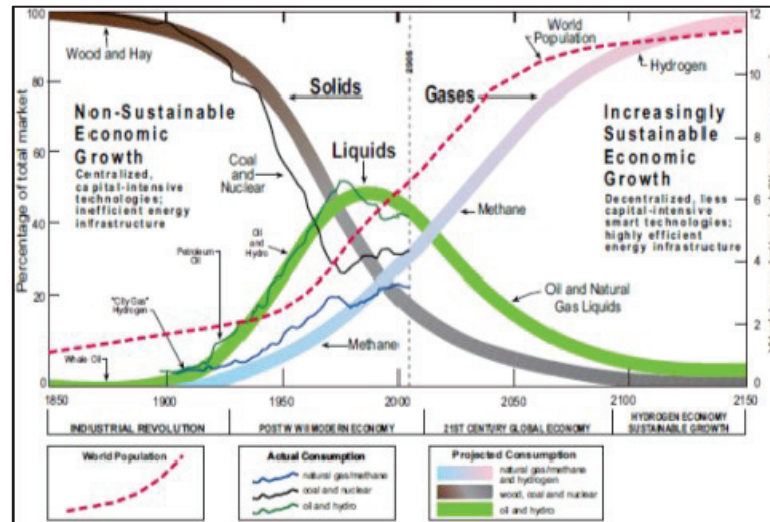


Fig.1.1 Global energy system transition, from 1850-2150 [66].

1.1.2 Environmental Impact

Hydrogen is the highest clean energy carrier which it can be used in the most energy applications such as generates electricity and transportation. Hydrogen fuel energy is expected to be the highest energy carrier's usage in the future; many advantages have been investigated that it can be used in transportation, long time storage and low environmental impact [70]. Figure (1.2) is presented the greenization factor (GF), the environmental impact factor (EIF) and the hydrogen content factor (HCF) of the different energy fuels (coal, oil, natural gas, and hydrogen) [71].

In order to take the hydrogen fuel advantages, the hydrogen economy is still the most important hydrogen production issue. So, the renewable energy sources should be used to produce hydrogen at low costs. The assessment methodology for hydrogen production methods has been implemented to study the environmental impact [72, 73]. Hydrogen fuel has been considered that to be the highest clean and renewable future energy source [74]. A comparative study has been developed to reduce the total environmental emissions from the marine transportations by using hydrogen fuel [75, 76].

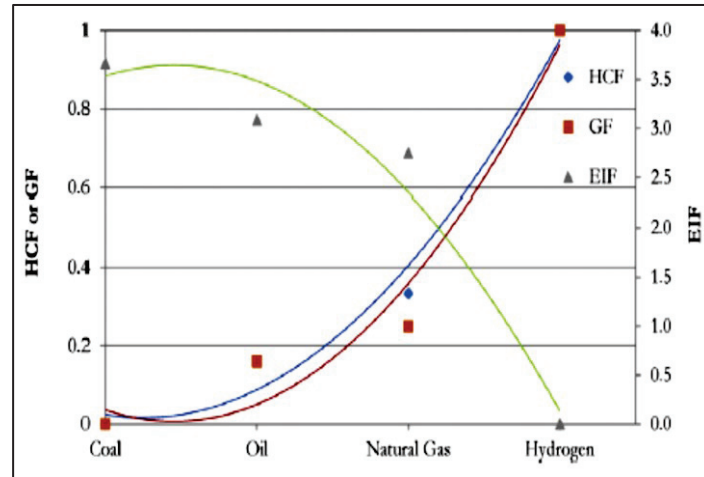


Fig.1.2 Hydrogen Content Factor (HCF), Greenization Factor (GF), and Environmental Impact Factor (EIF) of hydrogen and other fossil fuels [71].

1.2 Hydrogen Production Technology

Hydrogen gas became the most important fuel which can be used as an alternative feedstock in industrial application processes. As the utilization of hydrogen fuel grows as the global warming temperature still keeps rising, so, the hydrogen production should be on a large scale. The evaluation of hydrogen production methods has been studied in different reviews [56, 71, 77-89]. Currently, the main source of hydrogen production is based on the fossil fuels. It can be presented as a commercial mature technology which it can be applied at low costs and get high efficiencies [90]. The hydrogen production especially using the steam reforming process of methane can get the efficiency range of (65-75%). On the other hand, the efficiency of the partial oxidation process of methane is recorded about 50% [54]. Hydrogen gas can also produce from water using the water electrolysis method which acting about 95% of the total quantity of hydrogen produced [91]. In the next section of this article, we will present several methods of the hydrogen production technologies. Recently, Plasma technology is an important method to produce the hydrogen fuel using hydrocarbons or alcohols. Hydrogen production using ammonia decomposition is a novel method can be established to produce pure hydrogen by using the plasma membrane reactor. A comparison of two different ammonia decomposition methods using the plasma technology is developed. The hydrogen production technology can be divided into hydrocarbons reforming and non-hydrocarbons reforming technology [80]. Firstly, a brief review is conducted to describe the hydrogen production from non-hydrocarbons technology.

1.2.1 Water Electrolysis

It can be defined in the simplest form by using two electrodes in water and passing the electrical current water is converted into hydrogen and oxygen. The water electrolysis method can be divided into three different types of the electrolyte alkaline,

Chapter 1. Introduction

proton exchange membrane (PEM), and solid oxide electrolyzers (SOE) [92]. Table (1.2) has been listed the typical specifications of the water electrolysis technologies methods. The commercial low temperature electrolyzers were developed and have efficiencies of (56-73%) at conditions of (70.1- 53.4 kWh. kg⁻¹ H₂ at 1 atm and 25 °C) [93]. The proton exchange membrane (PEM) electrolysis and solid oxide electrolysis (SOE) units have been studied [94–96]. Alkaline electrolysis systems are the most commonly compared to other water electrolysis methods. Solid oxide electrolysis (SOE) is the most electrically efficient but still are under development. Corrosion, seals, thermal cycling, and chrome migration are the major challenges faced by the SOE technology. The Proton exchange membrane (PEM) electrolysis systems are more efficient than alkaline electrolyser. Also, the corrosion and seals issues don't exist as (SOE), but the cost of (PEM) is too high compared with alkaline electrolyzers systems. Alkaline electrolyser systems have the lowest capital cost and have the lowest efficiency, so the electrical energy cost is too high. Recently, electrolyzers are used for producing pure hydrogen and high-pressure units have been developed [97]. The advantage of using the high-pressure operation unit is to eliminate using expensive hydrogen compressors. The hydrogen production using the water electrolysis systems are showed the too high cost to generate hydrogen on large scale using the water electrolysis method. Additionally, the water electrolysis systems are utilized the non-renewable power generation source to produce electricity for the water electrolysis systems [98-102].

Table.1.2 The typical specifications of alkaline, PEM and SOE [103]

Specification	Alkaline	PEM	SOE
Technology maturity	State of the art	Demonstration	R&D
Cell temperature, °C	60-80	50-80	900-1000
Cell pressure, bar	<30	<30	<30
Current density, A/cm ²	0.2-0.4	0.6-2.0	0.3-1.0
Cell voltage, V	1.8-2.4	1.8-2.2	0.95-1.3
Power density, W/cm ²	Up to 1.0	Up to 4.4	-
Voltage efficiency, %	62-82	67-82	81-86
Specific system energy consumption, kWh/Nm ²	4.5-7.0	4.5-7.5	2.5-3.5
Partial load range, %	20-40	0-10	-
Cell area, m ²	<4	<300	-
Hydrogen production, Nm ² /hr	<760	<30	-
Stack lifetime, hr	<90000	<20000	<40000
System lifetime, yr	20-30	10-20	-
Hydrogen purity, %	>99.8	99.999	-
Cold start-up time, min	15	<15	>60

1.2.1.1 Alkaline electrolyser

This type is commonly used on the large-scale systems. Alkali solutions are divided into two different electrolyte types. The first electrolyte type is potassium hydroxide (KOH) with a weight percent of (20-40%) [104]. Sodium hydroxide

Chapter 1. Introduction

(NaOH) and sodium chloride (NaCl) have been used as the other alkaline electrolyte types [105]. The separating diaphragm between the two electrodes is made of the asbestos material with a thickness of 3 mm and due to the usage of the asbestos materials the water electrolyser operation temperature is limited to be 80 °C [103]. Hydrogen and hydroxide are generated at the cathode part, then the hydroxide is moved to the anode part generating oxygen. The anode and cathode part reactions can be expressed as follows:

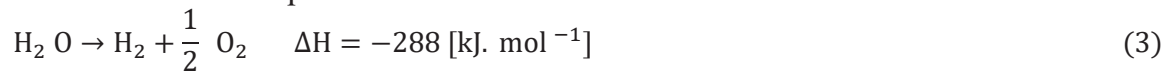
- Anode reaction:



- Cathode reaction:



- The overall equation is:

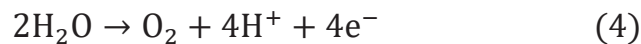


The gas-liquid separation unit is used to separate the generated hydrogen gas outside the electrolyser [106]. The efficiencies of alkaline electrolyzers process have been registered within range of (50-60%) at a current density of (100-300 mA.cm⁻²) and at the hydrogen gas lower heating value [93]. The corrosion problem is the main challenge of this method, according to using the alkali solution. So, new materials are also being developed to be used as an alternative diaphragm material.

1.2.1.2 Proton exchange membrane electrolyser

To overcome the corrosion has happened from the alkaline electrolyzers method, the solid polymer membrane has been investigated to use in the PEM fuel cells technology [107]. However, the deionized water with high purity has been required for the water electrolysis process [106]. The oxidation reaction of water is happened at the anode part generating oxygen, electrons, and protons. The electrons and protons are moved to the cathode side through the PEM. The hydrogen gas is generated at the cathode part after the protons reduced. The PEM reactions are expressed as follows:

- Anode reaction:



- Cathode reaction:



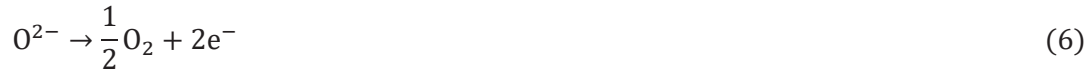
Where the overall equation is the same as for alkaline electrolyser eq. (3). The PEM electrolyser system has been investigated that it can be used with the fluctuation power supply source, according to the protons transportation through the PEM membrane is so quickly [103]. The high manufacturing cost is the major challenge of the PEM systems.

Chapter 1. Introduction

1.2.1.3 Solid oxide electrolyser

The solid oxide electrolyser (SOE) operation temperature can be reached at 1000°C compared with the PEM electrolyser. Figure (1.3) is illustrated that these systems typically are used the thermal energy instead of a part of the electrical energy [108]. It was investigated that the electrolyser efficiency is increased by increasing high temperature [108,109]. Therefore, compared to alkaline and PEM processes the SOE process has a higher efficiency. In the SOE system, hydrogen is generated at the cathode part and the oxide anions are passed to the anode where oxygen will form through the solid electrolyte [107]. The following reactions are taking place in an SOE:

- At anode:



- At cathode:



This method is also used in fuel cells as a solid oxidation electrolysis cells (SOEC). SOEC systems are operated at a high temperature from nuclear reactors and can achieve efficiency up to 60% [102-115].

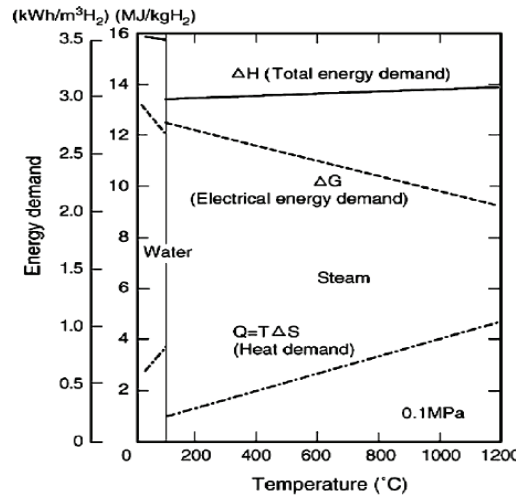
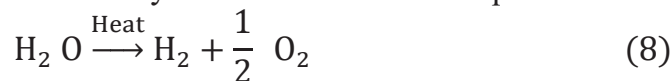


Fig. 1.3 Energy demands for water and steam electrolysis [108].

1.2.2 Thermolysis & Thermochemical water splitting

1.2.2.1 Thermolysis

In the thermolysis process water is directly split using thermal energy as the energy input or it can be split indirectly using some other chemical materials [113]. The following is the thermolysis chemical reaction equation:



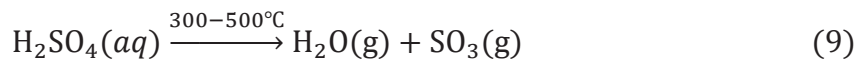
Chapter 1. Introduction

Thermolysis and thermochemical water decomposition methods can be seemed to be the same methods, regardless of the high temperature source. This means the thermochemical process deals with the chemical reactions and the heat transfer processes. It was investigated that if the temperature reached over 2000 °C, water is started to decompose without using other chemical materials [113]. It was presented that the thermolysis process is a direct thermal splitting of water at too high temperature [92]. This means that the material selection is very difficult to be suited with the high temperature. Also, it has been investigated that the main challenge of the thermolysis process is to develop an effective technique [92,104,116,117].

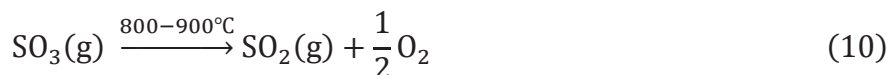
1.2.2.2 Thermochemical water splitting

In the thermochemical water splitting process, it was combining the thermolysis water splitting process and the chemical reactions to reduce the water decomposition temperature to 900°C [104]. The hydrogen production using the thermochemical water splitting has been involved in different chemical reactions. Many studies have been developed to review the water splitting cycles [106,118,119]. Different thermochemical cycles have been studied [105, 120] such as copper-chlorine, Zinc-zinc oxide, nickel-manganese ferrite and the sulfur-iodine process. For example, the sulfur-iodine process as follows:

The first reaction is the sulfuric acid which is decomposed at 300 °C to 500 °C to release water without a catalyst,



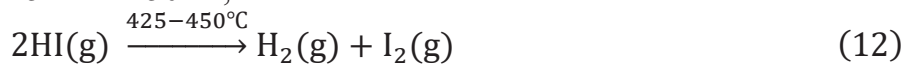
Then, SO_3 is separated at 800 °C to 900 °C to release oxygen,



The next reaction is done at low temperature to produce the sulfuric acid,



Finally, hydrogen is produced from iodine decomposition within a temperature range of 425 °C to 450 °C,



The challenge is faced this technology, the efficiency has to be increased by making scaling up [121].

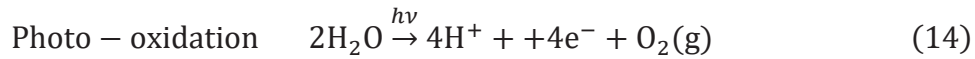
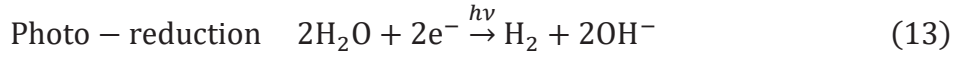
1.2.3 Photonic

Hydrogen is produced from the photonic process by using the photon energy. It can be divided into two methods the photocatalytic and the photoelectrolysis water splitting (photoelectrochemical water splitting).

Chapter 1. Introduction

1.2.3.1 Photocatalytic water splitting

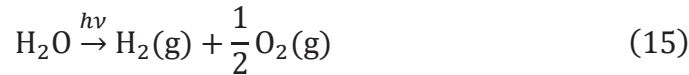
The hydrogen production by the Photocatalytic water splitting process is a direct method to produce hydrogen from water using the ordinary light. The low efficiency has been achieved by the photocatalytic method [122]. The main reactions of this process are as follows [123]:



The titanium oxide (TiO_2) is used in the photolysis reactions. Different researches are interested in photocatalyst development [124-128].

1.2.3.2 Photo electrolysis

Photo electrolysis has directly decomposed water into hydrogen and oxygen by using the sunlight. The photo electrolysis systems are the same as the photovoltaic systems, both technologies are used the semiconductor materials. In photovoltaic, p-type and n-type semiconductor materials are used [94]. The electric current is created, due to the forced movement in the opposite direction of the electron and hole [93,129]. In photo electrolysis process instead of generating the electric current water is decomposed into hydrogen and oxygen [93, 94, 100, 129]. The reaction of photo electrolysis is illustrated as follows [123]:



Different photo electrodes materials such as WO_3 , Fe_2O_3 , and TiO_2 have been investigated to use in photo electrolysis method as a thin-film [114,130,131]. The photo electrolysis systems performance is mainly based on the utilized materials of the photo electrodes and the semiconductor. The hydrogen production efficiency has been studied by [93, 94, 100, 129]. It has been investigated that the achieved efficiency of a single band gap is 18.3%, dual-band gap systems over 30% conversions [132].

1.2.4 Biomass

Biomass energy is used to generate hydrogen fuel as a renewable energy source. Biomass energy sources such as agricultural wastes, animal wastes, municipal solid wastes...etc. have been investigated [133–151]. A comparison between the fossil fuels and biomass energy is illustrated in Table (1.3).

Chapter 1. Introduction

Table 1.3 Advantages and disadvantages of hydrogen production from biomass [155]

Advantages	Disadvantages
Mitigating CO ₂ emissions	Seasonal availability and high handling costs
Crop residues conversion increases the value of agricultural output	Non-total solid conversion and tars production
Replacing fossil fuels with sustainable biomass fuel	Fuel process limitations: corrosion, pressure, resistance and hydrogen aging.
Cost of getting rid of municipal solid wastes	

The biomass technologies for hydrogen production can be divided into the gasification, pyrolysis which it was followed by the reforming process [149]. The basic reactions of biomass gasification process are listed as follows in Table (1.4). The hydrogen production yield of the biomass process has been affected with the biomass characteristics and compositions are affected with a number of process variables such as temperature, heating rate, moisture content, particle size, reactor system...etc. [152,153].

Table 1.4 Basic reactions biomass gasification processes [152]

Reaction mode	Reaction equation
Pyrolysis	$C_6H_{10}O_5 \rightarrow 5CO + 5H_2 + C$
	$C_6H_{10}O_5 \rightarrow 5CO + 3H_2 + CH_4$
Partial oxidation	$C_6H_{10}O_5 + \frac{1}{2}O_2 \rightarrow 6CO + 5H_2$
	$C_6H_{10}O_5 + O_2 \rightarrow 5CO + 5H_2 + CO_2$
	$C_6H_{10}O_5 + 2O_2 \rightarrow 3CO + 5H_2 + 3CO_2$
Steam reforming	$C_6H_{10}O_5 + H_2O \rightarrow 6CO + 6H_2$
	$C_6H_{10}O_5 + 3H_2O \rightarrow 4CO + 2CO_2 + 8H_2$
	$C_6H_{10}O_5 + 7H_2O \rightarrow 6CO_2 + 12H_2$

1.2.4.1 Biomass gasification process

The Gasification process can be commonly used in the biomass and coal gasification processes. It is commercially used in many processes and it has been based upon the partial oxidation process of the materials to get the mixture of hydrogen, carbon monoxide, methane...etc. [145]. Since the moisture has to be vaporized, the thermal efficiency of the gasification process is typically low [133]. Different studies have been presented for the gasification process with and without a catalyst using the fixed bed and the fluidized bed reactor [139,144,148,154]. The recorded performance of the fluidized bed reactors is higher than the fixed bed type reactors [144]. Syngas is produced from steam reforming process when steam or oxygen is added to the gasification process, which it can be utilized for hydrogen production in the water gas shift (WGS) or the Fischer-Tropsch reactor [144,149]. Biomass is dried by using superheated steam at 900 °C. The high hydrogen production

Chapter 1. Introduction

yields can be achieved from the dried biomass [133]. Based on the lower heating value, the achieved efficiencies of these reactors within range of (35–50%) [118, 106].

1.2.4.2 Biological hydrogen production process

Bio-hydrogen researches are increased last several years, as attention to sustainable development and waste minimization [156–183]. This is another biomass method to produce hydrogen gas fuel using the biological technologies. It has been investigated that it can be utilized the anaerobic bacteria which it is grown in the dark fermentation bioreactors or can be used algae in the light in the photo fermentative process [184]. The main processes include the photolytic process to produce hydrogen from water using the green algae, the hydrogen production using the dark-fermentative process of anaerobic digestion, the two-stage dark/fermentative process, the photo-fermentative processes and the WGS method for hydrogen production [160,165,185]. The biological methods have been presented with a low environmental impact and high hydrogen production efficiency [78]. By using the anaerobic microorganisms the dark fermentation reaction is carried out to convert the carbohydrate to hydrogen and other final products [105, 186]. The following is the chemical reaction equation:



The low hydrogen production capacity compared with the unit capital investment has been investigated that it was the major challenge of the dark fermentation method [187]. So, different extensive researches have been presented to get additional energy by adding and develop a new other two-stage system [188].

1.3 Hydrocarbons reforming technology

The hydrogen production from hydrocarbon fuels using reforming technology is presented. The Steam reforming process of hydrocarbons is considered the manufacturing dominating process of hydrogen production especially, for refineries. The hydrogen production technology using the hydrocarbon fuels can be divided into a steam reforming process, the partial oxidation process, and the auto-thermal reforming process (ATR). Table (1.5) is shown as a comparison between the reforming processes [189-191].

Chapter 1. Introduction

Table 1.5 Comparison of reforming technologies [189-191]

Technology	Advantages	Disadvantages
Steam reforming	Most extensive industrial experience Oxygen not required Lowest process temperature Best H ₂ /CO ratio for H ₂ production	Highest air emission
Auto-thermal	Lower process temperature than POX Low methane slip	Limited commercial experience Requires air or oxygen
Partial oxidation	Decreased desulfurization requirement No catalyst required Low methane slip	Low H ₂ /CO ratio Very high processing temperatures Soot formation/handling adds process complexity

In the steam reforming process, hydrogen gas, carbon monoxide and carbon dioxide gases are primarily composed in the gas flow stream; it has been investigated that by improving the operating conditions such as temperature, pressure, etc. in the fuel processing reactors will maximize the hydrogen production and minimize the carbon formation [192–198].

1.3.1 Steam Reforming

The steam reforming process is known as the hydrocarbons conversion with steam into hydrogen, carbon oxides, methane, and unconverted steam mixture. The typical feedstock ranges from natural gas and LPG to liquid fuels including naphtha and in some cases kerosene. In recent years steam reforming is also seen as an option for converting the primary feed into a gas suitable for a fuel cell. Different steam reforming reactors types have been used for specific applications [194]. The steam reforming process is considered the preferred hydrogen production process, the steam reforming process reactions are endothermic reactions, the operating temperature is typically lower than the POX and ATR methods while it can be produced a high H/CO ratio [192-196]. Table (1.6) shows the reactions of the steam reforming process.

It was investigated that in the fuel processing, moderate temperatures higher than 180 °C is required [192-198]. The limitations of mass and heat transfer have been investigated to enable the kinetics of steam reforming by employing a microchannel reactor [193, 200-202]. These systems have been utilized the noble Group VIII metals as alternatives catalysts such as Rh and Co-based catalyst [203-205]. It was showed a less coke formation and much higher activities compared with the nickel catalysts [200, 206- 208]. The hydrogen production from methane using the steam reforming process is considered the common industrial method where it is given a high thermal efficiencies up to 85% according to the higher heating values [209].

Chapter 1. Introduction

The hydrogen fuel storage and transportation are very difficult due to the hydrogen fuel have a low energy per weight, additionally is a gaseous fuel. Thus, different on-site studies have been developed for steam reforming of hydrocarbons [210-216].

Table 1. 6 Key reactions of steam Reforming [200]

Reactions	Reaction description	Standard enthalpy of reactions [kJ. mol ⁻¹]	
$\text{CH}_4 + \text{H}_2\text{O} \rightleftharpoons \text{CO} + 3\text{H}_2$	Steam reforming	206	R _①
$\text{CO} + \text{H}_2\text{O} \rightleftharpoons \text{CO}_2 + \text{H}_2$	WGS	-41	R _②
$\text{CH}_4 + \text{CO}_2 \rightleftharpoons 2\text{CO} + 2\text{H}_2$	CO ₂ reforming	247	R _③
$\text{C}_n\text{H}_m + n\text{H}_2\text{O} \rightleftharpoons n\text{CO} + \left(\frac{m}{2} + n\right)\text{H}_2$	Higher hydrocarbons steam reforming	1175*	R _④

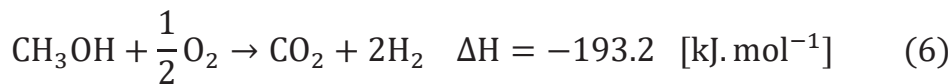
*[Standard conditions at P=1 atm, T=298 K, for n-C₇H₁₆]

1.3.2 Partial oxidation

The reaction of the partial oxidation (POX) method is an exothermic reaction and the reaction equation is presented in Eq. (5). In the POX method the hydrogen produced is sent to the water-gas shift (WGS) reactor, and then is purified by using a suitable purification method. Compared with the steam reforming process, it has been investigated that the efficiency of the POX process is low; in addition, the operation cost is too high due to using high quantities of the pure oxygen [217]. The enthalpy of reactions for methane and isooctane are shown in Table (1.7).



Example of the (POX) reaction:



The hydrogen production from the partial oxidation of hydrocarbon using catalysts has been utilized in commercial applications and automobile fuel cells [218–221]. The effect of addition ruthenium (Ru) on the molybdenum (Mo) catalysts has been investigated for the production of syngas from methane (CH₄) via partial oxidation process [223]. The principles of (CPO) are illustrated in figure (1.4).

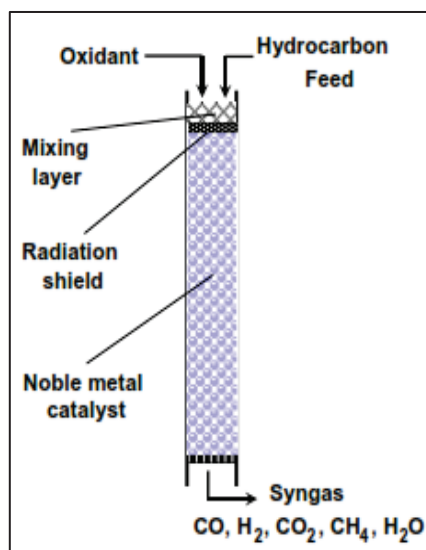


Fig 1.4 Catalytic partial oxidation principle [200].

Several studies have been carried to study CPO at different space velocities (low or moderate) and residence time (from 1s or above) [224-229]. The importance of operating and design parameters has been investigated in another feature of the CPO process to prevent the explosions risk [230]. It is proved that the temperature is hard to be controlled due to the hot spot formation and the reactions nature is exothermic [219-222]. The POX reactors efficiencies have been recorded based on the higher heating values for methane fuel is 60–75% [209].

Table 1.7 Standard enthalpies at (298 K, 1 atm), ΔH in [kJ/mol] [218]		
	Methane	Isooctane
Partial oxidation	-36.1	-675.8
Steam reforming	205.7	1258.8
Dry CO_2 reforming	246.9	1596.3

1.3.3 Auto-thermal

Auto thermal reforming process has been done at low pressure compared with the POX reforming process. The heat required in the catalytic zone to drive the steam reforming reactions has been generated using the POX process [199, 224, 231, 232]. Figure (1.5) is illustrated the auto-thermal reactor components. The combustion chamber reaction equations are shown in Table (1.8).

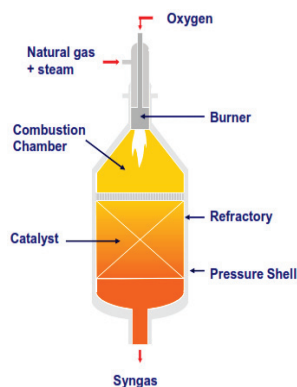


Fig 1.5 Illustration of an auto-thermal reactor [233].

Table 1.8 Simplified reactions in the combustion chamber of ATR [194]

Reactions	Reaction description	Standard enthalpy of reactions ΔH [kJ. mol ⁻¹]	
$\text{CH}_4 + 3/2\text{O}_2 \rightarrow \text{CO} + 2\text{H}_2\text{O}$	Combustion	-519	R _⑦
$\text{CH}_4 + \text{H}_2\text{O} \rightleftharpoons \text{CO} + 3\text{H}_2$	Steam reforming	206	R _①
$\text{CO} + \text{H}_2\text{O} \rightleftharpoons \text{CO}_2 + \text{H}_2$	WGS	-41	R _②

Compared with the POX process, a significant advantage of the auto-thermal reaction process, it can be produced a large amount of hydrogen gas while the starting and stop are very rapidly. In the auto-thermal reaction process, it was considered that it must be controlled the temperature and preventing the coke formation by using the both of the steam to carbon ratio and the oxygen to fuel ratio [199,224, 231].

1.3.4 Gasification

The gasification process is presented to be a sequence of a thermochemical transformations taking place at high temperatures between the organic part such as coal and the gasifying agent, like oxygen, steam, air, carbon dioxide [234-236]. The heat needed for the gasification process has been made by using the carbonaceous material (so it is called autothermic gasification) [234]. The water gas shift (WGS) process has been used to separate hydrogen and converting carbon monoxide into the carbon dioxide [104]. The gasification process heterogeneous and homogeneous reactions are summarized in Table (1.9) and Table (1.10) respectively.

Chapter 1. Introduction

Table 1.9 Major heterogeneous reactions taking place in the gasifier [234-237]

Reactions	Reaction description	Standard enthalpy of reactions ΔH [kJ. mol ⁻¹]
$C + CO_2 \rightleftharpoons 2CO$	Reverse boudouard	172.4 R ₍₈₎
$2H_2 + O_2 \rightleftharpoons 2H_2O$		131.3 R ₍₉₎
$C + 2H_2 \rightleftharpoons CH_4$	Methane formation	-74.9 R ₍₁₀₎
$2C + O_2 \rightleftharpoons 2CO$	Oxidation of CO	-221 R ₍₁₁₎
$2C + O_2 \rightleftharpoons 2CO$	Coke gasification	-393.6 R ₍₁₂₎

Table 1.10 Major homogenous reactions taking place in the gasifier [234-236, 238]

Reactions	Reaction description	Standard enthalpy of reactions ΔH [kJ. mol ⁻¹]
$2CO + O_2 \rightleftharpoons 2CO_2$	Oxidation of CO	-566 R ₍₁₃₎
$2H_2 + O_2 \rightleftharpoons 2H_2O$	Oxidation of H ₂	-483.6 R ₍₁₄₎
$CO + H_2O \rightleftharpoons CO_2 + H_2$	WGS	-41 R ₍₂₎
$CO + 3H_2 \rightleftharpoons CH_4 + H_2O$	Methanation/hydrogenation	-206 R ₍₁₅₎
$CH_4 + 2O_2 \rightarrow CO_2 + 2H_2O$	Combustion	-802.6 R ₍₁₆₎

The integrations of the coal gasification with other systems have been studied by different researches [239-249]. Thermodynamic evaluations using the first and second law of thermodynamics have been conducted on the integrated gasification systems in their analyses [242-250].

The hydrogen production from water decomposition using the Bryton cycle and a thermochemical copper-chlorine cycle have been investigated as a novel method to overcome the limitations of the hydrogen production from the coal composition and syngas hydrogen separation [251]. Koppers Totzek Coal gasification process can be produced pure hydrogen up to 97%, it has been investigated that it has the ability in the near and midterm to keep the hydrogen production from the fossil fuel in practice from the solar thermal processes and carbon sequestration application [252-261].

1.3.5 Pyrolysis

The Pyrolysis process "can be defined as the decomposition of organic substances by heat" [262]. These decomposition reactions have been performed at 350 °C to 400 °C depending on the coal properties [263]. The other hydrocarbons thermal decomposition have been occurred at high temperatures such as methane thermal decomposition temperature is at 1400 °C or higher. Significantly, the temperature of the pyrolysis process can be reduced by using the transition metal catalyst like (Ni, Fe, Co). It has been investigated that the pyrolysis process can be used the organic material [148, 264-266], additionally, it can be used for the hydrocarbons production, carbon nanotubes and spheres [148, 266-278]. The chemical reaction of the pyrolysis process can be generally expressed as follows [269]:



The chemical decomposition equation of hydrocarbons using the pyrolysis process, it is showed that water and air aren't used. Consequently, carbon oxides don't appear in the reaction by-products. It was presented that the pyrolysis process has the flexibility to use any organic fuel, in addition to its compactness and the process by-product is carbon-free [152, 265, 266, 269].

Although the pyrolysis process advantages, there is a major potential fouling problem by the carbon formed and it can be reduced by using appropriate reactor design [152].

1.4 Hydrocarbons reforming assisted by using plasma technology

Plasma "is known as the fourth state of the material" and it can be defined as an ionized gas. This technology has the challenge to produce hydrogen with the best energetic efficiency. The plasma technology can be classified into thermal and non-thermal plasma (non-equilibrium plasma) based on the energy level (temperature, plasma state, and electronic density). The electrically heated furnaces, combustion, flames, electric discharges, and shocks have been considered the plasma different generated methods [270]. Table (1.11) is shown the different plasma systems classifications and properties. The gas components temperature is the major difference between thermal plasma and no-thermal plasma technology [271, 272].

The high energetic densities can be released from the plasma process, so, the hydrogen production from hydrocarbons reforming applications using plasma with and without catalyst case studies have been discussed, in addition, the hydrogen production from ammonia decomposition using non-thermal plasma reactor.

The plasma torch (DC) direct current has been used in the first plasma-assisted reformers which it was thermal ones. A comparison between new and old plasmatron for methane and diesel fuels of H_2 yield for both kinds It has been shown in figure (1.6)& (1.7) respectively [273]. These figures are illustrated that the non-thermal plasma systems have a low energy consumption compared with the thermal plasma systems. We will briefly describe thermal and non-thermal plasma methods.

1.4.1 Thermal plasma technology

Thermal plasma can be applied to different applications which required high temperature such as vehicles ignition systems, lighting applications, gasification of solid fuels. Due to the thermal plasma technology high temperature, it has been limited for some liquid fuels reforming due to the electrode erosion. It has been characterized that the thermal plasma technology has a highly degree of dissociation and a substantial ionization degree [274]. Thermal plasma has an important range of application that includes synthesis of Nano-powders, destruction, and treatment of hazardous waste, metallurgy application (smelting operations and re-melting application in large furnaces) surface modification and coating, chemical synthesis [275]. Thermal degradation (gasification) of the organic carbon-based materials have

Chapter 1. Introduction

been carried out at a temperatures range of 400°C to 1500°C [276]. It has been investigated that the thermal plasma technology can be used in waste treatment such as healthcare wastes, steel making waste....etc. [277-283]. The economic studies have been presented that the insufficient control is the main disadvantages of the waste treatment using thermal plasma method [284]. In addition, the reforming process for alcohols using thermal plasma technology has been limited [288].

A high electric discharge over 1kW has been used in hydrocarbons reforming process by using thermal plasma technology; also, the cooling power has been required to decrease the electrode temperature to stop the vaporization of metal [274, 285, 286]. Figure (1.8) is shown the methane conversion with the input power to the thermal plasma reactor [274]. The thermal plasma is usually used high temperature, it will increase the energy cost, in addition to unwanted coking and soot. Catalysts have been utilized to reduce the reaction temperature, additionally; the required activation energy of fuel conversion is reduced.

Table 1. 11 Classification and Properties of Various Plasma [272]

Properties	Thermal Plasma(quasi-equilibrium plasma)	Non-thermal Plasma (Non equilibrium plasma)				
Temperature	$T_e \approx T_i \approx T_g \leq 2 \times 10^4$ K	$T_e \gg T_i \approx T_g \leq 300 \dots 10^3$ K				
Density	$\geq 10^{20}$ m ⁻³	$\sim 10^{10}$ m ⁻³				
Classification:	Thermal arc plasma	Gliding arc discharge	Dielectric barrier discharge	Corona discharge	Glow discharge	Atmospheric pressure plasma jet
Excitation	DC	DC/AC	AC/RF	Pulsed DC	DC/AC	RF(13.5 MHz)
Pressure, bar	0.1-100	~1	~1-3	~1	<10 mbar	~1
Electron energies, eV	1 - 10	1.4-2.1	1.0 - 30	~5	2.0 - 8.0	
Electron density, cm ⁻³	10^{15} - 10^{19}	$>10^{13}$	10^{12} - 10^{15}	10^9 - 10^{13}	10^9 - 10^{12}	10^{11} - 10^{12}
Breakdown voltage, kV	10-100	0.5 - 4.0	5.0 -25	10.0 -50.0		0.05-0.2
Current, A	30-30 000	10^{-1} -50	1.0 - 50	$<10^{-5}$	10^{-5} -1	
T _{mac} , K	5×10^3 - 10^4	1000-3000	~300	~ 400	~700	~ 400
Carrier gas	air, N ₂ , O ₂ ,etc.	N ₂ , O ₂ , Ar	N ₂ , O ₂ , rare gas	N ₂ , O ₂ , Ar	N ₂ , O ₂ , Ar	He, Ar
"RF inductivity coupled discharge. T _e , T _i and T _g refer to the temperature of electrons, ions, and neutral species (atoms, molecules, radicals and excited species) respectively.						

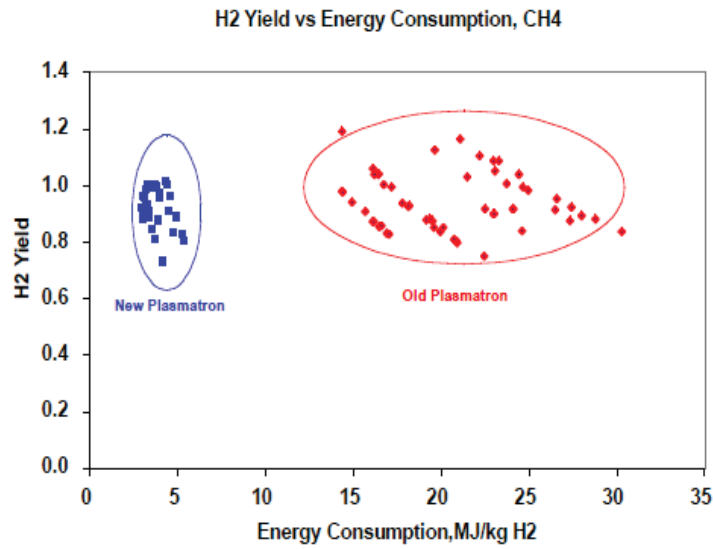


Fig 1.6 Comparisons of energy costs for non-thermal and thermal plasmas reforming of Methane [273]

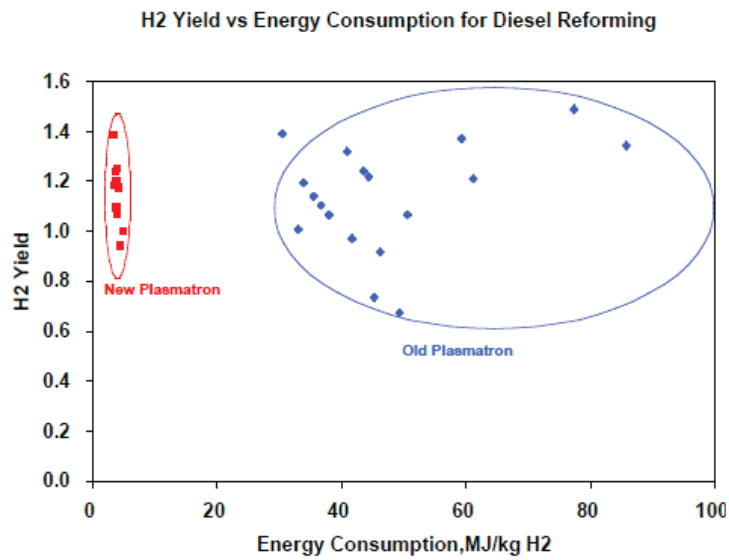


Fig 1.7 Comparisons of energy costs for non-thermal and thermal plasmas reforming of diesel [273]

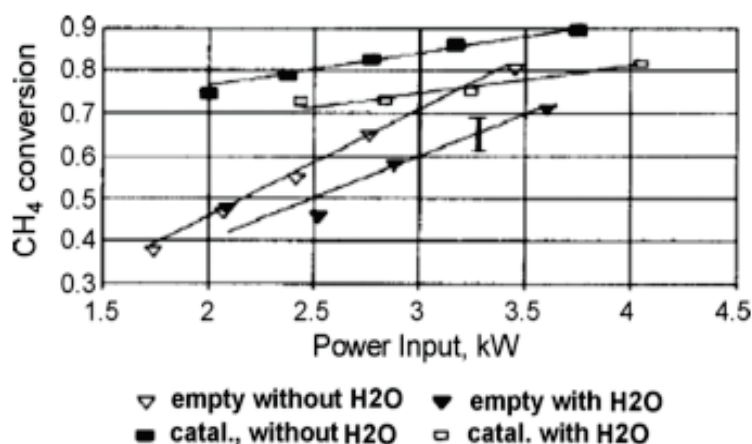


Fig 1.8 Methane conversion as a function of power input [274]

"Empty reactor: plasmatron air = 0.4 g/s, fuel = 0.27 g/s, additional air = 0.7 g/s. In the case of water addition, 0.2-0.5 g/s H₂O added. Catalytic case: plasmatron air = 0.35 g/s, fuel = 0.25-0.5 g/s, additional air = 0.5-1 g/s. In the case of water addition, 0.5-0.8 g/s water".

1.4.2 Non-thermal plasma technology

The non-thermal plasma method is more suitable for the hydrocarbons reforming and producing syngas. According to the non-thermal plasma method, the chemical reactions have been happened at low input power and at low temperatures [287]. In non-thermal plasma technology, the electron temperature can be reached (10,000 to 100,000 K) and at the same time, the gas temperature is at the room temperature [289, 290]. Different reactors have been used for applying the different plasma technologies like the dielectric barrier discharge (DBD) reactors [290,296], gliding arc discharge [285, 291-294], corona [290] and microwave [296-298]. It has been utilized in hydrocarbons reforming such as diesel, methane, and biofuels [274, 291, 299-305].

The non-thermal plasma process main effect parameter is the electron temperatures which temperatures are raised higher than 5000 K [285, 286, 306]. Dielectric barrier discharge (DBD), gliding arc discharge plasma, corona discharge and microwave plasma is the non-thermal plasma types [285, 306-315]. In the first three types, the dynamic discharge is used to create plasma. The main different parameters between non-thermal plasma types are the controlling method of the current and discharging power, additionally, reactor design, flow rate and the power supplies which have been described [285]. The gliding arc discharge which has a good selectivity and high production rate will briefly describe in this article. Table (1.12) differentiates the efficiencies of the non-thermal plasma methods and it is shown that the gliding arc discharge has the highest non-thermal plasma efficiency. Figure (1.9) illustrates the gliding arc discharge which has two electrodes and a simple feeding electrical system [312]. The arc is formed while the gas enters the reactor and the high voltage is applied. The arc is pushed down by the gas along the reactor length and is turned off at the reactor end, and then the new arc is formed again at the reactor gas inlet. It has been investigated that the gliding arc discharge method can be used the

Chapter 1. Introduction

DC or AC currents, in addition, a simple feeding power supply system compared with the other non-thermal plasma systems [285].

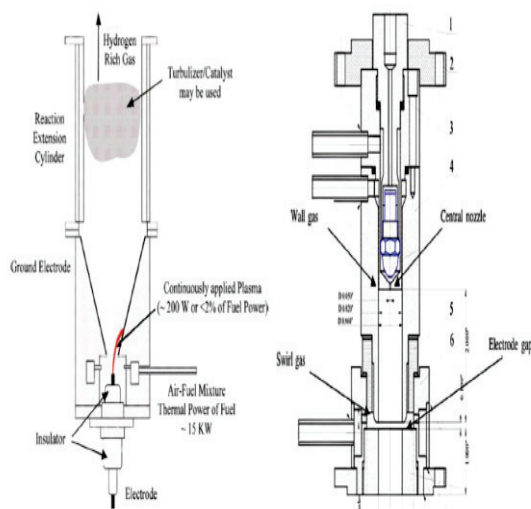


Fig 1. 9 Scheme of Gliding Arc reactor [312].

Table 1.12 Plasma reformer efficiencies [285].

Technology	Fuel	Experimental conditions			Products (dry vol. %)				Reformate Temperature[K]	Efficiency
		Chemical Reaction	Air Ratio	S/C	H ₂	CO	CO ₂	CH ₄		
Gliding arc non-thermal	Diesel	ATR	0.4	1.8	23	17	6.2	1.2	1000-1300	85
Corona discharge + catalyst	Iso-octane	ATR	0.28	1	46	16	16	-	900-1100	55
Gliding arc thermal	Iso-octane	POX	0.25	-	22	15	2	3	1200	9
Gliding arc thermal	Diesel	POX	0.25	-	23.5	23	0.1	0.03	1200	9
Microwave	Hexane	SR	-	2	66	25	4	-	?	?

Conclusion

Hydrogen fuel is believed that it will be a promising candidate to lead a new hydrogen economy. In this review paper, the hydrogen production key technologies are reviewed. The hydrogen production different technologies from both fossil and non-fossil fuels such as (water electrolysis, biomass, steam reforming, partial oxidation, auto thermal, pyrolysis, and plasma technology) are reviewed. The reforming and gasification technologies are the most mature hydrogen production technology. Water electrolysis can be combined with the renewable energy to get eco-friendly technology. Additionally, it is important to produce hydrogen from a wide range of feedstock. Currently, the maximum hydrogen fuel productions are registered from the steam reforming, gasification, and partial oxidation technologies using fossil fuels. The hydrogen production technology efficiencies are summarized in Table (1.13). These technologies still have challenges such as the total energy consumption and carbon emissions to the environment are too high. Ammonia decomposition using

Chapter 1. Introduction

plasma technology without and with a catalyst to produce pure hydrogen is considered as a compared case study.

Table 1. 13 Hydrogen Technology Efficiency summary table

Technology	Feed stock	Efficiency	Maturity	Reference
Steam reforming	Hydrocarbons	70-85%	Commercial	[209]
Partial Oxidation	Hydrocarbons	60-75%	Commercial	[209]
Autothermal reforming	Hydrocarbons	60-75%	Near term	[209]
Plasma reforming	Hydrocarbons	9-85%	Long term	[285]
Aqueous phase reforming	Carbohydrates	35-55%	Med. Term	[317]
Ammonia decomposition	Ammonia	28.3%	Near Term	[316]
Biomass gasification	Biomass	35-50%	Commercial	[106,117,318]
Photolysis	Sunlight+ Water	0.5%	Long term	[319]
Dark fermentation	Biomass	60-80%	Long term	[117, 163]
Photo fermentation	Biomass +Sunlight	0.1%	Long term	[117,318]
Microbial electrolysis cells	Biomass+ Electricity	78%	Long term	[319]
Alkaline electrolyzer	H ₂ O + Electricity	50-60%	Commercial	[93,318]
PEM electrolyzer	H ₂ O + Electricity	55-70%	Near term	[93,318]
Solid oxide electrolysis cells	H ₂ O + Electricity+ Heat	40-60%	Med term	[106]
Thermochemical water splitting	H ₂ O + Heat	NA	Long term	—
Photo electrochemical water splitting	H ₂ O + Sunlight	12.4%	Long term	[93,129]

1.5 Objectives of this Study

This study aims to investigate and analyze the hydrogen permeation through palladium-copper membranes and the hydrogen production from water vapour and ammonia gas using atmospheric pressure non-thermal plasma. The objectives of this study can be concluded in the following points:

Study of the hydrogen permeation through Pd-Cu membrane in the plate and cylindrical type reactors. The literature survey will be provided to understand the permeation mechanisms and membrane types. The experimental analysis of H₂ permeation through the Pd-Cu membrane thicknesses of 15 µm and 20 µm will be carried out under heating and plasma-heating in the plate type reactor. The effect of the plasma electrode gap distances of 4.5 mm and 1 mm on the hydrogen permeation process through both membrane thicknesses will be investigated. The gas-driven permeation and plasma-driven permeation will be experimentally compared. The hydrogen concentrations of 100% and 75% will be utilized in the hydrogen permeation analysis. The effect of the nitrogen gas on the hydrogen permeation through the cylindrical type reactor will be investigated. The catalyst effect on the hydrogen permeation process will be demonstrated in the cylindrical reactor. The performance of the H₂ permeation through Pd-Cu membrane will be evaluated under heating only, plasma only, and plasma-heating in the plate type reactor.

The water vapour decomposition using DBD plasma is experimentally investigated. Low-temperature steam is fed into the plasma reactor at different flow rates. The decomposed gases concentrations are determined by gas phase

Chapter 1. Introduction

chromatography. The preliminary results of H_2 production from water vapour decomposition by DBD plasma are analyzed. The reactor temperature effect on the water vapour decomposition by DBD plasma is investigated. The conversion rate and energy efficiency are determined for all tested flow rates.

One-dimensional simulation of the water vapour plasmolysis kinetic models is studied. Three water vapour plasmolysis models are simulated and compared. Simulation analysis is carried out using the COMSOL MultiphysicsTM program. Comparative study between the experimental and simulation results of H_2 production from pure water vapour decomposition by DBD plasma in the cylindrical reactor is investigated. Furthermore, the simulation analysis of hydrogen production from Ar-water vapour plasmolysis is determined and the results are compared with the experimental results

Hydrogen production from ammonia decomposition by DBD plasma is studied. The catalytic materials effects on the ammonia decomposition processes are experimentally investigated. The hydrogen concentration results from NH_3 gas decomposition by DBD plasma using Ruthenium materials are compared with the soda glass as catalyst material. The effect of alumina particle thickness on the NH_3 decomposition by DBD plasma is studied. Moreover, the energy and exergy efficiencies are determined and compared for different ammonia decomposition by DBD plasma systems. Also, new suggested formula named integrated effectiveness factor (*IEF*) is suggested to evaluate the system inefficiencies and irreversibility. The new relation (*IEF*) will be evaluated for furnace regenerative and thermal ammonia decomposition systems.

References

- [1] Hennicke, P., and Fishedick, M. Towards Sustainable Energy Systems: The Related Role of Hydrogen. *Energy Policy* 2006; 34:1260-70.
- [2] Marbán, G., and Valdés-Solís, T. Towards the Hydrogen Economy? *Int. J. Hydrogen Energy* 2007; 32(12):1625-37.
- [3] Dutta S. A review on production, storage of hydrogen and its utilization as an energy resource. *Industrial and Engineering Chemistry* 2014; 20:1148-1156.
- [4] R. Kothari, V.V. Tyagi, A. Pathak. Waste-to-energy: A way from renewable energy sources to sustainable development. *Renew Sustain Energy Rev* 2010; 14(9):3164-3170.
- [5] T. Hübert, L. Boon-Brett, G. Black, U. Banach. Hydrogen sensors – A review. *Sensors and Actuators B: Chemical* 2011; 157:329-352.
- [6] Ni M, Leung MKH, Sumathy K, Leung DYC. Water electrolysis-a bridge between renewable resources and hydrogen. *Proceedings of the International Hydrogen Energy forum* 25–28 May 2004; 1:475-480.
- [7] K. Zeng, D. Zhang. Recent progress in alkaline water electrolysis for hydrogen production and applications. *Progress in Energy and Combustion Science* 2010; 36(3):307-326.
- [8] J. Dunn. Hydrogen futures: toward a sustainable energy system. *Int. J Hydrogen Energy* 2007; 27:235-264.
- [9] S. Satyapal, J. Petrovic, C. Read, G. Thomas, G. Ordaz. The U.S. Department of Energy's National Hydrogen Storage Project: Progress towards meeting hydrogen-powered vehicle requirements. *Catalysis Today* 2007; 120: 246-256.
- [10] Ni M, Leung MKH, Sumathy K, Leung DYC. Potential of renewable hydrogen production for energy supply in Hong Kong. *Int. J Hydrogen Energy* 2006; 31:1401-12.
- [11] R.K. Ahluwalia, X. Wang. Direct hydrogen fuel cell systems for hybrid vehicles. *Journal of Power Sources* 2005; 139 (1) (2):152-164.
- [12] G. Gahleitner. Hydrogen from renewable electricity: An international review of power-to-gas pilot plants for stationary applications. *Int. J Hydrogen Energy* 2013; 38 (5):2039-61.
- [13] Balta-Ozkan N, Baldwin E. Spatial development of hydrogen economy in a low-carbon UK energy system. *Int. J Hydrogen Energy* 2013; 38(3):1209-24.
- [14] Houghton T, Cruden A. An investment-led approach to analysing the hydrogen energy economy in the UK. *Int. J Hydrogen Energy* 2009; 34(10):4454-62.
- [15] Pudukudy M, Yaakob Z, Mohammad M, Narayanan B, Sopian K. Renewable hydrogen economy in Asia opportunities and challenges: an overview. *Renew Sustain Energy Rev* 2014; 30: 743-57.
- [16] Fernandes T, Pimenta R, Correias L, García-Camús J, Cabral A, Reyes F, et al. Platform for promoting a hydrogen economy in southwest Europe: the HYRREG project. *Int. J Hydrogen Energy* 2013; 38(18):7594-98.
- [17] Bleischwitz R, Bader N. Policies for the transition towards a hydrogen economy: the EU case. *Energy Policy* 2010; 38(10):5388-98.
- [18] Ball M, Wietschel M, Rentz O. Integration of a hydrogen economy into the German energy system: an optimizing modelling approach. *Int. J Hydrogen Energy* 2007; 32(10):1355-68.

Chapter 1. Introduction

- [19] Andrews J, Shabani B. Where does hydrogen fit in a sustainable energy economy? *Procedia Eng* 2012; 49:15-25.
- [20] McLellan BC. Potential opportunities and impacts of a hydrogen economy for the Australian minerals industry. *Int. J. Hydrogen Energy* 2009; 34(9):3571-77.
- [21] Do Sacramento E, Carvalho PC, de Lima L, Veziroglu T. Feasibility study for the transition towards a hydrogen economy: a case study in Brazil. *Energy Policy* 2013; 62:3-9.
- [22] Liu H, Almansoori A, Fowler M, Elkamel A. Analysis of ontario's hydrogen economy demands from hydrogen fuel cell vehicles. *Int. J. Hydrogen Energy* 2012; 37 (11):8905-16.
- [23] Hajimiragha A, Fowler MW, Canizares CA. Hydrogen economy transition in Ontario Canada considering the electricity grid constraints. *Int. J. Hydrogen Energy* 2009; 34(13):5275-93.
- [24] Ren J, Gao S, Tan S, Dong L. Hydrogen economy in china: strengths, weaknesses, opportunities threats analysis and strategies prioritization. *Renew Sustain Energy Rev* 2015; 41:1230-43.
- [25] Ren J, Gao S, Tan S, Dong L, Scipioni A, Mazzi A. Role prioritization of hydrogen production technologies for promoting hydrogen economy in the current state of China. *Renew Sustain Energy Rev* 2015; 41:1217-29.
- [26] Lu J, Zahedi A, Yang C, Wang M, Peng B. Building the hydrogen economy in China: drivers, resources and technologies. *Renew Sustain Energy Rev* 2013; 23:543-556.
- [27] Pelaez-Samaniego MR, Riveros-Godoy G, Torres- Contreras S, Garcia-Perez T, Albornoz Vintimilla E. Production and use of electrolytic hydrogen in Ecuador towards a low carbon economy. *Energy* 2014; 64:626-631.
- [28] Lee D-H. Development and environmental impact of hydrogen supply chain in Japan: assessment by the CGELCA method in Japan with a discussion of the importance of bio hydrogen. *Int. J. Hydrogen Energy* 2014; 39(33):19294-310.
- [29] Chun D, Woo C, Seo H, Chung Y, Hong S, Kim J. The role of hydrogen energy development in the Korean economy: an input-output analysis. *Int. J. Hydrogen Energy* 2014; 39(15):7627-33.
- [30] Gim B, Yoon WL. Analysis of the economy of scale and estimation of the future hydrogen production costs at onsite hydrogen refueling stations in Korea. *Int. J. Hydrogen Energy* 2012; 37(24):19138-45.
- [31] Bae JH, Cho G-L. A dynamic general equilibrium analysis on fostering a hydrogen economy in Korea. *Energy Econ* 2010; 32:S57-66.
- [32] Milciuvienė S, Milcius D, Praneviciene B. Towards hydrogen economy in Lithuania. *Int. J. Hydrogen Energy* 2006; 31(7):861-866.
- [33] Ramírez-Salgado J, Estrada-Martínez A. Roadmap towards a sustainable hydrogen economy in Mexico. *J. Power Sources* 2004; 129(2):255-263.
- [34] Leaver JD, Gillingham KT, Leaver LH. Assessment of primary impacts of a hydrogen economy in New Zealand using UniSyD. *Int. J. Hydrogen Energy* 2009; 34(7):2855-65.
- [35] Amoo LM, Fagbenle RL. An integrated impact assessment of hydrogen as a future energy carrier in Nigeria's transportation, energy and power sectors. *Int. J. Hydrogen Energy* 2014; 39(24):12409-33.

Chapter 1. Introduction

- [36] Mirza UK, Ahmad N, Harijan K, Majeed T. A vision for hydrogen economy in Pakistan. *Renew Sustain Energy Rev* 2009; 13(5):1111-15.
- [37] Stygar M, Brylewski T. Towards a hydrogen economy in Poland. *Int. J. Hydrogen Energy* 2013; 38(1):1-9.
- [38] Murray ML, Seymour EH, Rogut J, Zechowska SW. Stakeholder perceptions towards the transition to a hydrogen economy in Poland. *Int. J. Hydrogen Energy* 2008; 33(1):20-27.
- [39] Murray ML, Seymour EH, Pimenta R. Towards a hydrogen economy in Portugal. *Int. J. Hydrogen Energy* 2007; 32(15):3223-29.
- [40] Iordache I, Gheorghe AV, Iordache M. Towards a hydrogen economy in Romania: statistics, technical and scientific general aspects. *Int. J. Hydrogen Energy* 2013; 38(28):12231-40.
- [41] Leben J, Ho_cesar S. Correlation between national development indicators and the implementation of a hydrogen economy in Slovenia. *Int. J. Hydrogen Energy* 2012; 37(7):5468-80.
- [42] Brey J, Brey R, Carazo A, Contreras I, Hernandez-Díaz A, Castro A. Planning the transition to a hydrogen economy in Spain. *Int. J. Hydrogen Energy* 2007; 32(10):1339-46.
- [43] Brey J, Brey R, Carazo A, Contreras I, Hernandez-Díaz A, Gallardo V. Designing a gradual transition to a hydrogen economy in Spain. *J Power Sources* 2006; 159(2):1231-40.
- [44] Lee D-H, Hsu S-S, Tso C-T, Su A, Lee D-J. An economy-wide analysis of hydrogen economy in Taiwan. *Renew Energy* 2009; 34(8):1947-54.
- [45] Lee D-H, Lee D-J. Hydrogen economy in Taiwan and Bio hydrogen. *Int. J. Hydrogen Energy* 2008; 33(5):1607-18.
- [46] Lattin W, Utgikar V. Transition to hydrogen economy in the United States: a 2006 status report. *Int. J. Hydrogen Energy* 2007; 32(15):3230-37.
- [47] Urbaniec K, Friedl A, Huisingh D, Claassen P. Hydrogen for a sustainable global economy. *J Clean Prod* 2010; 18:S1-3.
- [48] Blanchette S. A hydrogen economy and its impact on the world as we know it. *Energy Policy* 2008; 36(2):522-30.
- [49] Penner SS. Steps toward the hydrogen economy. *Energy* 2006; 31(1):33-43.
- [50] Maack MK, Skulason JB. Implementing the hydrogen economy. *J Cleaner Prod* 2005; 14:52-64.
- [51] Bertel E. Nuclear energy – the hydrogen economy. *Nucl Energy Agency News* 2004; 22:10-13.
- [52] Duffey R. Green atoms. *Power Energy* 2005; 2(2):8–12.
- [53] Scott DS. Smelling land: the hydrogen defense against climate catastrophe. Ottawa: Canadian Hydrogen Association; 2007.
- [54] Veziroglu TN, Barbir F. Hydrogen energy technologies. Vienna: UNIDO; 1998.
- [55] Veziroglu TN. Quarter century of hydrogen movement 1974-2000. *Int. J. Hydrogen Energy* 2000; 25(12):1143-50.
- [56] Dincer I, Zamfirescu C. Sustainable hydrogen production options and the role of IAHE. *Int. J. Hydrogen Energy* 2012; 37:16266-86.
- [57] Bockris J.O'M. The origin of ideas on a Hydrogen Economy and its solution to the decay of the environment. *Int. J. Hydrogen Energy* 2002; 27:731-40.

Chapter 1. Introduction

- [58] Sinigaglia T, Lewiski F, Martins MES, Siluk JCM. Production, storage, fuel stations of hydrogen and its utilization in automotive applications-a review. *Int. J. Hydrogen Energy* 2017; 42:24597-611.
- [59] Barbir F, Veziroglu TN, Plass Jr HJ. Environmental damage due to fossil fuel use. *Int. J. Hydrogen Energy* 1990; 15(10):739-50.
- [60] Baykara SZ. Hydrogen as fuel: a critical technology? *Int. J. Hydrogen Energy* 2005; 30(5):545-53.
- [61] Baykara SZ. Ecohealth problems and climate change I: anthropogenic climate change and ecohealth: worldwide environmental damage. *Book of Invited Background Papers. Istanbul: IFSSH World Congress Health Challenges of the Third Millenium; August 21-26, 2005:295-313.*
- [62] Veziroglu TN. Ecohealth problems and climate change II: permanent solution to environmental problems: hydrogen energy system. *Book of Invited Background Papers. Istanbul: IFSSH World Congress Health Challenges of the Third Millenium; August 21-26, 2005: 315-35.*
- [63] Veziroglu TN, Gurkan I, Padki MM. Remediation of greenhouse problem through replacement of fossil fuels by hydrogen. *Int. J. Hydrogen Energy* 1989; 14(4):257-66.
- [64] U.S. Energy Information Administration April 2016. Monthly energy review. DOE/ EIA-0035 (2016/04).
- [65] Arup and Siemens, 2016. "Distributed Energy Systems: Flexible and Efficient Power for the New Energy Era." http://w3.siemens.com/topics/global/en/intelligent_infrastructure/pages/intelligent-infrastructure.aspx.
- [66] Hefner RA, GHK Company. The age of energy gases (Fig. 1). *China's Opportunity for Global Energy Leadership*, 2007. Oklahoma City, 1-32.
- [67] Japan's Energy 2 017 <http://www.enecho.meti.go.jp/> Source: [Other than Japan] Data of figures in 2015, IEA Energy Balance of OECD Countries (2017 edition), [Japan].
- [68] Fri RW, Savitz ML. Rethinking energy innovation and social science. *Energy Res Soc Sci* 2014; 1(1):183-87.
- [69] Mach K, Mastrandrea M. Climate change 2014: impacts, adaptation, and vulnerability, vol. 1. Cambridge, New York, NY: Cambridge University Press; 2014.
- [70] Dincer I, Acar C. Smart energy solutions with hydrogen options. *Int. J. Hydrogen Energy* 2018; 43:8579-8599.
- [71] Dincer I, Acar C. Review and evaluation of hydrogen production methods for better sustainability. *Int. J. Hydrogen Energy* 2015; 40(34):11094-111.
- [72] Suleman F, Dincer I, Agelin-Chaab M. Comparative impact assessment study of various hydrogen production methods in terms of emissions. *Int. J. Hydrogen Energy* 2016; [41\(19\)](#): 8364-75.
- [73] Suleman F, Dincer I, Agelin-Chaab M. Environmental impact assessment and comparison of some hydrogen production options. *Int. J. Hydrogen Energy* 2015; 40(21): 6976-87.
- [74] Mandal T. K. and Gregory D.H. Hydrogen: a future energy vector for sustainable development. *J. Mechanical Engineering Since2009*; 224 Part C: 539-558.

Chapter 1. Introduction

- [75] Bicer Y, Dincer I. Environmental impact categories of hydrogen and ammonia driven transoceanic maritime vehicles: A comparative evaluation. 2018; 43(9):4583-4596.
- [76] Xie M, b, Ruan J, Bai W, Qiao Q, Bai L, Zhang J, Li H, Lv F, Fu H. Pollutant payback time and environmental impact of Chinese multi crystalline photovoltaic production based on life cycle assessment. *Journal of Cleaner Production* 2018; 184: 648-659.
- [77] Acar C, Dincer I. Comparative assessment of hydrogen production methods from renewable and non-renewable sources. *Int. J. Hydrogen Energy* 2014; 39:1-12.
- [78] Chaubey R, Sahu S, James OO, Maity S. A review on development of industrial processes and emerging techniques for production of hydrogen from renewable and sustainable sources. *Renew Sustain Energy Rev* 2013; 23:443-462.
- [79] Dincer I. Green methods for hydrogen production. *Int. J. Hydrogen Energy* 2012; 37(2):1954-71.
- [80] Holladay JD, Hu J, King DL, Wang Y. An overview of hydrogen production technologies. *Catal Today* 2009; 139:244-260.
- [81] Freedom CAR& Fuel Partnership, Hydrogen production overview of technology options, Website: http://www.energetics.com/resourcecenter/products/communication/documents/hydrogen_productionbrochure.pdf [Accessed on 19 December 2017].
- [82] Mueller-Langer F, Tzimas E, Kaltchmitt M, Peteves S. Techno-economic assessment of hydrogen production processes for the hydrogen economy for the short and medium term. *Int. J. Hydrogen Energy* 2007; 32:3797-810.
- [83] Ngoh SK, Njomo D. An overview of hydrogen gas production from solar energy. *Renew Sustain Energy Rev* 2012; 16:6782-92.
- [84] Trainham JA, Newman J, Bonino CA, Hoertz PG, Akunuri N. Whither solar fuels? *Curr Options Chem Eng* 2012; 1:204-10.
- [85] Yadav D, Banerjee R. A review of solar thermochemical processes. *Renew Sustain Energy Rev* 2016; 54:497-532.
- [86] Koroneos C, Rovas D. A review on exergy comparison of hydrogen production method from renewable energy sources. *Energy Environ Sci* 2012; 5:6640-51.
- [87] Yilmaz F, Balta MT, Selbas, R. A review of solar based hydrogen production methods. *Renew Sustain Energy Rev* 2016; 56:171-178.
- [88] Abanades A. The challenge of hydrogen production for the transition to a CO₂-free economy. *Agron Res Biosyst Eng Spec Issue* 2012; 1:11-16.
- [89] Bartels JR, Pate MB, Olson NK. An economic survey of hydrogen production from conventional and alternative energy sources. *Int. J. Hydrogen Energy* 2010; 35:8371-84.
- [90] Baykara SZ. Hydrogen: A brief overview on its sources, production and environmental impact. *Int. J. Hydrogen Energy* 2018; 43(23):10605-14.
- [91] Chang R. Chemistry. Boston: McGraw Hill; 2002.
- [92] Dincer I, Zamfirescu C. Sustainable energy systems and applications. Springer Science & Business Media; 2011.
- [93] J. Turner, G. Sverdrup, M.K. Mann, P.-C. Maness, B. Kroposki, M. Ghirardi, R.J. Evans, D. Blake. Renewable hydrogen production. *Int. J Hydrogen Energy* 2008; 32: 379-407.

Chapter 1. Introduction

- [94] J.M. Norbeck, J.W. Heffel, T.D. Durbin, B. Tabbara, J.M. Bowden, M.C. Montani. Hydrogen Fuel for Surface Transportation, Society of Automotive Engineers Inc. Warrendale, PA, 1996, p. 548.
- [95] J. Pettersson, B. Ramsey, D. Harrison. A review of the latest developments in electrodes for unitised regenerative polymer electrolyte fuel cells. *Journal of Power Sources* 2006; 157(1): 28-34.
- [96] S.A. Grigoriev, V.I. Porembsky, V.N. Fateev. Pure hydrogen production by PEM electrolysis for hydrogen energy. *Int. J Hydrogen Energy* 2006; 31 (2): 171-175.
- [97] H. Janssen, J.C. Bringmann, B. Emonts, V. Schroeder. The electrochemical behavior of Ni–MH battery, Ni(OH)₂ electrode and metal hydride electrode. *Int. J Hydrogen Energy* 2004; 29 (7): 759-770.
- [98] M.J. Bradley. Future Wheels Interviews with 44 Global Experts on the Future of Fuel Cells for Transportation and Fuel Cell Infrastructure and a Fuel Cell Primer. Northeast Advanced Vehicle Consortium, Boston, MA; 2000, p. 89.
- [99] C. Koroneos, A. Dompros, G. Roumbas, N. Moussiopoulos. Life cycle assessment of hydrogen fuel production processes. *Int. J Hydrogen Energy* 2004; 29 (14): 1443-50.
- [100] V.M. Aroutiounian, V.M. Arakelyan, G.E. Shahnazaryan. Metal oxide photoelectrodes for hydrogen generation using solar radiation-driven water splitting. *Solar Energy* 2005; 78 (5): 581-592.
- [101] P. Sujatha Devi, A. Das Sharma & H. S. Maiti. Solid Oxide Fuel Cell Materials: A Review. *Transactions of the Indian Ceramic Society* 2004; 63(2): 75-98
- [102] P.A. Erickson, D.Y. Goswami, in: *Proceedings of the Intersociety Energy Conversion Engineering Conference, Hydrogen from solar energy: an overview of theory and current technological status*, Institute of Electrical and Electronics Engineers Inc., Savannah, GA, United States; 2001: 573-580.
- [103] Bhandari R, Trudewind CA, Zapp P. Life cycle assessment of hydrogen production via electrolysis review. *J Clean Prod* 2014; 85:151-163.
- [104] Ball M, Wietschel M. *The hydrogen economy: opportunities and challenges*. Cambridge University Press; 2009.
- [105] Turner J, Sverdrup G, Mann MK, Maness P-C, Kroposki B, Ghirardi M, et al. Renewable hydrogen production. *Int J Energy Res* 2008; 32(5):379-407.
- [106] National Academy of Science, *The Hydrogen Economy: Opportunities, Costs, Barriers, and R&D Needs*, National Academies Press, Washington, DC, 2004.
- [107] Ursua A, Gandia LM, Sanchis P. Hydrogen production from water electrolysis: current status and future trends. *Proc IEEE* 2012; 100 (2):410-426.
- [108] R. Hino, K. Haga, H. Aita, K. Sekita. R&D on hydrogen production by high-temperature electrolysis of steam. *Nuclear Engineering and Design* 2004; 233(1-3): 363-375.
- [109] V. Utgikar, T. Thiesen. Life cycle assessment of high temperature electrolysis for hydrogen production via nuclear energy. *Int. J Hydrogen Energy* 2006; 31 (7): 939-944.
- [110] D.Y. Goswami, S.T. Mirabal, N. Goel, H.A. Ingley, *Fuel Cell Science, Engineering and Technology, A review of hydrogen production technologies*, American Society of Mechanical Engineers, New York, NY, United States/Rochester, NY, United States, 2003:61-74.

Chapter 1. Introduction

- [111] K.R. Schultz. Production of Hydrogen by Fusion Energy: A Review and Perspective. *Fusion Science and Technology* 2003; 44 (2): 393–399.
- [112] AlZahrana A. A., Dincer I. Modeling and performance optimization of a solid oxide electrolysis system for hydrogen production. *Applied Energy* 2018; 225: 471–485.
- [113] S.Z. Baykara. Hydrogen production by direct solar thermal decomposition of water, possibilities for improvement of process efficiency. *Int. J Hydrogen Energy* 2004; 29(14): 1451–1458.
- [114] S. Licht. Solar Water Splitting To Generate Hydrogen Fuel: Photothermal Electrochemical Analysis. *Journal of Physical Chemistry B*, 2003; 107(18): 4253–60.
- [115] S. Yalcin. A review of nuclear hydrogen production. *Int. J Hydrogen Energy* 1989; 14(8): 551–561.
- [116] Sharma S, Ghoshal SK. Hydrogen the future transportation fuel: from production to applications. *Renew Sustain Energy Rev* 2015; 43:1151–8.
- [117] J. M. Ogden, Review of small stationary reformers for hydrogen production, Report to the international energy agency.
- [118] U.S. Department of Energy Hydrogen, Fuel Cells and Infrastructure Technologies Program, Multi-Year Research, Development and Demonstration Plan, U.S. Department of Energy, 2007.
- [119] M. Lewis, M. Serban, J. Basco, J. Figueroa, Low Temperature Thermochemical Cycle Development, Chicago, IL, 2003.
- [120] Orhan MF, Dincer I, Rosen MA. Investigation of an integrated hydrogen production system based on nuclear and renewable energy sources: a new approach for sustainable hydrogen production via copper-chlorine thermochemical cycles. *Int J Energy Res* 2012; 36(15):1388–94.
- [121] J.E. Funk. Thermochemical hydrogen production: past and present. *Int. J Hydrogen Energy* 2001; 26 (3): 185–190.
- [122] Kothari R, Buddhi D, Sawhney R. Comparison of environmental and economic aspects of various hydrogen production methods. *Renew Sustain Energy Rev* 2008; 12(2):553–63.
- [123] Dincer I, Zamfirescu C. Sustainable energy systems and applications. Springer Science & Business Media; 2011.
- [124] Bashiri R, Mohamed NM, Kait CF, Sufian S. Hydrogen production from water photosplitting using Cu/TiO₂ nanoparticles: effect of hydrolysis rate and reaction medium. *Int. J. Hydrogen Energy* 2015; 40(18):6021–37.
- [125] Peng S, Zeng X, Li Y. Titanate nanotube modified with different nickel precursors for enhanced eosin y-sensitized photocatalytic hydrogen evolution. *Int. J. Hydrogen Energy* 2015; 40(18):6038–49.
- [126] Nakata K, Fujishima A. TiO₂ photocatalysis: design and applications. *J Photochem Photobiol C Photochem Rev* 2012; 13(3):169–89.
- [127] Li C, Yuan J, Han B, Shangguan W. Synthesis and photochemical performance of morphology-controlled CdS photocatalysts for hydrogen evolution under visible light. *Int. J. Hydrogen Energy* 2011; 36(7):4271–9.
- [128] Sathish M, Viswanathan B, Viswanath R. Alternate synthetic strategy for the preparation of CdS nanoparticles and its exploitation for water splitting. *Int. J. Hydrogen Energy* 2006; 31(7):891–898.

Chapter 1. Introduction

- [129] J. Turner, T. Deutsch, J. Head, P. Vallett, Photoelectrochemical water systems for H₂ production, in: DOE Hydrogen Program Annual Merit Review, U.S. Department of Energy, Washington, DC, 2007, http://www.hydrogen.energy.gov/pdfs/review07/pd_10_turner.pdf.
- [130] J. Akikusa, S.U.M. Khan. Photoelectrolysis of water to hydrogen in p-SiC/Pt and p-SiC/ n-TiO₂ cells. *Int. J Hydrogen Energy* 2002; 27(9): 863-870.
- [131] G.K. Mor, O.K. Varghese, M. Paulose, K. Shankar, C.A. Grimes. A review on highly ordered, vertically oriented TiO₂ nanotube arrays: Fabrication, material properties, and solar energy applications. *Solar Energy Materials and Solar Cells* 2006; 90 (14): 2011-2075.
- [132] Licht S, Wang B, Mukerji S, Soga T, Umeno M, Tributsch H. Over 18% solar energy conversion to generation of hydrogen fuel; theory and experiment for efficient solar water splitting. *Int. J. Hydrogen Energy* 2001; 26(7):653-659.
- [133] O. Yamada. Generation of hydrogen gas by reforming biomass with superheated steam. *Thin Solid Films* 2006; 509(1-2): 207–211.
- [134] M. Steinberg, Fuel Cell Science, Engineering and Technology–2004, A Highly Efficient Combined Cycle Fossil and Biomass Fuel Power Generation and Hydrogen Production Plant with Zero CO₂ Emission, American Society of Mechanical Engineers, New York, United States/Rochester, NY, United States, 2004: 401-408.
- [135] H.L. Chum, R.P. Overend. Biomass and renewable fuels. *Fuel Processing Technology* 2001; 71 (1-3): 187-195.
- [136] J.A. Satrio, B.H. Shanks, T.D. Wheelock, AIChE Annual Meeting Conference Proceedings, Application of combined catalyst/sorbent on hydrogen generation from biomass gasification, American Institute of Chemical Engineers, New York, NY, United States/Austin, TX, United States, 2004: 297-301.
- [137] P. Lu, Z. Xiong, T. Wang, J. Chang, C. Wu, Y. Chen. Taiyangneng Xuebao/Acta Energiæ Solaris Sinica. 2003; 24: 758-764.
- [138] H. Jacobsen. Heterogeneous Chemistry: Catalysts for Hydrogen Production from Biomass. *Angew. Chem. Int. Ed.* 2004; 43: 1912- 1914.
- [139] G. Chen, X. Lv, Q. Li, N. Deng, L. Jiao, in: Proceedings of the ASME Turbo Expo 2004, Production of hydrogen-rich gas through pyrolysis of biomass in a two stage reactor, American Society of Mechanical Engineers, New York, NY, United States/Vienna, Austria, 2004: 711-721.
- [140] G. Weber, Q. Fu, H. Wu. Energy Efficiency of an Integrated Process Based on Gasification for Hydrogen Production from Biomass. *Developments in Chemical Engineering and Mineral Processing* 2006; 14(1/2): 33-49.
- [141] S. Vasileiadis, Z. Ziaka-Vasileiadou. Biomass reforming process for integrated solid oxide-fuel cell power generation. *Chemical Engineering Science* 2004; 59(22-23): 4853–4859.
- [142] D.B. Levin, H. Zhu, M. Beland, N. Cicek, B.E. Holbein. Potential for hydrogen and methane production from biomass residues in Canada. *Bioresource Technology* 2007; 98 (3): 654–660.
- [143] A. Wood, *Chemical Week* 164 (2002) 30.
- [144] M. Asadullah, S.-I. Ito, K. Kunimori, M. Yamada, K. Tomishige. Energy efficient production of hydrogen and syngas from biomass: development of low-

Chapter 1. Introduction

temperature catalytic process for cellulose gasification. *Environmental Science and Technology* 2002; 36 (20): 4476-81.

[145] M.F. Demirbas. Hydrogen from various biomass species via pyrolysis and steam gasification processes. *Energy Sources* 2006; 28: 245–252.

[146] A. Demirbas. Yields of hydrogen of gaseous products via pyrolysis from selected biomass samples. *Fuel* 2001; 80: 1885-91.

[147] N. Canter. *Tribology and Lubrication Technology* 60 (2004) 14-15.

[148] A. Demirbas, M.F. Demirbas. Biomass and Wastes: Upgrading Alternative Fuels. *Energy Sources* 2003; 25: 317-329.

[149] A. Demirbas. Combustion characteristics of different biomass fuels. *Progress in Energy and Combustion Science* 2004; 30 (2): 219-230.

[150] B. Bagchi, J. Rawlston, R.M. Counce, J.M. Holmes, P.R. Bienkowski. Green Production of Hydrogen from Excess Biosolids Originating from Municipal Waste Water Treatment. *Separation Science and Technology* 2006; 41: 2613–28.

[151] J.R. Paterek. Method and Apparatus for Hydrogen Production from Organic Wastes and Manure. *Industrial Bioprocessing* 27 (2005) 5.

[152] Guo Y S, Fang W J, Lin R S. Coking-inhibition of pyrolysis-cracking of endothermic hydrocarbon fuel. *Journal of Zhejiang University (Engineering Science)* 2005; 39(4): 538–541.

[153] I.I. Salakhov, A.M. Ekimova, A.S. Eiyatdinov, I.N. Diyarov, K.K. Gil'manov, A.R. Shangareeva. Effect of Feedstock Hydrocarbon Composition on the Distribution of Products of Initiated Pyrolysis. *Chemistry and Technology of Fuels and Oils* 2005; 41 (5): 386-394.

[154] X. Hao, L. Guo. Review on investigation of hydrogen production by biomass catalytic gasification in supercritical water. *Journal of Chemical Industry and Engineering (China)* 2002; 53 (3): 221-228.

[155] Kirtay E. Recent advances in production of hydrogen from biomass. *Energy Convers Manag* 2011; 52(4):1778-89.

[156] J. Wills. Biohydrogen pathways. *Fuel Cell Review* 2006; 2 (6): 23-26.

[157] YT. Fan, YH. Zhang, SF. Zhang, HW. Hou, BZ. Ren. Efficient conversion of wheat straw wastes into biohydrogen gas by cow dung compost. *Bio resource Technology* 2006; 97 (3): 500-505.

[158] Y. W. Shu, N. L. Chi, S. C. Jian, S. C. Jo. Biohydrogen production with anaerobic sludge immobilized by ethylene-vinyl acetate copolymer. *Int. J Hydrogen Energy* 2005; 30 (13-14): 1375-1381.

[159] M. Cai, J. Liu, Y. Wei. Enhanced Biohydrogen Production from Sewage Sludge with Alkaline Pretreatment. *Environmental Science and Technology* 2004; 38 (11): 3195- 3202.

[160] D.B. Levin, L. Pitt, M. Love. Biohydrogen production: prospects and limitations to practical application. *Int. J Hydrogen Energy* 2004; 29 (2): 173-185.

[161] H.N. Gavala, I.V. Skiadas, B.K. Ahring, G. Lyberatos. Potential for biohydrogen and methane production from olive pulp. *Water Science and Technology* 2005; 52 (1-2): 209-215.

[162] S.K. Khanal, W.-H. Chen, L. Li, S. Sung. Biohydrogen Production in Continuous-Flow Reactor Using Mixed Microbial Culture. *Water Environment Research* 2006; 78 (2): 110-117.

Chapter 1. Introduction

- [163] K.L. Kovács, G. Maróti, G. Rákhely. A novel approach for biohydrogen production. *Int. J Hydrogen Energy* 2006; 31(11):1460-68.
- [164] K. Bélafi-Bako, D. Búcsu, Z. Pientka, B. Bálint, Z. Herbel, K.L. Kovács, M. Wessling. Integration of biohydrogen fermentation and gas separation processes to recover and enrich hydrogen. *Int. J Hydrogen Energy* 2006; 31 (11): 1490-1495.
- [165] K. Nath, D. Das. Biohydrogen production as a potential energy resource-Present state-of-art. *Journal of Scientific and Industrial Research* 2004; 63: 729-738.
- [166] Y. Takeuchi, Y. Amao. Biohydrogen Production from Sucrose Using the Light-Harvesting Function of Zinc Chlorophyll-a. *Bulletin of the Chemical Society of Japan* 2005; 78 (4): 622-625.
- [167] H. Sun-Kee, S. Hang-Sik. Biohydrogen production by anaerobic fermentation of food waste. *Int. J Hydrogen Energy* 2004; 29 (6): 569-577.
- [168] M.D. Redwood, L.E. Macaskie. A two-stage, two-organism process for biohydrogen from glucose. *Int. J Hydrogen Energy* 2006; 31(11): 1514-1521.
- [169] B. Bálint, Z. Bagi, A. Tóth, G. Rákhely, K. Perei, K.L. Kovács. Utilization of keratin-containing biowaste to produce biohydrogen. *Applied Microbiology and Biotechnology* 2005; 69 (4) 404-410.
- [170] YS. Zhao, XF. Teng, P. Zhang, TW. Tan, Beijing Huagong Daxue Xuebao (Ziran Kexueban)/Journal of Beijing University of Chemical Technology (Natural Science Edition) 2005; 32: 1-4.
- [171] C. Jo-Shu, L. Kuo-Shing, L. Pin-Jei. Biohydrogen Production with Fixed-Bed Bioreactors. *Int. J Hydrogen Energy (UK)* (2002); 1167-74 (Elsevier, Ede, Netherlands).
- [172] S.W. Van Ginkel, O. Sang-Eun, B.E. Logan. Biohydrogen gas production from food processing and domestic wastewaters. *Int. J Hydrogen Energy* 2005; 30 (15): 1535-42.
- [173] Y. Amao, N. Nakamura. Biohydrogen production with the light-harvesting function of grana from spirulina and colloidal platinum. *Int. J Hydrogen Energy* 2006; 31 (1): 39-42.
- [174] YF. Li, NQ. Ren, GX. Zheng, M. Liu, LJ. Hu, Y. Chen, XJ. Wang, *Journal of Harbin Institute of Technology (New Series)* 2005; 12:159-163.
- [175] K. Vijayaraghavan, D. Ahmad. Biohydrogen generation from palm oil mill effluent using anaerobic contact filter. *Int. J Hydrogen Energy*; 31(10): 1284-91.
- [176] K. Sang-Hyoun, H. Sun-Kee, S. Hang-Sik. Feasibility of biohydrogen production by anaerobic co-digestion of food waste and sewage sludge. *Int. J Hydrogen Energy* 2004; 29(15): 1607-16.
- [177] T.A. Kotsopoulos, R.J. Zeng, I. Angelidaki. Biohydrogen Production in Granular Up-Flow Anaerobic Sludge Blanket (UASB) Reactors With Mixed Cultures Under Hyper-Thermophilic Temperature (70°C). *Biotechnology and Bioengineering* 2006; 94(2): 296-302.
- [178] K. Vijayaraghavan, D. Ahmad, M.K.B. Ibrahim. Biohydrogen generation from jackfruit peel using anaerobic contact filter. *Int. J Hydrogen Energy* 2006; 31(5): 569-579.
- [179] R. Horváth, T. Orosz, B. Bálint, M. Wessling, G.H. Koops, G.C. Kapantaidakis, K. Bélafi-Báko. Application of gas separation to recover biohydrogen produced by *Thiocapsa roseopersicina*. *Desalination* 2004; 163: 261-265.

Chapter 1. Introduction

- [180] E. Franchi, C. Tosi, G. Scolla, G. Della Penna, F. Rodriguez, P.M. Pedroni. Metabolically Engineered *Rhodobacter sphaeroides* RV strains for Improved Biohydrogen Photoproduction Combined with Disposal of Food Wastes. *Marine Biotechnology* 2004; 6(6): 552-565.
- [181] P.M. Vignais, J.-P. Magnin, J.C. Willison. Increasing biohydrogen production by metabolic engineering. *Int. J Hydrogen Energy* 2006; 31(11): 1478-83.
- [182] K.-S. Lee, Y.-S. Lo, Y.-C. Lo, P.-J. Lin, J.-S. Chang, *Enzyme and Microbial Technology* 35 (2004) 605-612.
- [183] D. Carrieri, D. Kolling, G. Ananyev, G.C. Dismukes, Prospecting for biohydrogen fuel. *Industrial Biotechnology* 2006; 2(2): 133-137.
- [184] Hawkes FR, Hussy I, Kyazze G, Dinsdale R, Hawkes DL. Continuous dark fermentative hydrogen production by mesophilic microflora: principles and progress. *Int. J. Hydrogen Energy* 2007; 32(2):172-184.
- [185] I.K. Kapdan, F. Kargi, *Enzyme and Microbial Technology* 38 (2006) 569–582.
- [186] Cherryman S, Maddy J, Hawkes F, Hawkes D, Dinsdale R, Guwy A, et al. *Hydrogen and wales*. Pontypridd, Wales, UK: University of Glamorgan; 2004.
- [187] Dincer I, Acar C. A review on clean energy solutions for better sustainability. *International Journal of Energy Research* 2015; 39(5):585-606.
- [188] Guwy A, Dinsdale R, Kim J, Massanet-Nicolau J, Premier G. Fermentative biohydrogen production systems integration. *Bioresour Technol* 2011; 102(18):8534-42.
- [189] D.J. Wilhelm, D.R. Simbeck, A.D. Karp, R.L. Dickenson. Syngas production for gas-to-liquids applications: technologies, issues and outlook. *Fuel Processing Technology*; 71(1-3): 139-148.
- [190] J. Holladay, E. Jones, D.R. Palo, M. Phelps, Y.-H. Chin, R. Dagle, J. Hu, Y. Wang, E. Baker, *Materials Research Society Symposium—Proceedings, Miniature Fuel Processors for Portable Fuel Cell Power Supplies*, Materials Research Society, Boston, MA, United States, (2003), pp. 429–434.
- [191] R.M. Navarro, M.A. Pen a, J.L.G. Fierro. Hydrogen Production Reactions from Carbon Feedstocks: Fossil Fuels and Biomass. *Chemical Reviews* 2007; 107(10): 3952-91.
- [192] R. Farrauto, S. Hwang, L. Shore, W. Ruettinger, J. Lampert, T. Giroux, Y. Liu, O. Ilinich. New Material Needs for Hydrocarbon Fuel Processing: Generating Hydrogen for the PEM Fuel Cell Annual Review of Materials Research 2003; 33:1-27.
- [193] D.L. King, K.P. Brooks, C.M. Fischer, L. Pederson, G. Rawlings, S.V. Stenkamp, W. TeGrotenhuis, R. Wegeng, G.A. Whyatt, in: Y. Wang, J.D. Holladay (Eds.), *Microreactor Technology and Process Intensification*, ACS, Washington DC (2005) pp. 119-128.
- [194] J. Rostrup-Nielsen, in: I.T. Horvath (Ed.), *Encyclopedia of Catalysis*, Wiley Interscience, (2003) 4.
- [195] C.S. Song. Fuel processing for low-temperature and high-temperature fuel cells: Challenges, and opportunities for sustainable development in the 21st century. *Catalysis Today* 2002; 77(1-2): 17-49.
- [196] M.W. Twigg (Ed.), *Catalyst Handbook*, Wolfe Publishing Ltd., London, 1989.

Chapter 1. Introduction

- [197] G. Hoogers, Fuel Cell Technology Handbook, CRC Press, Boca Raton (2003) pp. 5-1–5-23.
- [198] Pietrogrande, P. and M. Bezzeccheri, “Fuel processing.” Fuel Cell Systems, chap. 4, Blomen, LJMJ and MN Mugerwa, pp. 121-151, Plenum Press, New York, 1993.
- [199] M. Krumpelt, T.R. Krause, J.D. Carter, J.P. Kopasz, S. Ahmed. Fuel processing for fuel cell systems in transportation and portable power applications. *Catalysis Today* 2002; 77(1-2): 3-16.
- [200] K. Aasberg-Petersen, I. Dybkjær, C.V. Ovesen, N.C. Schjødt, J. Sehested, S.G. Thomsen. Natural gas to synthesis gas - Catalysts and catalytic processes. *Journal of Natural Gas Science and Engineering* 2011; 3: 423-459.
- [201] A.M. Adris, B.B. Pruden. On the reported attempts to radically improve the performance of the steam methane reforming reactor. *Canadian Journal of Chemical Engineering* 1996; 74(2): 177-186.
- [202] G. Kolb, R. Zapf, V. Hessel, H. Lowe. Propane steam reforming in microchannels—results from catalyst screening and optimization. *Appl. Catal. A Gen* 2004; 227:155-166.
- [203] Y. Wang, Y. Chin, R.T. Rozmiarek, B.R. Johnson, Y. Gao, J.M. Watson, A.Y. Tonkovich, D.P. Vanderwiel. Highly active and stable Rh/MgOAl₂O₃ catalysts for methane steam reforming. *Catal. Today* 2004; 98(4): 575-581.
- [204] H. Song, L. Zhang, U.S. Ozkan. Effect of synthesis parameters on the catalytic activity of Co–ZrO₂ for bio-ethanol steam reforming. *Green Chemistry* 2007; 9(6): 686-694.
- [205] H. Song, L. Zhang, R.B. Watson, D. Braden, U.S. Ozkan. Investigation of bio-ethanol steam reforming over cobalt-based catalysts. *Catalysis Today* 2007; 129 (1-3): 346-354.
- [206] J.R. Rostrup-Nielsen. Activity of nickel catalysts for steam reforming of hydrocarbons. *Journal of Catalysis* 1973; 31 (2) 173-199.
- [207] J. Wei, E. Iglesia. Mechanism and Site Requirements for Activation and Chemical Conversion of Methane on Supported Pt Clusters and Turnover Rate Comparisons among Noble Metals. *J. Phys. Chem. B* 2004; 108(13): 4094–4103.
- [208] J.R.H. Ross, in: M.W. Roberts, J.M. Thomas (Eds.). *Surface and Defect Properties of Solids*. Chemical Society, London (1974) 34.
- [209] K. McHugh, *Hydrogen Production Methods*, MPR Associates Inc., 2005, p. 41.
- [210] Rostrup-Nielsen, J. R. Conversion of hydrocarbons and alcohols for fuel cells. *Phys. Chem. Chem. Phys.* 2001; 3: 283-288.
- [211] Pettersson L. J., Westerholm R. State of the art of multi-fuel reformers for fuel cell vehicles: problem identification and research needs. *Int. J. Hydrogen Energy* 2001; 26(3): 243-264.
- [212] Armor J. N. The multiple roles for catalysis in the production of H₂. *Appl. Catal. A, Gen.* 1999; 176(2): 159-176.
- [213] Schmidt V. M., Brockerhoff P., Hohlein B., Menzer R., Stimming U. Utilization of methanol for polymer electrolyte fuel cells in mobile systems. *J. Power Sources* 1994; 49(1-3): 299-313.

Chapter 1. Introduction

- [214] Takezawa N., Iwasa N. Steam reforming and dehydrogenation of methanol: Difference in the catalytic functions of copper and group VIII metals. *Catal. Today* 1997; 36(1): 45-56.
- [215] Haga, F., Nakajima T., Miya H., Mishima S. Catalytic properties of supported cobalt catalysts for steam reforming of ethanol. *Catal. Lett.* 1997; 48(3-4): 223-227.
- [216] Cavallaro S., Freni S. Ethanol steam reforming in a molten carbonate fuel cell. A preliminary kinetic investigation. *Int. J. Hydrogen Energy* 1996; 21(6): 465-469.
- [217] Angeli SD, Monteleone G, Giaconia A, Lemonidou AA. State-of-the-art catalysts for CH₄ steam reforming at low temperature. *Int. J. Hydrogen Energy* 2014; 39(5):1979-97.
- [218] Czernikowski A. Glidarc. assisted preparation of the synthesis gas from natural gas and waste hydrocarbons gases. *Oil Gas Sci Technol Rev IFP* 2001; 2(56):181–198.
- [219] Timm D.L., Onsan Z.I. On Board Fuel Conversion for Hydrogen-Fuel-Cell-Driven Vehicles. *Catalysis Review* 2001; 43: 31-84.
- [220] Hohn K.L., Schmidt L.D. Partial oxidation of methane to syngas at high space velocities over Rh-coated spheres. *Applied Catalysis A: General* 2001; 211(1): 53-68.
- [221] Krummenacher J.J., West K.N., Schmidt L.D. Catalytic partial oxidation of higher hydrocarbons at millisecond contact times: decane, hexadecane, and diesel fuel. *Journal of Catalysis* 2003; 215: 332-343.
- [222] Pino L., Recupero V., Beninati S., Shukla A.K., Hegde M.S., Bera P. Catalytic partial-oxidation of methane on a ceria-supported platinum catalyst for application in fuel cell electric vehicles. *Applied Catalysis A: General* 2002; 225: 63-75.
- [223] Halit Eren Figen E. H., Sema Z. Baykara Z. S., Effect of ruthenium addition on molybdenum catalysts for syngas production via catalytic partial oxidation of methane in a monolithic reactor. *Int. J Hydrogen Energy* 2018; 43(2): 1129-138.
- [224] Basini L., Aasberg-Petersen K., Guarinoni A., stberg M. Catalytic partial oxidation of natural gas at elevated pressure and low residence time. *Catalysis Today*. 64 (2001) 9-20.
- [225] Hickman D.A., Schmidt L.D. Synthesis gas formation by direct oxidation of methane over Pt monoliths. *Journal of Catalysis* 1992; 138(1): 267-282.
- [226] Hickman D., Hauptfear E., Schmidt L. Synthesis gas formation by direct oxidation of methane over Rh monoliths. *Catalysis Letters* 1993; 17(3-4): 223-237.
- [227] Hickman D.A., Schmidt L.D. Production of syngas by direct catalytic oxidation of methane. *Science*. 1993; 259: 343-346.
- [228] D. D. Nogare, N.J. Degenstein, R. Horn, P. Canu, L.D. Schmidt. Modeling spatially resolved profiles of methane partial oxidation on Rh foam catalyst with detailed chemistry. *Journal of Catalysis* 2008; 258:131-142.
- [229] D.D. Nogare, N.J. Degenstein, R. Horn, P. Canu, L.D. Schmidt. Modeling spatially resolved data of methane catalytic partial oxidation on Rh foam catalyst at different inlet compositions and flowrates. *Journal of Catalysis* 2011; 277:134-148.
- [230] Onsan Z. I., Avci A.K. Reactor Design for Fuel Processing. *Fuel Cells: Technologies for Fuel Processing*. Elsevier, Amsterdam, 2011. pp. 451-516.
- [231] Bellows R.J., Technical Challenges for Hydrocarbon Fuel Reforming, DOE, Balti- more, MD, 1999.

Chapter 1. Introduction

- [232] Joensen F., Reostrup-Neilsen J.R. Conversion of hydrocarbons and alcohols for fuel cells. *Journal of Power Sources* 2002; 105(2): 195-201.
- [233] Muhammad H. R. (2011) Experimental Studies and Modeling of Synthesis Gas Production and Fischer-Tropsch Synthesis. **Ph.D. Thesis**, Norwegian University of Science and Technology, Trondheim.
- [234] Ghosh De. Thermodynamic performance simulation of a coal gasification and SOFC based combined cogeneration plant by energy and exergy analyses. *Int J Exergy* 2005; 2:366-384.
- [235] Orhan MF, Dincer I, Rosen MA. Exergoeconomic analysis of a thermochemical copper-chlorine cycle for hydrogen production using specific exergy cost (SPECO) method. *Thermochim Acta* 2010; 497:60–66.
- [236] Orhan MF. Conceptual design, analysis and optimization of nuclear-based hydrogen production via copper-chlorine thermochemical cycles. Doctoral dissertation, Faculty of Engineering and Applied Science, Mechanical Engineering Program. University of Ontario Institute of Technology, Oshawa, Canada, April 2011.
- [237] Laurendeau N.M. Heterogeneous kinetics of coal char gasification and combustion. *Progress in Energy and Combustion Science* 1978; 4: 221-270.
- [238] H. Watanabe, M. Otaka. Numerical simulation of coal gasification in entrained flow coal gasifier. *Fuel* 2006; 85:1935-43.
- [239] Miller BG. Coal energy systems. Elsevier 978-0124974517; 2005.
- [240] Aghahosseini S, Dincer I, Naterer GF. Integrated gasification and Cu-Cl cycle for trigeneration of hydrogen, steam and electricity. *Int. J. Hydrogen Energy* 2011; 36:2845-54.
- [241] Giuffrida A, Romano MC, Lozza G. Thermodynamic analysis of air-blown gasification for IGCC applications. *Appl Energy* 2011; 88:3949-58.
- [242] Jordal K, Anantharaman R, Peters TA, Berstad D, Morud J, Neksa P, et al. Highpurity H₂ production with CO₂ capture based on coal gasification. *Energy* 2015; 88:9-17.
- [243] Gnanapragasam NV, Reddy BV, Rosen MA. Hydrogen production from coal gasification for effective downstream CO₂ capture. *Int. J. Hydrogen Energy* 2010; 35:4933-43.
- [244] Seyitoglu SS, Dincer I, Kilicarslan A. Assessment of an IGCC based trigeneration system for power, hydrogen and synthesis fuel production. *Int. J. Hydrogen Energy* 2015; 41:1-8.
- [245] Ozturk M, Dincer I. Thermodynamic assessment of an integrated solar power tower and coal gasification system for multi-generation purposes. *Energy Convers Manage* 2013; 76:1061-72.
- [246] Zhu L, Zhang Z, Fan J, Jiang P. Polygeneration of hydrogen and power based on coal gasification integrated with a dual chemical looping process: thermodynamic investigation. *Comput Chem Eng* 2016; 84:302-312.
- [247] Liszka M, Malik T, Manfrida G. Energy and exergy analysis of hydrogen-oriented coal gasification with CO₂ capture. *Energy* 2012; 45:142–50.
- [248] Al-Zareer M, Dincer I, Rosen MA. Development and analysis of an integrated system with direct splitting of hydrogen sulfide for hydrogen production. *Int J Hydrogen Energy* 2016; 41:20036–62.

Chapter 1. Introduction

- [249] Cohce MK, Dincer I, Rosen MA. Thermodynamic analysis of hydrogen production from biomass gasification. *Int. J. Hydrogen Energy* 2010; 35:4970–80.
- [250] Arabkhalaj A, Ghassemi H, Shahsavan Markadeh R. Thermodynamic evaluation of integrated gasification combined cycle: comparison between high-ash and low-ash coals. *Int J Energy Res* 2016; 40:1638–51.
- [251] Al-Zareer M, Dincer I, Rosen MA. Analysis and assessment of a hydrogen production plant consisting of coal gasification, thermochemical water decomposition and hydrogen compression systems. *Energy Conversion and Management* 2018; 157: 600-618.
- [252] Lylum S. CO₂-Free hydrogen from hydrocarbons-the Kvaerner CB&H process. In: 10th world hydrogen energy conference, Cocoa Beach, FL; June 1994.
- [253] Yan W, Hoekman K. Production of CO₂-free hydrogen from methane dissociation: a review. *Environ Prog Sustain Energy* 2014; 33(1):213-219.
- [254] Ashik UPM, Wan Daud WMA, Abbas HF. Production of greenhouse gas free hydrogen by thermocatalytic decomposition of methane ea review. *Renew Sustain Energy Rev* 2015; 44:221-256.
- [255] Gaudernack B, Lylum S. Hydrogen from natural gas without release of CO₂ to the atmosphere. *Int. J. Hydrogen Energy* 1998; 23(12):1087-93.
- [256] Damen K, Van Troost M, Faaij A, Turkenburg W. A comparison of electricity and hydrogen production systems with CO₂ capture and storage, Part A: review and selection of promising conversion and capture technologies. *Prog Energy Combust Sci* 2006; 32:215-246.
- [257] Agrafiotis C, Von Storch H, Roeb M, Sattler C. Solar thermal reforming of methane feedstocks for hydrogen and syngas production-a review. *Renew Sustain Energy Rev* 2014; 29:656-82.
- [258] Baykara SZ, Bilgen E. Synthesis gas and H₂ production from solar gasification of Albertan coal. *Energy Convers Manag* 1985; 25(4):391-398.
- [259] Zeng K, Gauthier D, Soria J, Mazza G, Flamant G. Solar pyrolysis of carbonaceous feedstocks: a review. *Sol Energy* 2017; 156:73-92
- [260] Coelho B, Oliveira AC, Mendes A. Concentrated solar power for renewable electricity and hydrogen production from water-a review. *Energy Environ Sci* 2010; 3:1398-405.
- [261] Steinfeld A. Solar thermochemical production of hydrogen a review. *Sol Energy* 2005; 78:603-615.
- [262] W. Jucks and A.G. Sandhoff, *Theory of Coal Pyrolysis*. The Pennsylvania State College, State College, Penna, 1980, pp. 567-569.
- [263] A.-G. Collot, Matching gasifiers to coals. IEA Clean Coal Centre, October 2002.
- [264] Wu W., Yoshikawa K. R&D on Micro-pyrolyzer for Solid Wastes Using High Temperature Steam and Air. *JSME International Journal Series B-Fluids and Thermal Engineering* 2002; 45(3):487-491.
- [265] A. Demirbas, G. Arin. Hydrogen from Biomass via Pyrolysis: Relationships between Yield of Hydrogen and Temperature. *Energy Sources* 2004; 26 (11): 1061-69.
- [266] A. Demirbas. Recovery of Chemicals and Gasoline-Range Fuels from Plastic Wastes via Pyrolysis. *Energy Sources* 2005; 27:1313-19.

Chapter 1. Introduction

- [267] J. Yi Zheng, G. Chao, H. Wen Kuang, Z. Yanqiu, A. Huczko, M. Bystrzejewski, M. Roe, L. Chi Young, S. Acquah, H. Kroto, D.R.M. Walton. A Systematic Study of the Large-Scale Synthesis and Characterization of Carbon Spheres Prepared By Direct Pyrolysis of Hydrocarbons. *Carbon* 2005; 43: 1944-1953.
- [268] Karaeva A.P., Mordkovich V.Z., Tretyakov V.F., *Solid Fuel Chemistry* 2005; 39: 61-76.
- [269] N. Muradov. Emission-free fuel reformers for mobile and portable fuel cell applications. *Journal of Power Sources* 2003; 118: 320-324.
- [270] Liu CJ, Xu GH, Wang T. Non-thermal plasma approaches in CO₂ utilization. *Fuel Process* 1999; 58:119-134.
- [271] Locke, B. R.; Sato, M.; Sunka, P.; Hoffmann, M. R.; Chang, J. S. Electrohydraulic Discharge and Nonthermal Plasma for Water Treatment. *Ind. Eng. Chem. Res.* 2006; 45: 882-905.
- [272] [Du](#) C, [Mo](#) J, and [Li](#). H. Renewable Hydrogen Production by Alcohols Reforming Using Plasma and Plasma-Catalytic Technologies: Challenges and Opportunities. *Chem. Rev.* 2015; 115(3): 1503–42.
- [273] Bromberg L, Cohn DR, Rabinovich A, Alexeev N. Hydrogen manufacturing using low current, non-thermal plasma boosted fuel converters. PSFC/RR-01-1, 2001.
- [274] Bromberg L., Cohn D. R., Rabinovich A., Alexeev N. Plasma catalytic reforming of methane. *Int. J. Hydrogen Energy* 1999; 24:1131-37.
- [275] Boulos, M.I. New frontiers in thermal plasma processing. *Pure Appl. Chem* 1996; 68(5): 1007- 1010.
- [276] Min, T. and K. Yoshikawa, 2004. Performance Demonstration of Dual-Fueled Diesel Engine Combine with a Gasifier of Solid Wastes. Paper presented at the 23rd International Conference on Incineration and Thermal Treatment Technologies, Phoenix, Arizona.
- [277] Inaba T; Nagano M.; Endo M. Investigation of Plasma Treatment for Hazardous Wastes Such As Fly Ash and Asbestos *Electrical Eng. In Japan.* 1999; 126(3): 831-838.
- [278] Park, H. S.; Lee, B. J.; Kim, S. J. J. Characteristics of PE Gasification by Steam Plasma. *J. Ind. Eng. Chem.* 2006; 12(2): 216-223.
- [279] G. Z. Ye, E. Burstrom, M. Kuhn, and J. Piret. Reduction of steel-making slags for recovery of valuable metals and oxide materials. *Scand. J. Metall.* 2003; 32(1): 7-14.
- [280] Ramachandran, K.; Kikukawa, N. Thermal Plasma In-Flight Treatment of Electroplating Sludge. *IEEE Trans. Plasma Sci.* 2002; 30(1): 310-317.
- [281] Nishikawa H., Ibe M., Tanaka M., Ushio M., Takemoto T., Tanaka K., Tanahashi N. and Ito T. A treatment of carbonaceous wastes using thermal plasma with steam. *Vacuum* 2004; 73:589-593.
- [282] Cubas, A. L. V.; Souza, I. G.; Debacher, N. A.; Carasek, E. Desenvolvimento de uma tocha de plasma de corrente continua com eletrodos de grafite e sistema de nebulização integrada para a decomposição de CCl₄. *J. Braz. Chem. Soc.* 2005; 16: 531-534.
- [283] Galeno, G.; Minutillo, M.; Perna, A. From waste to electricity through integrated plasma gasification/fuel cell (IPGFC) system. *Int. J. Hydrogen Energy* 2011; 36:1692 -701.

Chapter 1. Introduction

- [284] Gomez E., Rani D. A., Cheeseman C. R., Deegan D., Wise M., Boccaccini A. R. Thermal plasma technology for the treatment of wastes: A critical review. *J. Hazard. Mater.* 2009; 161: 614-626.
- [285] T. Paulmier, L. Fulcheri, Use of non-thermal plasma for hydrocarbon reforming. *Chemical Engineering Journal* 2005; 106: 59-71.
- [286] L. Bromberg, D.R. Cohn, A. Rabinovich, Plasma reformer-fuel cell system for decentralized power applications. *Int. J Hydrogen Energy* 1997; 22: 83-94.
- [287] Petitpas, G.; Rollier, J. D.; Darmon, A.; Gonzalez-Aguilar, J.; Metkemeijer, R.; Fulcheri, L. A comparative study of non-thermal plasma assisted reforming technologies *Int. J. Hydrogen Energy* 2007; 32: 2848-67.
- [288] Tsai, H. L.; Wang, C. S.; Lee, C. H. Hydrogen production in a thermal plasma hydrogen reformer using ethanol steam reforming. *J. Chin. Inst. Eng.* 2008; 31:417-425.
- [289] K. Bouamra, N.B. Simiand, F. Jorand, S. Pasquiers, C. Postel. Decomposition of isooctane using a dielectric barrier discharge. 16th International symposium on plasma chemistry, Taormina, 2003.
- [290] M.G. Sobacchi, A.V. Saveliev, A.A. Fridman, L.A. Kennedy, S. Ahmed, T. Krause. Experimental assessment of a combined plasma/catalytic system for hydrogen production via partial oxidation of hydrocarbon fuels. *Int. J Hydrogen Energy* 2002; 27: 635-42.
- [291] L. Bromberg, D.R. Cohn, A. Rabinovich, N. Alexeev, N. Samokhin, K. Hadidi. On-board plasmatron hydrogen production for improved vehicles. PSFC JA06-03. (2006).
- [292] K. Iskenderova, P. Porshnev, A. Gutsol, A. Saveliev, A. Fridman, L. Kennedy. Methane conversion into syn-gas in gliding arc discharge. 15th International symposium on plasma chemistry, Orleans, 2001.
- [293] C.S. Kalra, A.F. Gutsol, A.A. Fridman. Gliding arc discharges as a source of intermediate plasma for methane partial oxidation. *IEEE Trans Plasma Sci.* 33 (2005).
- [294] E.E. Ahmar, C. Met, O. Aubry, A. Khacef, J.M. Cormier. Hydrogen enrichment of a methane-air mixture by atmospheric pressure plasma for vehicle applications. *Chemical Engineering Journal* 2006; 116:13-18.
- [295] T. Kappes, W. Schiene, T. Hammer. Energy balance of a dielectric barrier discharge for hydrocarbon steam reforming. 8th international symposium of high pressure low temperature plasma chemistry, Pyhajarve, Estonia, 2002.
- [296] H. Sekiguchi, Y. Mori. Steam plasma reforming using microwave discharge. *Thin Solid Films.* 2003; 435: 44-48.
- [297] V. Rusanov, A. Babaritskii, E. Gerasimov, M. Deminskii, S. Demkin, V. Zhivotov, et al. Stimulation of the partial oxidation of methane in a microwave discharge. *Doklady Physics* 2003; 48: 119-122.
- [298] A.I. Babaritskii, I.E. Baranov, M.B. Bibikov, S.A. Demkin, V.K. Zhivotov, G.M. Konovalov, et al. Partial hydrocarbon oxidation processes induced by atmospheric-pressure microwave-discharge plasma. *High Energy Chemistry* 2004; 38:407-411.
- [299] J.M. Cormier, I. Rusu. Syngas production via methane steam reforming with oxygen: plasma reactors versus chemical reactors *Journal of Physics D: Applied Physics* 2001; 34:2798-803.

Chapter 1. Introduction

- [300] Y. Sekine, S. Asai, K. Urasaki, S. Kado, E. Kikuchi, M. Matsukata. Development of liquid fuel reformer using low energy pulse discharge at room temperature. 16th International symposium on plasma chemistry, Taormina, 2003.
- [301] F. Ouni, A. Khacef, J.M. Cormier. Methane steam reforming with oxygen in a sliding discharge reactor. 17th International symposium on plasma chemistry, Toronto, 2005.
- [302] L. Bromberg, A. Rabinovich. Homogeneous charge compression ignition control by the use of plasmatron fuel converter technology. PSFC/JA- 01-18. (2001).
- [303] L. Bromberg, D.R. Cohn, K. Hadidi. Plasmatron reformation of renewable fuels. PSFC/JA-05-03. (2005).
- [304] O. Aubry, C. Met, A. Khacef, J.M. Cormier. On the use of a non-thermal plasma reactor for ethanol steam reforming. Chemical Engineering Journal 2005; 106: 241-247.
- [305] A. Czernikowski, M. Czernikowski, K. Wesolowska. Glidarc-assisted production of synthesis gas from rapeseed oil. 1st European hydrogen energy conference, Grenoble, France, 2003.
- [306] Z. Yan, L. Chen, H. Wang, Hydrogen generation from reforming of lower alcohols aqueous solution by glow discharge plasma under liquid. Journal of Chemical Industry and Engineering (China) 2006; 57(6):1432-37.
- [307] Hammer, T.; Kappes, T.; Baldauf, M. Plasma catalytic hybrid processes: gas discharge initiation and plasma activation of catalytic processes. Catal. Today 2004; 89: 5-14.
- [308] R.B. Biniwale, A. Mizuno, M. Ichikawa. Hydrogen production by reforming of iso-octane using spray-pulsed injection and effect of non-thermal plasma. Applied Catalysis A: General; 276 (1-2):169-177.
- [309] C.J. O'Brien, S. Hochgreb, A. Rabinovich, L. Bromberg, D.R. Cohn, in: Proceedings of the Intersociety Energy Conversion Engineering Conference, Hydrogen Production via Plasma Reformers, IEEE, Piscataway, NJ, USA/Washington, DC, USA, 1996; pp.1747-1752.
- [310] O. Mutaf-Yardimci, A.V. Saveliev, A.A. Fridman, L.A. Kennedy. Employing plasma as catalyst in hydrogen production. Int. J Hydrogen Energy 1998; 23(12): 1109-1111.
- [311] Y. Matsui, S. Kawakami, K. Takashima, S. Katsura, A. Mizuno. Liquid-Phase Fuel Re-forming at Room Temperature Using Nonthermal Plasma. Energy and Fuels 2005; 19(4): 1561-65.
- [312] Bromberg, L.; Cohn, D. R.; Rabinovich, A.; Alexeev, N.; Samokhin, N.; Hadidi; Kaaja, R. Plasma Science and Fusion Center, JA- 02-30, 2006.
- [313] A. Czernichowski, P. Czernichowski, K. Wesolowska, Fuel Cell Science, Engineering and Technology—2004, Plasma-Catalytical Partial Oxidation of Various Carbonaceous Feeds into Synthesis Gas, American Society of Mechanical Engineers, New York, United States/Rochester, NY, United States, 2004, pp. 669-676.
- [314] T. Jiang, Y. Li, C.-J. Liu, G.-H. Xu, B. Eliasson, B. Xue, Plasma methane conversion using dielectric-barrier discharges with zeolite A, Catalysis Today (2002) 229-235 (Elsevier Science B.V., Washington, DC).

Chapter 1. Introduction

- [315] M. Moisan, G. Sauve, Z. Zakrzewski, J. Hubert. An atmospheric pressure waveguide-fed microwave plasma torch: the TIA design. *Plasma Sources Science and Technology*. 1994; 3: 584-592.
- [316] Hayakawa Y, Miura T, Shizuya K, Wakazono S, Tokunaga K, Kambara S, Hydrogen production system using a plasma membrane reactor. 9th International Conference on Hydrogen Production (ICH2P-2018)
- [317] B. Rozmiarek, in: J. Milliken (Ed.), *Hydrogen Generation from Biomass-Derived Carbohydrates via Aqueous Phase Reforming Process*, U.S. Department of Energy, Washington, DC, 2008, p. PD-6.
- [318] B. Sørensen, *Hydrogen and Fuel Cells Emerging Technologies and Applications*, Elsevier Academic Press, New York, 2005, p. 450.
- [319] D. Call, B.E. Logan. Hydrogen Production in a Single Chamber Microbial Electrolysis Cell Lacking a Membrane. *Environmental Science and Technology* 2008;42(9):3401-06.

Chapter 2 Hydrogen permeation through Pd-Cu membranes

2.1 Outlook

Currently, several global issues such as energy prices and global warming are related to using the current fossil fuels. Many efforts have been made towards developing a renewable and eco-friendly alternative fuel to decrease the dependency on fossil fuels [320, 321]. Hydrogen is considered the most critical solution of all issues because it has high energy content and is environmentally friendly [322, 323]. Different technologies, such as (water electrolysis, coal gasification, and steam reforming) can produce hydrogen [324]. However, most of the available hydrogen gas in the market is produced by steam reforming technology [325–332]. Also, hydrogen can be produced from water vapor at low temperature using a dielectric barrier discharge (DBD) plasma [333–337]. The purification and separation of hydrogen molecules are needed in most of the hydrogen production technologies. For the first time in 1784, the word “membrane” was suggested by Nollet to be used in the meaning of diaphragm, thin parchment, and capsule. The membrane was used to separate mixtures of alcohol and water [338]. The purification and separation of hydrogen gas using membrane technologies are widely utilized in different hydrogen production technologies such as gasification, and reforming processes [339]. Hydrogen separation using membrane technology has many advantages such as [340]: (i) low energy consumption, (ii) the ability to do separation continuously, (iii) the scaling up is easy, and (iv) it is possible to combine with other separation technologies. Pure palladium (Pd) and its Pd-based alloys can allow hydrogen monoatomic to diffuse and permeate through its structure [341]. Pd and its alloys can separate the hydrogen gas from hot mixture gases to a high purity level of hydrogen gas. The Pd-based membrane cost is still relatively high; therefore, new investigated materials are needed to combine with a little Pd without affecting the membrane properties.

Plasma science or ionized gas” is the fourth state of matter”. Francis Hauksbee, in 1705, investigated the first plasma gas charging and discharging using a small amount of mercury. Whereas in 1857 Siemens Company, has been created the first cold plasma (DBD) industrial application instrument used for ozone production. The “plasma” term or the gas discharge was named by Langmuir in 1927 [342]. Low-temperature or DBD plasmas are utilized in various applications [343, 344]. The DBD plasma is considered a specific type of AC discharge; it can provide high thermodynamics, non-equilibrium plasma at atmospheric pressure and low gas

Chapter 2. Hydrogen permeation through Pd-Cu membranes

temperature. The plasma ionized gas consists of ions, electrons, and neutral species that interact with each other to produce new radicals and a highly reactive plasma environment. In general, plasma can be divided into thermal or equilibrium plasmas and non-thermal or non-equilibrium plasmas. In thermal plasmas, the operating temperatures of the gas molecules and electrons are nearly same in the range of 10^3 - 10^5 °C, so it is called the equilibrium type [344]. The non-thermal plasma or low temperature plasmas, the operating temperature of the gas molecules (10^2 - 10^3 °C) is much lower than the electron temperatures of (10^4 - 10^5 °C). Therefore, this plasma type is called non-equilibrium plasma [344]. The hydrogen permeation through Pd-based membranes using DBD plasma has been previously investigated [345-347]. The results showed that the hydrogen permeability through the Pd-Cu membrane was enhanced by applying DBD plasma compared to gas-driven permeation (GDP). Pure hydrogen gas is important for the fuel cell applications, therefore the dependence on Pd and its alloys for the proton exchange membrane will increase to cover hydrogen gas demands [348-350]. An integrated membrane system using a Pd-Ag membrane type was experimentally investigated for generating pure hydrogen in a commercial PEMFC type [351]. The effects of CO and H₂O on the hydrogen permeance of Pd_{0.75}-Ag_{0.25} membranes were measured under (GDP) and plasma-driven permeation (PDP) [352]. The results of both GDP and PDP experiments indicated that CO has a greater effect on the permeability than H₂O. Furthermore, various studies recently investigated that the main reforming reaction components H₂O and CO negatively effects on the hydrogen permeation performance through Pd-based membranes because of the poisoning effect [353-360]

Low-temperature plasma or DBD plasma can increase the species reactivity at the contact surface of the gas mixture with plasma allowing the generation of new radicals [361]. The DBD plasma can be used in the hydrogen oxidation process such as oxidation in the H₂/O₂/N₂ gas mixture [362, 363]. The water vapour decomposition was discussed in different mechanisms and the initiation, propagation, and termination were investigated [344]. The water vapour plasmolysis kinetic modelling in micro-reactors was studied using corona-DBD plasma [364]. Hydrogen production from ammonia, hydrocarbons and biomass fuels were investigated [365-367]. Recently, Pd-based membranes were used to separate the produced hydrogen gas from steam reforming and ammonia decomposition using plasma [368].

The DBD plasma or low-temperature plasmas that are utilized in the plasma-catalytic reactions are characterized by the high reactivity of chemical species, and the energy distribution of electrons, ions and neutrals at various temperature scales. Furthermore, the combination between the plasma and catalytic materials will maximize the outputs compared with one system only. It has been reported that the

Chapter 2. Hydrogen permeation through Pd-Cu membranes

low-temperature plasma can modify the catalyst material physiochemical properties to be more durable and have higher activation. Moreover, a higher catalyst dispersion that leads to a more activated reaction area was observed by applying plasma [369–371]. These combination results from the plasma-catalyst system can contribute to decreasing the plasma-catalyst process operation temperature that will reduce the catalyst particles sintering and increase the catalyst dispersion. It has been reported that the large DBD plasma fluxes including high energetic molecules, ions, electrons and neutrals lead to change in the catalyst structure morphology [372]. The plasma effect on hydrogen permeation through Pd-based membranes is enhanced by combining with the heterogeneous catalysis. The interest in the plasma-based catalysis recently increased. The plasma-catalyst earliest NO_x removal study was reported by Henis in 1976 [373]. The transition metals such as Fe, Co, Zr, and Ni showed a high level of activity for dry reforming CH₄ process [374–383]. The catalysis and plasma performance of dry reforming of CH₄ were investigated [384]. The results showed that combining plasma and a catalyst type of Ni-based materials improved the efficiency of syngas generation. Furthermore, zeolites materials are solid catalytic acids and the main functions were reported regarding their shape and surface acidity [385, 386]. Zeolite catalyst materials were used in the plasma catalysis, and as a support for the catalyst materials [387–391].

2.1.1 Hydrogen separation techniques

The hydrogen separation and purification techniques were reviewed in this study. Three commercial hydrogen purification methods were used in large industrial applications. In this section, we will explain in detail the hydrogen separation methods.

2.1.1.1 Pressure swing adsorption (PSA)

In this hydrogen separation technique, the gas mixture is passed through the adsorber high surface area where the impurity gases were adsorbed while hydrogen permeates through the material. The impurity species at high partial pressure and desorb them at low gas partial pressures. The most known adsorbent material is zeolite. The pressure swing process was implemented to remove the impurities. In this process, more than one adsorber is used to preserve a constant feed flow, product, and tail gas. The partial pressure difference between the feed and the tail gas is typically considered the PSA driving force, the required hydrogen separation pressure ratio between the feed and tail gas is 4:1.

The PSA technique advantages can be concluded in its ability to generate a high purity hydrogen gas in a range of 99–99.999%, Furthermore, the impurities filtration is reached to part per million (ppm). The drawbacks of the PSA unit are the

Chapter 2. Hydrogen permeation through Pd-Cu membranes

high unit cost compared to the down tail gas that is usually used as a fuel at low pressure [392].

2.1.1.2 Cryogenic distillation

The energy-intensity of this process is high because the operating temperatures are typically low. The impurities in the cryogenic technique process are condensed to form liquid phase state while the hydrogen molecules remain in the gaseous state. One of the major disadvantages is the limited purity level of produced hydrogen [393]. Also, the cryogenic process is expensive because of the gas compression to maintain the process of cold conditions. Subsequently, the collected H₂ gas can be stored easily as a liquid [394]. The cryogenic is suitable for large-scale applications but for small-scale applications.

2.1.2 Hydrogen separation membrane types

The membrane material types can be classified into three main groups, namely hybrid, organic, and inorganic membranes. The organic membranes are divided into polymeric and biological membranes, while inorganic membranes can be subdivided into metallic and ceramic membranes [395]. Moreover, the hydrogen separation membranes can be classified according to the porosity as porous, non-porous and macro-porous membranes [396]. Figure (2.1) shows the different types of hydrogen separation membranes. The Pd-based membranes have the highest hydrogen permeability with a finite selectivity towards hydrogen molecules [397].

Porous membranes can be divided into micro-porous and mesoporous ceramic membranes. The separation process of the micro-porous ceramic membranes is prevailed by molecular sieving and selective adsorption with a complicated mixing process at intermediate conditions. While in mesoporous ceramic membranes, the low selectivity with the Knudsen diffusion is the main feature of this process [396, 398, 399].

The proton conducting membranes are one of the membrane separations types; and can be subdivided into dense and composite ceramic metal membranes. The dense ceramic membranes have low permeability, but it can give an extremely high purity of the hydrogen gas at a temperature of 1173K, because of the proton transport mechanism. There are two different types of dense ceramic membranes with high hydrogen flux, namely perovskite and non-perovskite types [396, 397]. The main

Chapter 2. Hydrogen permeation through Pd-Cu membranes

disadvantages of the dense ceramic membranes are limited permeability, low thermal stability, and low chemical stability [400].

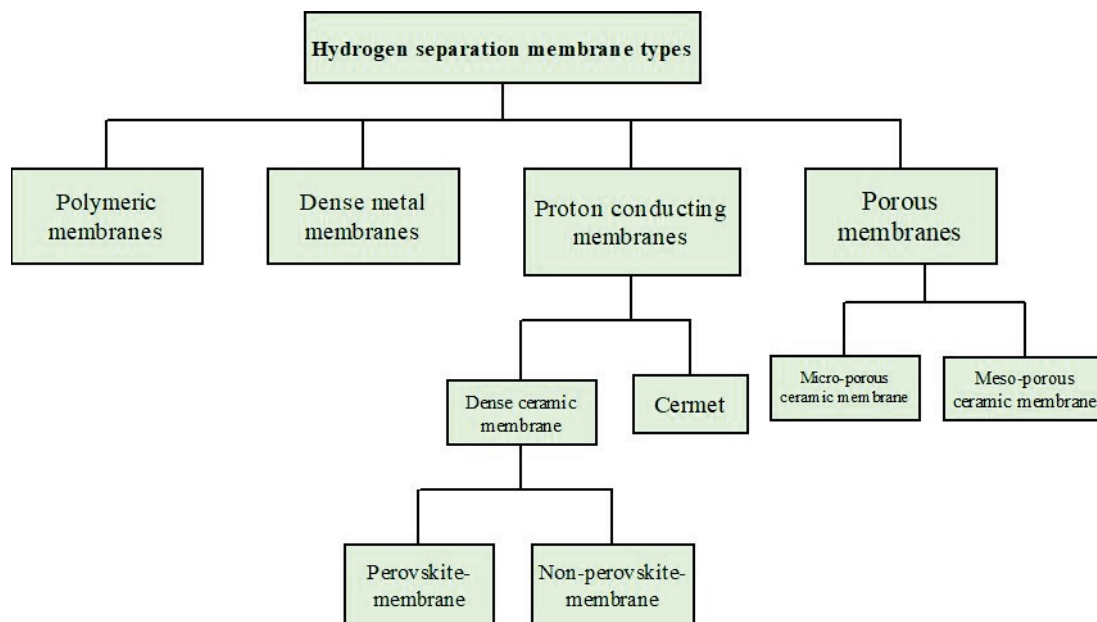


Fig 2.1 The block diagram of the H₂ separation membrane types.

2.1.3 Pd-based membranes

Hydrogen molecules dissolve through various metals to create metal hydrides or interstitial solid solutions. The metal Pd-based type is the most common metal that is commercially used in hydrogen separation technology. High pressures and temperatures are required to absorb hydrogen molecules in other metals. Pd-metals can dissociate H₂ molecules into a monatomic form that makes the H₂ atoms diffuse quickly through its lattice. Furthermore, Pd-metals can absorb hydrogen approximately 600 times by maintaining its physical and chemical properties [401]. Pd and Pd-alloy membranes can transport the hydrogen monatomic through the membrane structure to produce high purity hydrogen of $\geq 99.9999\%$ [341]. The high permeability, high hydrocarbons flow tolerance, and high chemical stability is the main advantages of Pd membranes. Pd and its alloys are still expensive; therefore, various studies were done to investigate more membrane materials for hydrogen separation. The Pd-alloys membranes can permeate hydrogen gas using little Pd without effects on the membrane properties. Recently, the Pd-based membranes, especially the Pd-Cu membranes received much attention due to their resistance to hydrogen embrittlement and catalytic recombination ability [402, 403], and has been registered as having a remarkable tolerance to H₂S [404, 405]. One of the most

Chapter 2. Hydrogen permeation through Pd-Cu membranes

commercial dense metal membranes is Pd-Ag binary alloys membranes because it can be used as a foil or cold rolled with a thickness of 50 μm . Hydrogen diffusion through Pd-based membranes is fast because of hydrogen molecules are dissociated into monatomic [406].

The Pd-based alloy membranes can be fabricated by different methods such as: electroless plating (ELP), chemical vapour deposition (CVD), and physical vapour deposition (PVD) [407-413]. ELP is known as a heterogeneous oxidation-reduction reaction involving metal deposition at the solid-liquid interface without electric energy [414, 415]. The main advantages of the ELP method are concluded in its simple equipment low cost and no need for an electric source. Furthermore, it can cover a complex geometry [397, 398]. The most important disadvantage of the ELP method is the long and complicated pretreatment processes before accomplishment which it takes long time [416]. The CVD method is a process that uses the thermal decomposition of one or more volatile precursors to form a thin film on the substrate [417]. It was found that the CVD method can provide a high film quality and thin film membrane thickness at good thermal stability and high volatility [418]. The drawbacks of this fabrication method are that it requires a high pure constituent and vacuum, along with a smaller H_2/N_2 selectivity leading to low hydrogen flux [419]. In the PVD process, the solid source is vaporized by using the gaseous plasma or at a high temperature vacuum. The target of this process is to coat the substrates with a thin film of energetic particles through condensation [420, 421]. It was considered that the PVD process is environmentally friendly because no liquid waste is produced from the chemical baths [422]. Furthermore, it can be used to coat thin and uniform metal alloy films, but it can't coat the interior part of the tubes [423, 424]. Furthermore, the efficiency of the PVD process is typically low and the cost of the required vacuum equipment is high [398]. Figure (2.2) shows the Pd-Ag membrane synthesis by using the PVD technique. The Pd and Ag along with the energetic argon particles are bombarding, and then the neutral metal species atoms are repulsed to be condensed on the support. The heated support is rotated between the inclined two magnetrons [425]. The fabrication methods were passed with two phases, namely body-centered cubic (bcc) and face-centered cubic (fcc). It was found that the combination between the bcc and fcc phases reported high mobility of H_2 molecules and permeability compared to single-phase data results [426-430]. The Pd-based membranes are typically operated at a temperature range of 300-600 $^\circ\text{C}$. The permeability of hydrogen gas through various pure metals is reported in Figure (2.3).

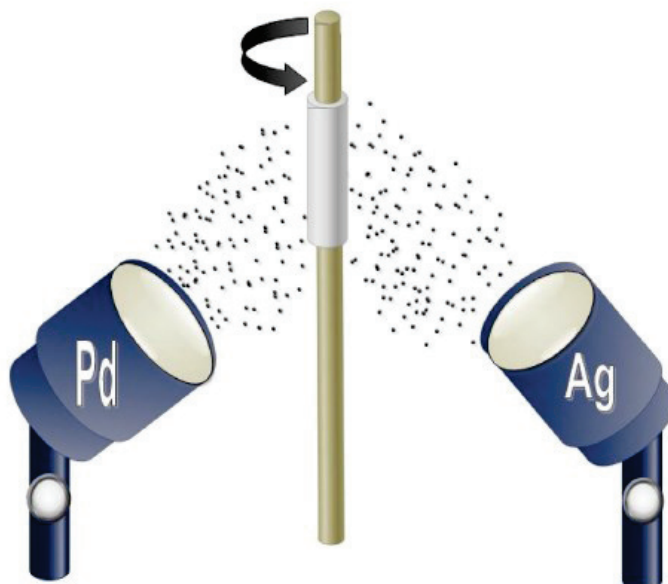


Fig. 2. 2 PVD magnetron sputtering method for Pd-Ag membrane synthesis [425].

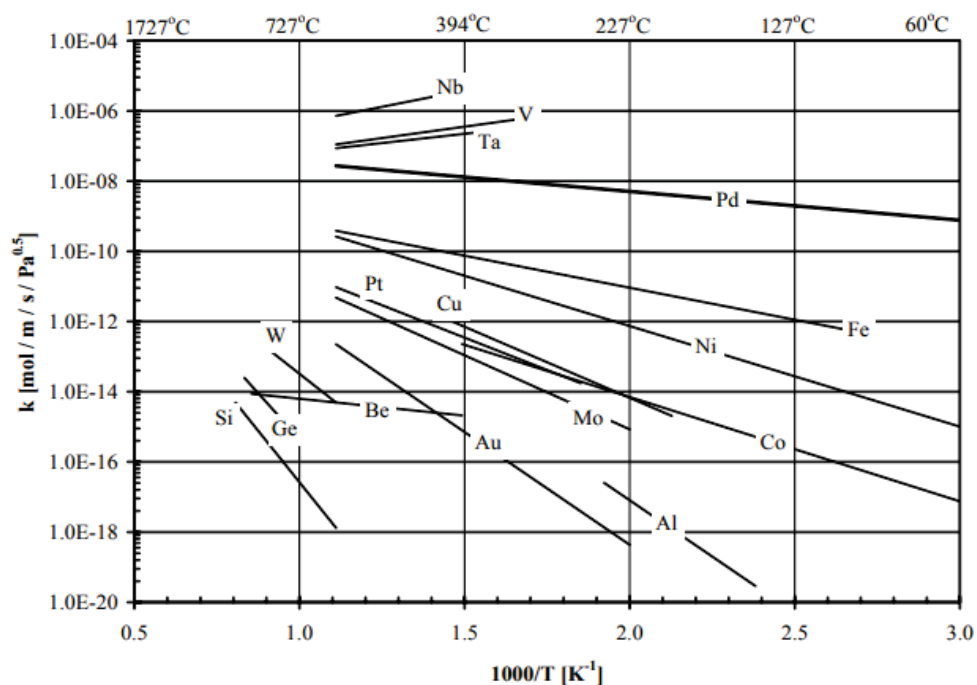


Fig. 2. 3 Hydrogen permeability of various metals at different temperature [431].

Chapter 2. Hydrogen permeation through Pd-Cu membranes

2.1.4 Permeation theory

2.1.4.1 Hydrogen separation membrane selectivity

The hydrogen separation driving force in the membrane separation technique is the partial pressure difference between the feed and permeate pressures. It is essential to maintain the feed gas pressure and is usually higher than the permeate side pressure. The mass transport mechanism is initiated to migrate H_2 molecules through the membrane at large partial pressure differences. The hydrogen membrane selectivity can be divided into six main types by identifying various parameters of each one as shown in Table (2.1). Generally, separation membranes can operate at a wide range of temperatures and pressures, and it can be scaled up easily and used for portable scales.

The membrane upper side is named the high-gas pressure side or the upstream side while the lower side is referred to the permeation or the downstream side. Figure (2.4) shows the schematic diagram of hydrogen gas flow through the membrane. The permeation rate can be measured over a wide range of upstream pressures and temperatures.

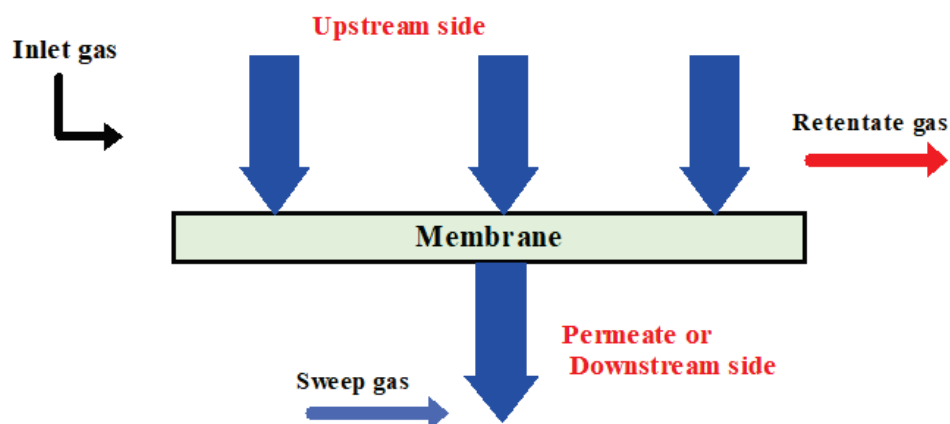


Fig. 2.4 Schematic diagram of gas flow through membrane.

Chapter 2. Hydrogen permeation through Pd-Cu membranes

Table. 2.1 Hydrogen selective membrane types properties [432].

	Dense polymer	Micro-porous ceramic	Dense metallic	Porous carbon	Dense ceramic
Temperature range (°C)	<100	200–600	300–600	500–900	600–900
H₂ selectivity	Low	5–139	>1000	4–20	>1000
H₂ flux (×10⁻³ mol.m⁻².s⁻¹) at ΔP=100kPa	Low	60–300	60–300	10–200	6–80
Stability issues	Swelling, compaction, mechanical strength	Stability in H ₂ O	Phase transition	Brittle, Oxidizing	Stability in CO ₂
Poisoning issues	HCl, SO _x , CO ₂		H ₂ S, HCl, CO	Strong adsorbing vapors, organics	H ₂ S
Materials	Polymers	Silica, alumina, zirconia, titania, zeolites	Pd alloy	Carbon	Proton conducting ceramics (mainly SrCeO _{3-δ} , BaCeO _{3-δ})
Transport mechanism	Solution/diffusion	Molecular sieving	Solution/diffusion	Surface diffusion; molecular sieving	Solution/diffusion (Proton conduction)
Development status	Commercial by air products, linde, BOC, air liquid	Prototype tubular silica membranes available up to 90 cm. other materials only small samples (cm ²)	Commercial by Johnson Matthey; prototype membrane tubes available up to 60 cm.	Small membrane modules commercial, mostly small samples (cm ²) available for testing.	Small samples available for testing

Hydrogen permeation modelling

The hydrogen permeation modelling through membranes has been investigated by Waelbroeck et al. [433, 434]. The model was related to the hydrogen flux from the membrane downstream side, J_H , and the bulk hydrogen concentration, c .

$$J_H = 2\sigma k_r c^2 \quad (1)$$

where 2 is expressed about two recombined atoms, σ is a surface roughness factor, and k_r is the rate constant of the recombination coefficient. The permeability term can be defined as the ability of a certain gas to diffuse through the membrane solid material. Figure (2.5) shows the hydrogen permeation through Pd- based membranes and it involves seven steps [435]:- (1) hydrogen diffusion from the bulk gas to the vicinity of the Pd membrane surface, (2) H₂ dissociative adsorption onto the surface, (3) H-atoms migration on the surface into the bulk metal, (4) H₂ diffusion through the Pd membrane lattice, (5) transition of H₂ gas from the bulk metal

Chapter 2. Hydrogen permeation through Pd-Cu membranes

membrane onto the surface on the permeate side, and (6) H₂ molecules associative desorption and diffusion from the permeate surface side into H₂ molecule bulk gas.

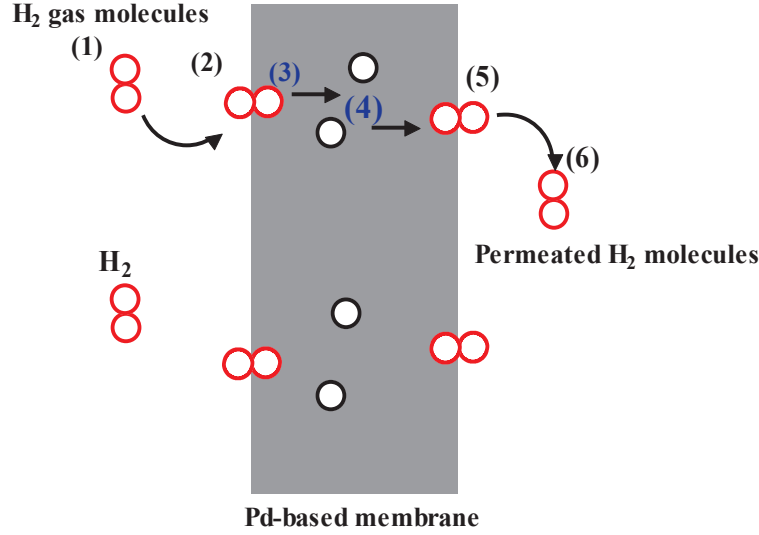


Fig. 2.5 Hydrogen permeation through metal Pd- based membrane.

The hydrogen flux can mathematically describe by Fick's law of diffusion. The hydrogen flux is known as the number of H₂ moles permeates through the perpendicular cross-section area per unit time. The hydrogen flux variation through a solid membrane can be determined from Fick's 1st law as follows:

$$J_H = -D \frac{\partial C}{\partial x} \quad (2)$$

where D is the diffusivity or the diffusion coefficient, $\partial C / \partial x$ is the concentration gradient, and the negative sign refers to the gas diffusion direction. It was noted that the permeation driving forces are the concentration, pressure, temperature and the electromotive force, and the reverse osmosis required two driving forces, namely concentration, and pressure. Henry's law is applied to the unknown gas surface concentration as follows:

$$S_H = \frac{C_{gas}}{P_{gas}} \quad (3)$$

where S_H is a constant, that can be defined as the ratio of non-dissociative gas molecules in a solid or liquid concentration (C_{gas}) to the gas vapour pressure (P_{gas}). The gas feed and permeate pressures can be measured and controlled during the permeation experiment. The S_H constant in Eq. (2) can be considered as the hydrogen

Chapter 2. Hydrogen permeation through Pd-Cu membranes

solubility (S), which is known as the concentration per unit pressure. The hydrogen diatomic molecules are dissociated through the membrane into monatomic form. Sievert's law investigated that the hydrogen molecular solubility and the dissociation through the metal membrane is a function of its square root pressure in the gas phase [436].

$$S = \frac{C_H}{P_{H_2}^{1/2}} \quad (4)$$

By substituting in Eq. (2), we can obtain the following formula:

$$J_H = -DS \frac{\partial P_{H_2}^{1/2}}{\partial x} \cong -DS \frac{\Delta P_{H_2}^{1/2}}{\Delta x} \quad (5)$$

where $\Delta P_{H_2}^{1/2}$ is the difference between the partial pressure square root between the feeding gas pressure and the permeated gas pressure of the membrane and Δx is the membrane thickness. The hydrogen permeability (Pe) is the product of the diffusivity and solubility through the membrane that can be expressed in DS constant. The permeability can be determined for the steady-state hydrogen flow rate by combining the Fick's and Sievert's laws as:

$$J_H = \frac{D S (P_f^{n-exponent} - P_p^{n-exponent})}{x} \quad [\text{Mol. m}^{-2} \cdot \text{s}^{-1}] \quad (6)$$

where P_f and P_p are the pressures at the feeding and permeate side, respectively. The partial pressure n-exponent value varies depending on the transport mechanism. Henry's law assumes that $n=1$ for the porous membrane types which are known as Knudsen diffusion. While for the dense metal membranes, according to Sieverts' law Eq. (6), the partial pressure n-exponent is $n=0.5$, it was seen that the H_2 flux depends on and is inversely proportional to the Pd-based membrane thickness [437].

It was seen that H_2 permeability is a temperature-dependent parameter. Furthermore, the hydrogen diffusion coefficient and the H_2 solubility coefficient are,

$$D = D_0 \exp\left(\frac{-E_{diff}}{RT}\right) \quad (7)$$

$$S = S_0 \exp\left(\frac{-\Delta_r H}{RT}\right) \quad (8)$$

In Eq. (7), E_{diff} is the activation energy for hydrogen diffusion in $[J \cdot \text{mol}^{-1}]$, R is the universal gas constant in $[J \cdot \text{mol}^{-1} \cdot K^{-1}]$ and T is the absolute temperature in $[K]$. While in Eq. [327], $\Delta_r H$ is the enthalpy of hydrogen absorption in Pd in $[J \cdot \text{mol}^{-1}]$. Furthermore, the permeability term is a dependent parameter and it can be defined in the following Arrhenius equation:

Chapter 2. Hydrogen permeation through Pd-Cu membranes

$$Pe = Pe_0 \exp\left(\frac{-E_a}{RT}\right) \quad (9)$$

where the maximum permeability relation is, $Pe_0 = D_0 S_0$ and the activation energy expression is: $E_a = E_{diff} + \Delta_r H$.

The hydrogen flux in Eq. (6) can be re-written again as:

$$J_H = \frac{Pe (P_f^{n-exponent} - P_p^{n-exponent})}{x} \quad (10)$$

The hydrogen permeance is defined as (Pe/x) and is considered the most important assessed characteristic parameter of hydrogen permeation for Pd-based membranes. Furthermore, the hydrogen permeance depends on the partial pressure range and showed a large or small effect based on the n-exponent value.

The H₂ separation membranes can also be assessed by defining the selectivity parameter towards the input gas mixtures. The selectivity parameter can be defined as the differences between various gaseous species in the H₂ permeability values. The selectivity factor $\alpha_{A/B}$ can be defined as follow:

$$\alpha_{A/B} = \frac{y_A/y_B}{x_A/x_B} \quad (11)$$

where the partial pressures of gas A and B at the permeate side are y_A and y_B , respectively, whereas x_A and x_B are the membrane feed side gas pressures of gas A and B, respectively [382]. The effectiveness of the membrane can also be measured by two other factors, the recovery (S_r) and volume reduction (V_r). The (S_r) is defined as the permeated hydrogen gas flow to the feed gas flow:

$$S_r = \frac{q_p}{q_f} \quad (12)$$

where q_p denotes the permeated gas flow and q_f is the feeding gas flow. The volume reduction (V_r) is known as the ratio of the feed gas flow to the retentate flow (q_r) as:

$$V_r = \frac{q_f}{q_r} \quad (13)$$

2.2 Introduction

Hydrogen gas has an importance relevant role to tackle the environmental issues in most energy systems that have raised the interest of the purification and separation of hydrogen gas using membrane technologies. In particular, Palladium-based membranes can provide high hydrogen selectivity and good hydrogen permeability values. Recently, the purification and separation processes demand are strongly increased due to their ability to provide pure hydrogen gas. Currently, most of the available hydrogen gas is produced by the steam reforming process [80, 324, 438]. Compared with the other common fossil fuels, hydrogen fuel has been registered the highest values of the higher and lower heating values [348]. On the other hand, the hydrogen production cost of most the hydrogen production methods are still high or have low efficiencies [349]. The environmental, financial, social, and technical performance of 19 selected hydrogen production methods has been comparatively evaluated. The results showed that the energy efficiency of the fossil fuel reforming method was the highest 83% and the photonic (solar) has the lowest energy efficiency among the selected hydrogen production methods [350]. In addition to, the 99.999% pure hydrogen is needed for the fuel cells industry applications, so, the proton exchange membrane using Pd and Pd-alloys membranes will be expected growing to cover pure hydrogen demands [439-441]. Ammonia is considered one of the most important hydrogen carrier gases [324]. Pure H₂ gas was produced with an energy efficiency of 28.5% in a plasma catalytic membrane reactor using Pd-Cu membrane [368]. The performance assessment of hydrogen and ammonia combustion with various fuels for power generators have been investigated [442].

However, the abundance of hydrogen gas in nature, it is always found in water, or hydrocarbons compounds. Preliminary results of hydrogen production from steam decomposition using DBD plasma have been investigated as a new method to generate hydrogen [337]. The recent advances in membrane technology for hydrogen purification were investigated [443], generally, the hydrogen gas is separated by a common three main processes, cryogenic distillation, pressure swing adsorption (PSA) [444] and membrane separation [445-447]. Currently, hydrogen separation using the membrane technologies are considered as the most promising process due to their cost effectiveness, low energy consumption and the operation is easy [448]. Furthermore, the membrane properties can be controlled and adjusted to meet the separation process requirements to be used in a wide range of applications.

Palladium and palladium alloys (Pd) membranes are considered as the most attractive hydrogen purification membrane types to separate hydrogen from gas mixtures due to their higher H₂ permeability, chemical compatibility with many hydrocarbons, high hydrogen selectivity and the durability is good [406, 449-452].

Chapter 2. Hydrogen permeation through Pd-Cu membranes

Therefore, many of researches have been developed to study the hydrogen permeation through Pd and Pd-alloys. The fabrication of the palladium composite membrane on porous stainless-steel substrate with NaY zeolite as an intermediate layer for hydrogen purification has been studied to prevent the intermetallic diffusion [453]. The hydrogen permeation through palladium-copper membranes alloys has been registered a high H_2 permeability than results obtained for pure palladium membranes. The hydrogen permeation through palladium alloys membranes like Pd-Ag25% and Pd-Cu40% have been investigated [426, 454,]. It can considered that the palladium-copper alloys membranes are the most promising membranes in purification technology applications because the membrane cost is low, has good resistance to H_2S poisoning and its H_2 permeability is higher than that obtained from pure Pd [427, 449, 454-459]. Therefore, the Pd-based alloy membranes can be used in H_2 production from H_2S gas [460]. The most efficient membrane properties must be characterized with high permeability, low expansion at saturation with hydrogen gas, high corrosion resistance, and stability at temperatures range of 300-600°C [459,461, 462].

The palladium-copper alloys membranes are fabricated by different techniques such as electroless plating (ELP), chemical vapor deposition (CVD), sputtering, etc. [407-413]. In the manufacturing process of the palladium-copper alloys with a composition of Pd60%-Cu40wt%, it was found that the combination between phases (body-centered cubic (bcc) and the face-centered cubic (fcc)) have been reported a high mobility of H_2 molecules and permeability compared to single-phase results [426-429]. In this study a mixed fcc-bcc Pd-Cu40% phase was used in the Pd-Cu membrane fabrication. The combination of the binary phases was made within a temperature range of 450~550°C which will increase the hydrogen permeation and the contamination resistance compared that obtained from the bcc phase only [463, 464].

In this study, the hydrogen permeation behavior under heating only and plasma-heating effect were studied in 15 μ m and 20 μ m Pd-Cu40% membrane thicknesses. A pure hydrogen gas with concentration of 99.999% was injected at pressure of 100kPa was injected in 1mm gap length plate micro-channel reactor (PMCR). The effect of H_2 gas flow rates and PMCR heating temperatures on the hydrogen permeation for both membrane thicknesses was investigated. The Fick's and Sievert's law equation were used in hydrogen permeability calculations. The feeding and permeate partial pressures n-value 0.5 was used in hydrogen permeation flux calculations. The hydrogen permeation rate percent was determined for both experiments to clarify the membrane thickness effect on the hydrogen permeation. A comparison between heating only and plasma-heating experiments was derived for both tested Pd-Cu membrane thickness.

Chapter 2. Hydrogen permeation through Pd-Cu membranes

2.2.1 Experimental

2.2.1.1 Membrane preparation and reactor assembly

The present permeation studies were performed in a new designed micro-channel plate reactor (PMCR), exploded view shown in figure (2.6). All the Pd-40%Cu membrane foils used in this permeation study were commercially known purchased from Tanaka Holdings Co., Ltd, and table (2.2) reports the geometrical characteristics of the investigated Pd-Cu membranes. The palladium 60%- copper40% alloy composition was selected due to the permeability is too high. Also, this membrane type was made at the mixed fcc and bcc region which it was shown the mixed fcc and bcc region can give the high permeability, high mechanical and chemical stability characteristics. In this study, two different Pd-Cu membrane thicknesses of (15 μ m, 20 μ m) were used. The new designed PMCR used in this study are composed of the following parts: the base plate, spacer, support plate, Pd0.60-Cu0.40wt% membrane foil, micro-flow channel top plate, Dielectric quartz glass (2mm thickness) and the electrode mesh with dimensions of (45mm \times 45mm \times 0.2mm). The reaction field gap length is 1mm. the gap length means the distance measured between dielectric glass part and Pd-Cu membrane. The PMCR parts were assembled with each other using gasket material. the Pd-Cu membrane foil was installed in this experiment to measure the permeate hydrogen flow rate at a definite reactor heating temperature of 423-573K and plasma applied voltage range of 0-16kV. Once the assembly process finished, the drying process started at a temperature of 373K for 4hrs.

In supported thin Pd membranes, the measurements of permeability are affected by leakage, substrate material transport resistance, and surface contamination. Though the leakage test was made using the vacuum pump after the PMCR cooled down. The PMCR is activated by heating at 573K for 12hrs with a continuous hydrogen gas flow rate.

Table. 2.2 Geometrical characteristics of the Pd-Cu membranes

Width[mm]	Thickness[μ m]	Area[cm ²]
50	15	25
50	20	25

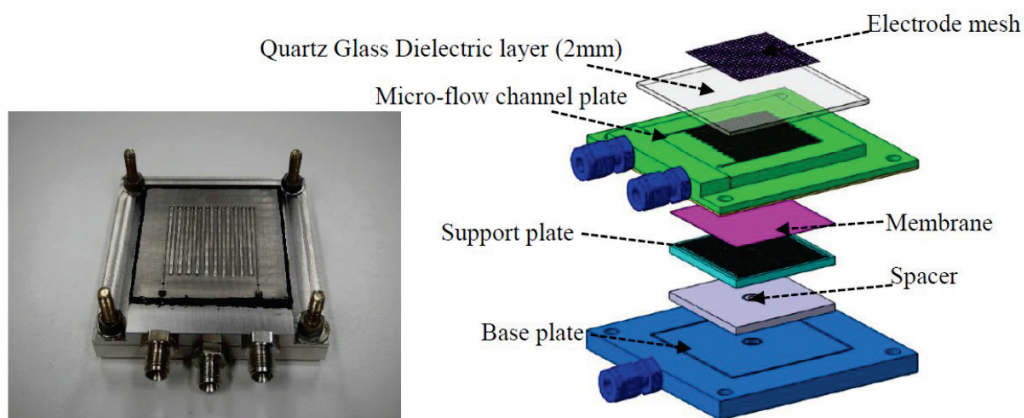


Fig.2.6 Exploded view of the micro-channel plate reactor (PMCR).

2.2.1.2 Experimental setup

Figure (2.7) shows a schematic of the experimental setup and the gas line connections. Pure hydrogen gas is fed from H₂ bottle into the PMCR via the mass flow controller. The flow rate of permeated hydrogen is measured using the soap flow meter. The measurements of permeated H₂ flow rate are taken after hydrogen gas concentration reach to 100% on the H₂ gas analyzer. Also, the vacuum pump type of N820.3FT.18 (KNF Company) is installed at the permeation side and is directly connected to the PMCR. The digital mass flow controller (MFC) is installed before the PMCR to control H₂ flow rate. While the feeding and permeate pressures are measured and monitored using the digital pressure gauges. The PMCR is heated using the surface stirrer heater which can be adjusted at the required permeation testing temperatures.

Before starting each permeation experiment, the PMCR has been activated at 573K for 2hrs using stirrer heater, and then the stirrer heater was adjusted at the testing temperature. The PMCR is tested using heating only and plasma-heating experiments. Dielectric barrier discharge (DBD) is used to generate non-thermal plasma at low H₂ gas temperatures and typical atmospheric pressure. DBD plasma provides high electron energy which can generate radicals, atoms and excited particles. The high voltage (H.V) source is connected into the mesh center on the upper side of the PMCR While the ground electrode is connected into the base plate.

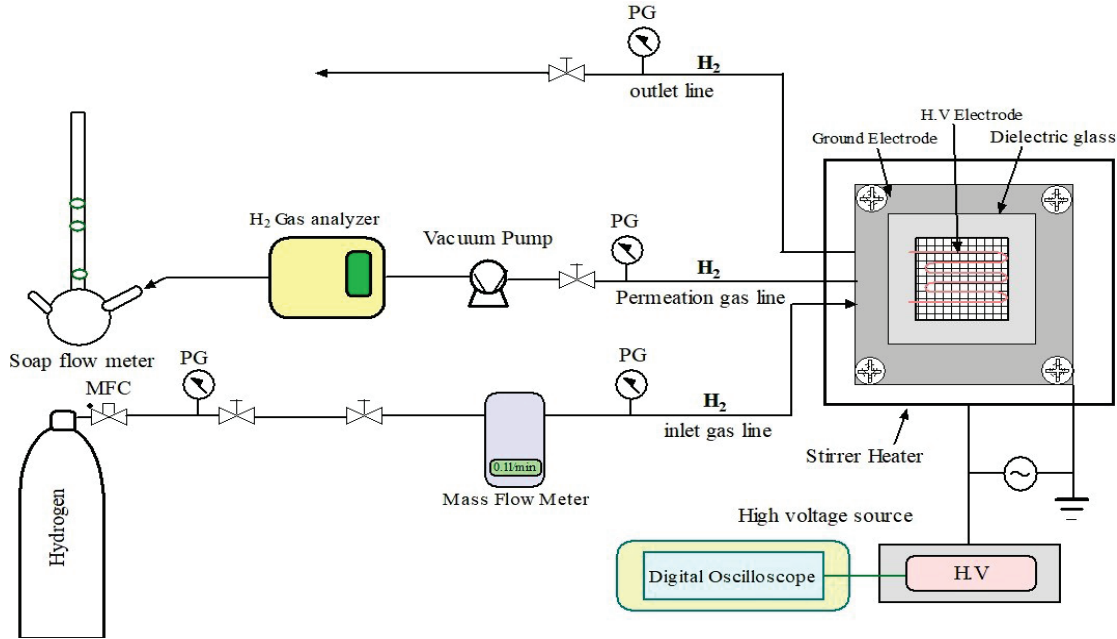


Fig. 2.7 Schematic diagram of the Experimental setup.

2.2.2 Results and discussion

2.2.2.1 Determination of H_2 flux and Permeability

The PMCR permeation experiments for Pd-Cu40% membranes were carried out across temperature range of 423-573K. Where the feeding high pressure side was atmospheric pressure and the permeate pressure, side was controlled by vacuum pump. In case of heating only experiment, the operating temperature was controlled by an electric stirrer heater, whereas in plasma-heating experiment it was controlled by the DBD plasma ignition and the electric stirrer heater.

Apure hydrogen gas concentration of 99.999% was used for both heating only and plasma-heating permeation experiments using membranes thickness of 15 μ m and 20 μ m. the pure H_2 gas was flowed in the PMCR flow channels along the membrane outer side, and the permeated hydrogen gas was dissociated through Pd-Cu40% membrane into the inner side and measured by H_2 gas analyzer and soap flow meter.

In this study, the permeation hydrogen flux formula was resulted from the combination of the Fick's first law and Sieverts law equations and it can be described from the following expression [465, 466]:

$$J = \frac{Pe}{\delta} (p_f^{0.5} - p_p^{0.5}) \quad (1)$$

Chapter 2. Hydrogen permeation through Pd-Cu membranes

Where J is the hydrogen gas flux ($\text{mol. m}^{-2}.\text{s}^{-1}$) was a function of the H_2 permeability, Pe ($\text{mol. m}^{-1}.\text{s}^{-1}.\text{Pa}^{-0.5}$), the difference between square root of the hydrogen gas partial pressure on the membrane feeding and downstream, or permeate sides was used, where p_f and p_p (Pa) was the partial pressure of the feeding and permeate sides respectively, and δ was the Pd-Cu40% membrane thickness (m). The permeance term ($\text{mol. m}^{-2}.\text{s}^{-1}.\text{Pa}^{-0.5}$) was defined as the ratio of the hydrogen permeability to the membrane thickness. It was observed that the hydrogen permeability Pe was depending on the PMCR heating temperature, in addition to the H_2 permeation process is a mass transfer phenomenon. It was typically seen in Arrhenius relationship between H_2 permeability Pe and the inverse of the PMCR heating temperature (K^{-1}). It can be described according to the Arrhenius's law as follows:

$$Pe = Pe_0 e^{-E_a/RT} \quad (2)$$

Where, the pre-exponential constant factor Pe_0 ($\text{mol. m}^{-1}.\text{s}^{-1}.\text{Pa}^{-0.5}$), the activation energy E_a (J. mol^{-1}), the universal gas constant R ($8.314 \text{ J.mol}^{-1}.\text{K}^{-1}$) and the PMCR heating temperature T (K) were used in yielding these Pd-Cu40% membranes.

2.2.2.2 Heating only experiment

The hydrogen flux was measured after the concentration of H_2 gas at the outlet of the permeate side reach to 100% H_2 . In this experiment the hydrogen flux J was measured under heating only at temperature range of 423-573K and at different H_2 gas flow rates. Figure (2.8a, 2.8b) show the plot of the H_2 flux of a 15 μm and 20 μm Pd-Cu40% membranes versus the change of the permeation driving force, it was observed that the hydrogen flux increased at low input H_2 flow rates for both membranes. The membrane thickness was an important factor where the H_2 flux in 15 μm Pd-Cu40% membrane thickness experiments was higher than H_2 flux obtained from 20 μm Pd-Cu40% membrane thickness at same conditions. It was clear that the H_2 flux of Pd-Cu40% alloy decreased with the difference of square root H_2 partial pressure increased in both membrane thicknesses.

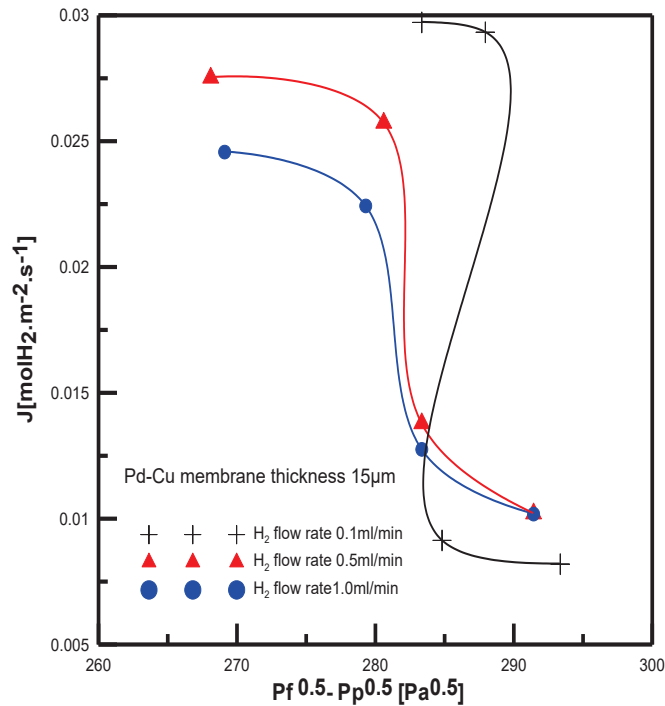


Fig.2.8a. Hydrogen flux of 15 μ m membrane thickness under heating only experiment.

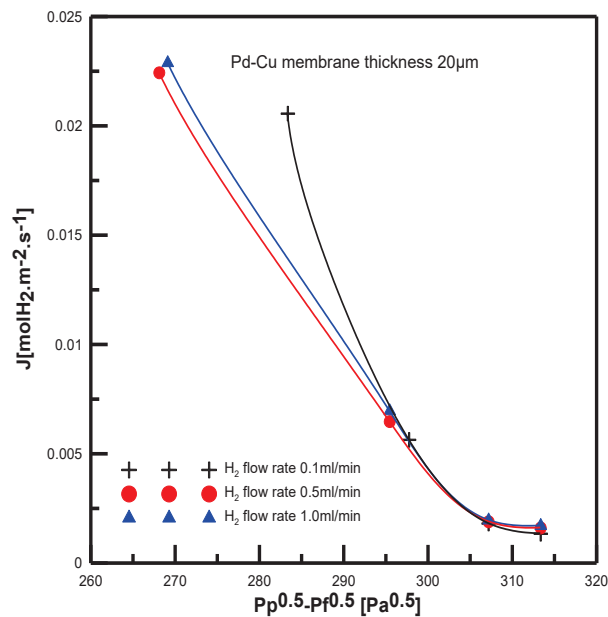


Fig. 2.8b. Hydrogen flux of 20 μ m membrane thickness under heating only experiment.

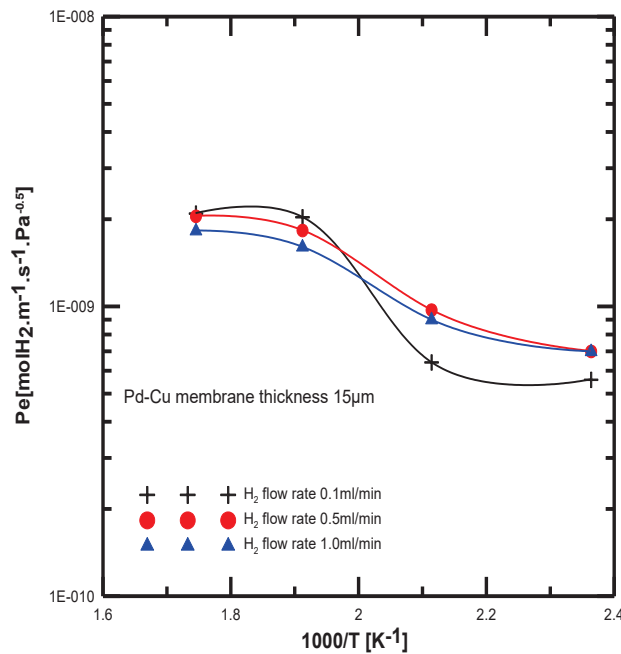


Fig. 2.9a. Arrhenius plot of typical H_2 permeability under heating only experiment of 15 μm membrane thickness.

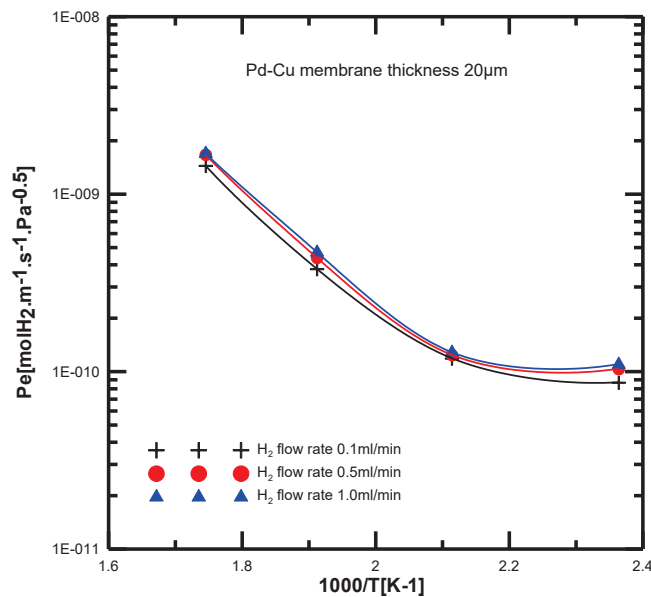


Fig. 2.9b. Arrhenius plot of typical H_2 permeability under heating only experiment of 20 μm membrane thickness.

The hydrogen permeability of 15 μm & 20 μm Pd-Cu membrane thicknesses versus the PMCR heating temperature are shown in figures (2.9a, 2.9b). It was seen that the hydrogen permeability increased with increasing the PMCR heating

Chapter 2. Hydrogen permeation through Pd-Cu membranes

temperature. One of the interesting results was the shape of the H_2 flow rate 0.1 L/min in both different membrane thicknesses experiments. It was observed that the permeability of Pd-Cu 20 μm did not show continues higher than 0.5 and 1 L/min H_2 flow rates while the permeability of H_2 flow rate 0.1 L/min is higher than other hydrogen gas inlet flow rates (0.5 and 1 L/min). Also, it was shown the hydrogen permeability of the 15 μm Pd-Cu membrane thickness was higher that obtained for 20 μm Pd-Cu membrane thickness at the same conditions. The maximum hydrogen permeability was obtained at the higher PMCR heating temperature 573K. It has been investigated that permeability is changed according to solubility and diffusivity [467]. In Palladium alloys, the solubility decreases and the H_2 diffusivity increases with the reactor temperature increases, which it was shown in the H_2 permeability increase at higher temperatures. Additionally, the palladium-copper alloy with a composition of Pd-Cu40 wt% is reported the highest H_2 permeability compared with the pure Palladium membranes [426, 449, 457, 468].

2.2.2.3 Plasma-Heating Experiment

The PMCR plasma-heating experiment was carried out using a 20 μm and 15 μm Pd-Cu40wt% membrane, gap length 1.0 mm and within a temperature range of 423-573K. The DBD plasma applied voltage was within range of 10-16kV, whereas the discharge frequency was maintained at 10 kHz for all experimental measurements. In this experiment, the applied voltage was controlled from high voltage regulator. The high voltage (H.V) electrode cable was connected at the center of stainless-steel mesh (SUS) and the ground cable was connected to the flow channel plate. The plot of the H_2 flux versus the plasma applied voltage is given in figure (2.10a, 2.10b) for a membrane thickness of 15 μm and 20 μm respectively. The experimental results denote that the H_2 flux did not increase continuously with the increasing of DBD plasma applied voltage, whether for a membrane thickness 15 μm or 20 μm experiments. Also, the H_2 flux behavior in plasma-heating experiment isn't similar to heating only experiment. In plasma-heating experiment, it was observed that H_2 flux increased by applying plasma compared to heating only experiment, additionally plasma did not modify the Pd-Cu40% membrane properties.

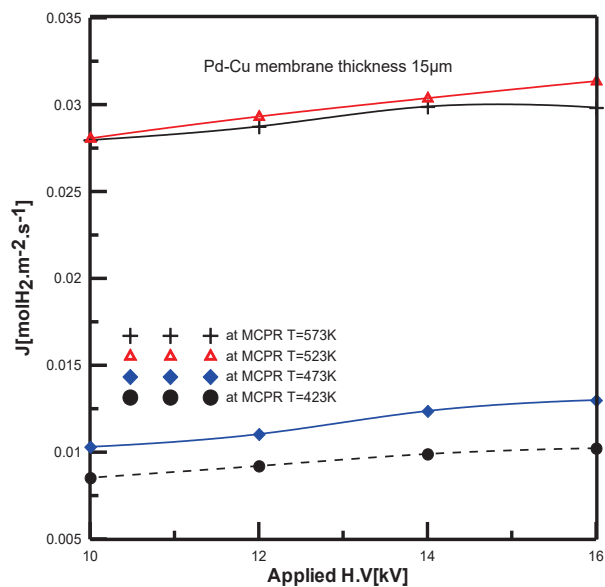


Fig. 2.10a. Effect of the plasma applied voltage on H₂ flux of 15μm Pd-Cu membrane thickness.

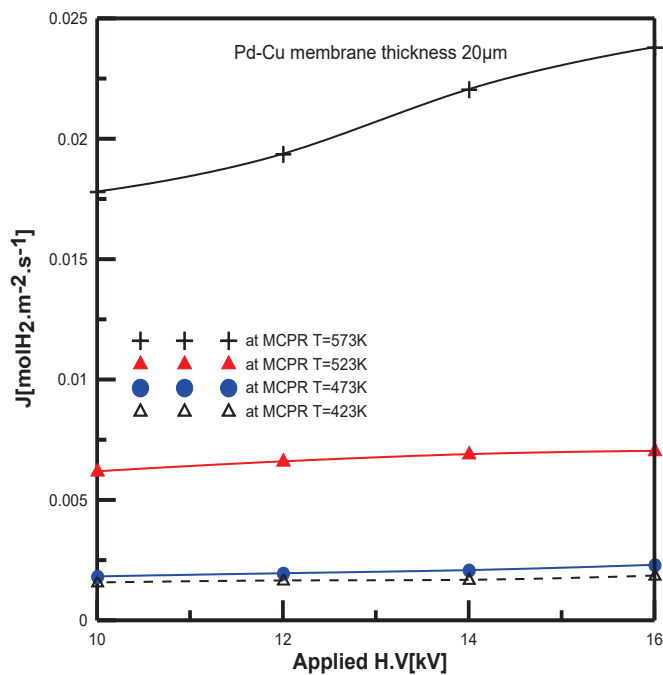


Fig. 2.10b. Effect of the plasma applied voltage on H₂ flux of 20μm Pd-Cu membrane thickness.

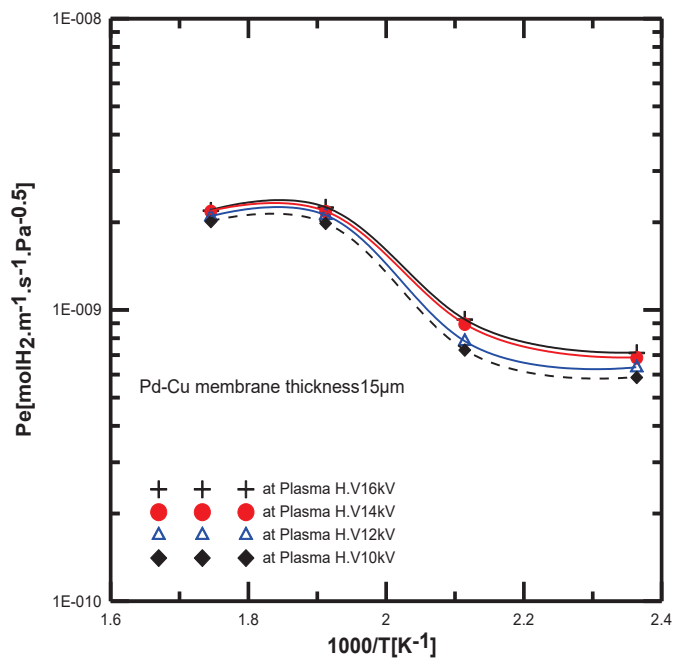


Fig.2.11a. Arrhenius plot of the H_2 permeability measured at different plasma applied high voltage for $15\mu\text{m}$ membrane thickness.

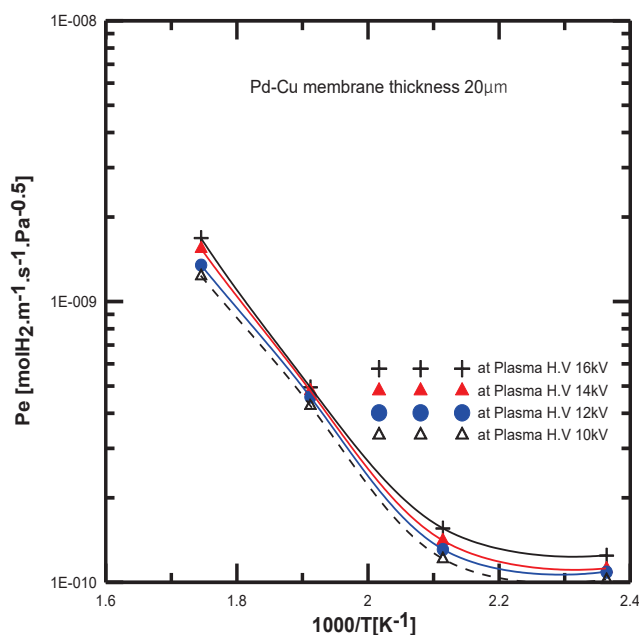


Fig.2.11b. Arrhenius plot of the H_2 permeability measured at different plasma applied high voltage for $20\mu\text{m}$ membrane thickness.

Chapter 2. Hydrogen permeation through Pd-Cu membranes

Figures (2.11a, 2.11b) show the Arrhenius plot of the H₂ permeability versus the PMCR temperature for a membrane thickness of 15µm and 20µm respectively. It was found that the H₂ permeability increased, whether the PMCR heating temperature and the plasma applied voltage increased for both thickness experiments. The plasma-heating experiments were utilized the 99.999% pure H₂ with flow rate of 0.1 L/min and feeding pressure of 1atm. In plasma-heating experiment of 15µm membrane thickness, although the plasma applied voltage increased the H₂ permeability behavior decreased. It was observed that the main cause was the plasma random effect on the hydrogen gas which resulted in H₂ gas reverse reaction during the permeation process.

The activation energy, the pre-exponential constant factor (P_{e_0}) and the linear regression of the coefficient of determination (R^2) values of the two membranes at different operating conditions of heating only and plasma-heating experiments are reported in Tables (2.3 & 2.4). The feeding H₂ pressure of heating only and plasma-heating experiments are maintained at atmospheric pressure. This analysis was made according to equation (2) and the data collected from these experiments, in particular, it was observed that very low hydrogen permeation flow rates at low PMCR heating temperature, high Pd-Cu membrane thickness. In heating only experiment, it was clear the effect of hydrogen gas flow rate on the hydrogen diffusion mechanism through different Pd-Cu membranes thickness. In plasma-heating experiment, the hydrogen flux and permeability increased by applying plasma in both membranes experiment, where the plasma effect increase at low hydrogen gas flow rates.

The hydrogen permeation through Pd-Cu40% membrane using DBD plasma and heating effect did not indicate a linearity change for the hydrogen the dissociation and recombination processes of H₂ molecules and the adsorption and desorption processes of H₂ atoms. The hydrogen diffusion through the palladium membranes have been studied by Flanagan et al. [469].

It was investigated that the non-linearity reason was the partial pressure n-value. Also, they have been described the effect of H/Pd ratio in the proposed following equation of hydrogen diffusivity as follow:

$$D_H(r) = D_H^* \left(\frac{\partial \ln p_{H_2}^{1/2}}{\partial \ln r} \right)_T = D_H^* f(r) \quad (3)$$

Where the dependent diffusion concentration constant is $D_H(r)$, D_H^* is the independent diffusion concentration constant and $f(r) = (\partial \ln p_{H_2}^{1/2} / \partial \ln r)_T$ is the thermodynamic factor which expressed the H/Pd ratio. From equation (3), it was clear that the H/Pd ratio is changed related to the hydrogen pressure, while the H₂ permeability is the product of combination between solubility and diffusivity

Chapter 2. Hydrogen permeation through Pd-Cu membranes

Table .2. 3 Activation energy and the pre-exponential factor values of the Pd-Cu40% membrane thickness 15 μ m under heating only and plasma-heating experiments.

H ₂ flow rate[L/min]	Applied voltage[kV]	Activation energy Ea [kJ.mol ⁻¹]	Peo [mol.m ⁻¹ .s ⁻¹ .Pa ^{-0.5}]	R-Squared (R ²)
0.1	16	17.27	9.21E-08	0.880
0.1	14	18.46	1.11E-07	0.863
0.1	12	18.46	1.11E-07	0.863
0.1	10	18.96	1.18E-07	0.872
0.1	0	20.54	1.69E-07	0.845
0.5	0	15.61	5.76E-08	0.953
1.0	0	13.93	3.52E-08	0.949

Table 2.4 Activation energy and the pre-exponential factor values of the Pd-Cu40% membrane thickness 20 μ m under heating only and plasma-heating experiments.

H ₂ flow rate [L/min]	Applied voltage [kV]	Activation energy Ea [kJ.mol ⁻¹]	Peo [mol.m ⁻¹ .s ⁻¹ .Pa ^{-0.5}]	R-Squared (R ²)
0.1	16	35.12	1.92E-06	0.883
0.1	14	35.71	2.05E-06	0.890
0.1	12	34.52	1.42E-06	0.886
0.1	10	34.24	1.23E-06	0.884
0.1	0	37.65	2.74E-06	0.893
0.5	0	37.53	3.02E-06	0.870
1	0	37.17	2.90E-06	0.869

To clarify the plasma effect on the H₂ permeability, a comparison between the permeability of heating only and plasma-heating experiments was introduced for both Pd-Cu membranes thickness at same operating conditions. Figure (2.12) shows the comparison between heating only and plasma-heating experiments for 15 μ m membrane thickness. It was found that the H₂ permeability increased with PMCR heating temperature. Also, the H₂ permeability improved and increased by applying

Chapter 2. Hydrogen permeation through Pd-Cu membranes

plasma effect. It can be concluded that the H₂ permeability improved with plasma in different applied voltage; it can also observed the plasma nonlinearity effect at 16kV, 573K conditions that at high plasma voltage and high PMCR heating temperature the permeability gas stream decreased due to the H₂ molecules reverse reaction.

The effect of plasma on 20μm membrane thickness was also carried out across applied voltage range of 12-16kV and PMCR heating temperatures of 423-573K. The H₂ permeability under heating only and plasma-heating experiments was investigated in Figure (2.13). The H₂ permeability trend shows trend with heating temperature and nonlinearity effect for applied plasma voltage. The pure hydrogen transported across 20μm membrane thickness was lower than that obtained from 15μm membrane thickness. It can be concluded that the plasma effect at high plasma applied voltage was limited due to hydrogen molecules reverse reaction. In plasma-heating experiment, it was investigated that the maximum obtained hydrogen permeability values of 15μm and 20μm membrane thickness experiments at PMCR heating temperature 573K and applied voltage of 14kV and 16kV respectively.

The H₂ permeation rate % was calculated based on the measurement date of both experiments for more investigation of the effect of thickness on the hydrogen permeation processes. The permeation rate% can be defined as the ratio of the hydrogen flux to the inlet hydrogen gas flow rate and it can be expressed as follows:

$$\text{Hydrogen permeation rate\%} = [\text{hydrogen flux (L/min)}] / [\text{hydrogen gas inlet flow rate (L/min)}] \times 100$$

Figure (2.14) presents a comparison between the heating only experiments results for 15μm & 20μm Pd-Cu40% membrane thickness at different H₂ flow rates. It was observed that the hydrogen permeation rate percent of 15μm Pd-Cu membrane thickness was higher than 20μm membrane thickness at all testing PMCR heating temperatures. The maximum permeated H₂ gas is obtained at 573K PMCR heating temperature and H₂ feeding flow rate 0.1 L/min for both Pd-Cu membrane thicknesses. One of the most interesting results of heating only experiment, the permeation rate percent of 20μm Pd-Cu membrane thickness is sharply decreased at lower PMCR heating temperature, while in 15μm membrane thickness the permeated hydrogen still high at low PMCR heating temperatures.

The effect of plasma-heating on H₂ permeability is shown in figure (2.15). The H₂ permeability trend was enhanced by applying plasma for both membrane thickness experiments. It can be interpreted in atmospheric plasma effect in terms of producing high electron temperature and high motion which increased the hydrogen dissociation and permeation effect. It was considered that the DBD plasma have a positive effect on the H₂ permeability but it has been reported a nonlinearity effect, while the plasma

Chapter 2. Hydrogen permeation through Pd-Cu membranes

applied voltage increased as in 15 μm membrane thickness. Our plasma-heating experiments results showed that the plasma effect increased by the reactor heating temperature increased.

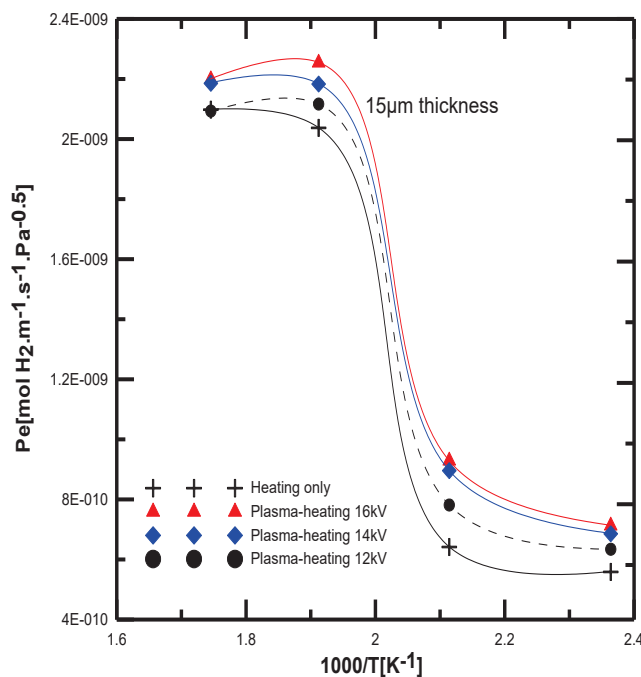
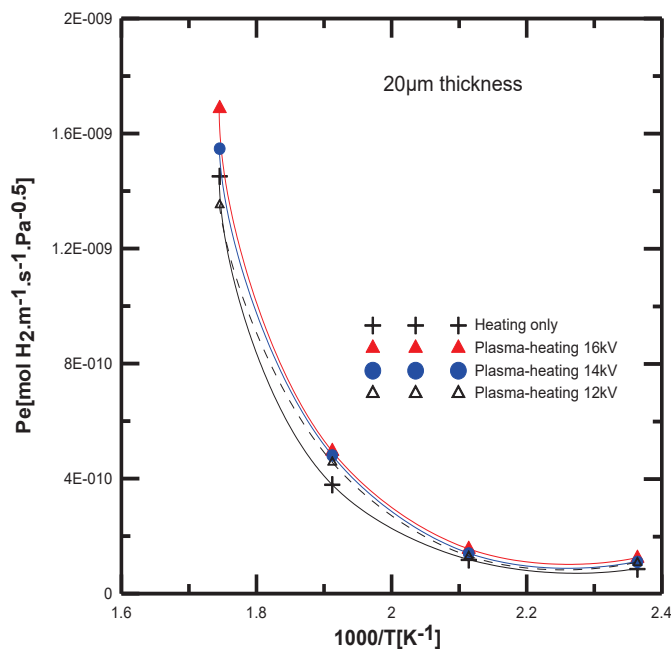


Fig.2.12 Effect of heating only and plasma heating experiment on H_2 permeability for 15 μm membrane thickness.



Chapter 2. Hydrogen permeation through Pd-Cu membranes

Fig.2.13 Effect of heating only and plasma heating experiment on H₂ permeability for 20 μ m membrane thickness.

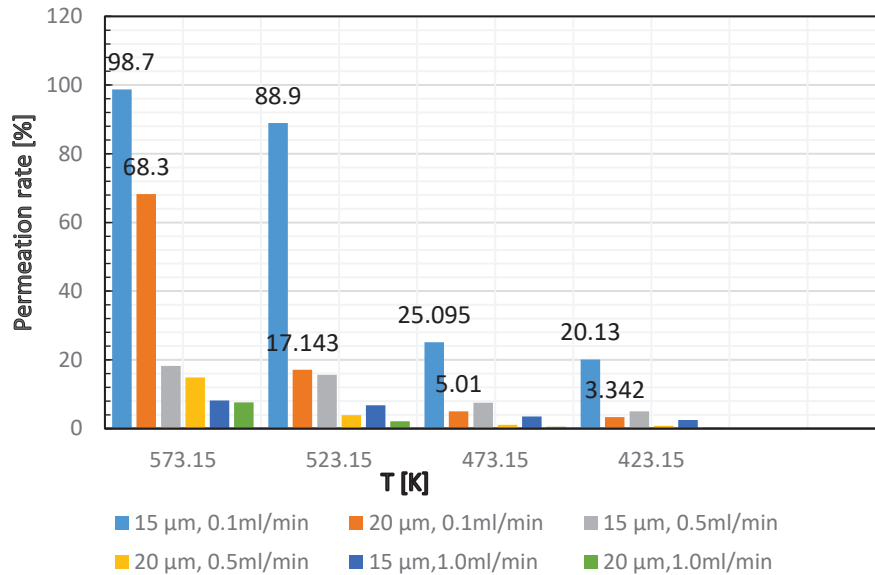


Fig.2.14 Comparison between 15 μ m & 20 μ m membrane thickness of heating only.

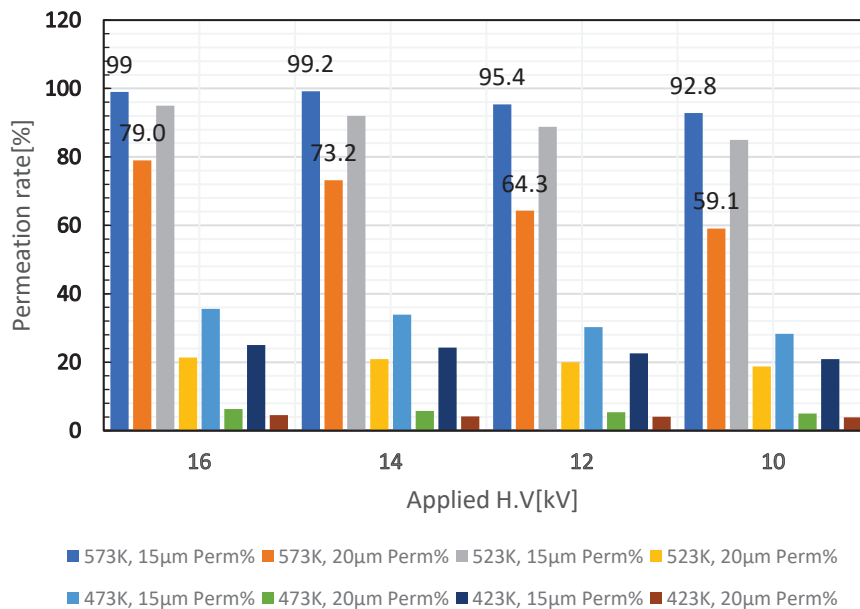


Fig.2.15. Comparison between 15 μ m & 20 μ m Pd-Cu40% membrane thickness of Plasma-heating experiment at different applied voltage.

Chapter 2. Hydrogen permeation through Pd-Cu membranes

The first interesting result of the Pd-Cu40% experiment, it was observed that the hydrogen permeability depends on the membrane thickness, the reactor heating temperature and the DBD plasma applied voltage, while the feeding pressure in this experiment was maintained at atmospheric pressure. It was found that the hydrogen flux and hydrogen permeability increased at low Pd-Cu membrane thickness and high PMCR heating temperature. Also, it is noticed that according to the values of activation energy and the pre-exponential factor reported in tables (2.3&2.4), additionally the low hydrogen flow rate the highest hydrogen adsorption residence time.

Another consideration from this experiment results is the effect of power pressure n-value 0.5 on the permeation results, the hydrogen flux and the hydrogen permeability are described adequately according to the hydrogen permeation mechanism and the experimental conditions. It was found that the activation energy of the plasma-heating experiment changed according to the plasma applied voltage in random behavior, it was seen that all adsorbed H₂ molecules weren't directly permeated to the membrane opposite direction due to the reverse reaction of hydrogen molecules at high plasma applied voltage.

Conclusion

The pure hydrogen permeability of Pd-Cu40% alloy membranes thickness of 15 μ m and 20 μ m were determined across a temperature range of 423-573K for 1mm gap length plate type reactor (PMCR) at atmospheric pressure on the feeding side for heating only and plasma-heating experiments. The effect of membrane thickness on hydrogen permeation under heating only and plasma-heating experiments were investigated in this study. The hydrogen permeation flux was calculated based on the Fick's and Sievert's law equation. The hydrogen permeation flux n-value 0.5 was used in calculations. It was observed that the n-value 0.5 did not describe the permeation specially, in the plasma-heating experiment. Further, the pre-exponential factor and the activation energy were determined for both experiments and showed a non-linearity in plasma-heating experiments.

It was found from the experimental results the hydrogen permeation dependence on the membrane thickness. The hydrogen permeation of 15 μ m Pd-Cu40% membrane thickness showed a higher hydrogen flux and permeability than 20 μ m Pd-Cu40% membrane thickness in heating only and plasma-heating experiments. The analysis of H₂ permeability for heating only experiment showed lower values than that obtained from the plasma-heating experiment for both Pd-Cu

Chapter 2. Hydrogen permeation through Pd-Cu membranes

membranes thicknesses. It was observed in 15 μ m membrane thickness plasma-heating experiment that the hydrogen permeability decreased while the DBD-plasma applied voltage was increased to 16kV, the main cause can be interpreted in the dissociated hydrogen gas reverse reaction. A comparison between the hydrogen permeability and the permeation rate% of both experiments has been developed to investigate the dependence on the membrane thickness and the effect of heating only and plasma-heating experiments. The analysis showed that the permeability of 15 μ m membrane thickness was always higher than 20 μ m membrane thickness results and the maximum hydrogen permeability was at PMCR heating temperature of 573K.

2.3 Introduction

According to the climate change and oil depletion, an alternative clean and sustainable energy source is needed. Hydrogen fuel has the ability to meet these requirements without any environmental impact. Hydrogen production is gradually increasing as a next generation energy carrier. A various method have been investigated to produce hydrogen gas using renewable or non-renewable energy as the energy source [80, 324, 337]. Compared with the conventional fossil fuels, hydrogen has been registered the highest values of the higher and lower heating values [348]. Different hydrogen economic comparative assessment studies have been developed [470-473]. It was found that the costs of hydrogen production of most hydrogen production methods are still high or have low efficiencies [349]. Additionally, the evaluation of environmental, financial, social, and technical performance of 19 selected hydrogen production methods have been comparatively studied [350]. It was seen that the energy efficiency of the reforming method has the highest value of 83%, while the photonic (solar) has registered the lowest energy efficiency among the selected hydrogen production methods. Currently, the steam reforming method using methane as a hydrocarbon fuel is acting the majority of available produced hydrogen gas in the market [438]. Among hydrogen gas production methods hydrogen gas is most often produced combining with other different gases. Because of this, a separation process is needed to get pure hydrogen gas. The palladium and palladium alloys' membranes have been utilized in fuel cells applications to separate hydrogen in the steam reforming and coal gasification processes [440, 441]. Three main processes are commonly used in hydrogen purification in industrial applications, cryogenic distillation, pressure swing adsorption [444] and membrane separation [445-447]. Recently, the membrane separation technique is considered the most efficient technology, due to its low energy consumption and lower cost compared to other separation processes [448]. Palladium based and its alloys are the most widely used due to the following characteristics: high

Chapter 2. Hydrogen permeation through Pd-Cu membranes

hydrogen permeability, chemical compatibility with many hydrocarbons containing gas streams, theoretically infinite high hydrogen selectivity and good durability [406, 449-452]. Palladium alloys often possess higher hydrogen permeation than pure palladium membranes. The binary alloys such as Pd_{0.75} Ag_{0.25} wt%, Pd_{0.60} Cu_{0.40} wt% have been investigated [426, 454]. Especially the palladium–copper alloy with composition Pd_{0.60}-Cu_{0.40}wt%, it presented a cost reduction benefit while maintaining a desirable set of properties [427, 449, 457–459]. In fact, these particular alloys are generally attributed to the higher diffusivity of atomic hydrogen [426]. Additionally, the dilution of palladium metal through alloying can reduce the high cost of the membrane process [400]. The Pd-Cu alloy with a composition of Pd_{0.60}-Cu_{0.40} wt% has the highest permeability compared to pure Palladium [426, 449, 457, 468].

Devices using Pd-Cu foil membranes being tested have shown good results in hydrogen permeation and poison resistance [346, 474, 475]. Those Pd-Cu alloys are fabricated using a variety of techniques beyond the metal rolling operations, [426, 407, 457-410] which included the individual and combined electroless plating [411, 412], the chemical vapor deposition, sputtering, etc. [413, 476]. In the palladium copper system, the composition of Pd_{0.60}wt% - Cu _{0.40}wt% contained a mixed phases, body centered cubic (bcc) and the face centered cubic (fcc), this resulted in the high mobility of hydrogen molecules within bcc phase structure relative to fcc phase [426-429]. In this study a mixed fcc-bcc Pd-Cu phase diagram of the membrane alloy foil is used. For the membrane Pd_{0.60} wt% Cu_{0.40} wt% composition the fcc phase is existed with the bcc phase and emerges within a temperature range of (450°C~550°C). This combination of the binary phases increases the hydrogen transport and increase the contamination resistance compared to bcc phase only [463, 464]. The effect of the positioned Pd_{0.60}-Cu_{0.40} wt% alloy thin film foil membrane on the high-pressure hydrogen feed side was also tested [477].

The Pd alloys membrane is mostly used in hydrogen separation for the hydrogen production technology. Especially for the Pd-Cu alloy which has a high mechanical and chemical stability, high hydrogen flux and lower cost than the other Pd alloys. The hydrogen permeation mechanisms through Pd-Cu membrane can be expressed that H₂ molecules it must be adsorbed from the membrane surface then diffused through the membrane lattice then hydrogen atoms recombination in the opposite side and desorption from the membrane surface.

In this paper the hydrogen permeation through a 20µm thickness, Pd_{0.60}-Cu_{0.40}wt% membrane foil is tested. The hydrogen gas concentration of 100% and the micro-channel plate reactor (MPR) with gap length 4.5mm are used. The hydrogen permeation was measured using the plasma-heating and heating only tests. The effect of plasma on the hydrogen permeation at different temperatures is investigated. The plasma voltage ranges of (10kV to 18kV) and the reactor heating temperature ranges

Chapter 2. Hydrogen permeation through Pd-Cu membranes

of (423K to 573K) are also tested in this experiment. Also, the effect of hydrogen gas flow rates on hydrogen permeation is studied. The hydrogen permeability, the hydrogen flux, the hydrogen permeation rate and the activation energy have been calculated.

2.3.1 Experimental

The micro-channel plate reactor (MPR) was made from stainless steel material (SUS304). The detailed reactor parts are shown in figure (2.16). The reactor is composed of the following parts: the base plate, permeate plate, Pd_{0.60}-Cu_{0.40}wt% membrane foil, micro-flow channel top plate (SUS304), Dielectric quartz glass (2mm thickness) and the electrode mesh (SUS304 mesh 45mm×45mm). There are three ports for hydrogen gas, inlet and outlet port in the top plate and the permeation port in the base plate. Also, the gap length drawing is shown in this figure, the gap length is the place of reaction which the input hydrogen gas can permeate through the Pd-Cu membrane. The gap length is 4.5mm and is measured between the quartz glass and the membrane foil. The Pd_{0.60}-Cu_{0.40}wt% membrane foil, thickness 20μm was made by TANAKA HOLDINGS Co., Ltd using the mixed fcc and bcc region. From the previous literature review it was shown that the mixed fcc and bcc region can have high permeability, in addition to the high mechanical and chemical stability characteristics.

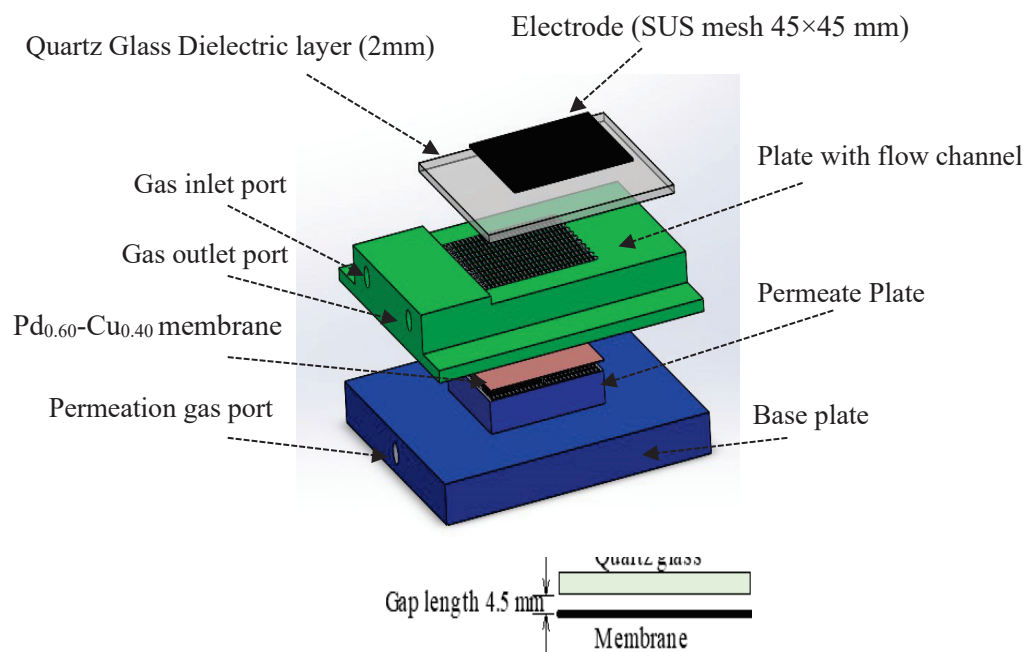


Fig. 2.16 Exploded view of the micro-channel plate reactor (MPR) and gap length.

Chapter 2. Hydrogen permeation through Pd-Cu membranes

The Pd-Cu membrane foil dimension is 50mm×50mm and is completely close to the support plate using gasket material. The drying process is made for the assembled (MPR) reactor inside the instantaneous heater at temperature of 100°C for 3 hours. The leakage check is after the complete assembly dries.

In this study pure hydrogen gas was into the MPR at atmospheric pressure and different flow rates. Figure (2.17) shows the experimental layout and the gas line connections, the hydrogen gas analyzer is connected at the permeate side to check the hydrogen gas concentrations. In addition, the soap flow meter is used to measure the permeated hydrogen gas flow rate. Also, at the permeate side vacuum pump type of N810.3FT.18 (KNF Company) is connected directly to the MPR reactor with a maximum flow rate of 10 l/min. The digital mass flow controller (MFC) is used to control the hydrogen gas inlet flow rate. The outlet valve (C.V4) is fully opened to ambient during the test operation. The feeding and the permeate pressures are monitored using the digital pressure gauges. The reactor temperature is raised using the surface stirrer heater which is adjusted to the required testing temperatures.

In the plasma-heating experiment, the high voltage source is directly connected at the electrode center on the upper side of the reactor which was also controlled by the high voltage regulator. In preparation, the PMR reactor is heated for 10hours with a continuous hydrogen gas flow rate to make the Pd-Cu membrane activation before starting the permeation experiment. Then, the reactor is heated to the permeation testing temperature for 1hour. Additionally, for plasma experiment, plasma firing test is firstly made using argon gas. Also, the leakage test is made before starting the hydrogen permeation experiment. The hydrogen flow rate is measured using the soap flow meter at the permeate side after the hydrogen gas concentration reading reached to 20mA on the hydrogen gas analyzer. In this experiment, the sweep gas is not used only the pure hydrogen gas.

Chapter 2. Hydrogen permeation through Pd-Cu membranes

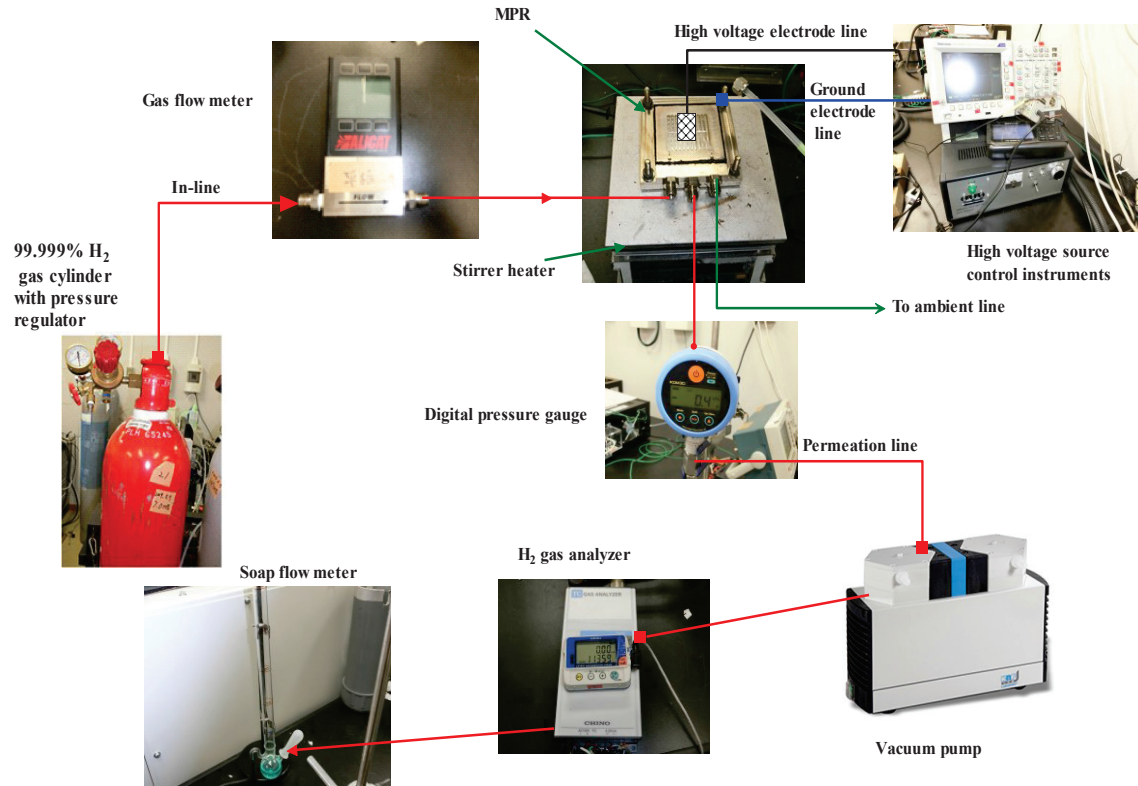


Fig. 2.17 Schematic diagram of the Experimental setup.

2.3.2 Results and discussion

The diffusion of hydrogen gas molecules through the palladium membranes has been investigated by different authors. Generally, the hydrogen flux formula is resulted from the combination of the Fick's first law and Sieverts law equations. The hydrogen flux formula can be described as follows:

$$J_H = \frac{Pe}{\delta} (p_f^{0.5} - p_p^{0.5}) \quad (1)$$

Where J_H is the hydrogen gas flux ($\text{mol. m}^{-2}.\text{s}^{-1}$), Pe is the hydrogen permeability ($\text{mol. m}^{-1}.\text{s}^{-1}.\text{Pa}^{-0.5}$), p_f and p_p are the hydrogen gas partial pressure (Pa) of the feeding and permeate sides respectively, and δ is the Pd-Cu membrane thickness (m). It was observed that the hydrogen flux is proportional to the difference of square root of the feeding and permeate side partial pressures and the inverse of the Pd-Cu membrane thickness.

In this study, the MPR reactor was tested under heating only in a temperature range of 423-573K and H_2 flow rates 0.1-11/min while in the plasma-heating

Chapter 2. Hydrogen permeation through Pd-Cu membranes

experiment was carried out at H₂ flow rate 0.1l/min and plasma applied voltage 10-18 kV.

2.3.2.1 Testing MPR reactor using heating only

In this experiment the hydrogen flux is measured using heating only at different temperatures and different hydrogen gas flow rates. The effect of the permeation driving force (the square root feed and permeate partial pressure differences) according to the eq. (1) is presented in figure (2.18). The hydrogen flux is measured after the hydrogen gas analyser reading reached to 20mA, it means that the hydrogen gas concentration at the outlet of the permeate side is 100% H₂. The permeated hydrogen gas flow rate is measured using the soap flow meter. The hydrogen flux is calculated using eq. (1).

Since the hydrogen permeability coefficient depends on the heating temperature of the MPR and the permeation process is a mass transfer phenomenon. The hydrogen permeability coefficient is assessed according to the Arrhenius's law as follows:

$$Pe = Pe_0 e^{-E_a/RT} \quad (2)$$

Where, Pe_0 is a constant describing the pre-exponential factor ($\text{mol. m}^{-1}.\text{s}^{-1}.\text{Pa}^{-0.5}$), E_a is the activation energy (J. mol^{-1}), R is the universal gas constant ($8.314 \text{ J.mol}^{-1}.\text{K}^{-1}$) and T is the heating temperature (K). The effect of temperature on the hydrogen permeability coefficient is shown in figure (2.19). It was observed that the hydrogen permeability of the hydrogen inlet flow rate 0.1 l/min is higher than the other tested hydrogen gas inlet flow rates (0.5 and 1 l/min), it means that the lower hydrogen gas flow rate, the higher hydrogen gas permeability. It can be described that as the residence time of 0.1l/min flow rate higher than residence time of 0.5and 1l/min subsequently, the H₂ permeability of 0.1l/min higher than that obtained for other flow rates. The residence time values for the hydrogen gas flow rates (0.1, 0.5 and 1 l/min) are (3.178s, 0.636s, 0.3178s) respectively.

Figure (2.20) shows the hydrogen permeation rate % versus the MPR heating temperatures at different H₂ flow rates. The highest hydrogen permeation rate was obtained at the highest MPR heating temperature for all tested H₂ flow rates. The permeation rate% was determined according to the following equation:

Hydrogen permeation rate% = $[\text{hydrogen flux (l/min)}] / [\text{hydrogen gas inlet flow rate (l/min)}] \times 100$

Chapter 2. Hydrogen permeation through Pd-Cu membranes

2.3.2.2 Testing MPR reactor using Plasma-Heating

The MPR plasma-heating testing experiment is carried out using a membrane type of Pd_{0.60}-Cu_{0.40}wt% with thickness of 20μm, gap length 4.5mm and within a temperature range of 423-573K. The discharging voltage range of the plasma firing testing is 10-18kV, where the frequency is constant at 10 kHz. In this experiment the voltage regulator is used to control the feeding high voltage to the MPR reactor. The high voltage source is connected at the center of electrode (SUS304 mesh) and the earth cable is connected to the upper plate with flow channels.

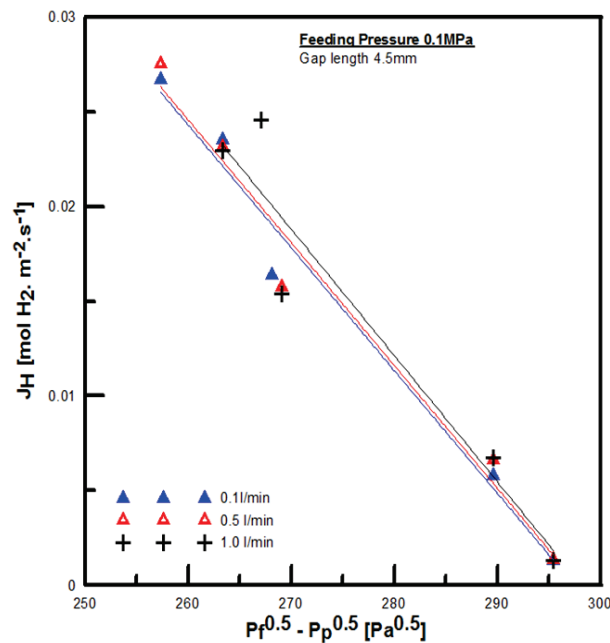


Fig.2.18 Hydrogen flux vs. the square root hydrogen partial pressure in feeding and permeation side for Pd-Cu membrane.

Chapter 2. Hydrogen permeation through Pd-Cu membranes

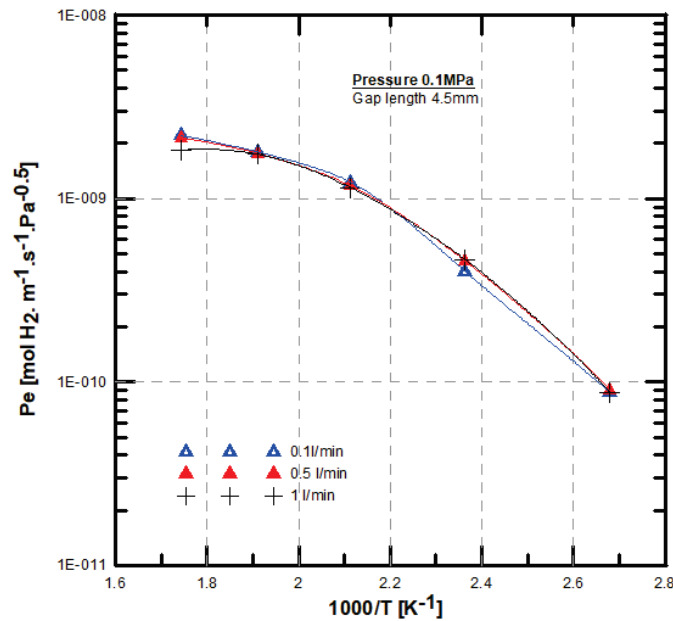


Fig. 2.19 Arrhenius plot of H₂ permeability for heating only experiment.

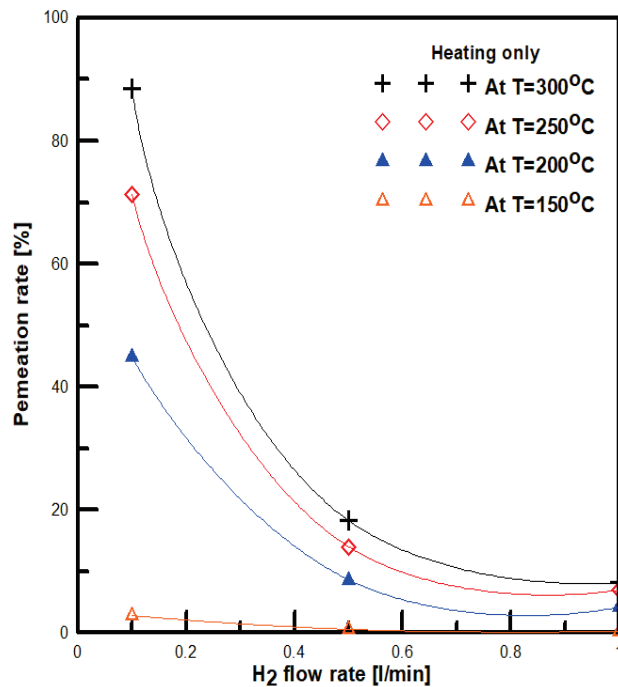


Fig.2.20 Hydrogen permeation rate% Vs. MPR heating temperatures.

Also, before starting the plasma-heating testing the reactor is heated for 1 hour at the determined permeation testing temperature. The plasma firing is first tested using argon gas. Figure (2.21) shows the testing of the plasma firing using argon gas.

Chapter 2. Hydrogen permeation through Pd-Cu membranes

It was found that the hydrogen permeation testing using plasma did not destroy or change the membrane properties. The effect of plasma is resulted in the appearance and the hydrogen permeation behavior.

The hydrogen permeation flux versus the different discharge voltage at different heating temperature is presented in figure (2.22). It is observed the highest hydrogen flux is at the highest heating temperature. The hydrogen flux using plasma is not linearly changed. It was investigated that the reason of non-linearity is the partial pressure n-value. Flanagan et al. [469] have studied the hydrogen diffusion through the Pd membranes. The hydrogen diffusivity equation has been derived to describe the effect of H/Pd ratio. Flanagan et al. proposed the following equation:

$$D_H(r) = D_H^* \left(\frac{\partial \ln p_{H_2}^{1/2}}{\partial \ln r} \right)_T = D_H^* f(r) \quad (3)$$

Where $D_H(r)$ is the dependent diffusion concentration constant, D_H^* is the independent diffusion concentration constant and $f(r) = (\partial \ln p_{H_2}^{1/2} / \partial \ln r)_T$ is the thermodynamic factor which expresses the H/Pd ratio.

The maximum hydrogen flux was obtained at 14kV and heating temperature 573K, although the high voltage is raised to 16kV and 18kV, the hydrogen permeation flux is not increased. It was found that the main reason of the hydrogen flux decreasing was the hydrogen gas reverse reaction. It occurred as follows:



Also, it was clear that the hydrogen flux is decreased with decreasing the MPR heating temperature, while the feeding pressure of all permeation experiments are made at 100kPa.

The hydrogen permeability using plasma and heating was determined based on the experiment data. Figure (2.23) investigates the change of hydrogen permeability with the inverse of the reactor heating temperature at different firing plasma voltage. It was clear from this experiment that the hydrogen permeation isn't always increased by increasing the plasma voltage. Also, although the temperature inside the MPR increased with plasma firing the permeated hydrogen gas did not increase. In the investigation of the hydrogen permeability using plasma, the permeation rate percent is calculated for all plasma experiment of the MPR. Figure (2.24) presents the change of the hydrogen permeation rate percent at different plasma applied voltage. The highest H_2 permeation rate value is obtained at 14kV and temperature of 573K. The plasma effect on the hydrogen gas permeability of the $Pd_{0.60}-Cu_{0.40}wt\%$ membrane

Chapter 2. Hydrogen permeation through Pd-Cu membranes

was increased compared to that obtained from the Pd_{0.75}-Ag_{0.25} test using plasma test which shows no hydrogen permeability change [352].

Table (2.5&2.6) present the activation energy, the pre-exponential constant factor (P_{e_0}) and the linear regression of the coefficient of determination (R^2) which are calculated for the heating only and the plasma heating experiment at feeding pressure 100kPa respectively. It is observed from the values in table (2.5) that the activation energy and the pre-exponential factor constant decrease as the hydrogen gas flow rate increases.

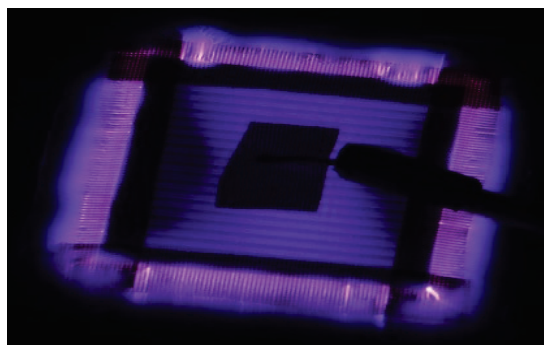


Fig.2.21 MPR plasma firing test photo using 20 μ m Pd_{0.60}-Cu_{0.40}wt% membrane.

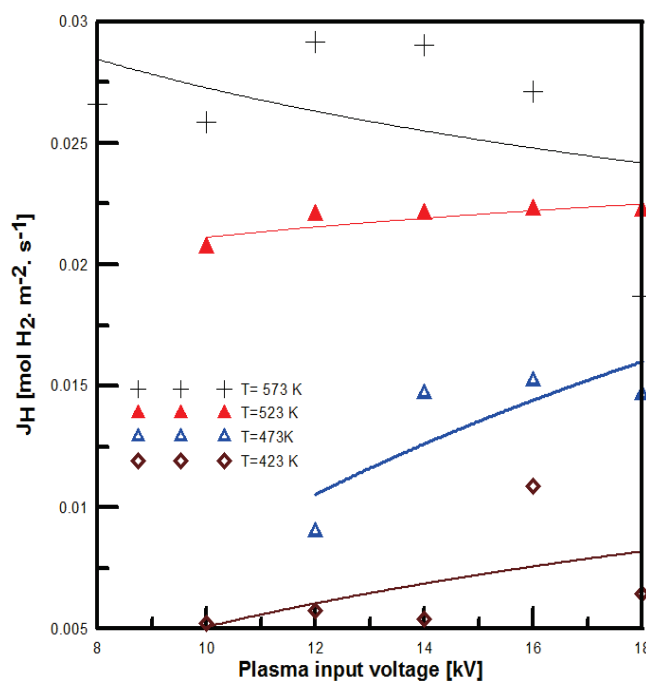


Fig.2.22 Hydrogen flux using plasma and heating at different voltage.

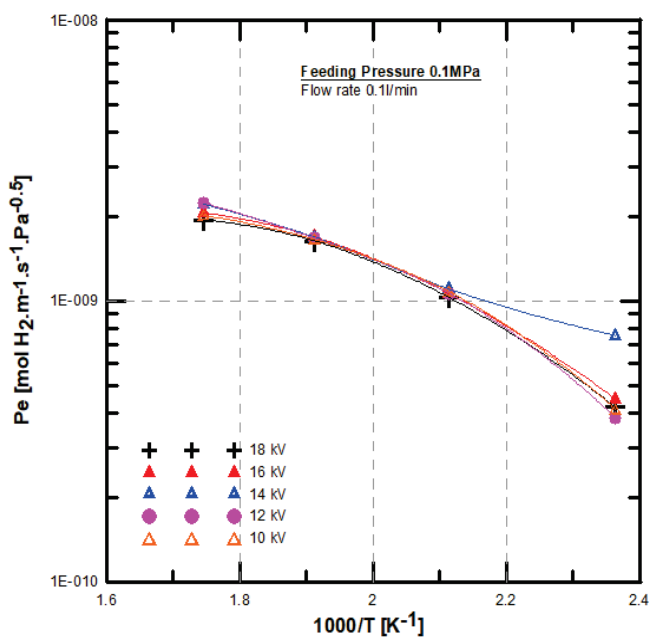


Fig.2.23 Arrhenius plot of hydrogen permeability using plasma and heating at different voltage.

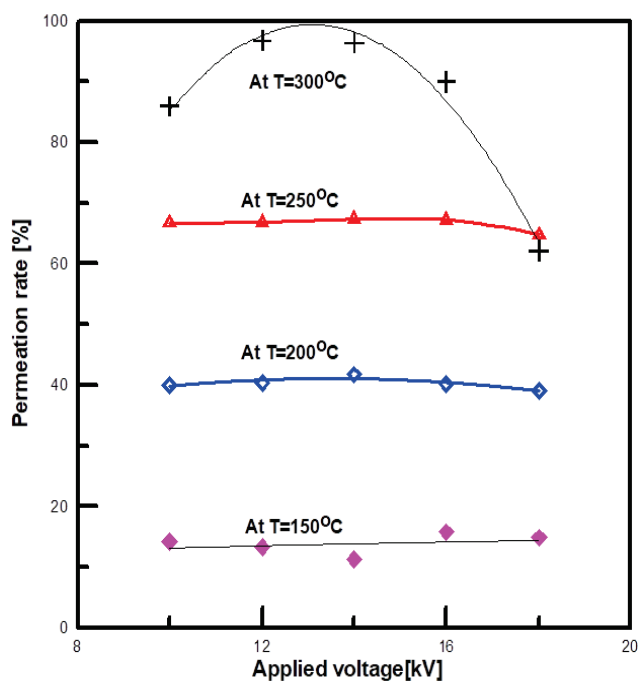


Fig.2.24 Hydrogen permeability using plasma and heating at different voltage.

Chapter 2. Hydrogen permeation through Pd-Cu membranes

So, the heating only experiment for the 20 μ m thickness membrane trend was opposite to the activation energy and pre-exponential factor constant. This experiment clearly presented the effect of the hydrogen gas flow rate on the hydrogen diffusion mechanism through Pd-Cu membrane. Table (2.6) investigates the plasma-heating experiment activation energy which showed the activation energy of the plasma-heating test at 14kV is the lowest value and has the highest hydrogen permeability value at temperature 573K. It was clear that the hydrogen permeability of the plasma-heating experiment is higher than the hydrogen permeability testing with the heating only experiment. The plasma effect was especially high at the lower hydrogen gas flow rates.

Table .2.5 Activation energy and the pre-exponential factor values of the Pd_{0.60}-Cu_{0.40} MPR reactor using heating only.

Feeding Pressure [kPa]	Inlet flow rate [l/min]	Activation energy E _a [kJ.mol ⁻¹]	Pe ₀ [mol.m ⁻¹ .s ⁻¹ .Pa ^{-0.5}]	R ²
100	0.1	28.881	1.268×10 ⁻⁶	0.945
100	0.5	28.303	1.121×10 ⁻⁶	0.946
100	1	27.520	8.791×10 ⁻⁷	0.925

Table .2.6 Activation energy and the pre-exponential factor values of the Pd_{0.60}-Cu_{0.40} MPR reactor using plasma and heating.

Pressure [kPa]	Applied voltage [kV]	Activation energy E _a [kJ.mol ⁻¹]	Pe ₀ [mol.m ⁻¹ .s ⁻¹ .Pa ^{-0.5}]	R ²
100	18	3.304	6.583×10 ⁻⁹	0.892
100	16	3.888	1.047×10 ⁻⁸	0.992
100	14	2.680	6.146×10 ⁻⁹	0.975
100	12	4.413	1.386×10 ⁻⁸	0.992
100	10	4.025	1.102×10 ⁻⁸	0.985

A comparison between the hydrogen flux of the MPR reactor experiment using heating only and plasma-heating experiment is investigated. Figure (2.25) shows a comparison between the obtained hydrogen fluxes in both experiments at feeding pressure of 100kPa and MPR heating temperature 573K. Additionally, to investigate

Chapter 2. Hydrogen permeation through Pd-Cu membranes

the effect of plasma on H₂ permeation the lower flow rates are tested. It was clear that the plasma effect increased with the H₂ gas input flow rate decreased. The energy efficiency of both experiments was calculated. Figure (2.26) presents a comparison between the energy efficiency values of heating only and plasma-heating experiments versus the total heat added. It was found that the energy efficiency of plasma-heating was lower than heating only experiment due to the plasma-heating experiment total power is high while the permeated H₂ gas of plasma-heating experiment is higher than heating only experiment. The energy efficiency was defined as follows: Energy efficiency [%] = $\text{HHV} \times \text{Permeated H}_2 \text{ flow rate} / (\text{System power consumption} + \text{HHV} \times \text{input H}_2 \text{ flow rate}) \times 100$, where HHV is the higher heating value of the permeated hydrogen.

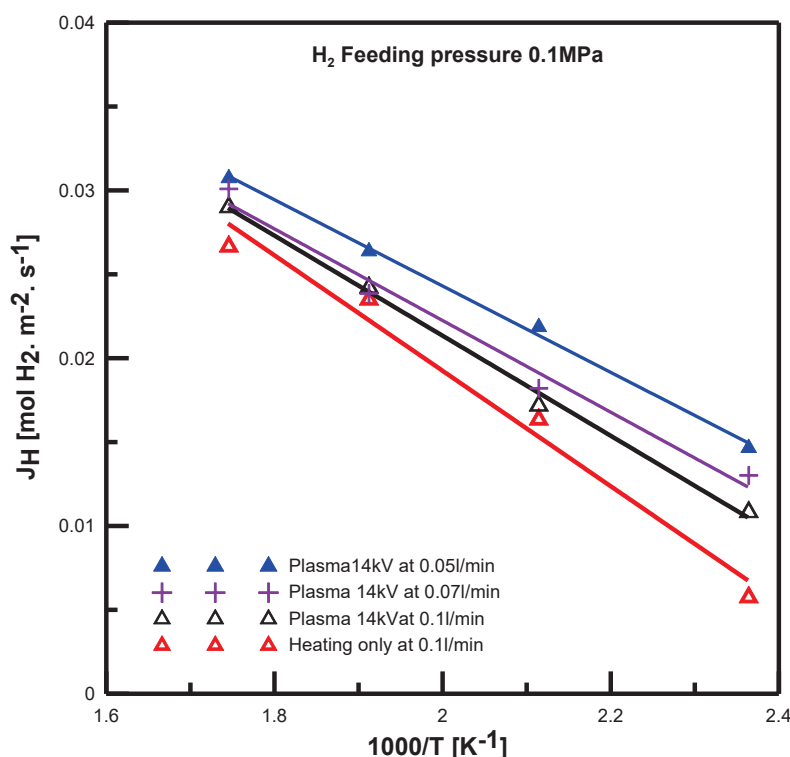


Fig.2.25. Comparison between heating and plasma plus heating.

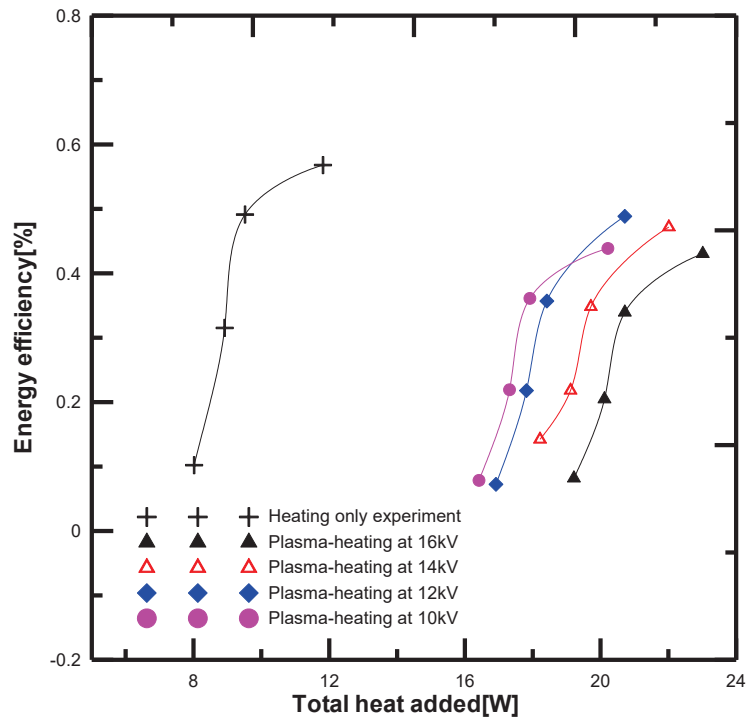


Fig. 2.26. Comparison of energy efficiency vs. total heat added.

Conclusion

In this study, the permeation test of 100% H_2 concentration through the MPR reactor is tested using the $20\mu m$ Pd_{0.60}-Cu_{0.40}wt% membrane with gap length of 4.5mm. The hydrogen flux and the hydrogen permeability is calculated by using the Fick's and Sievert's laws combining equation. The partial pressure n-exponent value of 0.5 is used for calculating the hydrogen permeation flux and the hydrogen permeability. The hydrogen permeation tests are performed for MPR at different heating temperatures in a range of 423-573K. The hydrogen flux, the hydrogen permeability, and the permeation rate percent are calculated for the heating only and the plasma-heating experiment. The plasma heating test is performed at high voltage ranges of 10-18kV while H_2 gas feeding pressure of 100kPa. The MPR heating only and plasma heating experiment results showed that the higher heating temperature, the higher hydrogen permeation flux and hydrogen permeability. In heating only experiment, the flow rate of 0.1l/min has higher hydrogen permeation flux and hydrogen permeability, additionally; the maximum hydrogen flux and hydrogen permeability is at the same low feeding hydrogen gas flow rate 0.1 l/min and the heating temperature of 573K. In the plasma heating experiment, it is observed that the maximum hydrogen flux, hydrogen permeability, and permeation rate percent at MPR

heating temperature of 573K and plasma firing voltage of 14kV. Also, the hydrogen permeation rate decreased due to the hydrogen reverse reaction even though the plasma voltage increased to 16kV and 18kV. The activation energy E_a and the pre-exponential constant factors P_{eo} have been calculated according to the Arrhenius equation for both experiments. The results also reveal that the activation energy and Pre-exponential constant factor decreased with increasing the feeding H_2 flow rate while the linear regression R^2 decreased with increasing H_2 feeding flow rate in the heating only experiment. In contrast, the plasma heating experiments showed non-linearity values of activation energies and pre-exponential constant factors. A comparison between the MPR heating only and plasma heating experiments showed the hydrogen permeation flux of the plasma heating results were higher than those obtained from the heating only experiment and the plasma effect increased at low flow rates.

2.4 A comparison between GDP and PDP experiments of hydrogen permeation through 15 μ m Pd60-Cu40% membrane thickness

The hydrogen separation by palladium (Pd) based membranes are considered the most convenient method to purify or remove hydrogen from gas mixtures due to their high permeability and selectivity [406, 449-452]. The available hydrogen gas in the market is produced from reforming methods [80, 324, 438, 478, 479]. Further, the pure hydrogen gas is mostly needed for the fuel cells applications, therefore the proton exchange membranes using Pd and Pd-alloys membranes will be expected growing to cover hydrogen gas demands [439-441]. Hydrogen permeation has been investigated by different methods such as gas pressure difference between the membrane surfaces (gas-driven permeation), exposure to hydrogen plasma (plasma-driven permeation), etc. [368, 480]. Hydrogen permeation through Pd-based membranes consists of the following steps: (i) H_2 adsorption on the feeding membrane surface side, (ii) dissociation of H_2 molecules into atoms on the same surface, (iii) dissolution of H atoms into bulk, (iv) the hydrogen bulk diffusion into the opposite side, (v) recombination of H_2 molecules from the H atoms, (vi) desorption of H_2 molecules on the membrane permeate side [481]. The role of the fusion fuel cycle is to recover and reprocessing of the deuterium-tritium fuel mixture from all fusion reactor systems. Un-reacted fuel and helium are produced by the nuclear fusion reaction as the plasma exhaust gases. Moreover, the plasma exhaust gas also contains some impurities such as methane, hydrogen (protium (H)) and water. The fusion fuel cycle systems recover

Chapter 2. Hydrogen permeation through Pd-Cu membranes

hydrogen isotopes from the plasma exhaust gas, separate the fuel from hydrogen isotope mixture and inject the fuel to the plasma. The Pd-alloy membranes studies offers the premises of their use in systems that deal with the separation/purification for the hydrogen isotopes, from both gas- and liquid-tritiated streams, with the aim of tritium recovery and reuse it in the fuel for fusion reactors [482]. Many studies have been investigated on the membrane applications to the nuclear fusion fuel cycle, an engineering approach to utilize the metallic catalytic membrane for the tritium extraction from liquid breeders has been developed [483]. H. Yoshida et al. [484] analysed and evaluated the Pd/Ag membrane separator required exchange area to recover the hydrogen isotopes at a high purity level. A conceptual design for a tritium recovery plant using a Pd/Ag separation unit has been developed [485]. The H₂ permeation through Pd-Cu membranes have been reported a high permeability than the obtained results from pure palladium membranes, especially palladium alloys membranes such as Pd-Ag25% and Pd-Cu40% [426, 454]. On the other hand, the Pd-Cu alloys membranes have a good resistance to H₂S poisoning and permeability is high [427, 449, 454-459, 486].

The fabrication of Pd-Cu alloys membranes can be made by different methods like electroless plating, chemical vapor deposition, sputtering, etc. In the Pd-Cu alloys composition of Pd- Cu40wt%, a mixed phase's body centered cubic (bcc) and the face centered cubic (fcc) were found. These mix between the phases have reported a high mobility of hydrogen molecules and permeability compared to single phase results [407-413, 428, 429]. In this study a combination between fcc and bcc phase was used in the Pd-Cu membrane fabrication. Figure (2.27) shows the combination of the binary phases in a temperature range of 450~550°C.

In this study, the performance evaluation of the hydrogen permeation under GDP and PDP effect were studied for 15µm Pd-Cu40% membrane thicknesses in a micro channel plate reactor (PMCR). Pure hydrogen gas is fed into the reactor at H₂ flow rates of 0.1-1L/min and PMCR heating temperature range of 423-573K. In PDP experiment, the dielectric barrier discharge plasma (DBD) was used at a discharge voltage range of 10-16kV, heating temperatures 423-573K and H₂ flow rate 0.1L/min. the hydrogen flux was determined according to Fick's and Sievert's law equation partial pressures n-value of 0.5. The effect of heating and plasma on the energy efficiency and yield ratio of both experiments were investigated. A comparison between both experiments yield ratio was developed to clarify the influence of plasma and heating on the hydrogen permeation process through the membrane.

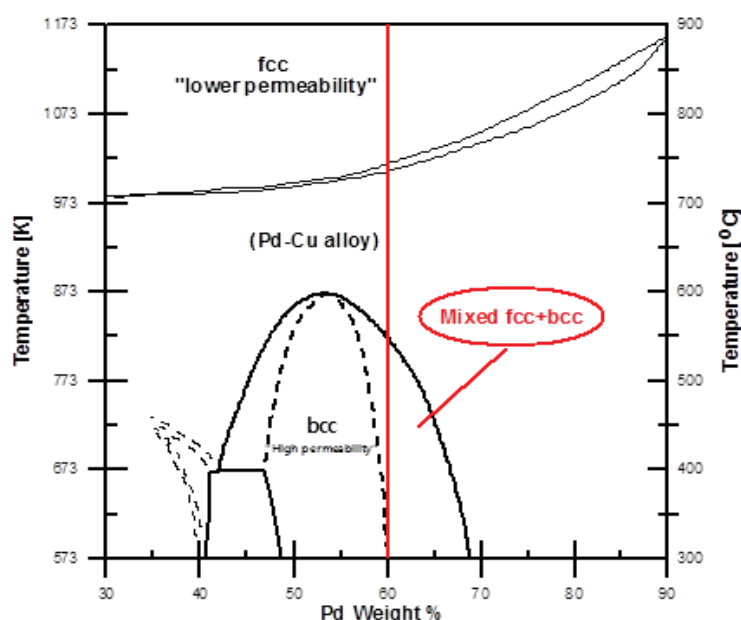


Fig.2.27 Palladium copper phase diagram, vertical line represents alloy composition and temperature range of membrane examined in this study [487].

2.4.1 Experimental

2.4.1.1 Pd-Cu membrane

In this study, the permeation experiment was performed for composite substrates of palladium–copper alloy membrane with 60 % pure palladium and 40% copper. The Pd-Cu membrane foil used in this study was purchased from Tanaka Holdings Co., Ltd, the membrane details are reported in Table (2.7). The causes of selection this alloy composition was concluded in its high hydrogen permeability, availability, high mechanical and chemical stability characteristics. Further, as we discuss in our literature review that this Pd-Cu alloy composition combines between fcc and bcc phases which increased the hydrogen permeability [429]. The thickness of the Pd-Cu membrane foil was 15 μ m and fabricated with a dimensions of 100mm \times 100mm. The Pd-Cu membrane foil was cut to the desired dimensions of 50mm \times 50mm and connected to the support plate using gasket material. Most of permeation /separation studies have been utilized the cylindrical type reactors, in this experiment we used a plate type reactor as a downsizing step to study and evaluate the results of 99.999% hydrogen gas permeation behavior through Pd-Cu40% membrane. Figure (2.28) shows the PMCR assembly photo. The leakage test was checked before finished the reactor assembly, additionally leakage check was carried out before each permeation experiment. Before starting the hydrogen permeation

Chapter 2. Hydrogen permeation through Pd-Cu membranes

experiment, the Pd-Cu membrane was activated at 573K for 2hrs in air, and then the stirrer heater was cooled down to the testing temperature.

Table. 2.7 Geometrical characteristics of the Pd-Cu membranes

Width[mm]	Thickness[μm]	Area[cm^2]
50	15	25

2.4.1.2 Plasma source

Dielectric barrier discharge (DBD) is a simple method to get the non-thermal plasma conditions at low gases temperature and atmospheric pressure. DBD plasma provides high electron energy which can produce radicals, atoms and exited particles. The full plasma was generated in the micro-channels area or can be defined as a 1mm gap between the dielectric (glass quartz plate) and the ground electrode. The applied high voltage (H.V) source was connected into the mesh electrode at the center point on the upper side while the ground electrode is connected into the base plate. The high applied voltage was supplied at a range of 10-16kV in a sinusoidal wave form at maintained frequency of 10 kHz. The PMCR heating temperatures in range of 423-573K are used as same as GDP experiment to compare both experiments results. Before starting PDP experiment, plasma firing test was carried out using argon gas at applied voltage of 16kV and PMCR heating temperature 573K. Moreover, the registered plasma power consumptions from this study are: 89, 102, 112 and 120W at 10, 12, 14 and 16kV, respectively.

2.4.1.3 Permeation experiment setup

A schematic diagram of the permeation experiment setup is presented in figure (2.29). The plate micro-channel reactor (PMCR) used in this study is composed of the following parts: the base plate, spacer, support plate, Pd-Cu40% membrane foil, micro-flow channel plate, Dielectric quartz glass (2mm thickness) and the electrode mesh with dimensions of (45mm \times 45mm \times 0.2mm). The PMCR parts are sealed and assembled with each other using gasket material, once the assembly process finished, the whole reactor was drying at a temperature of 373K for 4hrs in a constant heater type. Pure hydrogen is fed into the PMCR at atmospheric pressure (100kPa) via the mass flow controller installed at the outlet of the H₂ bottle. The PMCR reaction field volume is 5.295 cm³. The input hydrogen gas flow rate is controlled by the digital mass flow controller (MFC) installed before the reactor. While the inlet and permeate pressures are monitored using the digital pressure gauges. The permeated hydrogen flow rate is measured using the soap flow meter. The measurements of hydrogen gas concentration are taken by the H₂ gas analyzer type TC Gas Analyzer (CHINO Co.). The vacuum pump type of N820.3FT.18 (KNF Company) is installed at the PMCR

Chapter 2. Hydrogen permeation through Pd-Cu membranes

permeation side to increase the hydrogen permeation effect. The temperature of the PMCR is raised using the surface stirrer heater for both GDP and PDP experiments. In supported Pd membranes, the measured H_2 permeability are affected by leakage, substrate material transport resistance, and surface contamination. Firstly, the PMCR is activated by heating at 573 K for 20hrs with a continuous H_2 gas flow rate at 0.1L/min.

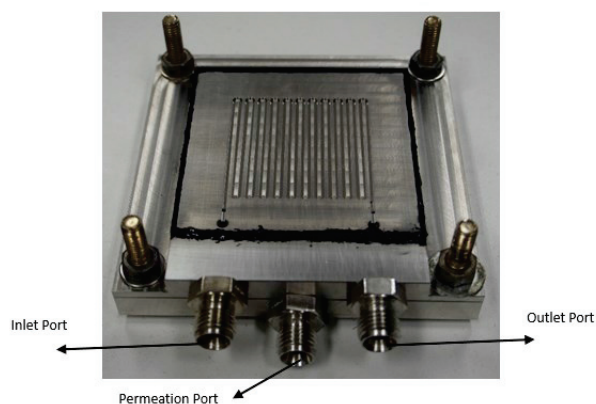


Fig. 2.28 the PMCR assembly photo.

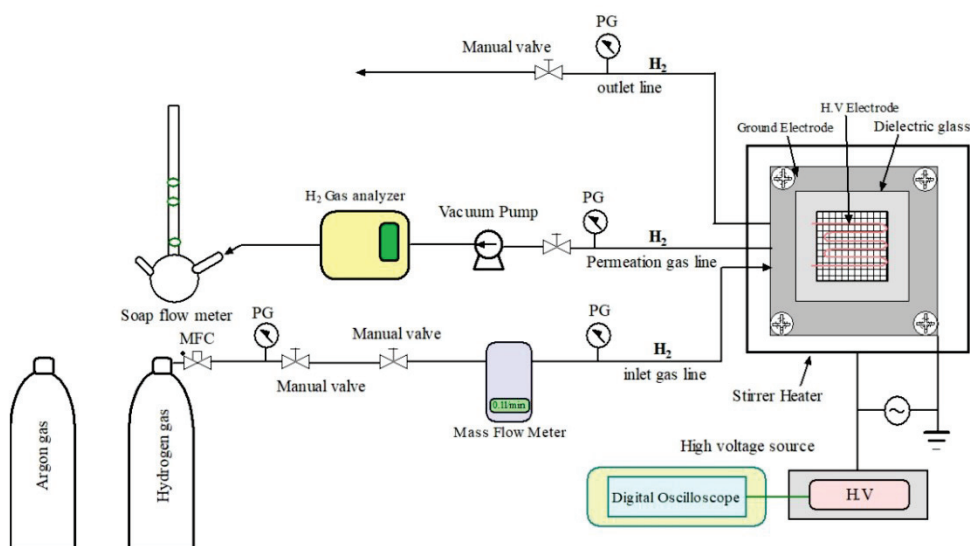


Fig. 2.29 Schematic diagram of the permeation experimental setup.

2.4.2 Results and discussion

2.4.2.1 Activation and determination of the H_2 permeability

The activation of the Pd-Cu membrane was carried out using pure hydrogen gas for 20hrs after the complete reactor assembly finished at the following operating conditions: atmospheric pressure at inlet, PMCR temperature 573 K and H_2 flow rate 0.1L/min. Figure (2.30) demonstrates the permeated H_2 gas with the activation time. The measurements were taken for one hour before the activation test finished. It is observed that the permeated hydrogen gas increased with the time.

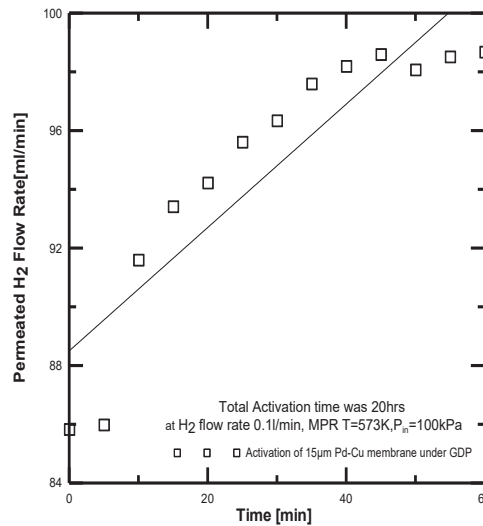


Fig. 2.30 Hydrogen permeation flow rate vs. time.

The hydrogen permeation can be determined by Fick's and Sieverts' laws as follows: $J = \frac{Pe}{\delta} (p_f^{0.5} - p_p^{0.5})$ Where J is the hydrogen gas flux ($\text{mol. m}^{-2}.\text{s}^{-1}$) was a function of the H_2 permeability, Pe ($\text{mol. m}^{-1}.\text{s}^{-1}.\text{Pa}^{-0.5}$), the difference between square root of the hydrogen gas partial pressure on the membrane feeding and downstream, or permeate sides was used, where p_f and p_p (Pa) was the partial pressure of the feeding and permeate sides respectively, and δ was the Pd-Cu40% membrane thickness (m).

2.4.2.2 GDP experiment

The PMCR permeation experiments for Pd-Cu40% membranes were carried out across the temperature range of 423-573K, where the feeding high pressure side was atmospheric pressure, and the permeate pressure side was controlled by vacuum pump while, the reactor temperature was controlled by electric stirrer heater. Figure

Chapter 2. Hydrogen permeation through Pd-Cu membranes

2.31 shows the hydrogen flux of GDP at different hydrogen flow rates. It was observed that the H_2 flux increased with the PMCR heating temperature, additionally, the permeated hydrogen at low input hydrogen flow rates was high. It was seen that the main reason is due to the effect of hydrogen gas residence time inside the PMCR reaction field volume (5.295 cm^3) which increased the hydrogen molecules dissociation through the Pd-Cu membrane. Also, it was clear from this study that the residence time was an important factor which it can be defined as (PMCR reaction volume [L] divided to the input H_2 flow rate [L/min]). The energy efficiency is calculated for GDP and PDP experiments according to the following formula: *Energy efficiency [%] = $HHV \times \text{Permeated } H_2 \text{ flow rate} / (\text{System power consumption} + HHV \times \text{input } H_2 \text{ flow rate}) \times 100$* , where HHV is the higher heating value of the permeated hydrogen gas. Figure 2.32 describes the energy efficiency change versus the reactor heating temperature. The lower input H_2 gas flow rate the higher energy efficiency was obtained. The maximum energy efficiency of GDP experiment was 63.37% at flow rate 0.1L/min and PMCR heating temperature 573K.

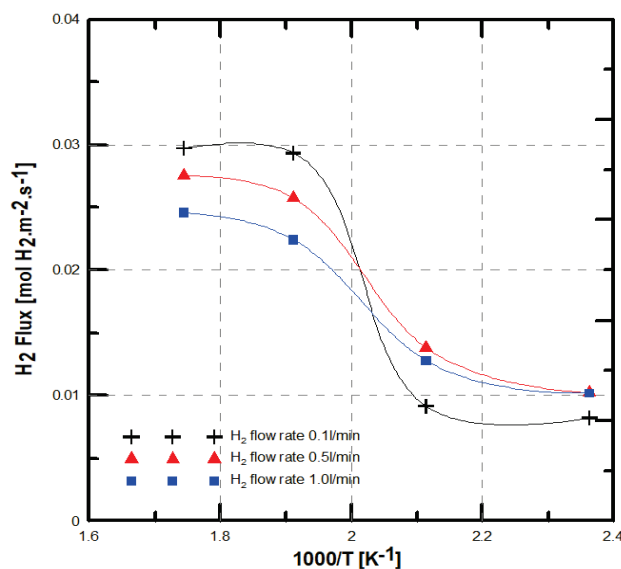


Fig. 2.31 Hydrogen flux under GDP experiment.

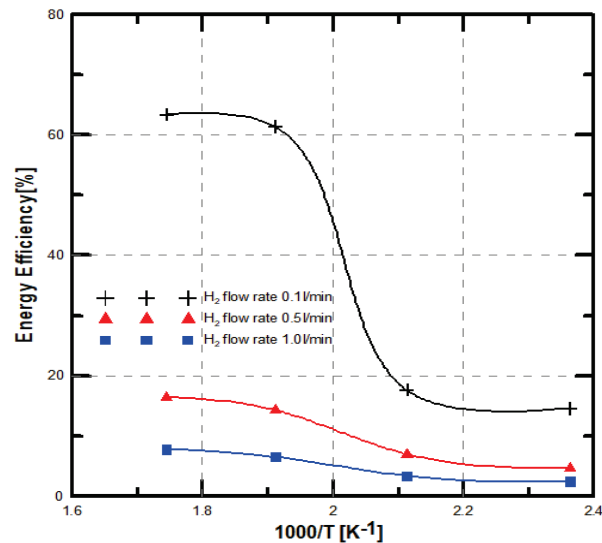


Fig. 2.32 The heating temperature effect on Energy efficiency of GDP experiment

Further, the yield ratio has been estimated for both experiments according to the following expression: $\text{Yield ratio [-]} = \text{Total output } H_2 \text{ gas [L/min]} / \text{total input } H_2 \text{ [L/min]}$. The yield ratio results show a continuous increase with energy consumption, as it can be seen clearly in Figure 2.33. Across the tested H_2 flow rates, the yield ratio of 0.5 and 1 L/min flow rates shows little increase.

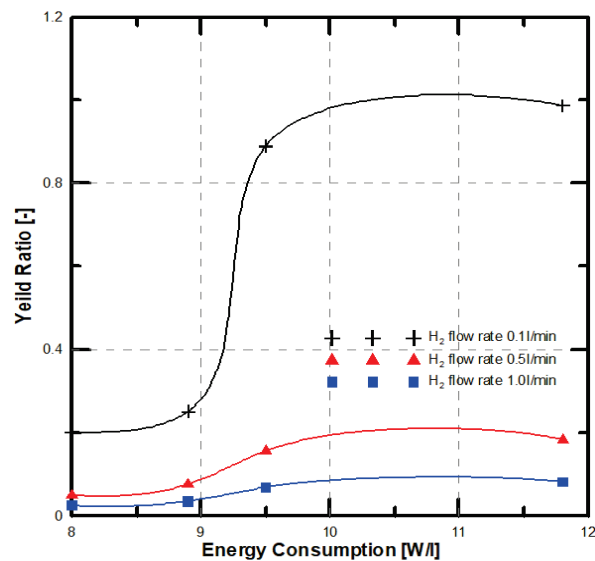


Fig.2.33 Yield ratio vs. energy consumption of GDP experiment.

Chapter 2. Hydrogen permeation through Pd-Cu membranes

2.4.2.3 PDP experiment

This experiment was carried out using the DBD plasma at a discharge voltage range of 10-16kV across PMCR heating temperature range of 423-573K and the H₂ flow rate was maintained at 0.1L/min. The plasma high voltage discharge frequency was maintained at 10 kHz at all PDP experiments. The plot of the H₂ flux versus the PMCR heating temperature is given in figure 2.34. The PDP experimental results indicate that the hydrogen flux increased with the plasma and heating effect. Also, the maximum values of H₂ flux were at temperature of 523K for all applied plasma voltage. The energy efficiency of PDP experiments versus the heating temperature is shown in figure 2.35. The maximum energy efficiency of the experimental results was 48.7% at plasma discharge voltage 14kV and PMCR heating temperature 573K; it is remarkable that energy efficiency of GDP experiment higher than PDP experiment due to the total heat added to the plasma system is high.

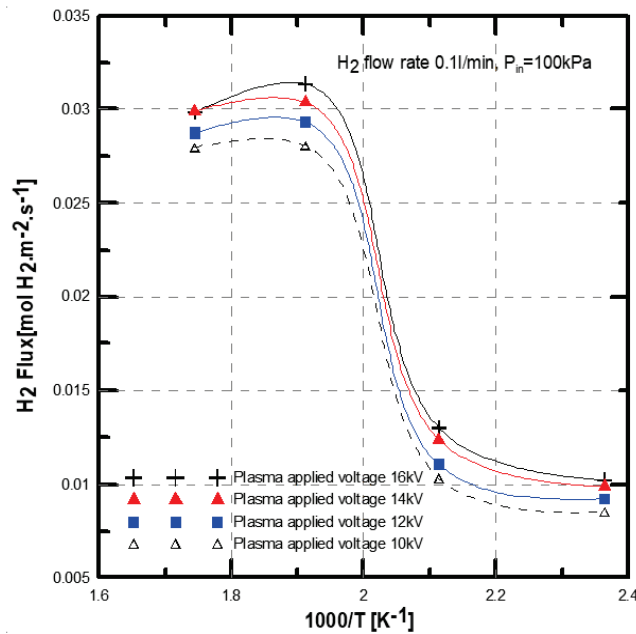


Fig. 2.34 Hydrogen flux under PDP experiment.

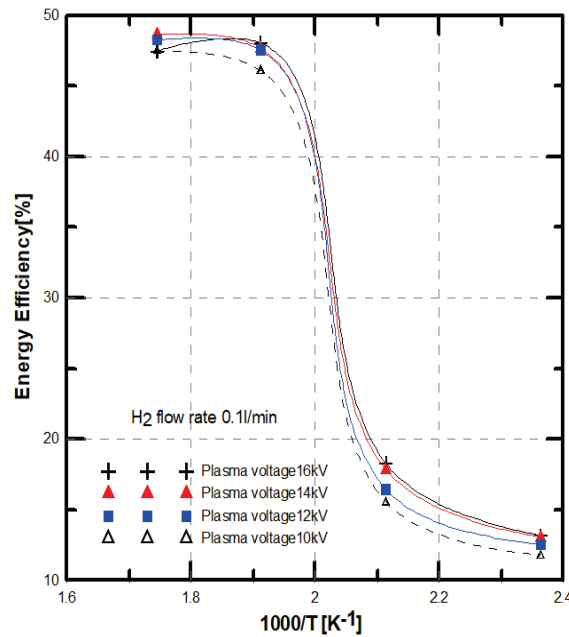


Fig. 2.35 The heating temperature effect on Energy efficiency of PDP experiment.

However, the permeated H_2 flow rate from PDP experiment was higher than that obtained from GDP experiment. To clarify the hydrogen permeation on the $15\mu m$ Pd-Cu40% membrane thickness, the yield ratio was presented versus the total energy consumption in figure 2.36. It was found that the yield ratio increased with energy added to the system and then decreased at high plasma discharge voltage 16kV. Also, it can be concluded that the DBD plasma has a non-linearity effect at high discharged plasma voltage which the H_2 dissociation through Pd-Cu membrane decreased. A comparison between yield ratio of the GDP and PDP experiments has been derived in figure 2.37 for more investigation of the plasma effect on H_2 permeation of Pd-Cu membrane. It was found that the plasma effect on yield ratio increased at low PMCR heating temperature while the plasma effect was little at the PMCR heating temperature of 573K. The hydrogen output energy versus the total energy consumption is given in figure 2.38. It was observed the permeated H_2 at low temperature was very low compared to the hydrogen output energy at 573K that in GDP experiment. The influence of plasma was clearly appeared at low and high PMCR heating temperature, but the maximum obtained output H_2 energy values were 20.89 and 20.997W at PMCR heating temperature of 573K for GDP and PDP experiments, respectively.

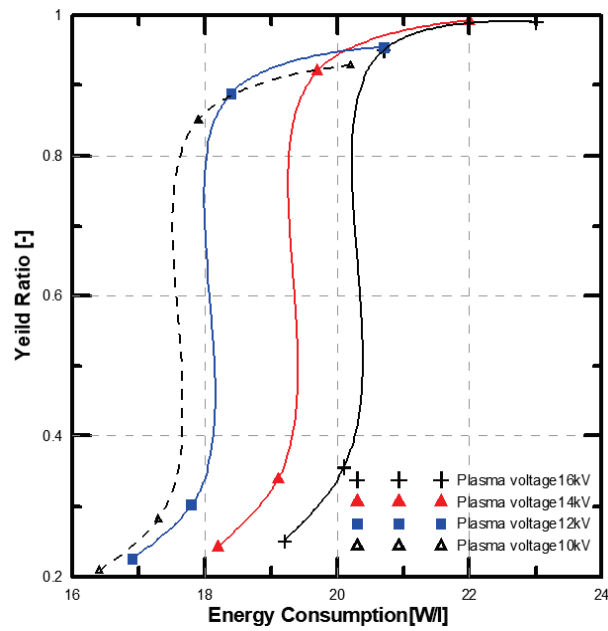


Fig. 2.36 Yield ratio vs. energy consumption of PDP experiment.

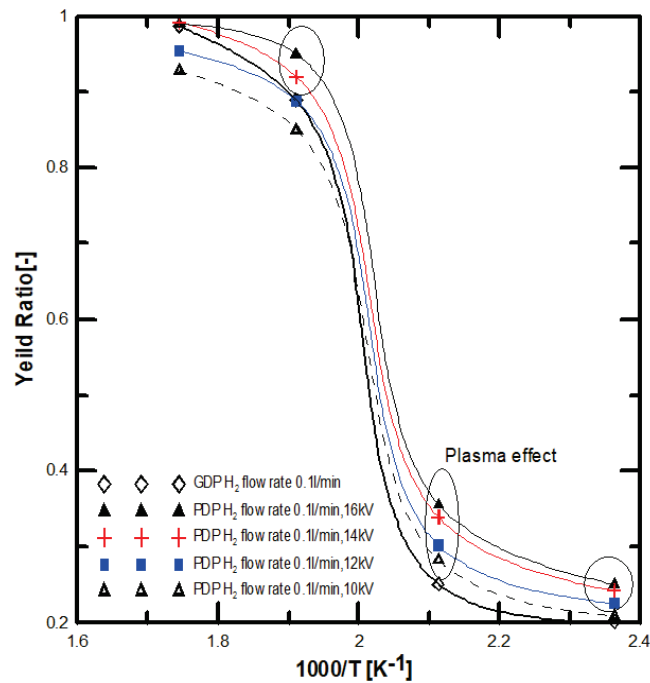


Fig. 2.37 A comparison between Yield ratio results of GDP & PDP experiments.

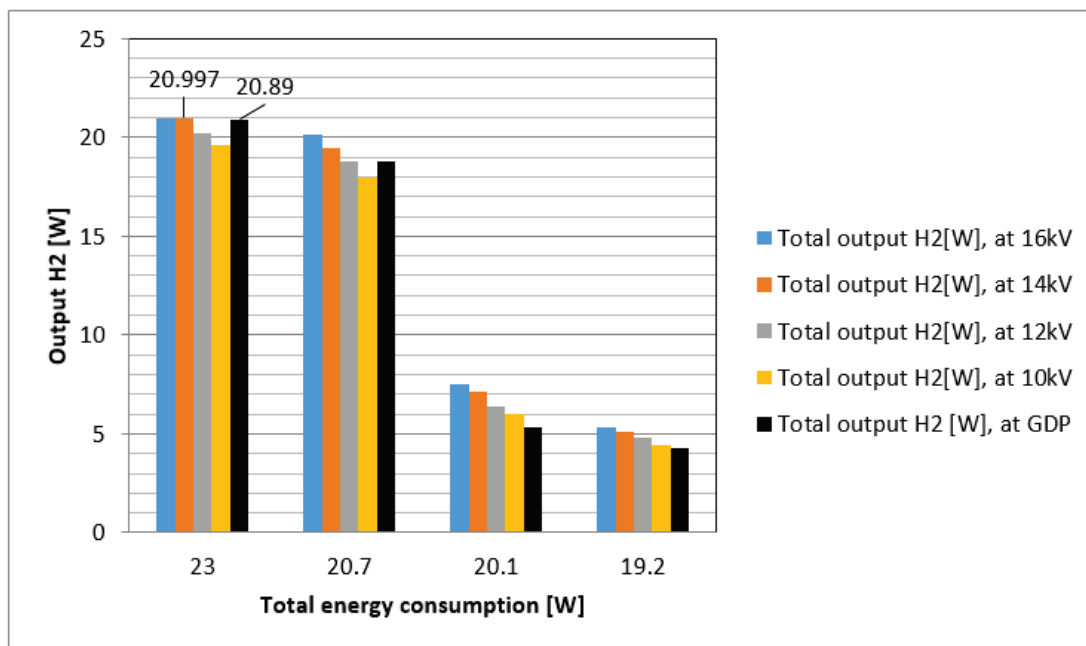


Fig. 2.38 A comparison between outputs H₂ versus the total energy consumption.

From this experiment results, it is showed the hydrogen permeation performance under GDP and PDP effect for 15 μ m membrane thickness at different operating conditions. It was found that the yield ratio of the PDP experiment changed according to the discharged plasma voltage in random behavior, it was seen that all adsorbed H₂ molecules weren't dissociated directly to the membrane permeation side due to the H₂ molecules reverse reaction at high plasma voltage.

Conclusion

The performance evaluation of pure H₂ permeation through 15 μ m Pd-Cu40% alloy membrane were determined under GDP and PDP over a heating temperature range of 423-573K for 1mm gap length plate type reactor (PMCR) at atmospheric pressure on the feeding side. Hydrogen permeation flux of GDP experiment showed a continuous increase with the PMCR heating temperature, while in PDP experiment the trend behavior showed a non-linearity at high plasma discharge voltage. The energy efficiency of both experiments were determined, the maximum energy efficiency value of GDP experiment was 63.37% 14kV at H₂ flow rate 0.1L/min and PMCR heating temperature 573K while The maximum energy efficiency of the PDP was 48.7% at plasma discharge voltage 14kV at flow rate 0.1L/min and PMCR heating temperature 573K. Although, the permeated H₂ flow rate from PDP was higher than that obtained from GDP experiment, but the energy efficiency of GDP

Chapter 2. Hydrogen permeation through Pd-Cu membranes

was higher than PDP due to the total energy consumption by the system. For more investigation, the yield ratio versus the total energy consumptions was calculated; the stronger effect was noted that energy added increased the yield ratio increased. Also, a comparison between the yield ratios of both experiments has been developed to clarify the plasma and heating effect on the hydrogen permeation, it was found that the influence of plasma on hydrogen permeation was higher than heating effect, additionally the plasma effect increased at low temperatures. Additionally, the hydrogen output energy versus the total energy consumption was compared; it was observed in GDP results that the output H_2 energy increased to the maximum value 20.89W at 573K, while the PDP results showed continuous increase with plasma to reach the maximum value 20.997 W at 14 kV and heating temperature 573 K. Regarding the next future step, an assessment will be investigated for Pd-based membranes especially Pd-Cu and Pd-Ag alloys to compare their behavior in H_2 permeation using different membrane thicknesses.

2.5 Assessment of H_2 permeation through Pd-Cu40% membrane cylinder type reactor

2.5.1 Material and methods

The Pd-based membranes are registered as highly commercial use in hydrogen separation. Most of the recent researches have been studied the Pd-Ag alloy due to the permeated hydrogen results are twice compared to the pure palladium membranes [488, 489]. Some disadvantages of using the Pd-Ag membrane are the short lifetime because of the lattice expansion and the grain coarsening of the membrane when exposed to high temperatures [423]. Although the Pd-Ag membranes have higher hydrogen permeability than the Pd-Cu membranes, the Pd-Cu membranes showed more advantages than the pure Pd membranes such as durability and the H_2S contamination resistance are too high. The maximum H_2 permeability is obtained from the Pd60%-Cu40% alloy [487,490]. The Pd-based membranes have unique characteristics because they can quickly dissociate of H_2 molecules into monatomic more than 600 times the membrane structure [401]. The dissociation process of hydrogen gas molecules through the membrane can be concluded as follows: the hydrogen molecules dissociate into monatomic then ionized to compose a proton (H^+) and an electron. It was found that the proton is recombined with the H-atom to form H_2 molecules that will penetrate and diffuse through the Pd-Cu membrane then desorbed into the permeate side in a gas phase. The driving force of the permeation process was the partial pressures on the difference between the feed and permeate side [436]. In this experiment, the hydrogen permeation through the Pd60%-Cu40%

Chapter 2. Hydrogen permeation through Pd-Cu membranes

membrane was measured using pure hydrogen gas under DBD plasma and the plasma-catalysis process. The DBD plasma is a specific type of plasma using AC discharge and working at atmospheric pressure. It can provide good thermodynamics and chemical stability of the non-equilibrium and atmospheric pressure plasma. The DBD plasma is generated in the CTR between the high voltage and ground electrodes which are also separated by a 2 mm thick quartz glass type. In this experiment, the DBD plasma discharge voltage is conducted with the sinusoidal signals around 10 kHz and applied plasma voltage of 10 kV. Two different feeding hydrogen gas concentrations were fed into the CTR, namely pure hydrogen gas with concentration of 99.999% and syngas 75% H₂/25% N₂. Figure 2.39 shows the CTR experimental setup. The Pd-Cu membrane is installed on the high voltage electrode while the ground electrode is connected to the outside part. The CTR reactor consists of two inner and outer glass quartz material tubes with outer diameters of 40 and 34 mm. The concentration of the permeated hydrogen gas is measured by the gas analyzer and the mass flow controller installed on the permeation line. Moreover, the vacuum pump type of N810.3FT.18 (KNF Company) is installed on the permeation line, and the inlet and permeated gas pressures are controlled using the digital pressure gauges. The feeding and permeate gauge gas pressures are controlled at 0 kPa, and -90 kPa, respectively. The Pd60%-Cu40% separation membrane has a thickness of 20 μm and is welded inside a thin punched metal (SUS 304). The reactor gap length was 2 mm, while the plasma reaction field volume is 51.6 cm³.

Two different hydrogen gas concentrations of 99.999% and 75% H₂/25% N₂ are used in this experiment. The hydrogen permeation through the Pd-Cu40% membrane thickness of 20 μm was measured at different H₂ input flow rates. The hydrogen permeation was determined at different input gas flow rates for both feeding hydrogen concentrations. The DBD plasma is ignited at an applied high voltage of 10 kV. The hydrogen permeation through the Pd-Cu membrane was previously determined in the plate type reactor at a plasma voltage range of 10-16 kV [345-347]. Although, the maximum H₂ permeability was found at 14 kV for the plate type, it was recommended in this permeation study to apply a plasma voltage of 10 kV. It is expected that the change of the reactor configuration into cylindrical will enhance the hydrogen dissociation through the membrane and reduce the plasma power consumption which are effective parameters in the permeation process. Different reactor configuration types have been investigated by Chiuta et al. [491]. The packed-bed reactors are commonly utilized for plasma-catalyst studies [492]. These reactor types can provide a short residence time; a high efficient heat and mass transfer of the hydrogen separation systems [493-495]. Moreover, these reactors are extremely sensitive to the hydrogen separation from N₂ and ammonia gas [496]. Therefore, the hydrogen separation and purifying from N₂ gas were studied.

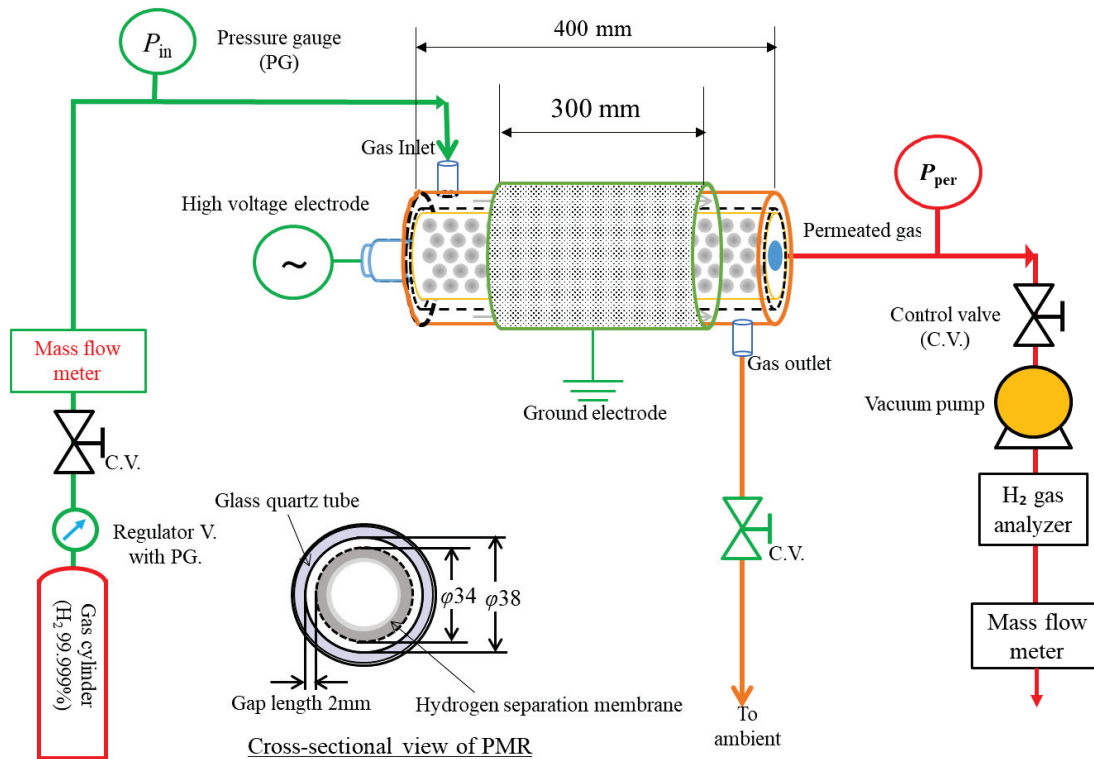


Fig. 2.39 The CTR experimental setup schematic diagram.

2.5.2 H₂ permeation in (CTR) using DBD plasma

The hydrogen flux was determined for pure H₂ gas and 75%H₂/25% N₂ at different feeding flow rates. A comparison between both input hydrogen gas concentrations at different feeding flow rates is shown in figure 2.40.

The hydrogen gas was injected into the CTR at ambient conditions while the permeate pressure is controlled at -90 kPa. The hydrogen flux increased with the feeding H₂ flow rate. The results also showed that the permeated hydrogen gas of syngas with 75%H₂ concentration was less than that obtained from the pure hydrogen gas concentration experiment because the penetrated hydrogen molecules through the Pd-Cu membrane of pure hydrogen is larger than the 75%H₂ concentration.

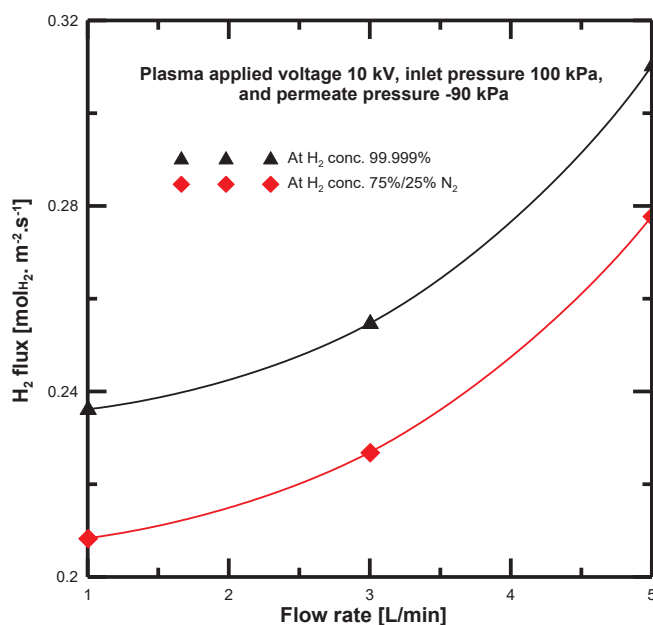


Fig. 2.40 Comparison of H₂ flux of pure H₂ gas and syngas at different input flow rates.

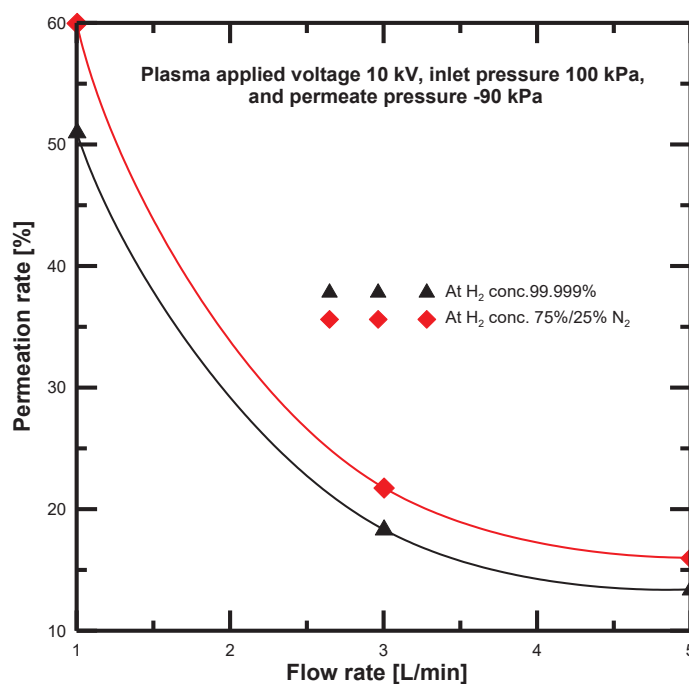


Fig. 2.41 The effect of N₂ gas on the hydrogen permeation rate.

The effect of N₂ gas on the hydrogen permeation process is investigated under the plasma experiment. The effect of CO and H₂O on the hydrogen permeation under PDP through the Pd-Ag membrane have been previously investigated [352]. To

Chapter 2. Hydrogen permeation through Pd-Cu membranes

clarify the adsorption process of hydrogen molecules through the Pd-Cu membrane, the hydrogen permeation rate % is determined according to the following expression,

$$\text{H}_2 \text{ permeation rate}\% = \frac{\text{Permeated H}_2 \text{ gas (L/min)}}{\text{H}_2 \text{ input flow rate (L/min)}} \times 100 \quad (14)$$

Figure 2.41 demonstrates the hydrogen permeation rate % at different feeding H₂ gas flow rates. The hydrogen permeation rate values of the H₂ input flow rate 1L/min are higher at 3 and 5 L/min, respectively. Moreover, the hydrogen permeation rate results of the input gas concentration 75%H₂/25%N₂ are higher than that obtained from pure feeding H₂ gas; therefore, the nitrogen gas has a positive effect on the hydrogen permeation process. Also, the hydrogen permeation rate maximum values are 51%, 60% at H₂ input concentrations of 99.999% H₂, and 75%H₂/25%N₂, respectively. The hydrogen permeation rate results of CTR showed similar trend behavior results of our previous 99.999%H₂ permeation studies [345-347]. However, the permeation rate of 75%H₂ gas is higher than pure input gas, but the hydrogen flux of pure H₂ gas is still larger because more hydrogen molecules are permeated through the membrane. The effect of residence time on the dissociation process through the Pd- Cu membrane was investigated. It was found that the residence time is critical factor in the hydrogen permeation process that appeared in the H₂ permeation rate % results of low H₂ input flow rates. Figure 2.42 presents the residence time values of the H₂ input flow rates estimated by:

$$\text{Residence time [min]} = \frac{\text{reactor volume[L]}}{\text{input flow rate}[\frac{\text{L}}{\text{min}}]} \quad (15)$$

It was clear that the low H₂ input flow rate has the highest residence time value. It means that the hydrogen dissociation and permeation rate through the Pd-Cu membrane increased at low input hydrogen flow rates.

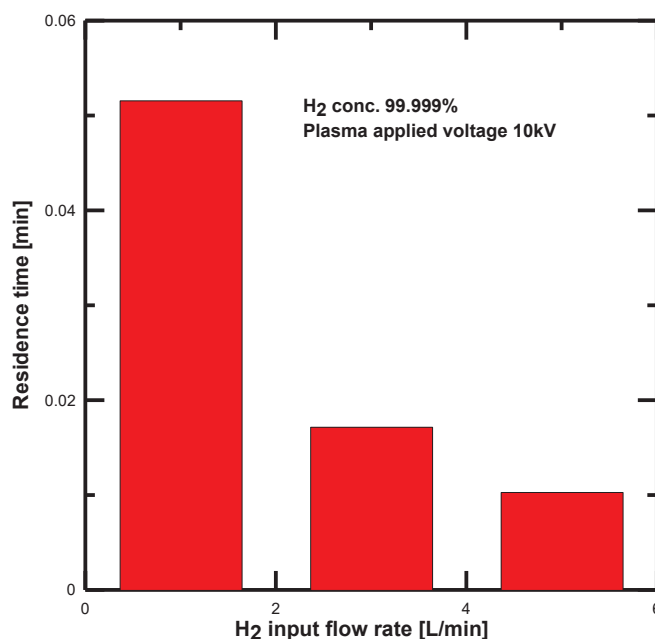


Fig. 2.42 Residence time values versus the hydrogen input flow rates.

2.5.3 The effect of feeding pressure on hydrogen production from syngas of (75%H₂/25%N₂)

In this experiment, the hydrogen production from the feeding hydrogen concentration of 75% was measured at different feeding pressure ranges of (0—100 kPa) (gauge pressure) and flow rate of 3.75 L/min. Also, the feeding H₂ gas was injected into the CTR at ambient temperature. The permeate pressure was controlled by the vacuum pump installed on the permeate side to be in the range of (-86 to -80 kPa). The permeation rate versus the plasma firing time at different feeding pressures is shown in figure 2.43. It was found that the permeated hydrogen molecules flow rate increased when the partial pressure difference between the feeding and permeable side increased [497]. As discussed previously that the main driving force of the permeation process is the difference between partial pressures in both feeding and permeate side, the hydrogen permeation rate of the feeding gas concentration of 75%H₂/25%N₂ enhanced with the feeding pressure increased from 0 kPa to 100 kPa with the plasma ignition time. On the other hand, it was reported that the increasing of partial pressure in the ammonia decomposition process was limited because of the low H-atoms transport through the Pd membrane [498].

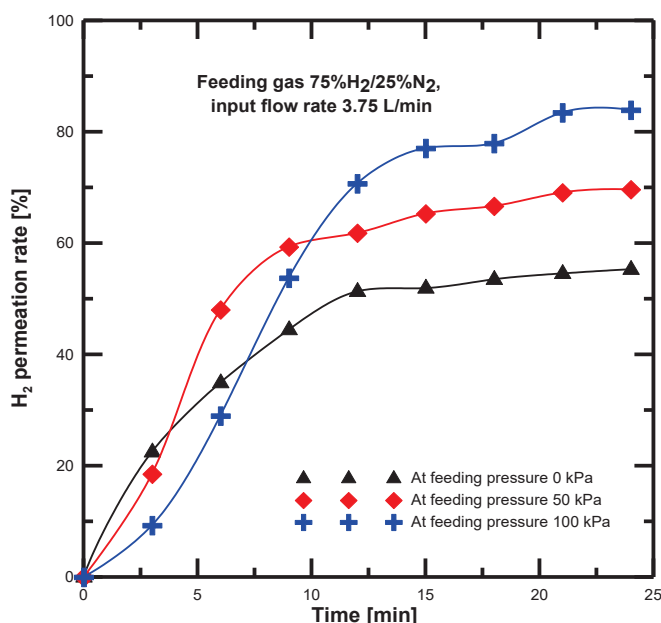


Fig. 2.43 The effect of feeding pressure on the hydrogen permeation rate.

2.5.4 Catalytic materials effect on H₂ permeation through Pd-Cu40% membrane

The main reason to use the Pd-Cu40% membrane in this experiment is because of its high H₂ permeability, better durability and its high thermodynamics and chemical stability. In this typical CTR configuration, zeolite catalyst materials are packed within the interior and surrounding the Pd- Cu membrane. The highest conversion was achieved in the catalytic packed bed reactor [499-501]. The DBD plasma type is used in the hydrogen permeation experiment to improve and increase the permeated hydrogen gas from the Pd-Cu membrane. In addition to the DBD plasma, the catalyst is also used to improve the H₂ permeation through the Pd-Cu membrane. Two different zeolite material types are utilized to fill the CTR. Table (2.8) presents the zeolite material types specifications.

Two different hydrogen gas concentrations of 99.999% H₂ and 75%H₂/25%N₂ were injected into the CTR at different input flow rates, and the DBD plasma applied voltage is 10 kV. This experiment was carried out using a Pd-Cu40% membrane foil with a thickness of 20μm. The measurements of the hydrogen permeation were taken for both catalytic materials and without using the catalyst materials at the same experimental conditions. Figure 2.44 shows the CTR after filling it with the zeolite ignited plasma increases because of the impact of exited neutrals, ions, electrons, and

Chapter 2. Hydrogen permeation through Pd-Cu membranes

the charge carriers. Investigations have shown that plasma heating influencing the catalysis processes, and plasma heating is related to the applied power [502-505]. Furthermore, the resulting plasma heat might help to reduce the required external heat. It has been reported that plasma heat has an important effect on the plasma-catalysis enhancement [506,507]. Moreover, the electric field is enhanced because of the energy density increase that will lead to high electron energies, and high energy efficiency of the hydrogen dissociation process. The plasma surface temperatures are measured for the input gas concentration of 75% H_2 /25% N_2 at different input plasma power. The CTR was filled with the zeolite materials type of SA-600A. Figure 2.45 demonstrates the plasma surface temperature with the plasma ignition time at different feeding gas pressures. It was found that the surface temperature increased with the plasma ignition time and plasma input power for both feeding gas gauge pressures (0 kPa–100 kPa). The plasma heat is influenced the dissociation process through the Pd-Cu membrane. A comparison between GDP and PDP on the hydrogen permeation process through the Pd-Cu membrane demonstrated that the PDP permeability results were much higher than the GDP permeation [345]. To differentiate between the effect of the plasma system and the plasma-catalysis, a comparison was conducted between the hydrogen permeability of CTR using both catalytic materials and CTR without catalyst material. The hydrogen flux at different flow rates with and without catalytic materials is shown in Figure 2.46. It was found that the hydrogen permeation through the Pd-Cu membrane increased by using zeolite catalyst materials at all input H_2 flow rates. Furthermore, the hydrogen flux using zeolite type SA-600A is higher than zeolite type of 330-HUDIA at an H_2 input flow rate of 5 L/min. The hydrogen flux of syngas (75% H_2 /25% N_2) experiment showed that the plasma-catalyst is higher than the non-catalytic DBD plasma reactor. Also, the trend behaviour of both zeolite materials for pure feeding H_2 gas and syngas are nearly same. The energy efficiency through the non-catalytic reactor can be enhanced depending on the type of input gas, and the reactor geometry [508]. Furthermore, the catalyst material shape is an important physical role in the plasma-catalyst process, and the discharge generation over the zeolite material surfaces was investigated [509]. It has been reported that the DBD plasma assisted with catalyst enhanced the conversion process depending on the gas flow direction that should be aligned perpendicular to the gas flow direction [510]. The Arrhenius plot of the H_2 permeability change with the different H_2 input flow rates is shown in Figure 2.47. It showed that the trend behaviour of the H_2 permeability is the same as the hydrogen flux trend. There was a minor change between the H_2 permeability results obtained from both zeolite material types at a flow rate of 5 L/min for both feeding gases. Furthermore, it was found that the results of the H_2

Chapter 2. Hydrogen permeation through Pd-Cu membranes

permeability Arrhenius plot of 75% H_2 /25% N_2 are smaller than that obtained from pure feeding hydrogen gas. Moreover, the hydrogen permeability results of the non-catalytic DBD plasma reactor are lower than that obtained from the CTR with catalytic materials due to the zeolite material effect that increases the electron density. It was realized from the plasma-catalyst experiment that the zeolite materials could enhance the permeated hydrogen molecules through the Pd-Cu membrane.

Table.2.8 Specifications of zeolite material types used in filling CTR

Type	Series	Type	Pore size [Å]	Diameter [mm]	Si/Al ratio [mol/mol]
SA-600A	F-9	Type X	9	1.5	2 — 2.5
330-HUD1A	HSZ-300	Type Y	9	1.5	6



Fig. 2.44. Zeolite materials in the CTR.

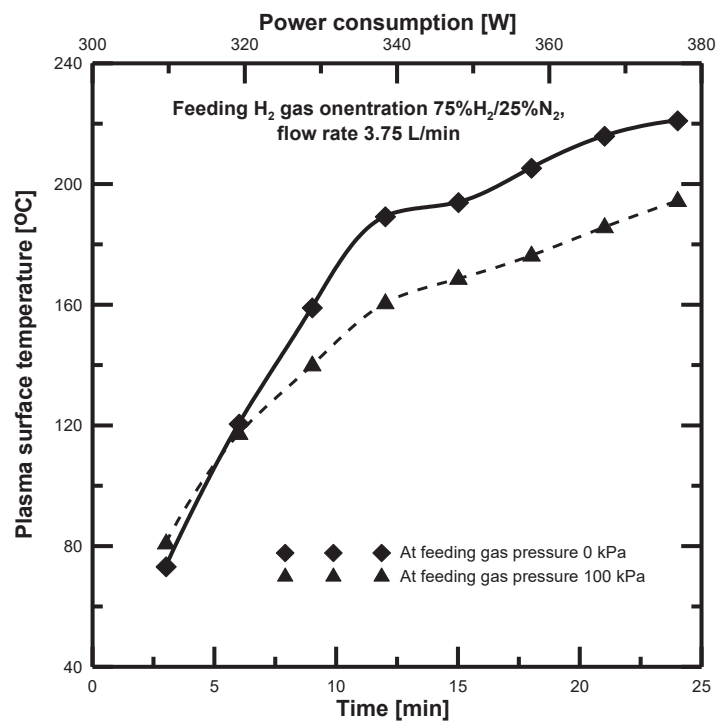
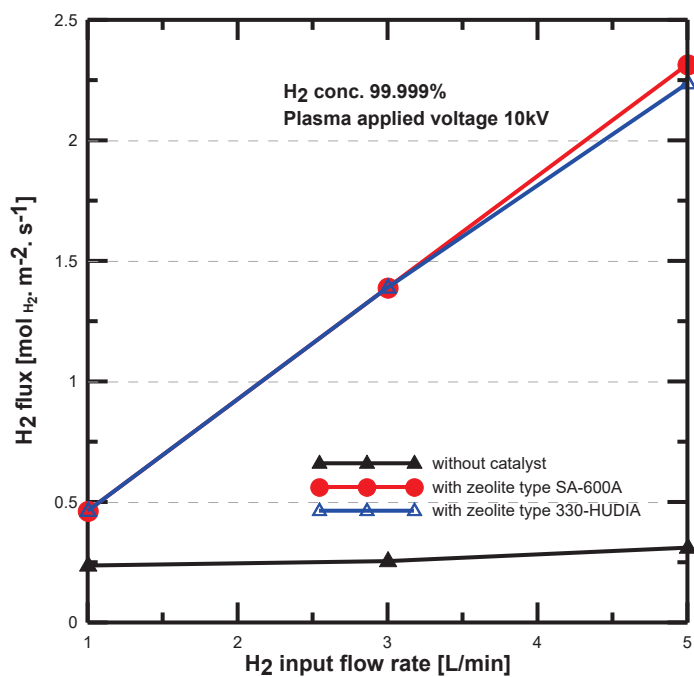
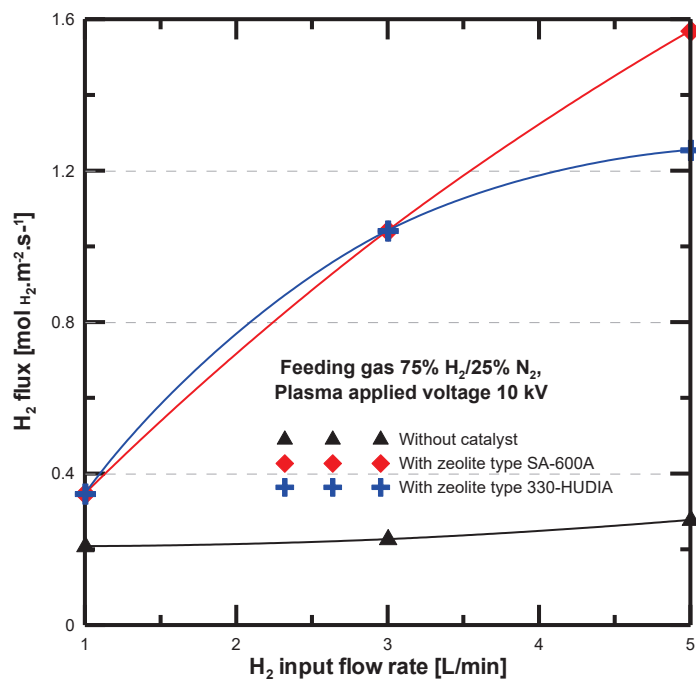


Fig. 2.45 The resulting plasma heating temperature versus time and input plasma power.

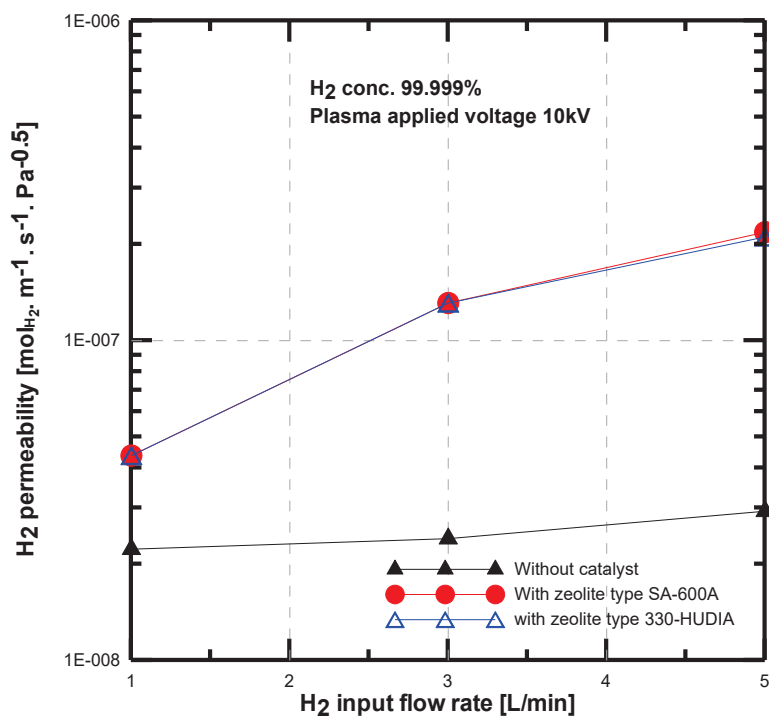


(a)



(b)

Fig. 2.46 The change of H_2 flux at different H_2 input flow rates with and without catalyst.



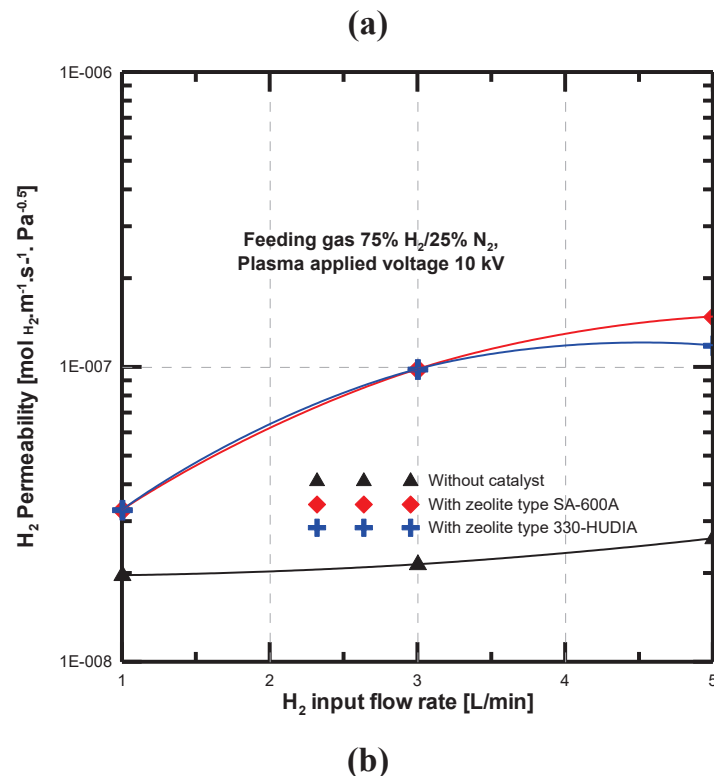


Fig. 2.47 The change of H_2 permeability at different H_2 input flow rates with and without catalyst.

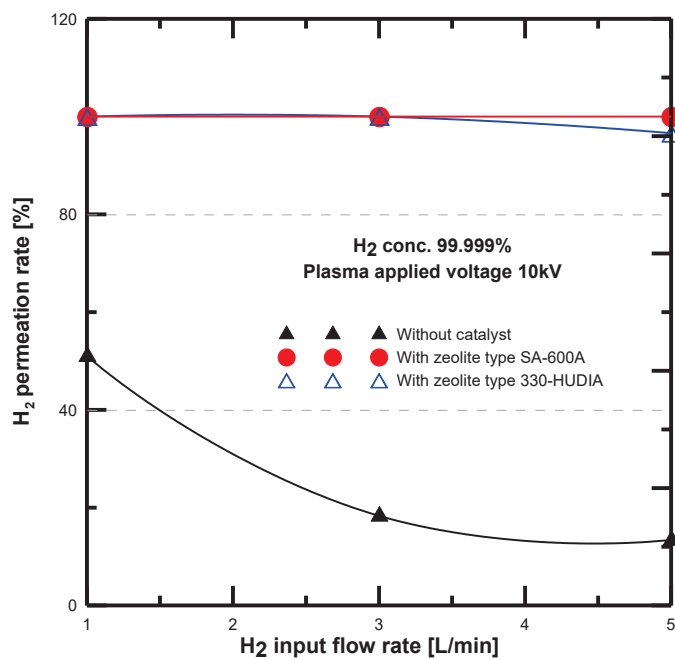
To clarify the hydrogen permeation through the Pd-Cu membrane using plasma-catalyst materials and under the non-catalytic DBD plasma reactor, the hydrogen permeation rate % is determined using Eq. (14) and is presented in Figure 2.48. The H_2 permeation rate reaches 100% by using the catalytic materials while the maximum H_2 permeation rate without filling the CTR with the catalytic materials is 51% and 60% for 99.999% H_2 gas concentration and 75% H_2 /25% N_2 , respectively. Moreover, it was found that the permeation rate of 75% H_2 /25% N_2 in the non-catalytic DBD plasma system is higher than the 99.999% H_2 concentration showing that the hydrogen dissociation process is enhanced with adding N_2 gas. These results mean that the catalytic materials improved the hydrogen permeation through the Pd-Cu membrane by 49% at all input hydrogen flow rates that for zeolite material type of SA-600A. Furthermore, the hydrogen permeation through the Pd-Cu membrane in the case of the CTR without using the catalytic materials decreased with increasing the feeding H_2 flow rates because the residence time of high input flow rates is low. In contrast, the hydrogen permeation through the CTR filling with zeolite materials are almost the same at different input H_2 flow rates. From this study, the zeolite materials

Chapter 2. Hydrogen permeation through Pd-Cu membranes

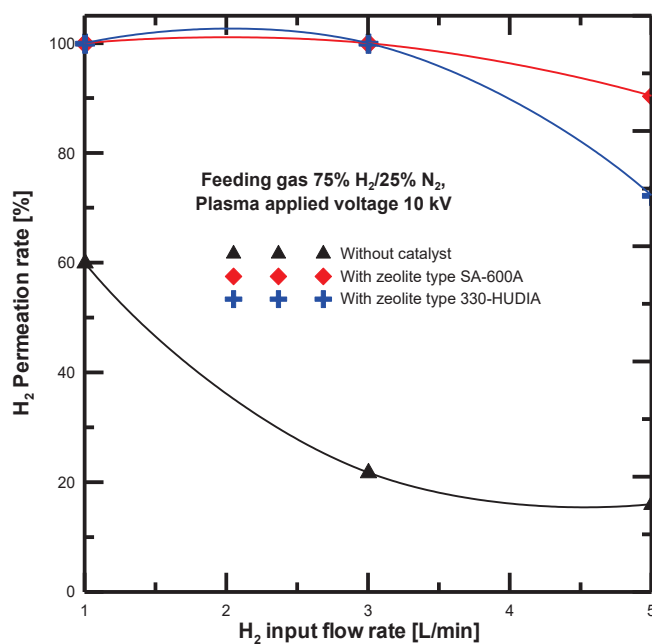
can be used in the hydrogen production from ammonia decomposition. Different catalyst materials were used in hydrogen production from ammonia such as Ni/Al₂O₃, and Ruthenium [368, 511]. The heterogeneous catalyst reaction of zeolite materials depends on the material shape selectivity [385, 512]. Catalyst materials are required in endothermic reactions such as dry methane reforming and CO₂ conversion process to decrease the operating temperature, different noble materials have been investigated [513-516]. To clarify the permeation process through the Pd-Cu membrane, the energy efficiency was determined for the H₂ input flow rates using the following expression:

$$\text{Energy efficiency [\%]} = \frac{\text{Permeated H}_2 \left[\frac{\text{L}}{\text{min}} \right] * HHV}{\text{input H}_2 \text{ flow} \left[\frac{\text{L}}{\text{min}} \right] * HHV + \text{Power consumption [W]}} \quad (16)$$

where *HHV* is the hydrogen gas higher heating value. Figure 2.49 compares the energy efficiency of the hydrogen permeation of both feeding gases. It was observed that the energy efficiency of the plasma-catalyst system is higher than that obtained from the non-catalytic DBD plasma reactor. Also, the energy efficiencies increased by using catalytic materials compared to the CTR without using the catalytic materials at all input hydrogen flow rates. In this experiment, the catalytic materials have an important function to decrease the activation energy than that required for the CTR without catalytic materials. The maximum energy efficiencies were obtained at feeding gas concentrations of 99.999%, 75%H₂/25%N₂ is 81%, and 54%, respectively. The zeolite material can be used as heterogeneous catalysis in hydrogen production from ammonia decomposition because of the high energy efficiency and energy density compared to the energy efficiencies obtained from Ni/Al₂O₃ and Ru catalysts [492,517]. Compared with the permeation results obtained from our previous results, the maximum PDP results of 99.999%H₂ input gas was 48.7% at plasma voltage of 14 kV and external heating temperature of 300 °C [345]. This study's results have a lower input plasma voltage assisted with zeolite materials, and the maximum efficiency of the same feeding gas was 81%. Therefore, the plasma-catalyst effect was much higher than the plasma-heating effect [345-347].



(a)



(b)

Fig. 2.48 The change of H₂ permeation rate at different H₂ input flow rates with and without catalyst.

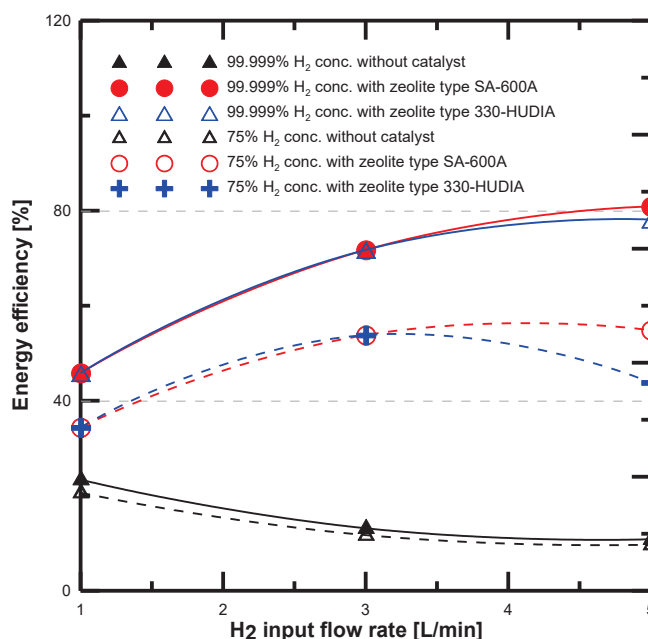


Fig. 2.49 The energy efficiency change at different H₂ flow rates with and without a catalyst.

The previous experimental results showed that the characteristic of DBD plasma is altered due to the change of electron energy distribution. Also, the catalyst micro-discharge enhanced the filamentary discharge and increased the electron density inside the plasma-catalyst ignition area, leading to a higher electric field. Moreover, catalyst geometry influenced the enhancement of the electric field [518-520]. Figure 2.50 presents the SEM photos of both zeolite types used in this experiment. The zeolite type SA-600A contains a higher surface area with more H₂ molecules than the zeolite type 330-HUDIA. The SEM cross section indicates that the morphology of the zeolite type SA-600A has large macropores compared with the SEM photo of 330-HUDIA. Furthermore, the SEM photo comparison confirmed the experimental results that the zeolite type SA-600A has the highest H₂ permeation through Pd-Cu40% membrane.

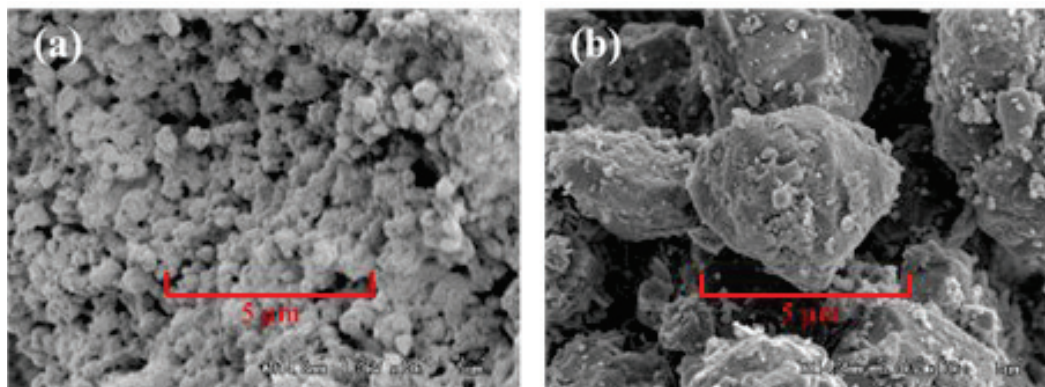


Fig. 2.50 SEM photos of (a) SA-600A and (b) 330-HUDIA.

Conclusion

Hydrogen separation using membrane technology is the most common method to separate hydrogen molecules from hot mixture gases. Pd and Pd-alloy membranes can separate hydrogen with a high hydrogen permeability, good mechanical properties and high purity of permeated hydrogen gas. The study describes the hydrogen permeation through the Pd- Cu membrane using plasma and the plasma-catalyst system using different input hydrogen concentrations (99.999% H_2 and 75% H_2 /25% N_2). Due to its high H_2 permeability and purity, the evaluation of hydrogen permeation through the Pd-Cu40% membrane is studied using DBD plasma in the CTR reactor. The most interesting result was the H_2 permeation rate of feeding gas concentration 75% H_2 /25% N_2 that was higher than that obtained from the 99.999% H_2 feeding gas for the non-catalytic plasma system. The hydrogen permeability with and without filling the CTR with catalytic materials was analyzed. A comparison showed that the hydrogen permeability improved and reaches values around 100% by using the catalytic materials. Moreover, the hydrogen permeability results of the zeolite type SA-600A were higher than the zeolite type 330-HUDIA at an H_2 input flow rate of 5 L/min. Furthermore, the combination between plasma and catalyst enhanced the hydrogen permeation process because of the increased electron density and the induced micro-discharges, resulting in increasing the energy efficiency. The plasma-catalyst system using zeolite materials showed high permeation rates and energy efficiencies compared to the non-catalytic DBD plasma system. It can be concluded that combining plasma with zeolite materials enhanced and induced the hydrogen permeation through the Pd- Cu membrane.

References

- [320] BP. Statistical review of world energy. 2015.
- [321] Bououdina M, Oral AY, Oral ZBB. Preface to the special section on “Hydrogen energy efficiency and advanced materials for hydrogen production, storage and fuel cells”. *Int J Hydrogen Energy* 2015; 40:14020.
- [322] Czyłkowski D, Hrycak B, Miotk R, Jasiński M, Dors M, Mizeraczyk J. Hydrogen production by conversion of ethanol using atmospheric pressure microwave plasmas. *Int J Hydrogen Energy* 2015; 40:14039-44.
- [323] Das D, Veziroğlu TN. Hydrogen production by biological processes: a survey of literature. *Int J Hydrogen Energy* 2001; 26:13-28.
- [324] M. El-Shafie, S. Kambara, Y. Hayakawa, Hydrogen Production Technologies Overview. *Journal of Power and Energy Engineering* 7(2019) 107-154.
- [325] Turner, J. A. Sustainable hydrogen production. *Science* 2004, 305 (5686), 972.
- [326] Sadooghi P, Rauch R. Experimental and modeling study of hydrogen production from catalytic steam reforming of methane mixture with hydrogen sulfide. *Int J Hydrogen Energy* 2015; 40:10418-26.
- [327] Kim NY, Yang E-H, Lim S-S, Jung JS, Lee J-S, Hong GH, et al. Hydrogen production by steam reforming of methane over mixed Ni/MgAl₂O₃/CrFe₃O₄ catalysts. *Int J Hydrogen Energy* 2015; 40:11848-54.
- [328] T. Rauscher, C. I. Müller, A. Schmidt, B. Kiebacka, L. Röntzsch. Ni-Mo-B alloys as cathode material for alkaline water electrolysis. *Int J Hydrogen Energy* 2016; 41:2165-76.
- [329] Giraldo MR, François J-L, Martin-del-Campo C. Life cycle assessment of hydrogen production from a high temperature electrolysis process coupled to a high temperature gas nuclear reactor. *Int J Hydrogen Energy* 2015; 40:4019-33.
- [330] Duan W, Yu Q, Xie H, Liu J, Wang K, Qin Q, et al. Thermodynamic analysis of synergistic coal gasification using blast furnace slag as heat carrier. *Int J Hydrogen Energy* 2016; 41:1502-12.
- [331] Jin H, Chen Y, Ge Z, Liu S, Ren C, Guo L. Hydrogen production by Zhundong coal gasification in supercritical water. *Int J Hydrogen Energy* 2015; 40:16096-103.
- [332] W. Nabgana, T. A. T. Abdullaha, R. Mat, B. Nabgana, Y. Gambo, M. Ibrahim, A. Ahmad, A. A. Jalila, S. Triwahyono, I. Saeh. Renewable hydrogen production from bio-oil derivative via catalytic steam reforming: An overview. *Renewable and Sustainable Energy Reviews* 2017; 79: 347–357.

- [333] Givotov, V.; Fridman, A.; Krotov, M.; Krasheninnikov, E.; Patrushev, B.; Rusanov, V.; Sholin, G. Plasmochemical methods of hydrogen production. *Int. J. Hydrogen Energy* 1981, 6 (5), 441–449.
- [334] Maehara, T.; Toyota, H.; Kuramoto, M.; Iwamae, A.; Tadokoro, A.; Mukasa, S.; Yamashita, H.; Kawashima, A.; Nomura, S. Radio frequency plasma in water. *Jpn. J. Appl. Phys.* 2006, 45 (11), 8864– 8868.
- [335] Koo, I. G.; Lee, W. M. Hydrogen generation by plasma-assisted electrochemical pumping. *Electrochem. Commun.* 2007, 9 (9), 2325– 2329.
- [336] Nguyen, S. V. T.; Foster, J. E.; Gallimore, A. D. Operating a radio-frequency plasma source on water vapor. *Rev. Sci. Instrum.* 2009, 80, 083503.
- [337] M. El-Shafie, S. Kambara, Y. Hayakawa, T. Miura. Preliminary results of hydrogen production from water vapor decomposition using DBD plasma in a PMCR reactor. *Int. J. Hydrogen Energy*, 2019; 44: 20239-48.
- [338] J.A. Nollet, *Leçons De Physique Expérimentale*, Guerin, 1784.
- [339] R. Dittmeyer, V. Höllein, K. Daub, Membrane reactors for hydrogenation and dehydrogenation processes based on supported palladium, *J. Mol. Catal. A: Chem.* 173 (2001) 135–184.
- [340] Mulder M. Basic principles of membrane technology. Dordrecht: Kluwer Academic Publishers; 2000.
- [341] Grashoff G, Pilkington C, Corti C. The purification of hydrogen. *Platin Met Rev* 1983; 27:157–69.
- [342] Mott-Smith, H. M. History of “Plasmas. *Nature* 1971, 233, 219.
- [343] Bogaerts, A.; Neyts, E.; Gijbels, R.; van der Mullen, J. Gas Discharge Plasmas and their Applications. *Spectrochim. Acta, Part B* 2002, 57, 609–658.
- [344] Fridman, A. *Plasma Chemistry*; Cambridge University Press: Cambridge, U.K., 2008.
- [345] M. El-Shafie, S. Kambara, Y. Hayakawa. A comparison between GDP and PDP experiments of hydrogen permeation through 15 μm Pd60-Cu40% membrane thickness in a micro channel plate type reactor, *Fusion Engineering and Design* 149 (2019) 111320.
- [346] M. El-Shafie, S. Kambara, Y. Hayakawa. Experimental analysis of plasma and heating effect on H_2 permeation behavior through Pd-Cu40% membranes in 1mm gap length plate reactor, *Int J of Hydrogen Energy*, 2019, In Press.

- [347] M. El-Shafie, S. Kambara, Y. Hayakawa. Study of the plasma and heating effect on hydrogen permeation through Pd_{0.60}-Cu_{0.40} membrane in a micro-channel plate reactor, *Int J of Hydrogen Energy*, 2019, In Press.
- [348] I. Dincer. “Green Methods for Hydrogen Production” *International Journal of Hydrogen Energy*, 2012, 37: 1954–1971.
- [349] C. Acar and I. Dincer. “Comparative Assessment of Hydrogen Production Methods from Renewable and Non-renewable Sources” *International Journal of Hydrogen Energy*, 2014, 39: 1–12.
- [350] I. Dincer and C. Acar. Review and evaluation of hydrogen production methods for better sustainability. *International Scientific Journal for Alternative Energy and Ecology (ISJAE)*, 2016, No. 2495, 14–36.
- [351] A. Brunetti, G. Barbieri, E. Drioli. Integrated membrane system for pure hydrogen production: A Pd–Ag membrane reactor and a PEMFC, *Fuel Processing Technology*, 2011, 92, 166–194.
- [352] T. H. Nguyen, S. Mori, M. Suzuki. Hydrogen permeance and the effect of H₂O and CO on the permeability of Pd_{0.75}Ag_{0.25} membranes under gas-driven permeation and plasma-driven permeation, *Chemical Engineering Journal* 155 (2009) 55–61.
- [353] B. Arstad, H. Venvik, H. Klette, J.C. Walmsley, W.M. Tucho, R. Homestad, A. Holme, R. Bredesen, Studies of self-supported 1.6 μm Pd/23 wt.% Ag membranes during and after hydrogen production in a catalytic membrane reactor, *Catal. Today* 118 (2006) 63–72.
- [354] J. Chabot, J. Lemonte, C. Grumet, J. Sannier, Fuel clean-up system: poisoning of palladium-silver membranes by gaseous impurities, *Fusion Tech.* 14 (1988) 614–618.
- [355] M. Amano, C. Nishimura, M. Komaki, Effect of high concentration CO and CO₂ on hydrogen permeation through the palladium membranes, *Mater. Trans. JIM* 31 (1990) 404–408.
- [356] D. Wang, T.B. Flanagan, K.L. Shanahan, Permeation of hydrogen through preoxidized Pd membranes in the presence and absence of CO, *J. Alloys Compd.* 372 (2004) 158–164.
- [357] H. Amadusson, L.G. Ekadahl, H. Dannetun, The effect of CO and O₂ on hydrogen permeation through a palladium membrane, *Appl. Surf. Sci.* 153 (2000) 259–267.

- [358] F. Gallucci, F. Chiaravalloti, S. Tosti, E. Drioli, A. Basile, The effect of mixture gas on hydrogen permeation through a palladium membrane: experimental study and theoretical approach, *Int. J. Hydrogen Energy* 32 (2007) 1387–1845.
- [359] A. Li, W. Liang, R. Hughes, The effect of carbon monoxide and steam on the hydrogen permeability of a Pd/stainless steel membrane, *J. Membr. Sci.* 165 (2000) 135–141.
- [360] K. Hou, R. Hughes, The effect of external mass transfer, competitive adsorption and coking on hydrogen permeation through thin Pd/Ag membrane, *J. Membr. Sci.* 206 (2002) 119–130.
- [361] K. Okazaki, T. Nozaki, Ultrashort pulsed barrier discharges and Applications. *Pure Appl. Chem.* 74(3), 447–452 (2002).
- [362] S. Kambara, R. Kuriyama, T. Osakabe, K. Yukimura. Hydrogen oxidation in H₂/O₂/N₂ gas mixture by pulsed DBD at atmospheric pressure. 2008, 33, 6792-99.
- [363] R. Satake, E. Yanase. Mechanistic studies of hydrogen-peroxide-mediated anthocyanin oxidation. *Tetrahedron* 2018, 74(42), 6187-619.
- [364] Rehman, F.; Lozano-Parada, J. H.; Zimmerman, W. B. A kinetic model for H₂ production by plasmolysis of water vapors at atmospheric pressure in a dielectric barrier discharge micro-channel reactor. *Int. J. Hydrogen Energy* 2012, 37 (23), 17678–17690.
- [365] F. Saleem, K. Adam, P. Harvey. Decomposition of benzene as a tar analogue in CO₂ and H₂ carrier gases, using a non-thermal plasma. *Chemical Engineering Journal* 2019, 360, 714-720.
- [366] F. Saleem, K. Adam, P. Harvey. Plasma-assisted decomposition of a biomass gasification tar analogue into lower hydrocarbons in a synthetic product gas using a dielectric barrier discharge reactor. *Fuel* 2019, 235, 1412-19.
- [367] E. Blanquet, M. A. Nahil, P. T. Williams. Enhanced hydrogen-rich gas production from waste biomass using pyrolysis with non-thermal plasma-catalysis. *Catalysis Today* 2019, In Press.
- [368] Y. Hayakawa, T. Miura, K. Shizuya, S. Wakazono, K. Tokunaga, S. Kambara. Hydrogen production system combined with a catalytic reactor and a plasma membrane reactor from ammonia. *Int. J. Hydrogen Energy* 2019, In Press.
- [369] Witvrouwen, T.; Paulussen, S.; Sels, B. The Use of Non- Equilibrium Plasmas for the Synthesis of Heterogeneous Catalysts. *Plasma Processes Polym.* 2012, 9, 750–760.

- [370] Liu, C.-j.; Vissokov, G. P.; Jang, B. W.-L. Catalyst Preparation Using Plasma Technologies. *Catal. Today* 2002, 72, 173–184.
- [371] Tang, X.; Li, K.; Yi, H.; Ning, P.; Xiang, Y.; Wang, J.; Wang, C. MnOx Catalysts Modified by Nonthermal Plasma for NO Catalytic Oxidation. *J. Phys. Chem. C* 2012, 116, 10017–10028.
- [372] Guo, Y.-F.; Ye, D.-Q.; Chen, K.-F.; He, J.-C.; Chen, W.-L. Toluene Decomposition Using a Wire-Plate Dielectric Barrier Discharge Reactor With Manganese Oxide Catalyst In Situ. *J. Mol. Catal. A: Chem.* 2006, 245, 93–100.
- [373] Henis, J. M. Nitrogen oxide decomposition process. U.S. Patent 3983021, 1976.
- [374] Bradford MCJ, Vannice MA. The role of metal–support interactions in CO₂ reforming of CH₄. *Catal Today* 1999;50:87–96.
- [375] Ji L, Tang S, Zeng HC, Lin J, Tan KL. CO₂ reforming of methane to synthesis gas over sol–gel-made Co/ γ -Al₂O₃ catalysts from organo metallic precursors. *Appl Catal A Gen* 2001; 207:247–55.
- [376] Bouarab R, Akdim O, Auroux A, Cherifi O, Mirodatos C. Effect of MgO additive on catalytic properties of Co/SiO₂ in the dry reforming of methane. *Appl Catal A Gen* 2004;264:161–8.
- [377] Hao Z, Zhu Q, Jiang Z, Li H. Fluidization characteristics of aerogel Co/Al₂O₃ catalyst in a magnetic fluidized bed and its application to CH₄–CO₂ reforming. *Powder Technol* 2008;183:46–52.
- [378] Tian X, Zeng Y, Xiao T, Yang C, Wang Y, Zhang S. Fabrication and stabilization of nanocrystalline ordered mesoporous MgO–ZrO₂ solid solution. *Micro- porous Mesoporous Mater* 2011;143:357–61.
- [379] Wang S, Lu G Q M. CO₂ reforming of methane on Ni catalysts: effects of the support phase and preparation technique. *Appl Catal B Environ* 1996; 16:269–77.
- [380] Juan-Juan J, Román-Martínez MC, Illán-Gómez MJ. Catalytic activity and characterization of Ni/Al₂O₃ and NiK/Al₂O₃ catalysts for CO₂ methane reforming. *Appl Catal A Gen* 2004;264:169–74.
- [381] Guo J, Lou H, Zhao H, Chai D, Zheng X. Dry reforming of methane over nickel catalysts supported on magnesium aluminate spinels. *Appl Catal A Gen* 2004;274:75–82.
- [382] Pompeo F, Nichio NN, González MG, Montes M. Characterization of Ni/SiO₂ and Ni/Li–SiO₂ catalysts for methane dry reforming. *Catal Today* 2005;107–108:856–62.

- [383] Su YJ, Pan KL, Chang MB. Modifying perovskite-type oxide catalyst LaNiO₃ with Ce for carbon dioxide reforming of methane. *Int J Hydrogen Energy* 2014;39:4917–25.
- [384] W. C. Chung, M. B. Chang. Review of catalysis and plasma performance on dry reforming of CH₄ and possible synergistic effects. *Renewable and Sustainable Energy Reviews* 62(2016)13–31.
- [385] Weitkamp, J. Zeolites and Catalysis. *Solid State Ionics* 2000, 131, 175–188.
- [386] Zholobenko, V. L.; Lukyanov, D. B.; Dwyer, J.; Smith, W. J. Ferrierite and SUZ-4 Zeolite: Characterization of Acid Sites. *J. Phys. Chem. B* 1998, 102, 2715–2721.
- [387] Liu, C. j.; Mallinson, R.; Lobban, L. Comparative Investigations on Plasma Catalytic Methane Conversion to Higher Hydrocarbons over Zeolites. *Appl. Catal., A* 1999, 178, 17–27.
- [388] Eliasson, B.; Liu, C.-j.; Kogelschatz, U. Direct Conversion of Methane and Carbon Dioxide to Higher Hydrocarbons Using Catalytic Dielectric-Barrier Discharges with Zeolites. *Ind. Eng. Chem. Res.* 2000, 39, 1221–1227.
- [389] Trinh, Q. H.; Gandhi, M. S.; Mok, Y. S. Adsorption and Plasma-Catalytic Oxidation of Acetone over Zeolite-Supported Silver Catalyst. *Jpn. J. Appl. Phys.* 2015, 54, 01AG04–6.
- [390] Zhang, K.; Eliasson, B.; Kogelschatz, U. Direct Conversion of Greenhouse Gases to Synthesis Gas and C₄ Hydrocarbons over Zeolite HY Promoted by a Dielectric-Barrier Discharge. *Ind. Eng. Chem. Res.* 2002, 41, 1462–1468.
- [391] Jwa, E.; Lee, S. B.; Lee, H. W.; Mok, Y. S. Plasma-assisted Catalytic Methanation of CO and CO₂ over Ni-zeolite catalysts. *Fuel Process. Technol.* 2013, 108, 89–93.
- [392] Miller GQ, Stocker J. Selection of a hydrogen separation process. San Francisco, CA: National Petrochemical and Refiners Association; 1989.
- [393] NETL. Capital and operating cost of hydrogen production from coal gasification. National Energy Technology Laboratory; 2003.
- [394] Hinchliffe A, Porter K. A comparison of membrane separation and distillation. *Chem Eng Res Des* 2000; 78:255–68.
- [395] M.R. Rahimpour, F. Samimi, A. Babapoor, T. Tohidian, S. Mohebi, Palladium membranes applications in reaction systems for hydrogen separation and purification:

- A review. *Chemical Engineering & Processing: Process Intensification* 121 (2017) 24–49.
- [396] B. Lukyanov, D. Andreev, V. Parmon, Catalytic reactors with hydrogen membrane separation, *Chem. Eng. J.* 154 (2009) 258–266.
- [397] F. Gallucci, E. Fernandez, P. Corengia, M. van Sint Annaland, Recent advances on membranes and membrane reactors for hydrogen production, *Chem. Eng. Sci.* 92 (2013) 40–66.
- [398] K. Yeung, S. Christiansen, A. Varma, Palladium composite membranes by electroless plating technique: relationships between plating kinetics, film microstructure and membrane performance, *J. Membr. Sci.* 159 (1999) 107–122.
- [399] S. Tennison, Current hurdles in the commercial development of inorganic membrane reactors, *Membr. Technol.* 2000 (2000) 4–9.
- [400] A. Julbe, D. Farrusseng, C. Guizard, Porous ceramic membranes for catalytic reactors-overview and new ideas, *J. Membr. Sci.* 181 (2001) 3–20.
- [401] Graham T. On the absorption and dialytic separation of gases by colloid septa. *PhilosTransRSocLond* 1866; 156:399–439.
- [402] Pan, X.; Kilgus, M.; Goldbach, A. *Catal. Today* 2005, 104, 225.
- [403] P. L. Andrew and A. A. Haasz. Hydrogen permeation through copper coated palladium, *J. Appl. Phys.* 1991, 70 (7), 3600-04.
- [404] Kulprathipanja, A.; Alptekin, O.; Falconer, L.; Way, J. D. *J. Membr. Sci.* 2005, 254, 49.
- [405] Kamakoti, P.; Morreale, B. D.; Ciocco, M. V.; Howard, B. H.; Killmeyer, R. P.; Cugini, A. V.; Sholl, D. S. *Science* 2005, 307, 569.
- [406] N. Al-Mufachi, N. Rees, R. Steinberger-Wilkens, Hydrogen selective membranes: a review of palladium-based dense metal membranes, *Renew. Sustain. Energy Rev.* 47 (2015) 540–551.
- [407] D.J. Edlund. A membrane reactor for H₂S decomposition, DOE/ER/81419-97/C0749, Contract DE-FG03-92ER81419.
- [408] S. E. Nam, K. H. Lee. Hydrogen separation by Pd alloy composite membranes: introduction of diffusion barrier. *J. Membr. Sci.* 2001, 192, 177-185.
- [409] D.J. Edlund. A catalytic membrane reactor for facilitating the water gas-shift reaction at high temperatures, phase II, Final Report to the US DOE on Grant DE-FG03-91ER81229 Bend Research, 1995.

- [410] B.D. Morreale, M.V. Ciocco, R.M. Enick, B.I. Morsi, B.H. Howard, A.V. Cugini, K.S. Rothenberger. The permeability of hydrogen in bulk palladium at elevated temperatures and pressures. *J. Membr. Sci.* 2003, 212, 87-97.
- [411] A.S. Zetkin, G.E. Kagin, A.N. Varaksin, E.S. Levin. Diffusion and penetrability of deuterium in the alloy Pd-53 at. % Cu. *Sov. Phys. Solid State.* 1992, 34 (1), 83-85.
- [412] M. Henson. *Constitution of Binary Alloys*, McGraw-Hill, 1958, pp. 612-613.
- [413] F. Roa, M.J. Block, J.D. Way. The influence of alloy composition on the H₂ flux of composite Pd-Cu membranes. *Desalination.* 2002, 147 (1), 411-416.
- [414] M. Kitiwan, D. Atong, Effects of porous alumina support and plating time on electroless plating of palladium membrane, *J. Mater. Sci. Technol.* 26 (2010) 1148-1152.
- [415] Y. Cheng, K. Yeung, Effects of electroless plating chemistry on the synthesis of palladium membranes, *J. Membr. Sci.* 182 (2001) 195-203.
- [416] R. Bhandari, Y.H. Ma, Pd-Ag membrane synthesis: the electroless and electroplating conditions and their effect on the deposits morphology, *J. Membr. Sci.* 334 (2009) 50-63.
- [417] G. Xomeritakis, L. Yue-Sheng, CVD synthesis and gas permeation properties of thin palladium/alumina membranes: American Institute of Chemical Engineers, *AIChE J.* 44 (1998) 174.
- [418] M.C. Iliuta, B.P. Grandjean, F. Larachi, Methane nonoxidative aromatization over Ru-Mo/HZSM-5 at temperatures up to 973 K in a palladium-silver/stainless steel membrane reactor, *Ind. Eng. Chem. Res.* 42 (2003) 323-330.
- [419] R. Hughes, Composite palladium membranes for catalytic membrane reactors, *Membr. Technol.* 2001 (2001) 9-13.
- [420] J. Zaman, A. Chakma, Inorganic membrane reactors, *J. Membr. Sci.* 92 (1994) 1-28.
- [421] D.M. Mattox, Handbook of physical vapor deposition (PVD) processing, film formation, adhesion, *Surf. Prep. Contam. Control* (1998) (and).
- [422] S. Deshmukh, S. Heinrich, L. Mörl, M. van Sint Annaland, J. Kuipers, Membrane assisted fluidized bed reactors: potentials and hurdles, *Chem. Eng. Sci.* 62 (2007) 416-436.
- [423] S. Paglieri, J. Way, Innovations in palladium membrane research, *Sep. Purif. Rev.* 31 (2002) 1-169.

- [424] H. Klette, R. Bredesen, Sputtering of very thin palladium-alloy hydrogen separation membranes, *Membr. Technol.* 2005 (2005) 7–9.
- [425] P. Pereira, S. Pérez, A. Rodrigues, L. Mendes, C. Madeira, Deposition of Pd? Ag thin film membranes on ceramic supports for hydrogen purification/separation, *Mater. Res. Bull.* 61 (2015) 528–533.
- [426] D.L. McKinley. Metal alloy for hydrogen separation and purification, US Patent 3,350, 845 (1967).
- [427] J. Völkl and G. Alefeld, *Hydrogen in Metals–I. Topics in Applied Physics*, Vol. 28, New York: Springer-Verlag, Berlin, 1978.
- [428] B. Howard, R. Killmeyer, K. Rothenberger, A. Cugini, B. Morreale, R. Enick, F. Bustamante. Hydrogen permeance of palladium–copper alloy membranes over a wide range of temperatures and pressures. *J. Membr. Sci.* 2004, 241, 207–218.
- [429] P. Kamakoti, D.S. Sholl. A comparison of hydrogen diffusivities in Pd and Cu Pd alloys using density functional theory. *J. Membr. Sci.* 2003, 225, 145–154.
- [430] M.A. Armenta, V.M. Maytorena, R.G. Alamilla, R. Valdez, A. Olivas. Thermodynamic and catalytic properties of Cu- and Pd- oxides over mixed geceAl₂O₃ for methanol dehydration toward dimethyl ether. *Int. J. Hydrogen Energy*, 2019, 44, 7276 -87.
- [431] B.D. Morreale, *The Influence of H₂S on Palladium and Palladium-copper Alloy Membranes*, University of Pittsburgh, 2006.
- [432] Kluiters SCA. Status review on membrane systems for hydrogen separation. Intermediate Report EU project MIGREYD NNE5-2001; 2004. p. 670.
- [433] F. Waelbroeck, P. Wienhold, J. Winter, E. Rota, and T. Banno, Kemforschungsanlage, Jilich, Germany, KFA Report No. Jul. 1966 (1984).
- [434] W. T. Shmayda, F. Waelbroeck, I. Winter, P. Wienhold, T. Banno, and N. P. Kherani, *Fus. Technol.* 8, 2285 (1985).
- [435] F. Guazzzone, (2006). Engineering of substrate surface for the synthesis of ultra-thin Pd and Pd-Cu membranes for H₂ separation. Ph.D. Dissertation Worcester Polytechnic Institute, Worcester, MA.
- [436] Steward SA. Review of hydrogen isotope permeability through materials. CA, USA: Lawrence Livermore National Laboratory; 1983.
- [437] Koros W, Fleming G. Membrane-based gas separation. *J Membr Sci* 1993; 83:1–80.

- [438] L. Barelli, G. Bidini, F. Gallorini, S. Servili, Hydrogen production through sorption-enhanced steam methane reforming and membrane technology: a review, *Energy* 33(2008)554–570.
- [439] A. Faur Ghenciu, Review of fuel processing catalysts for hydrogen production in PEM fuel cells systems, *Curr. Opin. Solid State Mater. Sci.* 6 (2002) 389–399.
- [440] A. Kirubakaran, S. Jain, R.K. Nema, A review on fuel cell technologies and power electronic interface, *Renew. Sust. Energ. Rev.* 13 (9) (2009) 2430–2440.
- [441] B. van Ruijven, D.P. van Vuuren, B. de Vries, The potential role of hydrogen in energy systems with and without climate policy, *Int. J. Hydrogen Energy* 32 (12) (2007) 1655–1672.
- [442] A. Yapicioglu and I. Dincer. Performance assessment of hydrogen and ammonia combustion with various fuels for power generators. *International Journal of Hydrogen Energy*, 2018, 43, 21037–48.
- [443] G. Bernardo, T. Araujo, T. d. S. Lopes, J. Sousa, A. Mendes. Recent advances in membrane technologies for hydrogen purification. *International Journal of Hydrogen Energy*, 2019, *in press*.
- [444] A.M. Ribeiro, C.A. Grande, F.V.S. Lopes, J.M. Loureiro, A.E. Rodrigues, A parametric study of layered bed PSA for hydrogen purification, *Chem Eng Sci* 63 (21) (2008) 5258–5273.
- [445] E. David, J. Kopac, Development of palladium/ceramic membranes for hydrogen separation. *Int. J. Hydrogen Energy*. 2011, 36 (7), 4498–4506.
- [446] G.Q. Lu, J.C. Diniz da Costa, M. Duke, S. Giessler, R. Socolow, R.H. Williams, T. Kreutz. Inorganic membranes for hydrogen production and purification: a critical review and perspective, *J. Colloid. Interface Sci.* 2007, 314 (2), 589–603.
- [447] S. Yun, S. Ted Oyama. Correlations in palladium membranes for hydrogen separation: a review. *J. Memb. Sci.* 2011, 375 (1–2), 28–45.
- [448] N.W.O.a.T. Nenoff. Membranes for hydrogen separation, *Chemical Reviews*. 2007, 107, 4078–4110.
- [449] A.G. Knapton. Palladium alloys for hydrogen diffusion membranes. *Platin. Met. Rev.* 1977, 21, 44–50.
- [450] S. Adhikari, S. Fernando. Hydrogen membrane separation techniques. *Ind. Eng. Chem. Res.* 2006, 45, 875–881.

- [451] S.N. Paglieri, J.D. Way. Innovations in palladium membrane research. *Sep. Purif. Methods*. 2002, 31, 1–169.
- [452] K. Zhang, J.D. Way. Palladium-copper membranes for hydrogen separation. *Sep. Purif. Technol.* 2017, 186, 39–44.
- [453] A. D. Kiadehi and M. Taghizadeh. Fabrication, characterization, and application of palladium composite membrane on porous stainless steel substrate with NaY zeolite as an intermediate layer for hydrogen purification. *International Journal of Hydrogen Energy*, 2019, 44, 2889–2904.
- [454] X. Zhang, W. Wang, J. Liu, S. Sheng, G. Xiong, W. Yang, Hydrogen transport through thin palladium–copper alloy composite membranes at low temperatures *Thin Solid Films*. 516 (2008) 1849–1856.
- [455] N. Pomerantz, Y.H. Ma, E.A. Payzant, Isothermal solid-state transformation kinetics applied to Pd/Cu alloy membrane fabrication. *AIChE J.* 56 (2010) 3062–3073.
- [456] C. Zhao, A. Goldbach, H. Xu, Low-temperature stability of body-centered cubic PdCu membranes. *J. Membr. Sci.* 542 (2017) 60–67.
- [457] D.J. Edlund, D. Newbold and C. Frost. US Patent 5,646,626 (1996).
- [458] D.J. Edlund, EP Patent 783919 (1997).
- [459] F.A. Lewis. *The Palladium Hydrogen System*. Academic Press, Vol. 71, London, New York 1967.
- [460] A. G. D. Crisci, A. Moniri, Y. Xu. Hydrogen from hydrogen sulfide: towards a more sustainable hydrogen economy. *International Journal of Hydrogen Energy*, 2019, 44, 1299–1327.
- [461] A.A. Popov, Yu.V. Shubin, P.E. Plyusnin, M.R. Sharafutdinov, S.V. Korenev. Experimental redetermination of the Cu-Pd phase diagram. *Journal of Alloys and Compounds* 777(2019) 204–212.
- [462] V.V. Krisyuk, Y.V. Shubin, F. Senocq, A.E. Turgambaeva, T. Duguet, I.K. Igumenov, C. Vahlas, Chemical vapor deposition of Pd/Cu alloy films from a new single source precursor. *J. Cryst. Growth* 414 (2015) 130–134.
- [463] N. Pomerantz, Y.H. Ma. Effect of H₂S on the performance and long-term stability of Pd/Cu membranes. *Ind. Eng. Chem. Res.* 2009, 48, 4030–4039.
- [464] B. Morreale, M. Ciocco, B. Howard, R. Killmeyer, A. Cugini, R. Enick. Effect of hydrogen-sulfide on the hydrogen permeance of palladium–copper alloys at elevated temperatures. *J. Membr. Sci.* 2004, 241, 219–224.

- [465] B. Morreale, M. Ciocco, R. Enick, B. Morsi, B. Howard, A. Cugini, et al. The permeability of hydrogen in bulk palladium at elevated temperatures and pressures. *J Membr Sci* 2003; 212:87–97.
- [466] Bustamante F, Enick RM, Cugini AV, Killmeyer RP, Howard BH, Rothenberger KS, et al. High-temperature kinetics of the homogeneous reverse water-gas shift reaction. *AIChE J* 2004; 50:1028–40.
- [467] S.N. Paglieri, Palladium membrane, in: A.F. Sammells, M.V. Mandschau (Eds.), *Nonporous Inorganic Membrane*, Wiley-VCH, 2006, pp. 77–107.
- [468] D.L. McKinley. Method for hydrogen separation and purification, US Patent 3,439,474 (1969).
- [469] T.B. Flanagan, D. Wang, K.L. Shanahan. Diffusion of H through Pd membranes: effects of non-ideality. *J. Memb. Sci.* 2007, 306 (1–2), 66–74.
- [470] C. Acar, I. Dincer. Impact assessment and efficiency evaluation of hydrogen production methods. *Int. J. of Energy Res.*, 2015; 39: 1757–68.
- [471] M. Granovskii, I. Dincer, M. A. Rosen. Greenhouse gas emissions reduction by use of wind and solar energies for hydrogen and electricity production: Economic factors. *Int. J. Hydrogen Energy*, 2007; 32, 927–931.
- [472] Y. Kalinci, A. Hepbasli, I. Dincer. Techno-economic analysis of a stand-alone hybrid renewable energy system with hydrogen production and storage options. *Int. J. Hydrogen Energy*, 2015; 40, 7652–64.
- [473] M. Granovskii, I. Dincer, M. A. Rosen. Economic and environmental comparison of conventional, hybrid, electric and hydrogen fuel cell vehicles. *Journal of Power Sources*, 2006; 159, 1186–93.
- [474] S. Uemiya, N. Sato, H. Ando, Y. Kude, T. Matsuda, E. Kikuchi. Separation of hydrogen through palladium thin film supported on a porous glass tube. *J. Membr. Sci.* 1991, 56, 303–313.
- [475] W. Juda, C.W. Krueger, R.T. Bombard. Method of producing thin palladium–copper and the like, palladium alloy membranes by solid–solid metallic interdiffusion, and improved membrane, US Patent 6,238,465, 2001.
- [476] F. Roa, J.D. Way, R.L. McCormick, S.N. Paglieri. Preparation and Characterization of Pd–Cu composite membranes for hydrogen separation, *Chem. Eng. J.* 2003, 93 (1), 11–22.

- [477] N. Al-Mufachi, S. Nayeibossadri, J. Speight, W. Bujalski, R. Steinberger-Wilckens, D. Book. Effects of thin film Pd deposition on the hydrogen permeability of Pd 60 Cu 40 wt% alloy membranes. *J. Membr. Sci.* 2015, 493, 580–588.
- [478] Lee B, Lim H. Cost competitive methane steam reforming in a membrane reactor for H₂ production: Technical and economic evaluation with a window of a H₂ selectivity. *Int J Energy Res.* 2019; 1–11.
- [479] S. Tosti, A. Basile, G. Chiappertta, C. Rizzello, V. Violante, Pd–Ag membrane reactors for water gas shift reaction, *Chem. Eng. J.* 93 (2003) 23–30.
- [480] Y. Fujii, M. Takizawa, Y. Sokawa, T. Endo, M. Okamoto, Hydrogen plasma driven permeation through selected metals, in: *International Tritium Workshop on Present Status and Prospect of Tritium–Material Interaction Studies*, Toyama, Japan, 1996, p. 26.
- [481] J. Wang, *Proc. Cambridge Philos. Soc.* 32 (1936) 657.
- [482] V. Violante, A. Basile * and E. Drioli. Membrane separation technologies: their application to the fusion reactor fuel cycle, *Fusion Engineering and Design* 22 (1993) 257-263.
- [483] C. Hsu, R.E. Buxbaum, Palladium catalyzed oxidative diffusion for tritium extraction from breeder blanket fluids low concentration, *J. Nucl. Mater.* 141 (1986) 238- 243.
- [484] H. Yoshida et al., Preliminary design of a fusion reactor fuel cleanup-system by the palladium-alloy membrane method, *Nucl. Fusion Technol.* 3 (1983) 471-484.
- [485] A. Iasonna, V. Violante et al., Water gas shift reaction section in the tritium recovery plant, in: *Proc. 16th Symp. on Fusion Technology.*, Vol. I, Eds. Keen, Huguet, Hensworth (Elsevier Science Pub., Amsterdam, 1990) 723-727.
- [486] W. H. Chen, M. H. Hsia, Y. H. Chi, Y. L. Lin, C. C. Yang. Polarization phenomena of hydrogen-rich gas in high-permeance Pd and Pd–Cu membrane tubes, *Applied Energy* 113 (2014) 41-50.
- [487] B.D. Morreale, M.V. Ciocco, B.H. Howard, R.P. Killmeyer, A.V. Cugini, R.M. Enick. Effect of hydrogen-sulfide on the hydrogen permeance of palladium–copper alloys at elevated temperatures. . *J. Membr. Sci.* 241 (2004) 219–224.
- [488] Dolan MD, Non-Pd BCC. alloy membranes for industrial hydrogen separation. *J Membr Sci* 2010;362:12–28.

- [489] Mazzolai F, Lewis F. Elastic energy dissipation in the palladium-silverhydrogen (deuterium) system. I. Hydrogen-dislocation interaction effects. *J Phys F: Met Phys* 1985;15:1249.
- [490] Iyoha O, Enick R, Killmeyer R, Morreale B. The influence of hydrogen sulfideto-hydrogen partial pressure ratio on the sulfidization of Pd and 70 mol% Pd–Cu membranes. *J Membr Sci* 2007;305:77–92.
- [491] Chiuta, S.; Everson, R. C.; Neomagus, H.; van der Gryp, P.; Bessarabov, D. G. Reactor technology options for distributedhydrogen generation via ammonia decomposition: A review. *Int. J. Hydrogen Energy* 2013, 38, 14968–14991.
- [492] Satyapal, S.; Petrovic, J.; Read, C.; Thomas, G.; Ordaz, G. The U.S. Department of energy’s national hydrogen storage project: Progress towards meeting hydrogen-powered vehicle requirements. *Catal. Today* 2007, 120, 246–256.
- [493] Ganley, J. C.; Seebauer, E.; Masel, R. I. Porous anodic alumina microreactors for production of hydrogen from ammonia. *AIChE J.* 2004, 50, 829–834.
- [494] Ganley, J. C.; Seebauer, E.; Masel, R. I. Development of a microreactor for the production of hydrogen from ammonia. *J. Power Sources* 2004, 137, 53–61.
- [495] Liu, Y.; Wang, H.; Li, J.; Lu, Y.; Xue, Q.; Chen, J. Microfibrous entrapped Ni/Al₂O₃ using ss-316 fibers for H₂ production from NH₃. *AIChE J.* 2007, 53, 1845–1849.
- [496] Ohi, J. M.; Vanderborgh, N. Hydrogen fuel quality specifications for polymer electrolyte membrane fuel cells in road vehicles; DOE/EE- 1493; U.S. Department of Energy, U.S. Government Printing Office: Washington, DC, 2012.
- [497] Hayakawa Y, Matsunami D, Miura T, Kambara S. Hydrogen production from ammonia by plasma membrane reactor. In: *Proceedings of International Symposium on Electrohydrodynamics*; 2017. No. EHD-4.
- [498] Israni, S. H.; Nair, B. K. R.; Harold, M. P. Hydrogen generation and purification in a composite pd hollow fiber membrane reactor: Experiments and modeling. *Catal. Today* 2009, 139, 299–311.
- [499] Collins, J. P.; Way, J. D. Catalytic decomposition of ammonia in a membrane reactor. *J. Membr. Sci.* 1994, 96, 259–274.
- [500] Garcia-Garcia, F. R.; Ma, Y. H.; Rodriguez-Ramos, I.; Guerrero- Ruiz, A. High purity hydrogen production by low temperature catalytic ammonia decomposition in a multifunctional membrane reactor. *Catal. Commun.* 2008, 9, 482–486.

- [501] Itoh, N.; Oshima, A.; Suga, E.; Sato, T. Kinetic enhancement of ammonia decomposition as a chemical hydrogen carrier in palladium membrane reactor. *Catal. Today* 2014, 236, 70–76.
- [502] Yu, S.; Liang, Y.; Sun, S.; Zhang, K.; Zhang, J.; Fang, J. Vehicle Exhaust Gas Clearance by Low Temperature Plasma-Driven Nano- Titanium Dioxide Film Prepared by Radiofrequency Magnetron Sputtering. *PLoS One* 2013, 8, e59974:1–8.
- [503] Rafiq, M. H.; Jakobsen, H. A.; Hustad, J. E. Modeling and Simulation of Catalytic Partial Oxidation of Methane to Synthesis Gas by Using a Plasma-Assisted Gliding Arc Reactor. *Fuel Process. Technol.* 2012, 101, 44–57.
- [504] Nozaki, T.; Muto, N.; Kadio, S.; Okazaki, K. Dissociation of Vibrationally Excited Methane on Ni Catalyst Part 2: Process Diagnostics by Emission Spectroscopy. *Catal. Today* 2004, 89, 67– 74.
- [505] Zhang, X.; Lee, C. S.-M.; Mingos, D. M. P.; Hayward, D. O. Oxidative Coupling of Methane Using Microwave Dielectric Heating. *Appl. Catal., A* 2003, 249, 151–164.
- [506] Neyts, E. C.; Ostrikov, K.; Han, Z. J.; Kumar, S.; van Duin, A. C. T.; Bogaerts, A. Defect Healing and Enhanced Nucleation of Carbon Nanotubes by Low-Energy Ion Bombardment. *Phys. Rev. Lett.* 2013, 110, 065501–5.
- [507] Neyts, E. C.; Bogaerts, A. Ion Irradiation for Improved Graphene Network Formation in Carbon Nanotube Growth. *Carbon* 2014, 77, 790–795.
- [508] Chen, H. L.; Lee, H. M.; Chen, S. H.; Chang, M. B. Review Of Packed-Bed Plasma Reactor For Ozone Generation And Air Pollution Control. *Ind. Eng. Chem. Res.* 2008, 47, 2122–2130.
- [509] Kim, H.-H.; Kim, J.-H.; Ogata, A. Microscopic Observation Of Discharge Plasma On The Surface Of Zeolites Supported Metal Nanoparticles. *J. Phys. D: Appl. Phys.* 2009, 42, 135210.
- [510] Chen, H. L.; Lee, H. M.; Chen, S. H.; Chao, Y.; Chang, M. B. Review of Plasma Catalysis on Hydrocarbon Reforming for Hydrogen Production – Interaction, Integration, and Prospects. *Appl. Catal., B* 2008, 85, 1–9.
- [511] Zhenyu Zhang, Simona Liguori, Thomas F. Fuerst, J. Douglas Way, and Colin A. Wolden. Efficient Ammonia Decomposition in a Catalytic Membrane Reactor To Enable Hydrogen Storage and Utilization, *ACS Sustainable Chem. Eng.* 2019, 7, 6, 5975-85.

- [512] Csicsery, S. M. Catalysis by Shape Selective Zeolites – Science and Technology. Pure Appl. Chem. 1986, 58, 841–856.
- [513] Chen YG, Tomishige K, Yokoyama K, Fujimoto K. Promoting effect of Pt, Pd and Rh noble metals to the Ni_{0.03}Mg_{0.97}O solid solution catalysts for the reforming of CH₄ with CO₂. Appl Catal A Gen 1997; 165:335–47.
- [514] Wang HY, Ruckenstein E. Carbon dioxide reforming of methane to synthesis gas over supported rhodium catalysts: the effect of support. Appl Catal A Gen 2000; 204:143–52.
- [515] Portugal UL, Marques CMP, Araujo ECC, Morales EV, Giotto MV, Bueno JMC. CO₂ reforming of methane over zeolite-Y supported ruthenium catalysts. Appl Catal A Gen 2000; 193:173–83.
- [516] Gheno SM, Damyanova S, Riguette BA, Marques CMP, Leite CAP, Bueno JMC. CO₂ reforming of CH₄ over Ru/zeolite catalysts modified with Ti. J Mol Catal A Chem 2003; 198:263–75.
- [517] Schueth, F.; Palkovits, R.; Schloegl, R.; Su, D. S. Ammonia as a possible element in an energy infrastructure: Catalysts for ammonia decomposition. Energy Environ. Sci. 2012, 5, 6278–6289.
- [518] Chung WC, Pan KL, Lee HM, Chang MB. Dry reforming of methane with dielectric barrier discharge and ferroelectric packed-bed reactors. Energy Fuels 2014; 28:7621–31.
- [519] Holzer F, Kopinke FD, Roland U. Influence of ferroelectric materials and catalysts on the performance of non-thermal plasma (NTP) for the removal of air pollutants. Plas Chem Plas Process 2005; 25:595–611.
- [520] Takuma T. Field behavior at a triple junction in composite dielectric arrangements. IEEE Trans Electr Insul 1991; 26:500–9.

Chapter 3 Hydrogen Production from Water Vapour

Chapter 3 Hydrogen Production from Water Vapour

3.1 Introduction

The energy demand of the world has increased in the last century depending on the fossil fuel [320, 521]. The depletion, high cost, and environmental issues are the most serious concerns of the fossil fuel utilization [321]. Sustainable and clean alternative energy resources are needed to overcome these issues, additionally with a comparable price with fossil fuel [522]. Hydrogen fuel can be utilized as alternative clean energy carriers [322, 323]. Therefore, the fuel cell systems are becoming the most important technology for producing electrical energy and in mobile systems [523-528]. Many efforts have been done to enhance the efficiency by improving the electrode materials in PEM systems [529, 530]. Hydrogen gas can be produced from different sources such as coal, natural gas and renewable energy sources including biomass, hydropower, geothermal, solar and wind energy [324]. Different hydrogen production technologies are used such as coal gasification, water electrolysis etc. however, the 90% of the produced hydrogen in the global market is produced by steam reforming method [325-331]. DBD plasma is utilized to produce hydrogen gas from ammonia, hydrocarbons and biomass fuels [365-368]. Water vapor dissociation by plasmolysis has been studied theoretically and experimentally [333-336, 344, 364, 531]. The water vapor chemical reactions and breakdown has been discussed by different mechanisms and pointed to the water vapor plasmolysis initiation, propagation and termination [344]. Recently, the kinetic modelling of water vapor plasmolysis in micro-reactors has been identified using corona-DBD plasma [336]. Plasma technology can be utilized in the oxidation process of hydrogen gas such as the H_2 oxidation in $H_2/O_2/N_2$ gas mixture by pulsed DBD plasma at atmospheric pressure has been studied [362, 363]. The production efficiency of water vapor plasmolysis can be improved if the power consumption mode for plasma is relatively low. It has been discussed in detail that it was difficult to detect the hydrogen gas in water vapor decomposition using plasma by direct method using gas phase chromatography (GC) [532]. Also, the plasma properties have been analyzed in which demonstrated the non-localized thermal equilibrium of the plasma bulk compared to the measured plasma bulk data. The decomposition of water vapor is the most attractive chemical processes to get pure hydrogen gas and to ensure the future energy carrier [533, 534]. The total free energy of hydrogen and oxygen species is much higher than the free energy of the starting water vapor molecule [535]. The current study investigates the preliminary results obtained in the experimental study of the water vapor dissociation into hydrogen and oxygen species using Direct-Barrier Discharge (DBD) plasma in a plate micro-channel reactor (PMCR). The DBD plate micro channel reactor (PMCR) has been designed and utilized for water vapor decomposition using plasma. The water vapor molecules are injected without using carrier gas into the PMCR reactor at pressure of 100kPa and temperature of 573K. The applied high voltage of the DBD plasma was within range of 14-18kV. The steam flow rates have been analyzed within range of 100-200ml/h. The ice trap was connected directly to the PMCR to prevent

Chapter 3 Hydrogen Production from Water Vapour

the recombination process of hydrogen and oxygen species. The concentration of the outlet species has been measured in a gas chromatography (GC) instrument. The hydrogen mole fraction and conversion rate have been obtained and discussed. The reactor heating temperature effect on the steam dissociation has been analyzed. Also, the energy efficiencies versus the heat supplied have been determined.

3.1.1 Hydrogen formation kinetics

Dielectric barrier discharge (DBD) plasmas is a specific plasma type of AC discharge, which working at atmospheric pressure and provides a good thermodynamics non-equilibrium plasma, additionally, it is known to be effective in the chemical and physical processes in gases [536]. The main advantages of the DBD plasma are its ability to produce highly reactive plasma at near to room temperature with low power consumption using simple reactor system at atmospheric pressure condition and its very short time response [361]. The DBD plasma is produced in the PMCR between the two electrodes which is separated by the glass quartz dielectric layer (2mm thickness). In this experiment, The DBD plasma working with either sinusoidal signals around 10 kHz, where the dielectric prevents the high temperature arc formation and eliminates the electrode etching and corrosion. The water vapor is injected into the PMCR in the area between the dielectric layer and the ground electrode. In order to obtain stable DBD plasma, the interelectrode gap length was reduced to be 4.5mm as shown in figure (3.1).

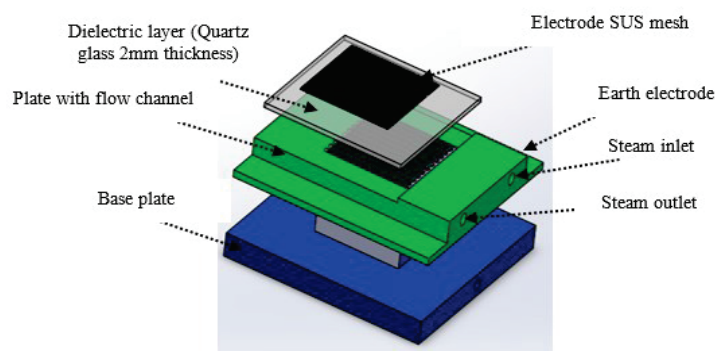
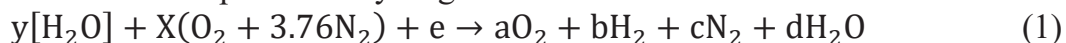


Fig.3.1 PMCR exploded view parts with gap length of 4.5mm.

The DBD plasma has a high energetic electron ionization and it has been dissociated the water vapor species into their constituent's hydrogen and oxygen gas elements. In this experiment the water vapor flow pathway included some of air. Consequently, the dissociation reaction kinetics affecting with the air content and hence significantly the reaction of the produced hydrogen concentration was written as follows:



While the main water decomposition equation can be written as follows:

Chapter 3 Hydrogen Production from Water Vapour



3.1.2 Experimental

The atmospheric DBD plasma was generated in the 4.5mm gap between the Dielectric quartz glass (70mm×70mm×2mm) and the flow channel part. The dielectric glass quartz part is fixed on the top of the flow channel part; Table (3.1) represents the PMCR geometrical characteristics. Figure (3.2) shows the schematic diagram of the steam decomposition experiment setup. In this experiment, the plasma was generated between the reactor two electrodes, the high voltage electrode (mesh part) and ground electrode (base plate). These electrodes are insulated from each other by the dielectric quartz glass layer with thickness of 2mm. The high voltage electrode is fixed on the top center of the SUS mesh dimension of 45mm×45mm which it is fixed on the center of dielectric glass quartz plate. The ground electrode is connected on the flow channel plate part in a ring shape with length of 10mm. The steam dissociation reactions are happened inside the gap length between the dielectric part and the PMCR flow channel part with length of 4.5mm.

The distilled water vapor only has been used at flow rate ranges of 100-200ml/h by means without carrier gas. The steam flow rate was calibrated before starting experiment to confirm the steam flow adjusted values. The steam flow path was included the air content (oxygen and nitrogen gas). The PMCR is placed inside the constant temperature drying oven type of Yamato DVS-402. In this study, the effect of ambient temperature on the steam decomposition has been investigated. The PMCR heating temperature effect has been studied at a range of 20°C-130°C. The plasma applied voltage at a range of 14-18kV has been tested. Just the water vapor flowing between the two electrodes in the gap length area, inside the flow channel the plasma is generated at a constant frequency of 10 kHz. The DBD plasma power has been measured 89, 102 and 120W according to the typical applied plasma voltage 14, 16 and 18kV, respectively. The applied voltage waveform has been followed by Tektronix TDS 3034C digital oscilloscope and controlled by high voltage regulator (Variac). The concentration of the outlet gases species (H₂, O₂ & N₂) have been measured by the gas chromatography instrument (GC) which it was calibrated before starting the steam decomposition experiment. The separation of the outlet steam dissociation species is made at cold conditions using ice trap in which it filled with the frozen liquid at a temperature of -1.5 to -2°C. The outlet gases samples have been taken by syringe 0.5ml and then injected to the GC instrument. The samples of outlet gases are taken after 2minutes of the plasma firing time that's for all experiments. The distilled water is used to get the preliminary results of steam decomposition at low temperature 300°C. The steam flow path contained air (oxygen and nitrogen gas). The analysis of output gases are made using the gas chromatographic (GC).

Chapter 3 Hydrogen Production from Water Vapour

Table 3.1 Geometrical characteristics of the PMCR

No. of flow channels [-]	Channel diameter [mm]	Gap length [mm]	Reaction volume [cm ³]
21	1	4.5	4.0635

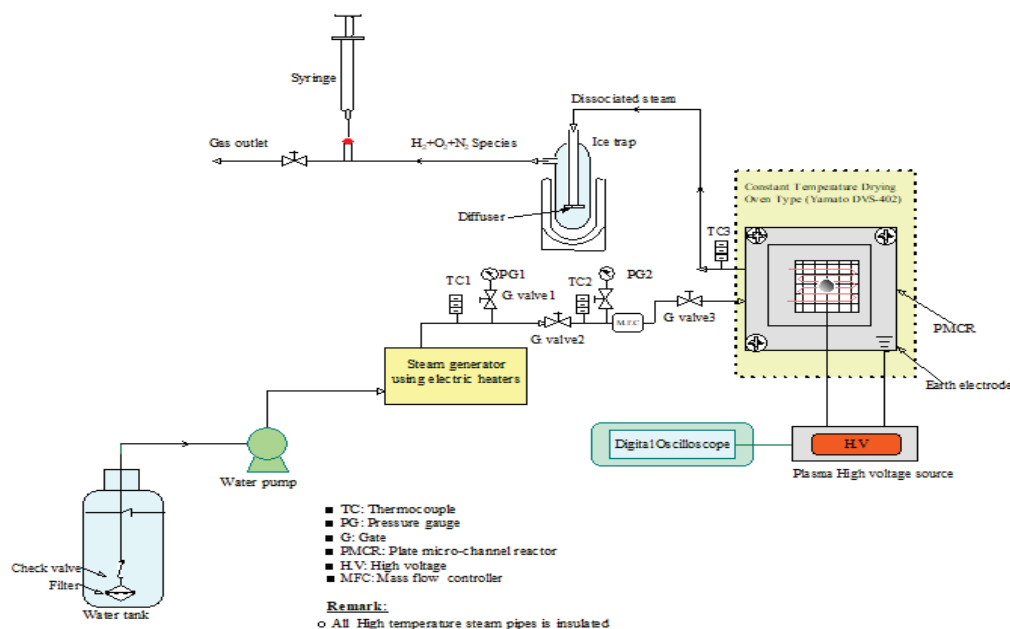


Fig 3.2 Schematic diagram of the steam decomposition apparatus.

3.1.3 Results & discussions

In a first step of this experiment, steam was injected into the PMCR and flow rate was calibrated. In the following experiment steam is injected to the PMR reactor at temperature of 573K and at atmospheric pressure (100kPa) with a different steam flow rates. The steam decomposition experiments were made at different reactor heating and surrounding temperatures within range of 293K-403K. The DBD plasma was tested in a high voltage range of 14-18kV, the plasma firing photo during the steam dissociation experiment is shown in figure (3.3).

Chapter 3 Hydrogen Production from Water Vapour

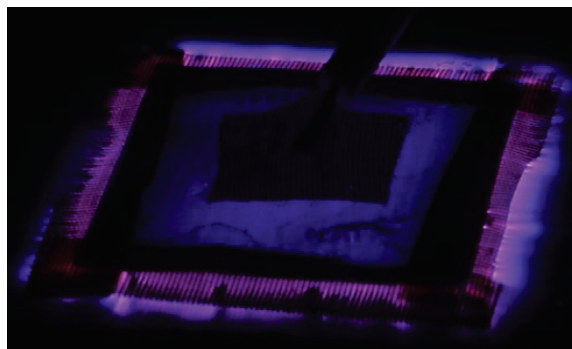


Fig 3.3 Photo of the PMCR during DBD plasma firing.

The plasma generated converts the steam molecules into its radical's hydrogen and oxygen gas. The separation of the outlet gases were made by ice trap using a frozen liquid to condensate water molecules and separate the outlet species. The steam was fed into the PMCR reaction area or the gap length area between the quartz glass and base plate. The outlet gases are collected and samples are fed to the gas phase chromatography using 0.5ml syringe. Before starting experiment, the calibration is carried out by performing GC analysis for known standard hydrogen gas concentration samples, 0.2%, 0.5%, 9.87% and 75% and 100% of standard H_2 gas concentrations are used. The samples are taken after 2minutes of firing plasma that in all steam dissociation experiments. The gas chromatography (GC) concentration analysis showed the hydrogen, oxygen and nitrogen gas concentrations. The mole fraction, hydrogen flow rate and the conversion rate have been calculated as a steam experiment results. Also, the energy efficiencies are estimated based on the total heat supplied to the steam decomposition system. Different steam inlet flow rates are injected into the PMCR in a range of 100-200ml/h at steam temperature of 573K. The effect of plasma applied voltage has been studied in a range of 14kV-18kV. Figures (3.4-6) show the hydrogen molar fraction at different steam inlet flow rates and different plasma applied voltage. The maximum hydrogen molar fraction was found as a value of 2.30% at steam inlet flow rate of 200ml/h, while the minimum value was found in which of 0.628% at low steam inlet flow rate at 100ml/h. The mole fraction is determined according to the following expression:

$$\text{Mole fraction} [X_{H_2}] \% = \frac{\text{The hydrogen moles} [n_{H_2}]}{\text{The total hydrogen moles} [n_{\text{total}}]} \times 100 \quad (3)$$

The effect of the PMCR heating temperature on the hydrogen production from steam is investigated. The main reason behind the low molar fraction percent in all experiments is the low density of hydrogen gas.

Chapter 3 Hydrogen Production from Water Vapour

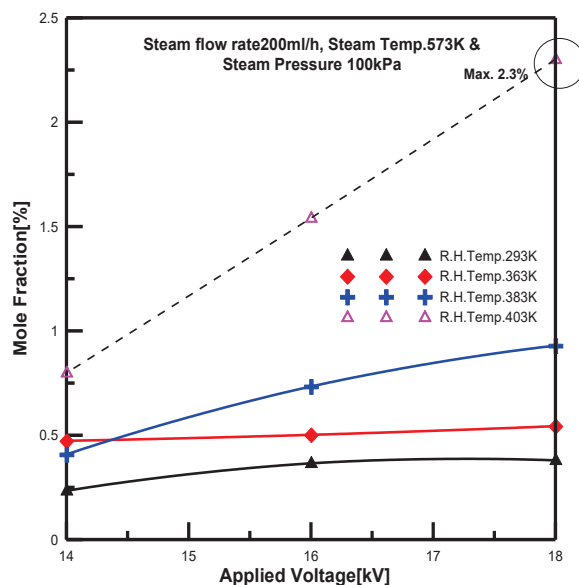


Fig 3.4 H₂ mole fraction at steam inlet flow rate 200ml/h vs. applied voltage.

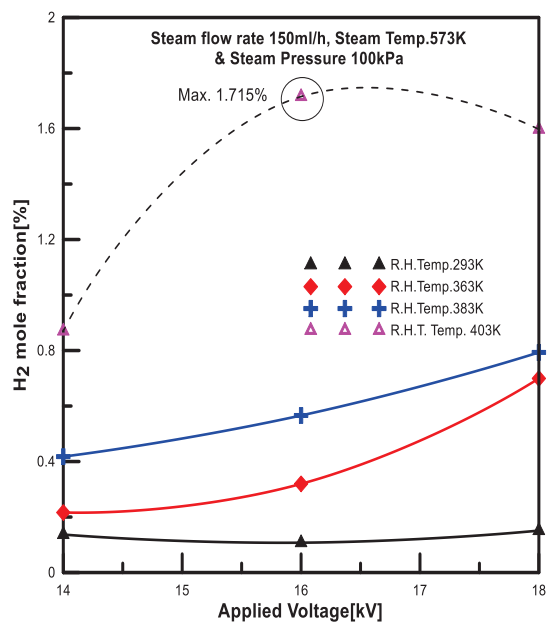


Fig 3.5 H₂ mole fraction at steam inlet flow rate 150ml/h vs. applied voltage.

Chapter 3 Hydrogen Production from Water Vapour

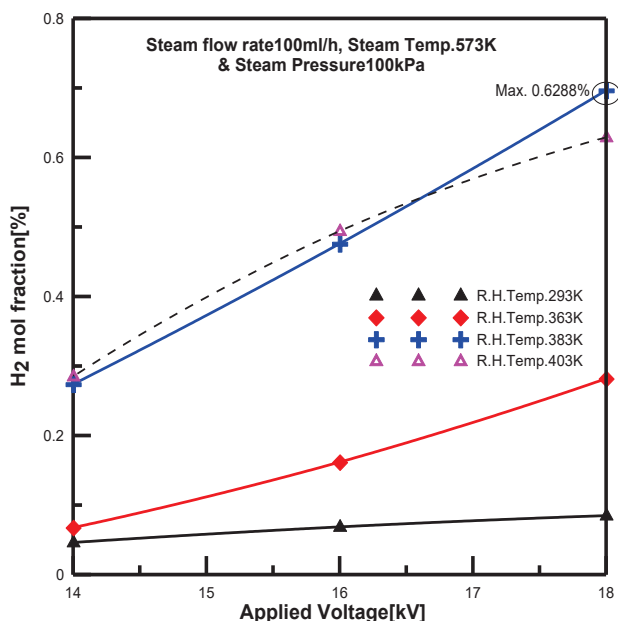
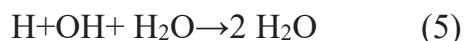
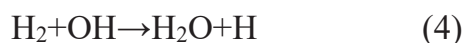


Fig 3.6 H₂ mole fraction at steam inlet flow rate 100ml/h vs. applied voltage.

Also, the PMCR heating temperature (R.H.T) was an important factor which increases the hydrogen mole fraction in the dissociated elements. Consequently, the higher molar fraction obtained at the reactor heater temperature of 403K at different applied DBD plasma voltage. The cooling process is performed by ice trap to prevent the recombination of water molecules, the recombination reactions can be expressed as follows [535]:



The plasma power consumption at the applied voltage ranges of 14kV, 16kV and 18kV were 89W, 102W and 120W respectively. The plasma power consumption is remained constant during the plasma firing time, additionally; the frequency was maintained at 10 kHz in all steam decomposition experiment.

The hydrogen flow rates were determined based on the GC concentrations measurement data. To be more precisely, the hydrogen flow rates versus the PMCR heating temperature at different steam inlet flow rates and at the same DBD plasma applied voltage have been analyzed. Figures (3.7-9) demonstrate the change of produced hydrogen flow rates versus the PMCR heating temperatures in which the maximum obtained hydrogen flow rate values at the plasma applied voltage of 14kV, 16kV and 18kV was 2.43g/h, 7.62 g/h and 9.42 g/h respectively. Further, it was observed that the maximum obtained hydrogen flow rate at plasma applied voltage 14 and 16 kV was at steam flow rate 150 ml/h while at plasma applied voltage 18 kV, the maximum obtained hydrogen flow rate at 200ml/h. It was seen that this change due to some of dissociated species are still remained inside the ice trap, additionally some of produced H₂ gas is consumed in the recombination reactions.

Chapter 3 Hydrogen Production from Water Vapour

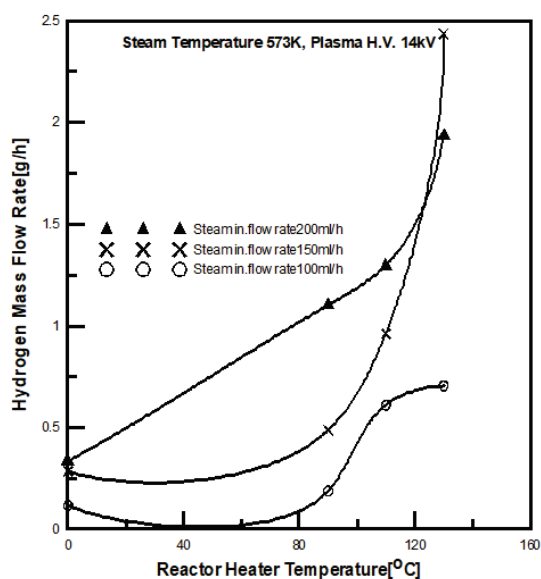


Fig 3.7 H₂ mass flow rate at 14kV versus temperature.

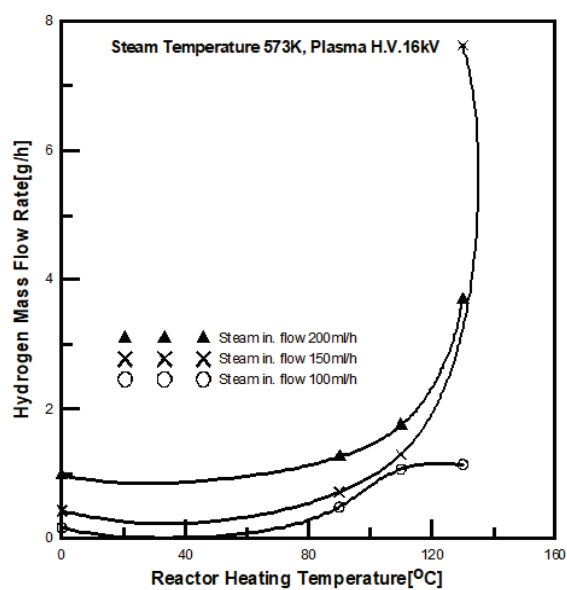


Fig 3.8 H₂ mass flow rate at 16kV, Vs. PMCR heating temperature.

Chapter 3 Hydrogen Production from Water Vapour

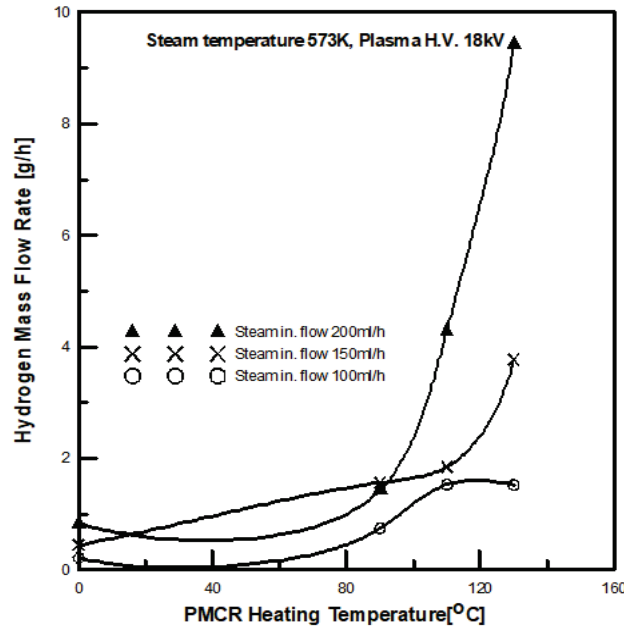


Fig 3.9 H₂ mass flow rate at 18kV, Vs. PMCR heating temperature.

The highest values were obtained at the highest PMCR heating temperatures of 403K. This means the heat loss to the ambient is high subsequently the hydrogen gases concentration decreased with the PMCR temperature decrease. The heat is transferred from steam to the quartz glass by forced convection heat transfer then by conduction through the quartz glass thickness and finally is transferred to the ambient by convection heat transfer. The total heat transfer rate is then written

$$dQ = n \cdot U \cdot (T_s - T_a) \cdot dA \quad [W] \quad (6)$$

Where n is the number of flow channels in the PMCR, U the overall heat transfer coefficient, A the total heat transfer area, T_s and T_a the steam temperature and the PMCR ambient temperature respectively. According to the PMCR flow channels short length, it can be considered that the flow is laminar. The heat is transferred from steam to the quartz glass by forced convection, the Nusselt number values cannot be used with its limiting value of $Nu=3.66$, the relationship proposed by Kays [537] can be used for unestablished laminar flow regime and $(0.7 < Pr < 1)$ as follows:

$$Nu = 3.66 + \frac{0.104(d/l)Re \times Pr}{1 + 0.016[(d/l)Re \times Pr]^{0.8}} \quad (7)$$

Where, Re is the Reynolds number determined from the flow channel diameter d , l the flow channel length and Pr the prandtl number. Thermodynamic properties of steam were obtained from superheated steam tables at steam temperature 300°C and pressure 100kPa. The forced convection heat transfer coefficient h_i obtained from the Nusselt number relation of $Nu = h_i d_i / k_s$, where k_s is the thermal conductivity of steam. The effect of

Chapter 3 Hydrogen Production from Water Vapour

reactor heating temperature (R.H.T) on the total heat transfer rate is given in figure (3.10). This plot indicates that the total heat transfer decreased with R.H.T increased; additionally, the plasma effect improved and appeared in the H₂ production.

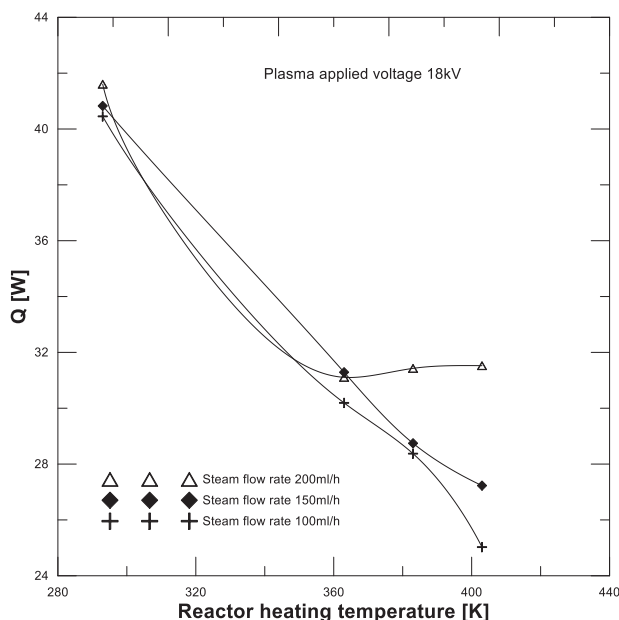


Fig 3.10 Total heat transfer rate Vs. PMCR heating temperature.

It is observed that the studies of hydrogen generation have been successfully quantified the hydrogen production by the gas phase chromatography (GC) analysis [531, 538]. However, the hydrogen gas produced in this experiment with small flow rates, it might be some of hydrogen gas quantity escaped during the sample collection or other hydrogen quantity remained inside the ice trap due to the hydrogen low density and different outlet species velocity.

The hydrogen conversion rate percent was determined for all steam dissociation experiments as an indirect method to evaluate the hydrogen production from steam. The hydrogen conversion rate percent can be defined as the ratio of the produced hydrogen gas to the input steam flow rate. It can be determined using the following equation:

$$\text{H}_2\text{Conversion rate}[\%] = \frac{\text{The produced hydrogen H}_2 [\text{mol / h}]}{\text{The input steam flow rate} [\text{mol / h}]} \times 100 \quad (8)$$

The hydrogen conversion rate % was determined for the different steam inlet flow rates and was shown in figures (3.11-13). The maximum obtained H₂ conversion rate% values at steam inlet flow rates of 100ml/h, 150ml/h and 200ml/h were 13.82%, 45.88% and 42.51% respectively.

Chapter 3 Hydrogen Production from Water Vapour

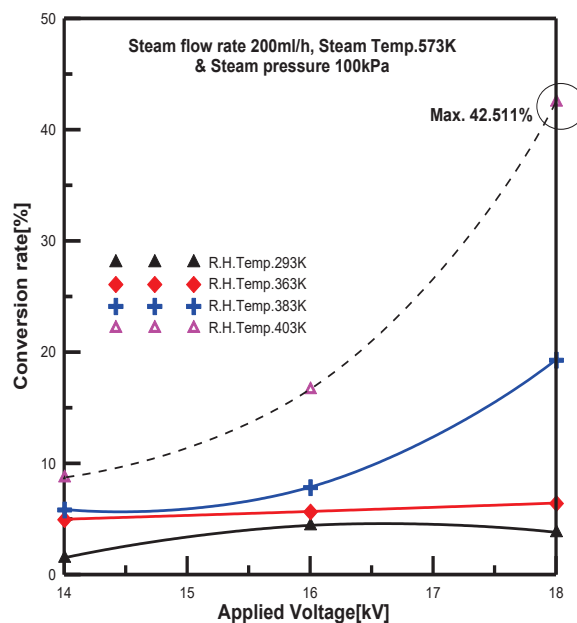


Fig 3.11 H₂ Conversion rate% at steam flow rate of 200ml/h vs. plasma applied voltage.

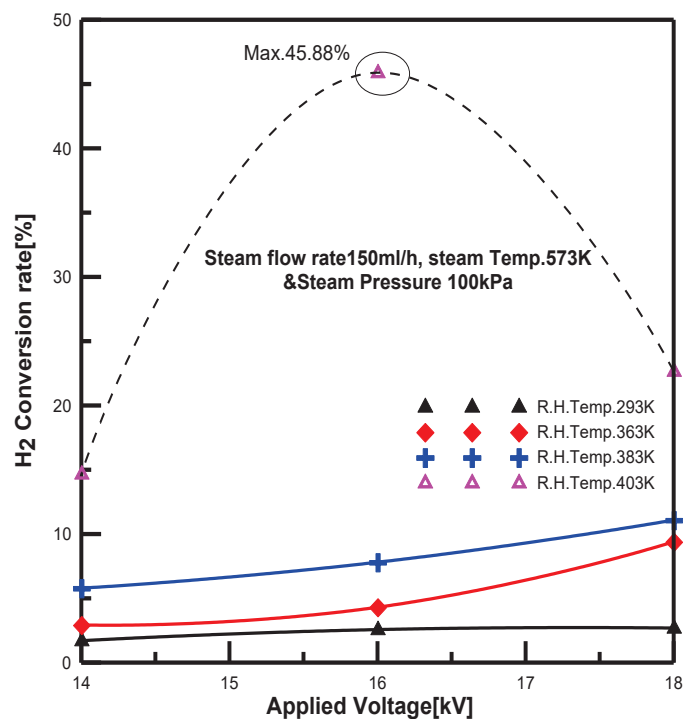


Fig 3.12 H₂ Conversion rate% at steam flow rate of 150ml/h vs. plasma applied voltage.

Chapter 3 Hydrogen Production from Water Vapour

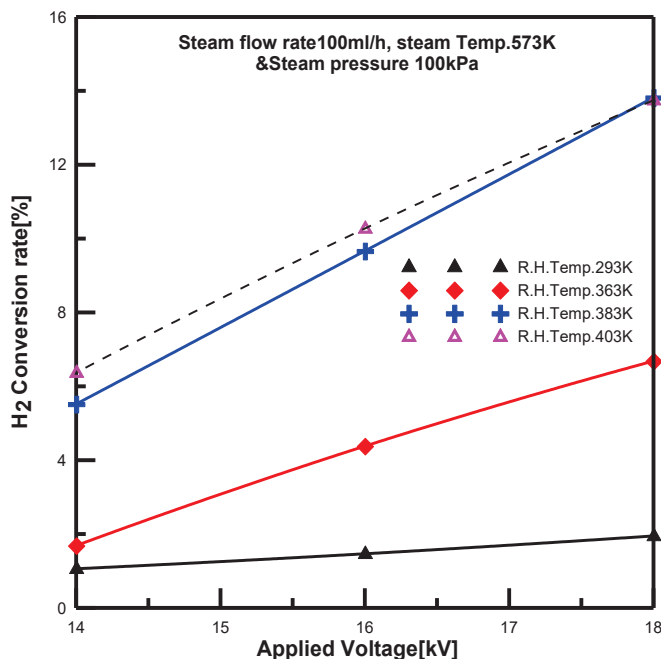


Fig 3.13 H₂ Conversion rate% at steam flow rate of 100ml/h vs. plasma applied voltage.

It was observed that maximum H₂ conversion rate % was at steam inlet flow rate of 150ml/h and at the plasma applied voltage of 16kV, the main reason was found that the sample collection method which it is important and should be considered, additionally the fast recombination of the H₂ molecules.

The hydrogen production using water vapor by the DBD plasma is a promising method considering the sample collection method which effects the produced hydrogen concentration and fast cooling of dissociated species are important factors in steam dissociation processes. The evaluation of the steam dissociation using DBD plasma is completed by determining the system energy efficiency. The energy efficiency can be calculated as the ratio of the H₂ gained energy to the total amount of heat added and consumed by the system as follow [539]:

$$\text{Energy efficiency}[\%] = \frac{\text{HHV} * \text{H}_2 \text{ output flow rate} [\text{W}]}{[\text{Plasma Power} + \text{Qadd} + \text{R.Heat} + \text{Condensation heat}] [\text{W}]} \times 100 \quad (9)$$

Where HHV is the hydrogen higher heating value, Qadd is the heat added to convert water to steam, R. Heat is the reactor heat added to raise temperature and the condensation heat to cool down steam and get hydrogen and oxygen gas using ice trap. Figures (3.14-16) present the energy efficiency of the produced hydrogen versus the total heat supplied to the steam decomposition system. The highest energy efficiencies were obtained at the steam inlet flow rates of 100ml/h, 150ml/h and 200ml/h were 10.96%, 46.68% and 49.42% respectively. It was observed that energy efficiency increased with the steam inlet flow rate increase and the PMCR heating temperature increase. However, the heat supplied to the steam dissociation system increased, also, the heat gain in the produced hydrogen was

Chapter 3 Hydrogen Production from Water Vapour

increased. In this experiment, the total heat supplied to the system was introduced in generating steam at atmospheric pressure, the PMCR heat and the outlet water species condensation heat.

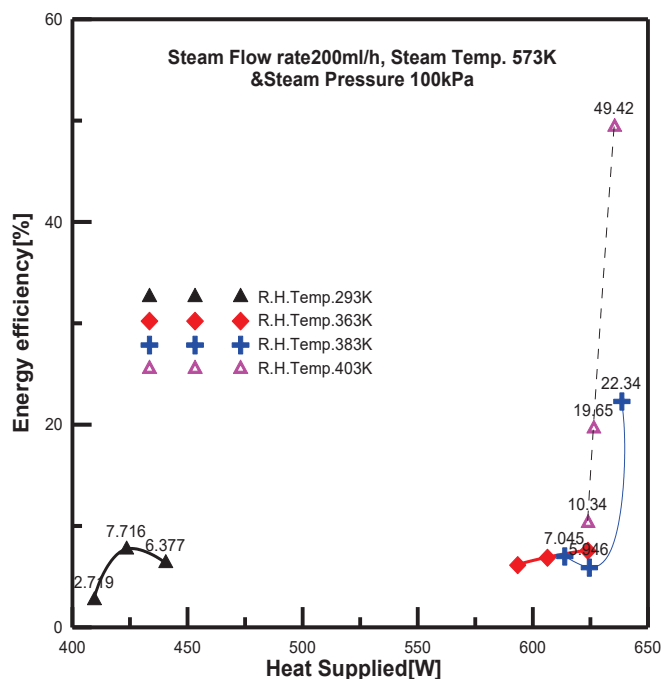


Fig 3.14 Energy efficiency vs. Heat supplied at steam flow 200ml/h.

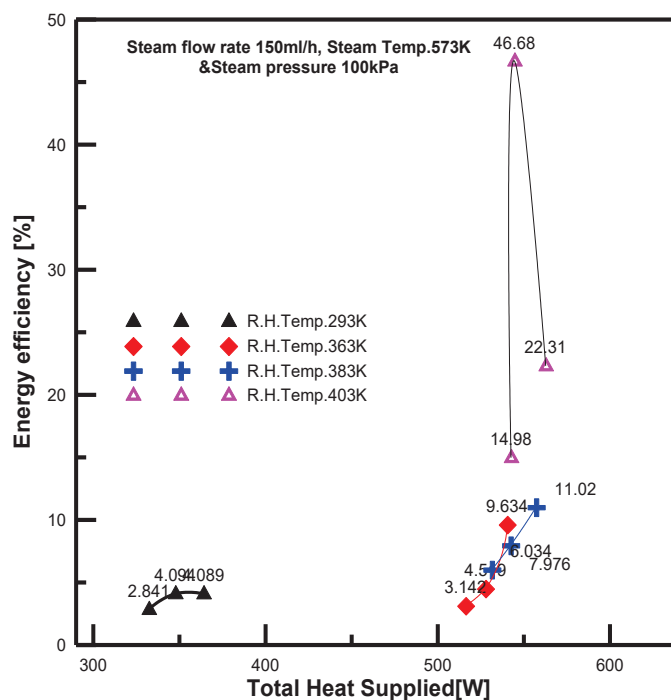


Fig 3.15 Efficiency vs. Heat supplied at steam flow 150ml/h.

Chapter 3 Hydrogen Production from Water Vapour

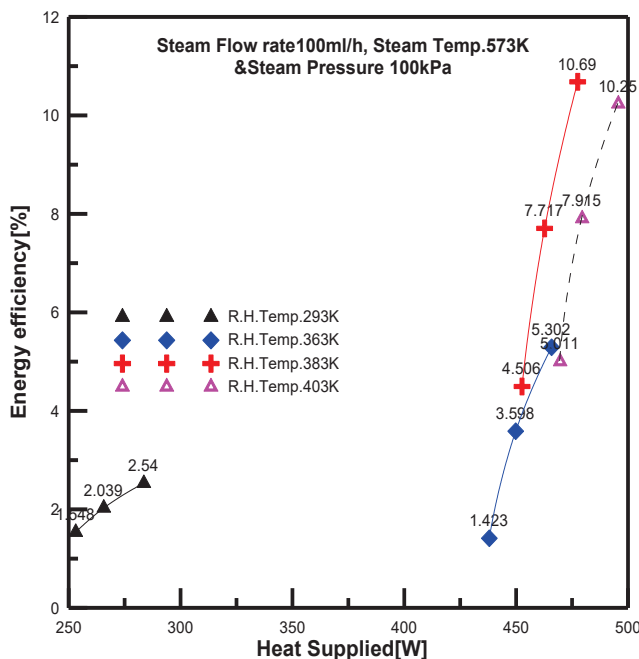


Fig 3.16 Efficiency vs. Heat supplied at steam flow 100ml/h.

The produced hydrogen gas from steam dissociation using DBD plasma experiment was improved by increasing the PMCR temperature. Also, the plasma discharge voltage was an important factor by means the higher plasma voltage the higher water vapor dissociation to their constituent's elements hydrogen gas and oxygen gas. The steam decomposition using DBD plasma is considered a promising method to generate H_2 gas in which the hydrogen quantity produced is higher than other plasma methods, additionally, the DBD plasma is utilized gases at low temperature and it is more stable than other methods.

Conclusion

This study represented the preliminary results of hydrogen production from steam decomposition using DBD plasma at applied voltage range of 14-16kV. A super-heated steam is fed into the PMCR at flow rate in range of 100-200ml/h, pressure of 100kPa and temperature of 573K. The outlet gases are cooled down using ice trap to prevent the dissociated species recombination. The effect of PMCR heating temperature on the steam dissociation process was investigated at PMCR heating temperature range of 293-403K. It was found that the hydrogen mole fraction and mass flow rate increased with the PMCR heating temperature, additionally the maximum obtained H_2 flow rate was 9.42 g/h at PMCR temperature 403K, steam flow rate of 200ml/h and plasma applied voltage of 18kV. The conversion rate percent was determined for tested steam flow rates, further it was observed that the maximum conversion rate percent was 42.51%. Also, the energy efficiencies versus the total heat added were calculated and the maximum obtained efficiency values was 49.42%, 46.68%, and 10.69% at steam flow rate of 200ml/h, 150ml/h and 100ml/h respectively. One of the most attractive results of this study that the maximum

Chapter 3 Hydrogen Production from Water Vapour

energy efficiency values wasn't always at the highest applied plasma voltage due to some of the dissociated species are still remained inside ice trap. It was clear from this study that the DBD plasma has the ability to dissociate water molecules to their elements hydrogen and oxygen. Also, it can be concluded that there are several factors can improve the hydrogen production yield from steam decomposition using DBD plasma as follows: the reactor temperature, the applied plasma voltage, steam temperature, sample collection method and optimization of the cooling down process to prevent the recombination reactions.

3.2 The Reactor Temperature Effect on H₂ Production from Steam Decomposition Using DBD Plasma

Hydrogen production from water decomposition is considered one of the attractive chemical processes to generate pure hydrogen and oxygen gas. Hydrogen production technologies such as biomass, thermolysis, steam reforming etc. have been studied [80, 324, 438]. Water electrolysis is considered the most classical one which hydrogen was produced at ordinary or intermediate temperature [93]. The steam reforming process with plasma has been studied in different plasma modes using different types of feedstock such as water, natural gas, and ethanol. Hydrogen production using plasma electrolysis has been studied [337, 540-543]. Hydrocarbons have also been studied as a feedstock including methanol, ethanol etc. [306, 285, 544-547]. The prediction of heat transfer between fluids and the surrounding walls are considered the most important roles in the design of hydrogen production by plasma devices like, gaseous fuel reactors, etc., the heat transfer from plasma in tube flow has been studied [548]. Heat transfer measurements were developed for different plasma reactor types [549, 550]. These studies declared the importance of heat transfer information for plasma devices design and the operating temperatures. In this study, the effects of the PMCR heating and surrounding temperatures on the steam decomposition using DBD plasma were investigated. The PMCR temperature was raised by constant temperature heater type and tested at a temperatures range of 20-130°C. The plasma was generated at atmospheric pressure and applied voltage range of 14-18kV. The water vapour was fed into the PMCR at a temperature of 300°C, pressure of 100kPa and flow rates of 100-200ml/h. The outlet gases were cooled down using ice trap and the hydrogen concentrations were measured using gas phase chromatography (GC). The total thermal resistances and overall heat transfer coefficient were determined and compared at different input steam flow rates and PMCR temperatures range of 20-130°C.

3.2.1 Experimental

Experiment was done to focus on the effect of the reactor and surrounding temperature on the steam dissociations processes. The DBD plasma was generated in the gap between the Dielectric glass quartz type (70mm×70mm×2mm) and the flow channel part as shown

Chapter 3 Hydrogen Production from Water Vapour

in figure (3.17). The dielectric glass part was installed between the high voltage electrode and ground electrode part. The PMCR was installed inside the insulated constant temperature heater type of Yamato DVS-402, the PMCR and its surrounding temperatures are heated to the same temperature before starting experiment for 1hr. The heating temperature range of 20°C-130°C and steam flow rates 100-200 ml/h were studied at the plasma applied voltage range of 14-18 kV. Water was fed into the reactor through the insulated pipes as a super-heated steam at a temperature of 300°C and pressure 100 kPa. The plasma applied voltage was controlled by the high voltage regulator; additionally the plasma power consumption was measured using digital power meter. Through the PMCR flow channels, the temperature of injected steam increased due to the plasma effect and steam dissociated in to hydrogen and oxygen. To avoid the recombination between hydrogen and oxygen molecules, the outlet gases were quickly cooled down in the ice trap. The outlet species samples were collected using 0.5ml syringe and analysed using the gas chromatography instrument (GC).

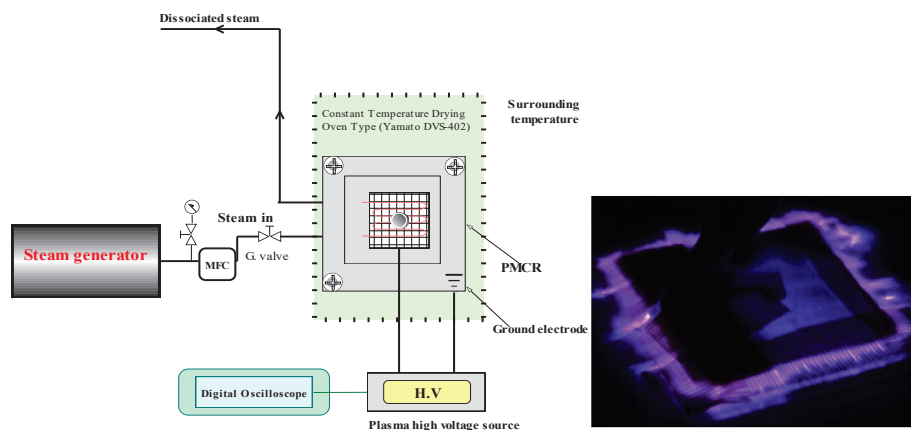


Fig 3.17 Schematic diagram of the experimental setup and plasma firing photo.

3.2.2 Results& Discussion

The effect of PMCR heating and surrounding temperature on the steam decomposition using DBD plasma was studied at different input steam flow rates and plasma applied voltage. The sample time collection was 2 min that for each steam decomposition experiment after starting the plasma firing. In this experiment, the outlet species concentrations were measured by GC, it is remarked that the hydrogen concentrations values were low because of the low density of hydrogen gas. To clarify the reactor and surrounding heating temperature effect, the PMCR was tested at heating temperature range of 20-130°C. The change of H₂ concentrations versus the PMCR heating temperatures at different plasma applied voltage are shown in Figures (3.18). The temperature and flow rates of steam were 300°C and 100-200 ml/h respectively, while the applied plasma voltage was in range of 14-18 kV. It was observed that the hydrogen concentration % increased with the reactor temperature increased at all tested steam flow rates. Also, it was seen that

Chapter 3 Hydrogen Production from Water Vapour

the maximum obtained H_2 concentration at steam flow rates 200ml/h was 2.3% at reactor heating temperature 130°C and plasma applied voltage of 18kV, While the maximum H_2 concentration at steam flow rate 150ml/h was 1.7151% at plasma applied voltage 16kV. For instance, at steam input flow rate of 100ml/h the highest value of H_2 concentration was 0.6965% at reactor temperature of 110°C while at reactor temperature 130°C the H_2 concentration value was 0.6288%, this difference in H_2 concentration data indicates that some of dissociated species were still remained inside the ice trap.

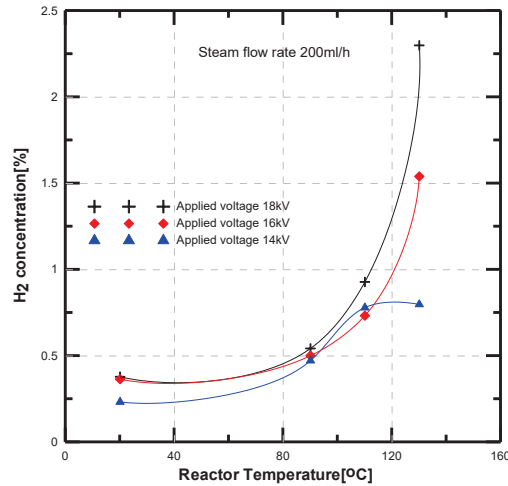


Fig 3.18 the effect of surrounding temperature at steam inlet flow rate 200ml/h.

The analysis showed the importance and effect of the reactor heating temperature on the steam decomposition process, therefore the heat transfer processes through the PMCR were investigated. The heat was transferred from steam to the quartz glass by forced convection heat transfer then by conduction through the quartz glass thickness and finally the heat was transferred by convection to the ambient. The total heat transfer rate can be written according to Incropera and Dewitt (2007) [551] as follow:

$$dQ = n \cdot U (T_s - T_a) dA \quad [W] \quad (1)$$

Where n is the number of flow channels in the PMCR, U the overall heat transfer coefficient ($W/m^2.K$), A the total heat transfer area (m^2), T_s and T_a the steam temperature and the PMCR surrounding temperature (K) respectively.

In this reactor, the overall heat transfer coefficient was determined according to three distinct thermal heat transfer resistances as given in figure (3.19) as follow: The forced convection heat transfer resistance from inside PMCR flow channel to reactor wall (R_{in}), the conduction resistance through the reactor wall (R_{wall}) and the convection resistance between the reactor wall and surrounding air (R_{out}).

Chapter 3 Hydrogen Production from Water Vapour

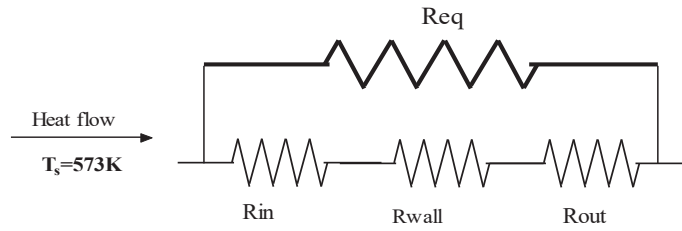


Fig 3.19 Heat transfer resistances from flow channels to outside.

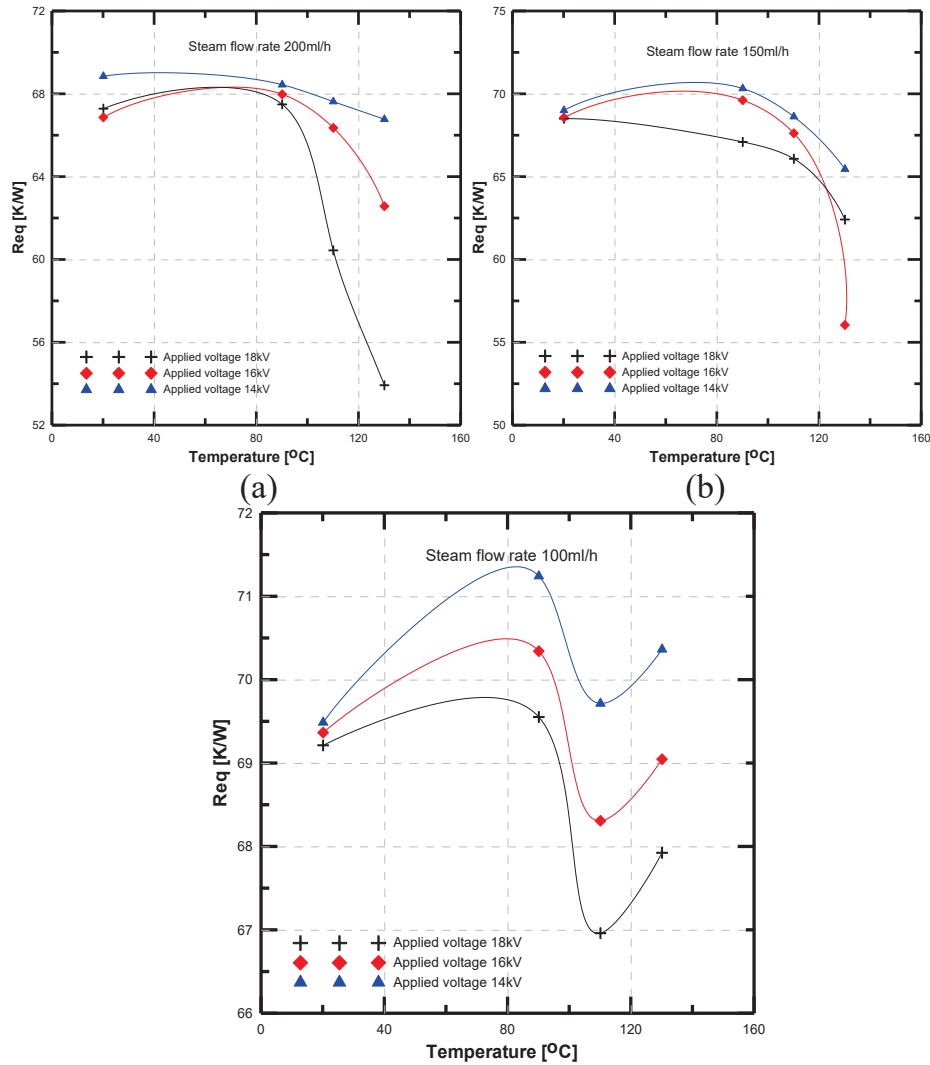


Fig 3.20 Heat transfer resistances from flow channels to outside.

The total heat transfer resistances (R_{eq}) are incorporated from the sum of the previous resistances ($R_{eq} = R_{in} + R_{wall} + R_{out}$) and the overall heat transfer coefficient can be calculated as from the following expression: $(U = 1 / R_{eq} \times A_i) [W/m^2]$.

For internal heat transfer resistance calculations, the heat is transferred from steam to the quartz glass by forced convection, additionally the PMCR flow channels length was too

Chapter 3 Hydrogen Production from Water Vapour

short, and it can be considered that the flow inside the reactor channels is laminar flow. The Nusselt number values cannot be used with its limiting value of $Nu=3.66$, the relationship proposed by Kays (1955) [537] can be used for unestablished laminar flow regime and $(0.7 < Pr < 1)$ as follows:

$$Nu = 3.66 + \frac{0.104(d/L)Re \times Pr}{1 + 0.016[(d/L)Re \times Pr]^{0.8}} \quad (2)$$

Where, Re is the Reynolds number determined from the flow channel diameter d [m], L [m] is the flow channel length and Pr is the Prandtl number. The thermodynamic properties of steam were obtained from superheated steam tables at steam temperature 300°C and pressure 100kPa . The forced convection heat transfer coefficient h_i [W/m^2] obtained from the Nusselt number relation of $Nu = h_i d / k_s$, where k_s [$\text{W}/\text{m.K}$] is the thermal conductivity of steam.

For the conduction and outside heat transfer resistance calculations, it was calculated using the thermal conductivity of the glass quartz and its thickness. The outside heat transfer coefficient was determined from the Nusselt number relation $Nu = h_o l / k_{air}$, while the Nusselt number was determined from Churchill and Chu (1975) [552] relation as a function of Rayleigh and Prandtl number as follows:

$$Nu = 0.68 + \frac{0.670 Ra^{1/4}}{[1 + (0.492 / Pr)^{9/16}]^{4/9}} \quad (3)$$

Where Ra is the Rayleigh number determined from $(Ra = Gr Pr)$. While the Grashof number was estimated using,

$$Gr = \frac{g \beta (T_w - T_a) L^3}{\nu^2} \quad (4)$$

Where β [K^{-1}] was thermal expansion coefficient, ν [m^2/s] was kinematic viscosity, L [m] was the flow channel length, and the reactor wall and outside air temperatures were T_w and T_a [K] respectively. The effect of reactor heating temperature on the total heat transfer resistances at different steam inlet flow rates are shown in figure (3.20). These plots indicate the influence of reactor and surrounding temperature on the total heat transfer resistances at different applied voltage, it was clear that the total heat transfer resistance decreased with the PMCR reactor and surrounding temperature increased. Also, each of the total heat transfer resistances plot represents a specific steam inlet flow rate which it depends on the reactor temperature and operational conditions. The behavior of these resistances as the reactor temperature changes reveals interesting information about how these resistances interact and distribute according to the reactor heating temperature.

The overall heat transfer coefficient was determined based on the equation (1). The change of overall heat transfer coefficient at different PMCR heating temperatures and steam flow rates 200ml/h , 150ml/h , and 100ml/h are shown in figure (3.21). It was found that the overall heat transfer coefficient increased by the PMCR heating temperature and plasma applied voltage increased. Therefore, the steam decomposition into their constituent's

Chapter 3 Hydrogen Production from Water Vapour

molecular elements is affected by the PMCR heating temperature and its surrounding temperature. Also, it was observed that the plasma effect increased by decreasing the temperature difference between input steam and reactor temperature. It was concluded from this study that the steam decomposition using DBD plasma was influenced by the reactor and surrounding temperature.

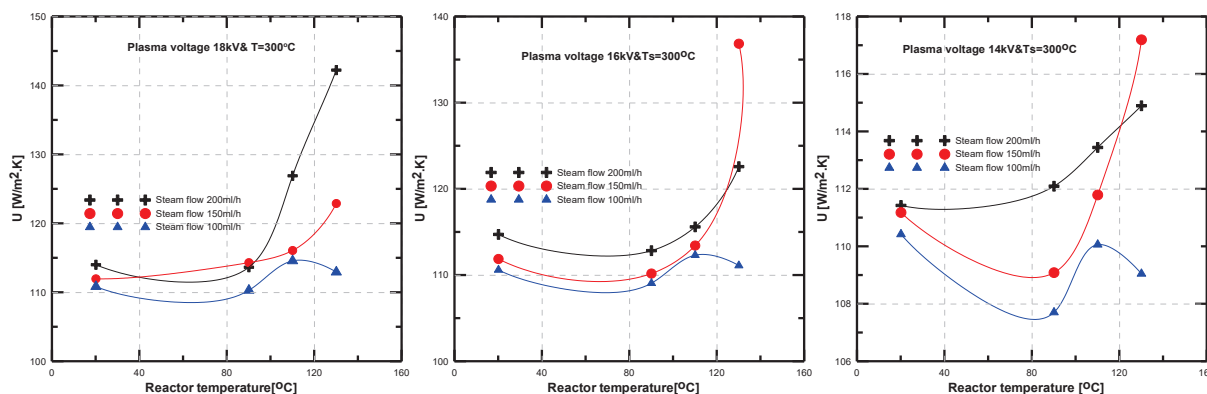


Fig 3.21 overall heat transfer coefficient at different steam flow rates.

Conclusion

The effects of PMCR and surrounding and PMCR temperature on the steam decomposition processes using plasma were studied. This experiment was tested the PMCR heating temperature in a range of 20-130°C, while the steam temperature and flow rates were 300°C and 100-200ml/h respectively. It is observed that the hydrogen concentration percent increased with the reactor and surrounding temperature, additionally, the maximum H₂ concentration was obtained at steam flow rate 200ml/h, reactor temperature 130°C and plasma applied voltage of 18kV. The effect of the PMCR reactor temperature on the total heat transfer resistances and overall heat transfer coefficient were investigated. It is showed that the total heat transfer resistances decreased with the reactor temperature increased, further the trend of these resistances showed how these resistances interact and distribute according to the PMCR temperature. Also, the most interesting thing was that the DBD plasma effect increased by decreasing the temperature difference between input steam and the PMCR temperature. Furthermore, it was found that the steam dissociation processes not mainly depend on the plasma applied voltage but also the surrounding and reactor temperature.

References

- [521] Du C, Wu J, Ma D, Liu Y, Qiu P, Qiu R, et al. Gasification of corn cob using non-thermal arc plasma. *Int J Hydrogen Energy* 2015; 40(37):12634-49.
- [522] Ni, M.; Leung, D. Y. C.; Leung, M. K. H.; Sumathy, K. An overview of hydrogen production from biomass. *Fuel Process. Technol.* 2006, 87 (5), 461–472.
- [523] Orhan Özcan, Ayşe N. A. Thermodynamic analysis of methanol steam reforming to produce hydrogen for HT-PEMFC: An optimization study. *Int. J. Hydrogen Energy* 2019; 11: 11117-26.
- [524] Ribeirinha P, Mateos-Pedrero C, Boaventura M, Sousa J, Mendes A. CuO/ZnO/Ga₂O₃ catalyst for low temperature MSR reaction: synthesis, characterization and kinetic model. *Appl. Catal B Environ* 2018; 221:371-9.
- [525] Vidal Vázquez F, Simell P, Pennanen J, Lehtonen J. Reactor design and catalysts testing for hydrogen production by methanol steam reforming for fuel cells applications. *Int. J. Hydrogen Energy* 2016; 41:924-35.
- [526] Ellamla HR, Bujlo P, Sita C, Pasupathi S. Comparative analysis on various reformers supplied with different fuels and integrated with high temperature PEM fuel cells. *Chem. Eng. Sci.* 2016; 154:90-9.
- [527] Rosli RE, Sulong AB, Daud WRW, Zulkifley MA, Husaini T, Rosli MI, et al. A review of high-temperature proton exchange membrane fuel cell (HT-PEMFC) system. *Int. J. Hydrogen Energy* 2017; 42:9293-314.
- [528] Islam MR, Shabani B, Rosengarten G, Andrews J. The potential of using nanofluids in PEM fuel cell cooling systems: a review. *Renew Sustain Energy Rev.* 2015; 48:523-39.
- [529] Ece A., Begum Y. K., Ahmet M. M., Selmiye Alkan G., Solen K. An effective electrocatalyst based on platinum nanoparticles supported with graphene nanoplatelets and carbon black hybrid for PEM fuel cells. *Int. J. Hydrogen Energy* 2019; 11:11175-83.
- [530] Ikechukwu S. A., Yuze H., Fuqiang X., Xiaoyang W., Yan Y., Qing D., Kui J., Comparative analysis of two-phase flow in sinusoidal channel of different geometric configurations with application to PEMFC. *Int. J. Hydrogen Energy* 2019; 44: 13807-19.
- [531] Burlica, R.; Shih, K. Y.; Locke, B. Formation of H₂ and H₂O₂ in a water-spray gliding arc nonthermal plasma reactor. *Ind. Eng. Chem. Res.* 2010, 49, 6342–6349.

- [532] Rehman F, Abdul Majeed WS, Zimmerman WB. Hydrogen production from water vapor plasmolysis using DBD-Corona hybrid reactor. *Energy & Fuels* 2013; 27:2748-61.
- [533] J. Gretz, Commission of the European Communities, Ispra, Italy, 9-13 May, 1977.
- [534] S. Kakac and T. N. Veziro~lu, 10th World Energy Conference, Istanbul, Turkey, 19-23 September, 1977.
- [535] J. Lede, F. Lapicque, J. Villermaux, B. Cales, A. Ounalli, J.F. Baummard, A. M. Anthony. Production of Hydrogen by Direct Thermal Decomposition of Water: Preliminary Investigations. *Int. J. Hydrogen Energy* 1982, 7(12), 939-950.
- [536] G. Borcia, C.A. Anderson, N.M.D. Brown, Dielectric barrier discharge for surface treatment: application to selected polymers in film and fibre form. *Plasma Sources Sci. Technol.* 12, 335–344 (2003).
- [537] W. M. Kays, Numerical solutions for laminar low heat transfer in circular tubes. *Trans. Am. Soc. Mech. Engrs* 77, 1265 (1955).
- [538] Porter, D.; Poplin, M. D.; Holzer, F.; Finney, W. C.; Locke, B. R. Formation of hydrogen peroxide, hydrogen, and oxygen in gliding arc electrical discharge reactors with water spray. *IEEE Trans. Ind. Appl.* 2009, 45 (2), 623–629.
- [539] Mahlia TMI, Saktisahdan TJ, Jannifar A, Hasan MH, Matseelar HSC. A review of available methods and development on energy storage; technology update. *Renew Sustain Energy Rev* 2014; 33:532–45.
- [540] J.H. Chaffin, S. M. Bobbio, H. I. Inyang, L. Kaanagbara. Hydrogen production by plasma electrolysis. *J. Energy Eng.* 2006, 132, 104.
- [541] M. Jasinski, M. Dors, J. Mizeraczyk. Production of hydrogen via methane reforming using atmospheric pressure microwave plasma. *J. Power Sources* 2008, 181 (1), 41–45.
- [542] A. H. Khojaa, M. Tahira, N. A. S. Amina. Recent developments in non-thermal catalytic DBD plasma reactor for dry reforming of methane. *Energy Conversion and Management* 2019, 183, 529–560.
- [543] W. Wang, C. Zhu, Y. Cao. DFT study on pathways of steam reforming of ethanol under cold plasma conditions for hydrogen generation. *Int. J. Hydrogen Energy* 2010, 35 (5), 1951–1956.
- [544] A. Babaritskii, I. Baranov, M. Bibikov, S. Demkin, V. Zhivotov, G. Kononov, G. Lysov, A. Moskovskii, V. Rusanov, R. Smirnov. Partial hydrocarbon oxidation processes induced by atmospheric pressure microwave-discharge plasma. *High Energy Chem.* 2004, 38 (6), 407–411.

- [545] D. Czyłkowski, B. Hrycak, Mari J. nski, Mirosław Dors, Jerzy Mizeraczyk. Hydrogen production by direct injection of ethanol microdroplets into nitrogen microwave plasma flame. *Int. J. Hydrogen Energy* 2018, 43, 21196-208.
- [546] B. Sarmiento, J. J. Brey, I. G. Viera, A. R. Gonzalez-Elipé, J. Cotrino, V. J. Rico. Hydrogen production by reforming of hydrocarbons and alcohols in a dielectric barrier discharge. *J. Power Sources* 2007, 169 (1), 140–143.
- [547] L. Xi Zhen, C. J. Liu, B. Eliasson. Hydrogen production from methanol using corona discharges. *Chin. Chem. Lett.* 2003, 14 (6), p631–633.
- [548] P.S. Schmidt, G. Leppert. Heat transfer from plasma in tube flow, *Journal of Heat Transfer* 1970, 483-489.
- [549] E. Acayanka, J. Tarkwa, S. Laminsi, Evaluation of Energy Balance in a Batch and Circulating Non-thermal Plasma Reactors During Organic Pollutant Oxidation in Aqueous Solution. *Plasma Chemistry and Plasma Processing* 2019, (39), 75–87.
- [550] J. F. Daviet, L. Peccoud. Heat transfer in a microelectronics plasma reactor. *J. Appl. Phys.* 1993, 73(3), 1471-79.
- [551] F.P. Incropera, D.P. Dewitt, T.L. Bergman, A.S. Lavine, Introduction to heat transfer, 5th edition, J.Wiley & Sons, Inc. (2007).
- [552] S. W. Churchill, and H.H.S. Chu. Correlating Equations for Laminar and Turbulent Free Convection from a Vertical Plate. *International Journal of Heat and Mass Transfer.* (1975), 18, 1323-1329.

Chapter 4 Water vapour decomposition simulation

Chapter 4 Water vapour decomposition simulation

4.1 Introduction

Hydrogen fuel offers many advantages such as lower emissions of greenhouse gases (GHGs) which could be utilized as alternative fuel. Hydrogen fuel can be produced by different methods using a renewable energy sources [78-81, 324]. Steam methane reforming process is act 80-85% of the total world hydrogen production. All of hydrogen production technologies are directly or indirectly utilized fossil fuel, subsequently GHGs emit to the environment. One-dimensional heat diffusion equation has been developed to find solution for the heat transfer problems [553, 554]. The results have been showed accuracy for the analytical solution. Moreover, a new integral solution has been developed for solving the heat and diffusion equations [555, 556]. The current work simulates and analyzes one-dimensional model of the hydrogen production from water vapor using dielectric barrier discharge plasma (DBD) which is cleaner than the hydrogen production from the conventional methods.

Studying of plasma and species characteristics has more attention due to their successful experimental results and applications at atmospheric pressure such as engineering, sterilization and surface treatment [557-561]. DBD plasma is considered the most important plasma type due to their high efficiency, productivity of new radicals, easy setup and operation. Hydrogen production from water vapor using plasma has recently more interest because of the high specific productivity [337]. DBD Plasma can be generated from electrical energy between two electrodes separated by dielectric quartz glass; it will transform it to kinetic electrons energy which transformed into new molecular kinetic energy of heavy particles [562].

Water is considered the third most important abundant molecule in the world after hydrogen and carbon monoxide gases [563]. Because of the continuous increasing of global temperature, more water vapor will be evaporated and holding by the atmosphere. Hence, it was clear that it has an implication on the warming effect. Additionally, it can be considered an important greenhouse gas and also, contributing more than half of 33K of natural warming [564]. Further, water is one of the dominant components of the biological cells and furthermore, water is the main of hydrocarbon fuels combustion products. Due to the importance of water stated above, electron collisions are stated to play an important role to determine the population of water molecules using plasma technique [565]. The water vapor electron collisions have been studied by many researchers for many years and reporting the cross section data for many interactions [566-570]. All water vapor collision processes including the total scattering, elastic scattering, momentum transfer, excitation of rotational, vibrational, and electronic states, ionization, electron attachment, dissociation, and

Chapter 4 Water vapour decomposition simulation

emission of radiation have been reviewed by Y. Itikawa and N. Mason [571]. The electron collision cross sections are important inputs data to executing simulation. Many simulation studies for atmospheric DBD plasma have been carried out such as modeled of co-axial reactor in pure helium [572-575]. Most of plasma studies have been carried out and reported at low pressure [285, 334, 531, 576-578].

4.1.1 Water molecular properties

Water molecule can be found in the electronically ground state, additionally water has a permanent of electric dipole moment which appears in its direction as shown in Figure (4.1). The ionization energy of H₂O has been investigated as follow [579]:

$$E_i = 12.621(\pm 0.002) \text{ eV}$$

A critical assessment and a very extensive analysis have been implemented to determine the dissociation energy of the water molecules to be [580],

$$D(\text{H} - \text{OH}) = 5.0992(\pm 0.0030) \text{ eV}$$

Several reviews have been executed for electron collisions with water. The water vapor dissociation cross sections data have been prepared from the published collision cross sections pervious work [571, 581].

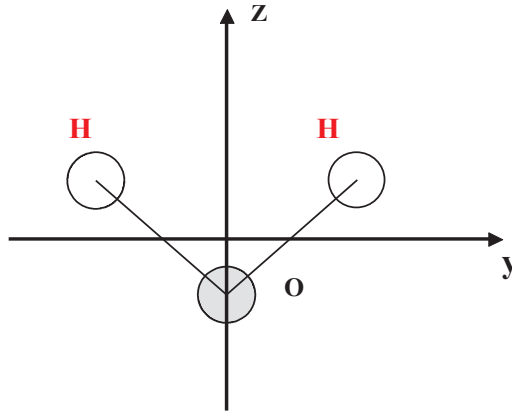


Fig 4.1 Nuclear configuration of H₂O.

In this study, three models were simulated for water vapor plasmolysis at atmospheric pressure in the plate type reactor. These models are gradually complicated in their chemical reaction mechanisms pathway from model I to model III. The first model was analyzed for the direct water vapor decomposition reaction mechanism pathway. Model II and model III are more complicated included different ions. The electron collision cross sections for all models are prepared and utilized. In this simulation

Chapter 4 Water vapour decomposition simulation

study, the electron density, electric field, electric potential, electron temperature and the hydrogen mass fraction are analyzed across the discharge gap and over time. Comparison between the hydrogen mass fractions of these models over the time across the discharge gap was investigated.

4.1.2 Simulation models kinetics

In recent years, many researchers' efforts have been carried out for modelling the water vapor decomposition using plasma. Electronic and ionic collisions with the water vapor for a single type plasma- chemical reaction to overall kinetic models have been investigated [80, 562, 577, 581]. A mathematical model for the water chemical reactions inside the discharge channel has been proposed by Mededovic and Loke [576]. The discharge channel is divided into the core and recombination zones, the molecular hydrogen evolution has been described. The water vapor molecule at very low pressure (133-150P1), zero dimensional models has been studied [577]. They found that the major positive and negative species were H_3O^+ and OH^- , respectively. Vibrational excitation and dissociative electron attachment of the water vapor plasmolysis mechanism have been discussed [571]. The distribution of electron energy through different pathways in water vapor plasma is shown in Fig 4.2. It can be observed that 80% of energy is absorbed by the vibrational excitation channel at low electron energy levels lower than 1eV, while the most of energy is absorbed in the dissociative attachment reaction type at typical plasma electron temperatures levels of 3-5eV [582]. The recommended ionization energy of H_2O is determined as follows [579]: $E_i = 12.62(\pm 0.002)\text{eV}$.

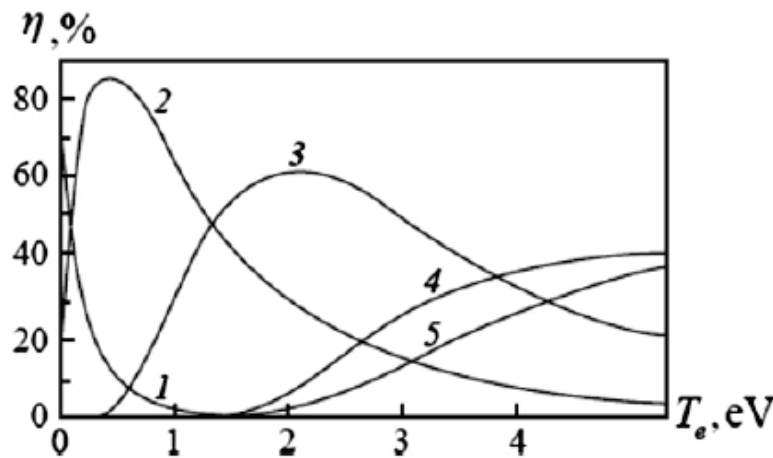


Fig4.2 Electron energy distribution between excitation dissociation and ionization channels in water vapor. 1) Elastic scattering; 2) vibrational excitation; 3) dissociative attachment; 4) electron excitation; 5) Ionization (Ref. [583]).

Chapter 4 Water vapour decomposition simulation

4.1.2.1 Geometry

In this paper, the water vapor decomposition using DBD plasma in a plate type reactor was simulated. Figure (4.3) shows the MPR plasma discharge gap and the 1-D simulated geometry. Three models with different reaction mechanisms of water vapor plasmolysis were simulated using the water vapor cross section of electron collisions. The DBD plasma was driven by a sinusoidal typical power with high voltage source of 18kV and frequency of 10 kHz. The electron density assumed to be 10^6 m^{-3} , the vapor pressure $1.01 \times 10^5 \text{ Pa}$ and temperature of 573K. The cross sections of electron collisions of water vapor were obtained from the published cross section data. The selection criteria of the cross sections data were concluded as follows: the priority for experimental methods, the reliability of the experimental methods [571]. The plasma discharge gap is 4.5mm. The thicknesses of the dielectric glass and mesh parts are 2mm and 0.3mm, respectively.

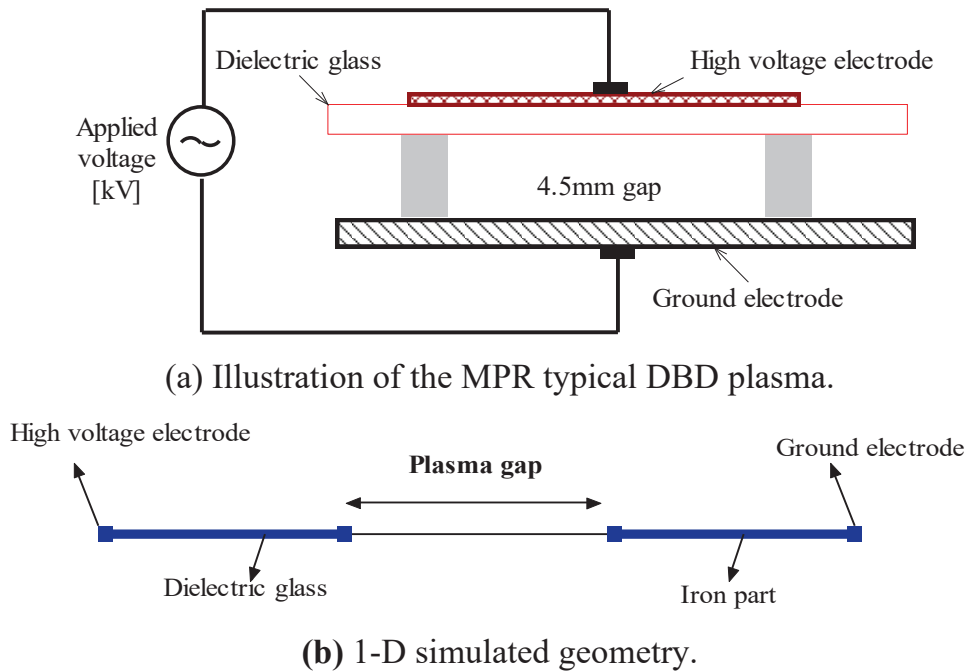


Fig 4.3 (a) illustration of the MPR typical DBD plasma. (b) 1-D simulated geometry.

4.1.2.2 DBD Modeling equations

In this simulation, the DBD fluid dynamics equations were used. The surface chemistry reactions were considered for different species to calculate the production rate and the electrode surface losses [584]. The simulation models are implemented using COMSOL Multiphysics package [585]. The electron density and the electron mean energy were determined by solving a pair of drift diffusion equations. The

Chapter 4 Water vapour decomposition simulation

convection of electrons due to fluid motion in these calculations is neglected. The simulation modelling equations are,

$$\frac{\partial n_e}{\partial t} + \nabla \cdot \vec{\Gamma}_e = R_e - (\vec{u} \cdot \nabla) n_e \quad (1)$$

$$\vec{\Gamma}_e = -(\vec{\mu}_e \cdot \vec{E}) n_e - \vec{D}_e \cdot \nabla n_e \quad (2)$$

Where n_e is the electron density, the electron diffusion coefficient D_e , $\vec{\Gamma}_e$ is the electron flux, \vec{u} is the average fluid velocity, and R_e is the rate of electron production.

The electron flux is caused by the electric field and by the density gradient. The electron energy density equation can be expressed as follow:

$$\frac{\partial n_\varepsilon}{\partial t} + \nabla \cdot \vec{\Gamma}_\varepsilon [-n_\varepsilon (\vec{\mu}_\varepsilon \cdot \vec{E}) - \vec{D}_\varepsilon \cdot \nabla n_\varepsilon] + \vec{E} \cdot \vec{\Gamma}_\varepsilon = R_\varepsilon - (\vec{u} \cdot \nabla) n_\varepsilon \quad (3)$$

$$\vec{\Gamma}_\varepsilon = -n_\varepsilon (\vec{\mu}_\varepsilon \cdot \vec{E}) - \vec{D}_\varepsilon \cdot \nabla n_\varepsilon \quad (4)$$

The amount of energy gained from the electric field by the electron indicates in this term $\vec{E} \cdot \vec{\Gamma}_\varepsilon$. The energy rate from the inelastic collisions can be estimated by:

$$R_\varepsilon = S_{en} + \frac{Q + Q_{gen}}{q} \quad (5)$$

Where S_{en} indicates the power dissipation, Q_{gen} is the main heat source and q is the electron charge. The electron diffusion coefficient D_e , the energy mobility μ_e , and the energy diffusion coefficient can be determined by:

$$D_\varepsilon = \mu_\varepsilon T_e, D_e = \mu_e T_e, \mu_\varepsilon = \frac{5}{3} \mu_e \quad (6)$$

While the electron energy source R_e and the energy loss due to inelastic collision R_ε can be given by:

$$R_e = \sum_{j=1}^M x_j k_j N_n n_e \quad (7)$$

Where the mole fraction x_j of the target species reaction j , k_j is the reaction rate coefficient (m^3/s), and the total neutral number of density N_n ($1/\text{m}^3$). The electron energy loss is determined by summing all reactions collisional energy loss as follow:

$$R_\varepsilon = \sum_{j=1}^P x_j k_j N_n n_e \Delta \varepsilon_j \quad (8)$$

Chapter 4 Water vapour decomposition simulation

The energy loss from the reaction j is $\Delta\varepsilon_j$ (V), it can be computed from the reactions cross section data as follow:

$$k_k = \gamma \int_0^\infty \varepsilon \sigma_k(\varepsilon) f(\varepsilon) d\varepsilon \quad (9)$$

Where $\gamma = (2q/m_e)^{1/2} [C^{1/2}/kg^{1/2}]$, where q is the electron charge, and m_e is the electron mass [kg], ε is the energy [V], σ_k is the collision cross section [m^2] and will be explained for each model, and f is the electron energy distribution function. In non-electron species, the following equation is solved from the mass fraction for each species:

$$\rho \frac{\partial w_k}{\partial t} + \rho(\vec{u} \cdot \nabla) w_k = \nabla \cdot \vec{J}_k + R_k \quad (10)$$

Where w_k is the density of ions, and $\nabla \cdot \vec{J}_k$ is the ions energy flux. The electrostatic field can be determined from the following equation:

$$-\nabla \cdot (\varepsilon_0 \varepsilon_r E) = \rho \quad (11)$$

Where ε_0 is the permittivity of vacuum, and ε_r is the relative dielectric constant. Due to the DBD plasma random motion effect of resulted electrons the boundary conditions of the electron flux and electron energy flux can be estimated as follows,

$$n \cdot \vec{\Gamma}_e = \left(\frac{1}{2} v_{e,th} n_e \right) - \sum_p \gamma_p (\vec{\Gamma}_p \cdot n) \quad (12)$$

$$n \cdot \vec{\Gamma}_\varepsilon = \left(\frac{5}{6} v_{e,th} n_e \right) - \sum_p \varepsilon_p \gamma_p (\vec{\Gamma}_p \cdot n) \quad (13)$$

In equation (12), the term on the right side is the produced electrons due to the secondary emission effect, where the secondary emission coefficient is γ_p . The secondary emission of energy flux is indicated in Eq. (13), ε_p is the mean energy of the secondary electrons.

In this DBD plasma simulation, the high voltage discharge electrode is driven by a sinusoidal electric potential and applied for the mesh electrode part,

$$V = V_0 \sin(\omega t) [V] \quad (14)$$

Where V_0 is the applied peak voltage ($V_0=750V$), and ω is the angular frequency. While the DBD applied frequency is 10 kHz. Furthermore, the ground electrode is connected to the bottom plate as shown in [Fig. \(4.3\)](#).

Chapter 4 Water vapour decomposition simulation

4.1.3 Reaction mechanism and cross sectional of Model I

In this model a direct water decomposition reaction mechanism are used, the reaction mechanism of model I is shown in Table (4.1).

Table 4.1 Ionization Cross section for electrons on H₂O gas [586]

Reaction	Reaction type	Type
1	H ₂ O+e→ H ₂ O+e	Momentum transfer reaction
2	H ₂ O+e→ H ₂ +1/2O ₂	Dissociation reaction

In this model a direct and simple water vapor dissociation reaction mechanisms are investigated [586], the gross and partial ionization cross section for electrons in the energy range of 0.1-20 keV have been used as shown in Table 4. 1. It can be determined from the following relation,

$$\sigma = \left(\frac{I^+}{I^-}\right) (\iota_p)^{-1} [T/(273 \times 3.535 \times 10^{16})] cm^2 \quad (15)$$

Where I^+ is the current of positive ions to the measuring electrode; I^- is the electron current to the Faraday cage; l is the length from which ions are extracted in centimeters; p is the gas pressure in Torricelli; T is the gas temperature in degrees Kelvin (room temperature). This is the first successful trail of water vapor decomposition simulation using DBD plasma. Firstly, to simplify the water plasmolysis simulation we started using the direct water vapor decomposition reaction mechanism with the following cross section.

Table4.2 Ionization Cross section for electrons on H₂O gas [586]

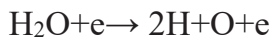
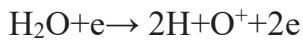
<i>Energy [keV]</i>	$\sigma_{H_2O} \times 10^{-16}$ <i>[cm²/molecule]</i>	$\sigma_{H_2+1/2O_2} \times 10^{-16}$ <i>[cm²/molecule]</i>
0.08	1.98	...
0.09	2.01	...
0.1	1.98	2.1
0.12	1.96	2.05
0.16	1.83	1.89
0.2	1.71	1.75
0.3	1.46	1.34
0.4	1.26	1.22
0.5	1.12	1.06
0.6	1	0.94
0.8	0.77	0.75

Chapter 4 Water vapour decomposition simulation

1	0.622	0.649
2	0.375	0.374
3	0.261	0.271
4	0.22	0.214
5	0.183	0.182
6	0.16	0.153
8	0.123	0.121
10	0.101	0.101
12	0.088	0.086
14	0.078	0.076
16	0.064	0.069
18	0.058	0.062
20	0.054	0.058

4.1.4 Reaction mechanism and cross sectional of Model II

In this model, the simulation was carried out for more complicated water plasmolysis reaction mechanism. The electron collisions of H₂O molecules are excited to these levels: rotational, vibrational and electronic levels [571]. There is some of water vapor plasma reactions may occur but aren't considered in this simulation study due to its high energy requirement and low probability [581],



The formation of produced radicals like hydrogen-H, hydroxyl-OH and oxygen-O in the non-thermal plasma are considered the most important process. After that these species react with each other to form new molecular products [271,576, 587]. Several pathways of water molecule dissociation by electron have been reported [577]. These pathways reaction types are included the momentum transfer, ionization, dissociative attachment, dissociative ionization, dissociation and dissociative excitation reactions. It has been reported that the rate of negative species produced by the dissociative attachment reactions (H⁻, OH⁻ and O⁻) was very small because of their cross sections are weak ($1-6 \times 10^{-18}$ cm²/molecule) [581].

The produced electron by the electron detachment would then participate in starting reaction with another water molecule and make a chain of reactions. This chain of reactions can be recombined by ion-ion or ion-molecular reaction.

Chapter 4 Water vapour decomposition simulation

In the current model, it was considered that the water vapor dissociation reactions pathway are included OH^+ , O^+ and H_2O^+ radicals. The chemical reactions list considered in this model are shown in Table (4.3). According to the literature survey, it is observed that the initiation of water vapor plasmolysis dissociation reaction with the previous radical as a reaction products is better than to start with the unlike reactions [581]. The simulation has been implemented using COMSOL Multiphysics plasma module and the electron collision cross sections as inputs import data [585].

Table 4.3 Reaction mechanism of model II

Reaction	Reaction type	Type	Rate constant(K) [m ³ /mol-sec, m ⁶ /mol-sec]	Ref.
1	$\text{H}_2\text{O} + \text{e} \rightarrow \text{H}_2\text{O} + \text{e}$	Momentum transfer reaction	3.65776E+11	[541]
2	$\text{H}_2\text{O} + \text{e} \rightarrow 2\text{e} + \text{H}_2\text{O}^+$	Ionization reaction	2.990E+05	[541]
3	$\text{H}_2\text{O} + \text{e} \rightarrow 2\text{e} + \text{H} + \text{OH}^+$	Dissociative ionization reaction	3.268E+02	[541]
4	$\text{H}_2\text{O}^+ + \text{e} \rightarrow \text{H}_2 + \text{O}$	Dissociative ion-recombination reaction	$f \times (0.3 \times 10^{-13} (0.01 / T_e))$	[541]
5	$\text{H} + \text{OH}^+ \rightarrow \text{O}^+ + \text{H}_2$	Charge transfer reaction	$f \times (4.9 \times 10^{-16} \exp(-0.36/T))$	[541, 588]
$f=6.02 \times 10^{17}$; $g=3.62404 \times 10^{35}$; T , gas temperature; T_e , electron temperature				

Table (4.4) represents the surface reactions which are implemented in addition to the volumetric reactions.

Table 4.4 surface reactions

Reaction	Reaction type	Sticking coefficient
1	$\text{O}^+ \rightarrow \text{O}$	1
2	$\text{H}_2\text{O} + \text{O}^+ \rightarrow \text{H}_2\text{O}^+ + \text{O}$	1

The momentum transfer cross section can be determined by the following formula [571],

$$Q_m = 2\pi \int_0^\pi (1 - \cos\theta) q_{elas}(\theta) \sin\theta d\theta \quad (16)$$

Chapter 4 Water vapour decomposition simulation

Where the elastic differential cross section is q_{elas} . The momentum transfer cross section can be determined by swarm experiments due to their low energies. Q_m can be obtained from the DCS (Differential cross section) measured by the beam experiments. The momentum cross section data has been reported [589, 590]. The swarm values of momentum cross section are almost shows a good agreement with the beam data [589]. Finally, Table (4.5) presents the recommended momentum cross section data of electron collision with water.

Table 4. 5 The recommended momentum transfer cross section for $e+H_2O$ [571].

<i>Energy (eV)</i>	<i>Cross section ($10^{-16} cm^2$)</i>
0.001861	430.3
0.005393	325
0.01563	228.4
0.04528	139.2
0.1312	60.71
0.3802	21.11
1.102	6.042
1.989	3.975
3.16	4.334
5.02	5.055
6.909	7.769
9.386	8.529
12.75	9.052
17.32	7.244
23.53	5.15
31.96	3.561
43.42	2.5
70	1.5
100	1

The electron impact ionization cross sections of water vapor plasmolysis have been reviewed using the available experimental data [570, 591,-592]. The recommended values of the ionization cross section for H_2O are presented in Table (4.6).

It was seen that the cross section for OH^+ has a nonzero value at 17.5eV, due to the uncertainty in the energy of the electron beam.

Chapter 4 Water vapour decomposition simulation

Table 4. 6 The recommended ionization cross section for $e+H_2O$ [571].

<i>Energy</i> (<i>eV</i>)	H_2O^+ (10^{-16} cm^2)	OH^+ (10^{-16} cm^2)	H^+ (10^{-16} cm^2)	H_2^+ (10^{-18} cm^2)	O^+ (10^{-18} cm^2)
13.5	0.025				
15	0.126				
17.5	0.272	0.0013			
20	0.411	0.0145	0.0024		
22.5	0.549	0.05	0.0091		
25	0.652	0.0855	0.0207		0.22
30	0.815	0.16	0.0433	0.018	0.37
35	0.958	0.222	0.0759	0.039	0.7
40	1.05	0.264	0.11	0.057	1.32
45	1.12	0.3	0.145	0.07	2.07
50	1.18	0.329	0.178	0.065	2.75
60	1.24	0.364	0.235	0.066	3.94
70	1.27	0.389	0.279	0.069	4.84
80	1.31	0.409	0.317	0.063	5.94
90	1.31	0.412	0.343	0.078	6.66
100	1.31	0.418	0.36	0.075	6.95
110	1.29	0.415	0.37	0.073	7.38
125	1.27	0.412	0.375	0.064	7.63
150	1.21	0.393	0.371	0.077	7.52
175	1.16	0.381	0.366	0.071	7.31
200	1.12	0.363	0.351	0.054	7.07
250	1.01	0.334	0.316	0.05	6.34
300	0.921	0.311	0.284	0.045	5.51
400	0.789	0.266	0.237	0.04	4.34
500	0.696	0.23	0.198	0.032	3.73
600	0.618	0.203	0.172	0.029	3.13
700	0.555	0.185	0.149	0.033	2.71
800	0.502	0.169	0.135	0.022	2.4
900	0.465	0.156	0.12	0.032	2.2
1000	0.432	0.143	0.109	0.024	1.94

Chapter 4 Water vapour decomposition simulation

4.1.5 Reaction mechanism and cross sectional of Model III

Water vapor molecules are decomposed to their elements hydrogen and oxygen gas by the dissociation reaction using DBD plasma. In this model, the reaction mechanism has been proposed by [Fahad et al. \[593\]](#) for water vapor decomposition using DBD plasma is simulated. Water vapor in this model is decomposed to combine O₂ and H₂ molecules after a chain of chemical reactions. [Table \(4.7\)](#) presents the reaction mechanism pathway.

Table4. 7 Reaction mechanism of model III

<i>Reac.</i>	<i>Reaction type</i>	<i>Type</i>	<i>Rate constant(K)</i> <i>[m³/mol-sec, m⁶/mol-sec]</i>	<i>Ref.</i>
1	H ₂ O+e→ H+ OH +e	Dissociation reaction	9.978E+07	[541, 578]
2	H ₂ O+e→ H ⁻ +OH	Ionization reaction	3.706E+07	[541, 583]
3	OH+OH→ H ₂ O ₂	Neutral-neutral reaction	1.02E+07	[578]
4	OH+ H ₂ O ₂ → H ₂ O+ HO ₂	Neutral-neutral reaction	1.02E+06	[578]
5	HO ₂ + HO ₂ → H ₂ O ₂ + O ₂	Surface reaction 1	9.64E+05	[578]
6	HO ₂ +H→ H ₂ + O ₂	Surface reaction 2	3.91E+07	[578]

In model III, we considered reaction (5) and (6) in [Table \(4.7\)](#) as the surface reactions. The reaction mechanism model presents that the water vapor is decomposed to form H, OH and H⁻, then hydroxyl OH combines together to form H₂O₂. Water molecules and HO₂ are produced in reaction (4) then HO₂ reacts together to form H₂O₂ and O₂ molecules, then HO₂ react with H to form hydrogen and oxygen molecules in reaction (5) & (6), respectively.

In this simulated reaction mechanism model, the water vapor molecules are decomposed to produce negative hydrogen (H⁻) ions. Although, the negative hydrogen ions have a weak cross sections due to the dissociative attachment are very small but it is expected to generate a chain of chemical reactions. The recommended cross section of electron attachment of negative hydrogen ions is given in [Table \(4. 8\)](#).

Chapter 4 Water vapour decomposition simulation

Table4. 8 The recommended cross section for H^- production from H_2O [571].

<i>Energy (eV)</i>	<i>Cross section (10-18 cm2)</i>
5.5	0.02
5.74	0.16
5.9	0.985
6.01	4.3
6.1655	6.22
6.286	6.317
6.4	6.37
6.52	6.25
6.65	5.79
6.81	4.89
7	3.56
7.465	1.29
7.69	0.877
7.89	0.74
8	0.79
8.09	0.995
8.14	1.09
8.235	1.166
8.395	1.04
8.79	0.76
9.01	0.62
9.57	0.28
9.8	0.17
10	0.098

4.1.6 Analysis & Simulation Results

4.1.6.1 Simulation results of Model I

In this water vapor decomposition using DBD plasma simulation, the electron temperature, electric potential and the active species density are investigated. As explained in the previous section that model I presented the direct decomposition of water vapor using the DBD plasma to form hydrogen and oxygen molecules. [Figure \(4.4\)](#) shows the evolution of the electric potential at time zero and 0.225 s. It was clear the change of the electric potential between power and ground electrodes due to the positive charges aggregation on the dielectric covering the ground electrode.

Chapter 4 Water vapour decomposition simulation

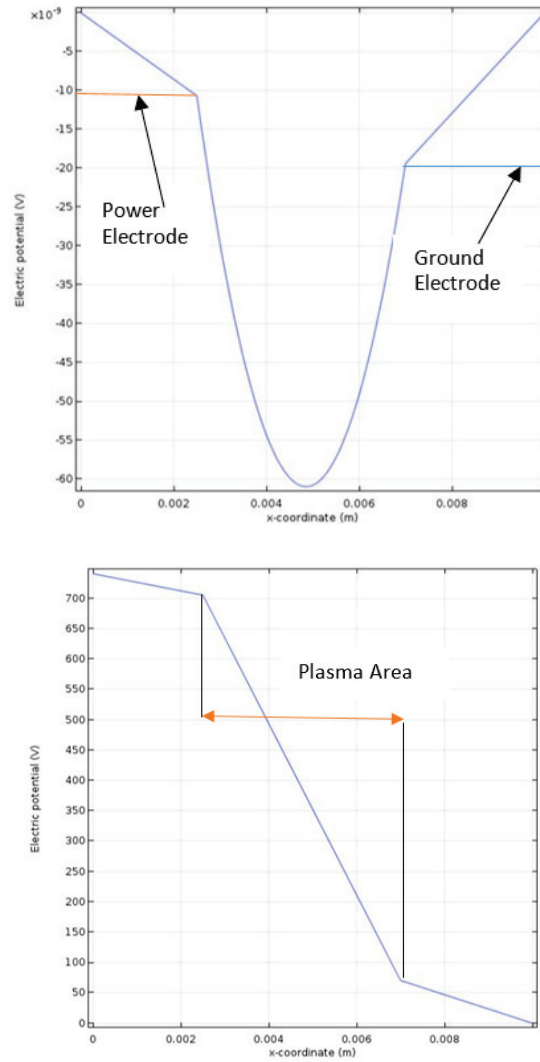


Fig 4.4. electric potential between both electrodes at 0s and 0.225s.

The applied voltage evolutions across the applied plasma discharge gap with distance of (4.5mm) are presented in [Figure \(4.5\)](#) at different times. The electric field and electric potential between both electrodes are indicated in [Figure \(4.6\)](#). It was seen that the electric field is reach to maximum in the gap between power and ground electrodes.

Chapter 4 Water vapour decomposition simulation

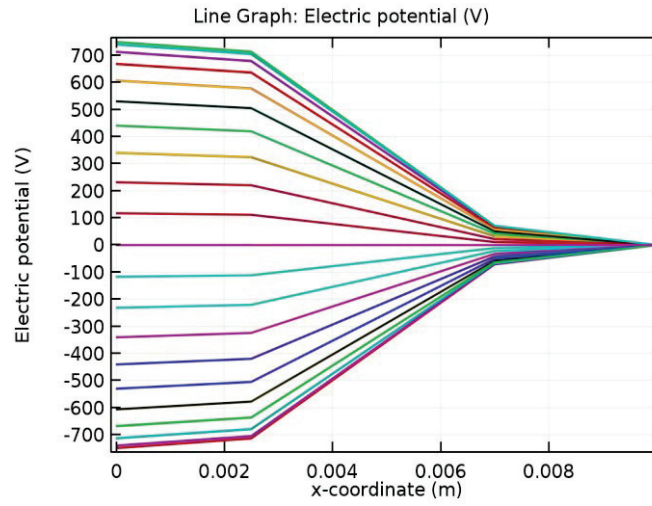


Fig 4. 5 The applied voltage at different times versus the discharge gap.

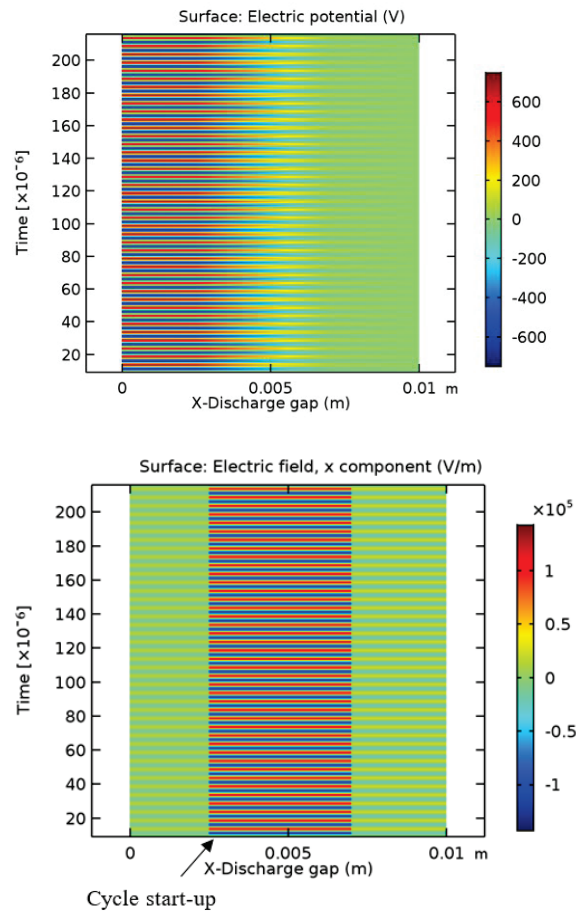


Fig4.6 The electric potential and the electric field versus the discharge gap.

Chapter 4 Water vapour decomposition simulation

The hydrogen mass fraction and the electron density are shown in Figure (4.7). In the first picture the hydrogen mass fraction is presented, it is showed that the mass fraction increased over the time to reach the maximum value of 6.31×10^{-10} . It was observed that the electron density changed twice with the applied voltage positive and negative cycle, the maximum obtained electron density was $3.5 \times 10^8 \text{ m}^{-3}$.

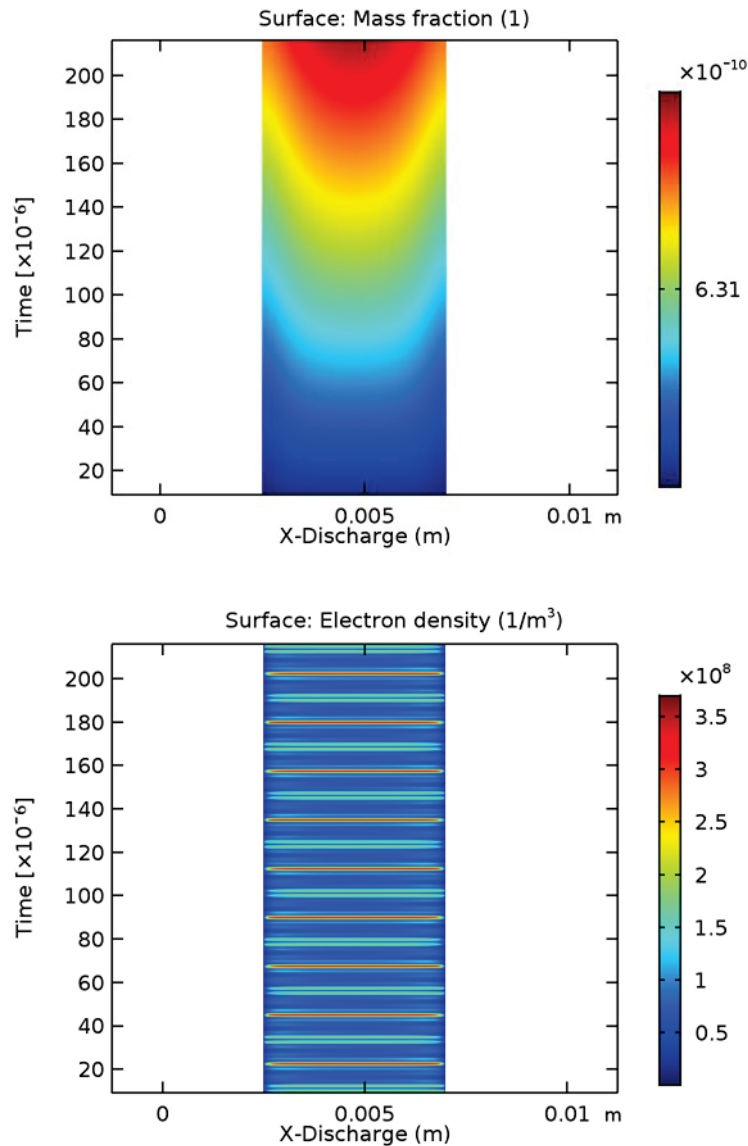


Fig4.7 The hydrogen mass fraction and the electron density versus the plasma discharge gap.

The electron density and electron temperature across the discharge gap at different times are shown in Figure (4.8) and (4.9), respectively. It was observed that the

Chapter 4 Water vapour decomposition simulation

electron density increased with time as well as in the electron temperature. Furthermore, the electron temperature and electron density reach to the maximum value inside the plasma discharge gap.

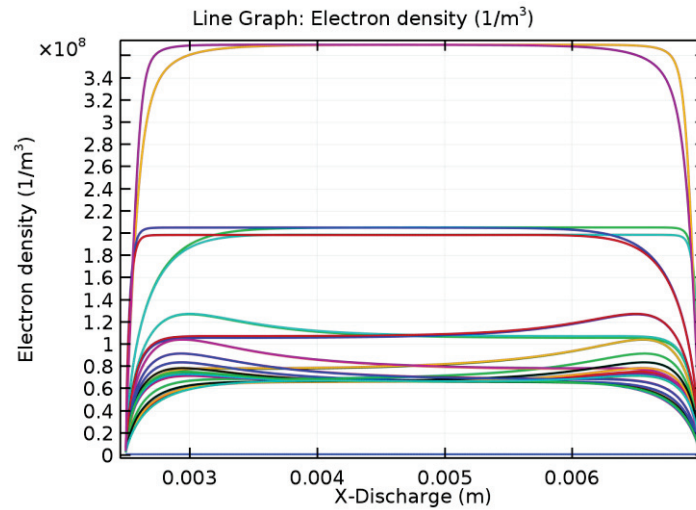


Fig4.8 The electron density versus the discharge gap.

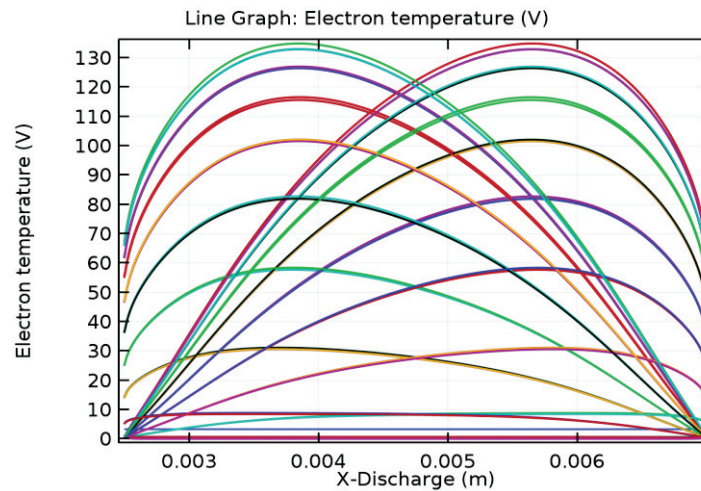


Fig4.9 The electron temperature versus the discharge gap.

Chapter 4 Water vapour decomposition simulation

4.1.6.2 Simulation results of Model II

In this new proposed water vapor dissociation reaction mechanism simulation model II, the boundary conditions are same as model I, the reaction mechanisms pathway are more complicated than the first model, the reaction mechanisms are included H_2O^+ , OH^+ , and O^+ ions. It is considered in model II the unlike chemical reactions dissociation pathway have been explained in the previous section are excluded due to their low probability and high energy requirement [581]. Furthermore, it is expected that the hydrogen molecules produced from this mechanism will be higher than model I (direct water vapor decomposition). The results of the 1-D model II are analyzed by extruding the solution results in two dimensions. The surface plot has been investigated because of it can represents how the variables evolve over time. Figure (4.10) presents the electric potential across the discharge gap over time. The plasma applied voltage is relatively changed in the positive and negative cycles between the power and ground electrode. The electric field and the electric potential are shown in Figure (4.11) as a 2-D plot. It was clear from these pictures that the voltage is relatively uniform, it can more clearly seen in the examining electric field. It was observed that the electric field was much stronger in the plasma reaction area. The active species H_2 mass fraction and the electron density are indicated in Figure (4.12). The hydrogen mass fraction was much higher than that obtained from the model I. Additionally; the excited species have a long lifetime in the plasma gap. The revolution of the electron density inside the gap also is presented in next picture.

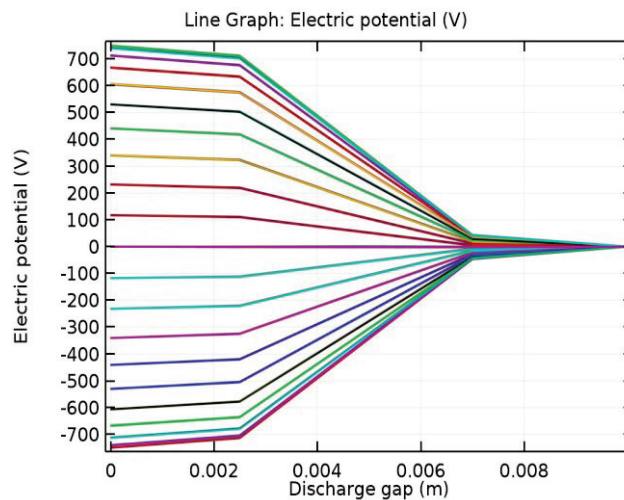


Fig 4.10 The applied voltage over different times versus the discharge gap.

Chapter 4 Water vapour decomposition simulation

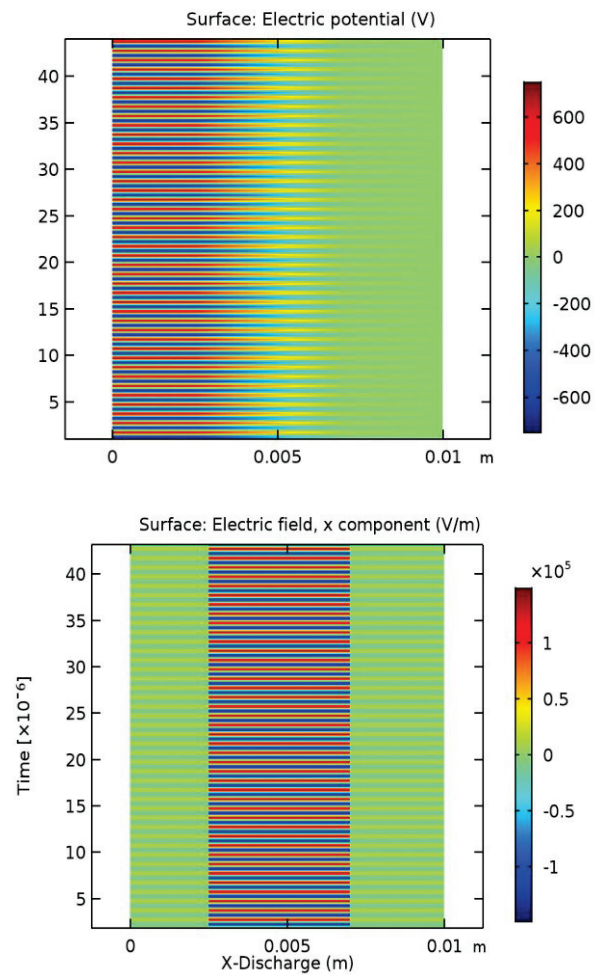
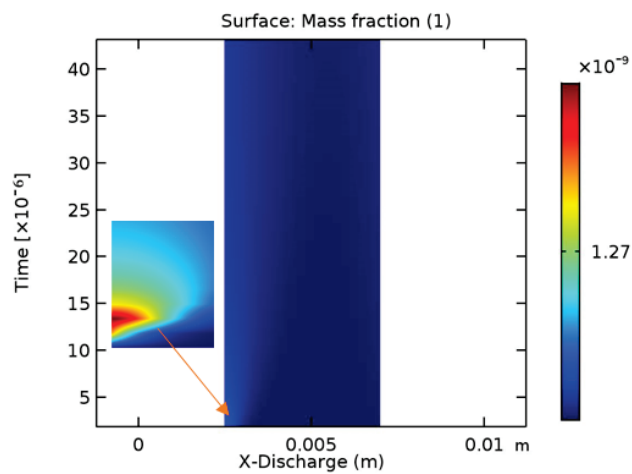


Fig4.11 The electric field and the electric potential versus the discharge gap.



Chapter 4 Water vapour decomposition simulation

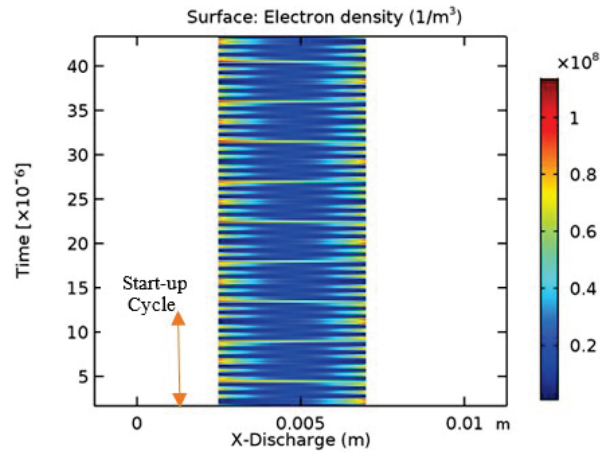


Fig4.12 Model II hydrogen mass fraction and the electron density versus the discharge gap.

The electron density and the electron temperature across the discharge gap are shown in Figure (4.13 & 14), respectively. The electron temperatures are changed across the discharge gap over time to reach the maximum value of 180V.

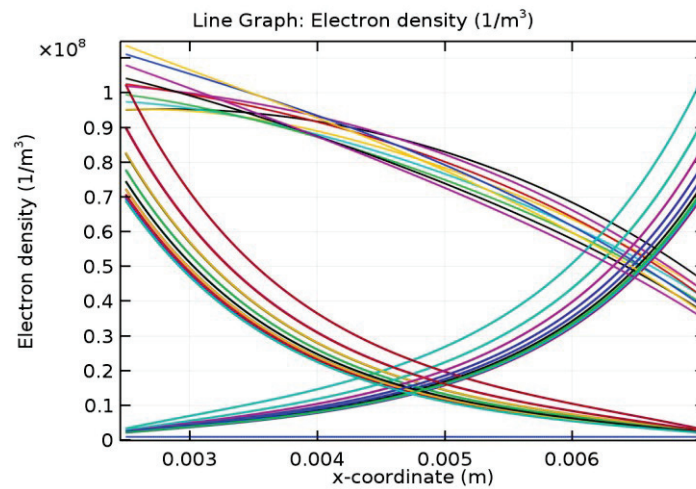


Fig4.13 The electron density versus the discharge gap.

Chapter 4 Water vapour decomposition simulation

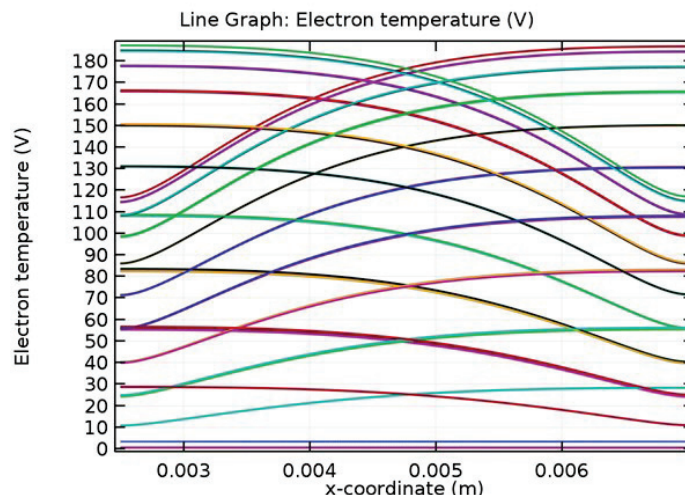


Fig4. 14 The electron temperature versus the discharge gap.

4.1.6.3 Simulation results of Model III

This model simulates the water vapor plasmolysis reaction mechanisms have been proposed by [Fahad et al \[593\]](#). The water vapor molecules electrical breakdown are very complicated process, the dielectric plasma was formed inside the discharge gap at atmospheric pressure. The boundary conditions of this model are same as the previous models and the plasma is generated in the plasma gap (4.5mm). This one dimensional simulation is considered the first trail for water vapor decomposition using DBD plasma in the plate type reactor. This model reaction mechanisms pathway includes negative hydrogen ions (H^-). The simulation results were implemented using a 2-D plot. [Figure \(4.15\)](#) shows the applied voltage change across the discharge distance in the negative and positive cycles.

Chapter 4 Water vapour decomposition simulation

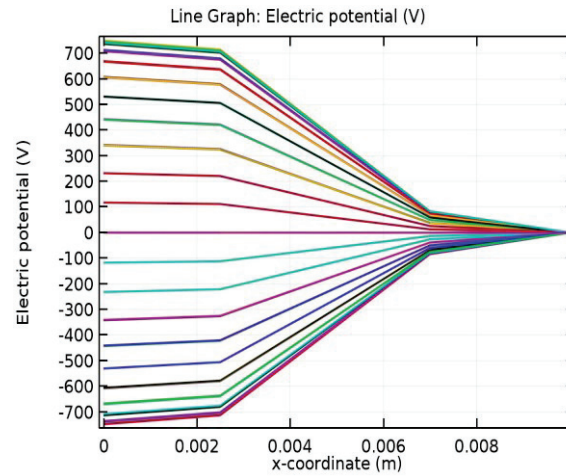


Fig4. 15 Model III applied voltage over different times versus the discharge gap.

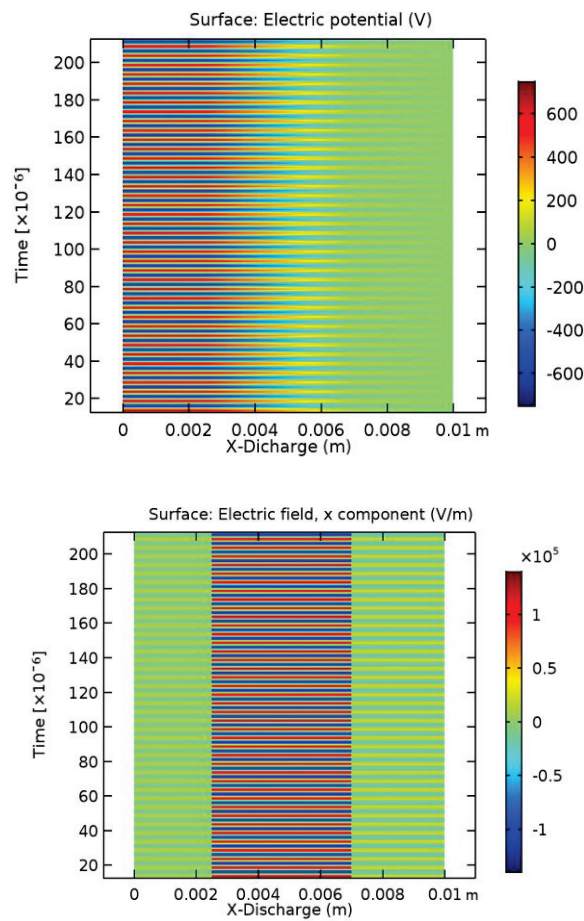


Fig4.16 Model III electric field and the electric potential versus the discharge gap.

Chapter 4 Water vapour decomposition simulation

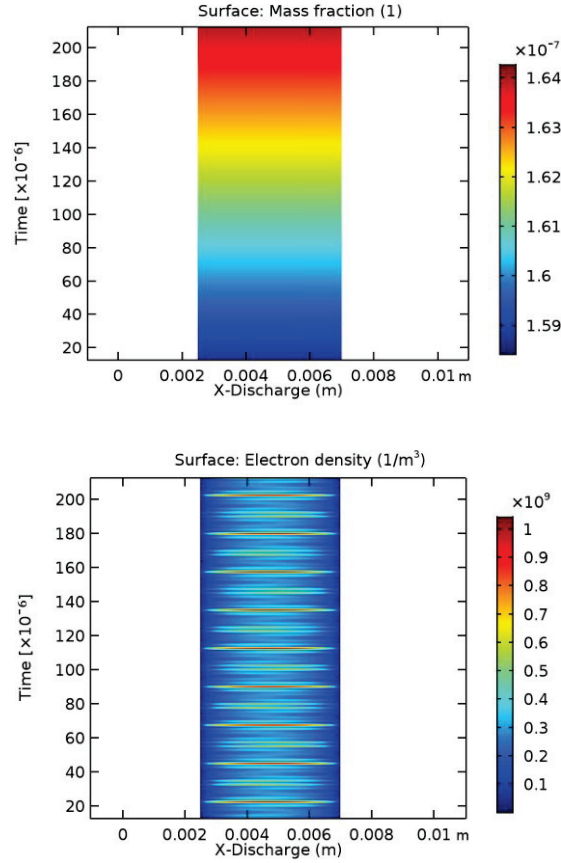


Fig4. 17 Model II hydrogen mass fraction and the electron density versus the discharge gap.

Also, the applied voltage of model III is clearly seen uniform in the 2-D picture in [Figure \(4.16\)](#). For more investigation of the effective area of the applied plasma, it can be seen in the electric field picture across the plasma discharge gap. In this model the electron collision cross section of H^- production from water vapor was utilized. The produced hydrogen molecules from the water vapor dissociation mechanism using DBD plasma in model III are presented in [Figure \(4.17\)](#). It can be observed that the hydrogen produced from model III is much higher than that obtained from model I and model II. Furthermore, the produced hydrogen molecules mass fraction increased with the time to reach value of 1.64×10^{-7} . The electron density evolutions are depicted in the next picture of [Figure \(4.17\)](#) versus the discharge gap distance. It was seen that the discharge cycle changed twice, one in the positive and the other in negative half cycle. The electron density and electron temperature change across the discharge gap distance are shown in [Figure \(4.18& 19\)](#), respectively. It was observed

Chapter 4 Water vapour decomposition simulation

that the maximum electron density values at the discharge gap center. The electron temperature revolution graph was clearly indicated the discharge cycles change over the time.

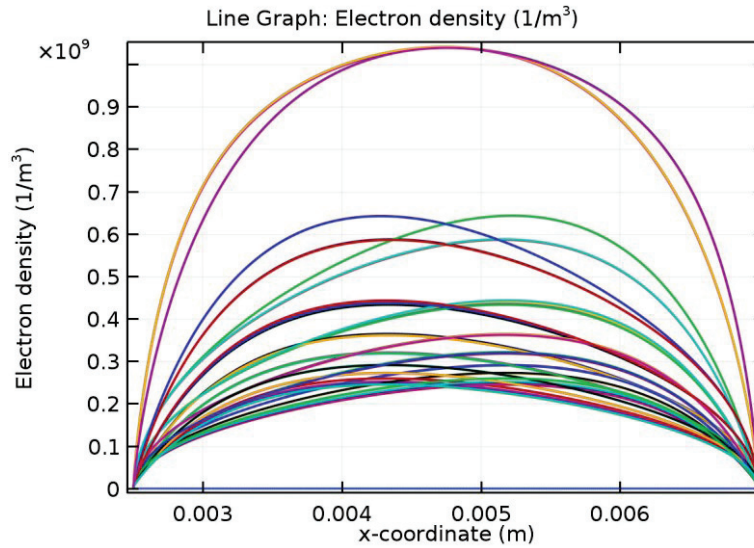


Fig4. 18 The electron density versus the discharge gap.

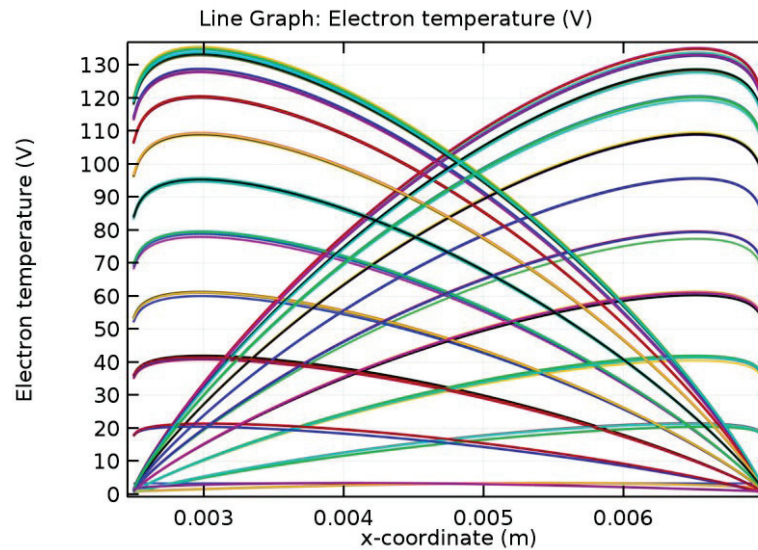


Fig4.19 The electron temperature versus the discharge gap.

Chapter 4 Water vapour decomposition simulation

4.1.7 Comparison and discussions between models

A comparison between three models was developed in Figure (4.20) for the produced hydrogen molecules mass fraction. To compare the available data of three models log scale was used. It was clear that the model III hydrogen mass fraction was much higher than that obtained from model II and model I. Further, the hydrogen mass fraction of model II was higher than model I. It can be observed that the water vapor dissociation reaction mechanism pathway in the model III has much higher hydrogen production molecules. This simulation results have a good agreement with [Fahad et al. \[593\]](#) recommendation for water vapor decomposition reaction mechanisms pathway using DBD plasma.

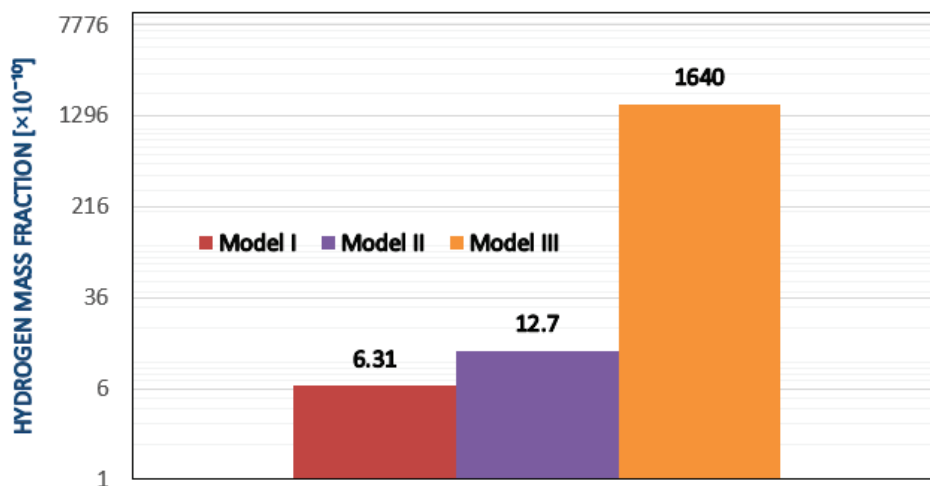


Fig 4. 20 Comparison between three models for H_2 mass fraction.

Conclusion

Hydrogen production from water vapor using plasma has a great interest as a good solution for environmental issues. Further, the dielectric barrier discharge (DBD) is considered the simplest method to produce plasma at low gas temperature and atmospheric pressure. This simulation was carried out to study the DBD plasma characteristics and the densities of species using COMSOL Multiphysics package. Three models with different water vapor dissociation reaction mechanisms pathway were investigated. In the first model, the direct water vapor decomposition reaction was utilized; it was revealed that the hydrogen mass fraction increased across the plasma discharge gap over the time. More complicated reaction mechanism pathway in model II has been simulated included H_2O^+ , OH^+ , and O^+ ions, the electron collision

Chapter 4 Water vapour decomposition simulation

cross sections have been prepared. It was observed that the produced H_2 molecules from model II was higher than model I. The electric potential and electric field across the discharge gap were simulated. It was found that the electric potential and electric field showed a significant changes inside the gap between the power and ground electrodes due to the charged species and plasma effect. The proposed and recommended water vapor plasmolysis dissociation model by [Fahad et al \[593\]](#) has been simulated in model III. This model reaction mechanism pathway introduced H^\cdot radical, the electron collision cross section of produced H^\cdot from water vapor plasmolysis was utilized. It was seen that H^\cdot radical controlled the H production by the electron detachment and H_2 was mainly produced from the reaction between HO_2 and H species. It was seen from the reaction kinetic modelling that $H-H$ atom recombination wasn't the responsible for H_2 production. One of the most interesting simulation results was the growing of the H_2 mass fraction over time, additionally; it was found that the produced hydrogen molecules from model III were higher than model II and model I. The electron density and electron temperature evolution of these models were investigated across the plasma gap versus time. From the simulation results it was clear that model III water vapor reaction mechanisms pathway was better than model II and model I.

Chapter 4 Water vapour decomposition simulation

4.2 Comprehensive assessment of hydrogen production in argon-water vapours plasmolysis

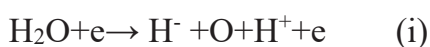
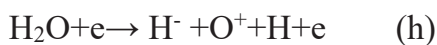
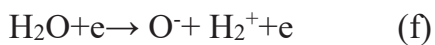
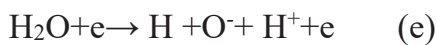
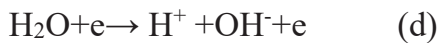
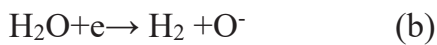
In the last decades, there is a high interest to reduce greenhouse gases (GHGs) by replacing the conventional fossil fuels with good alternative fuel [79, 594-598]. Hydrogen is considered the most important solution to overcome global environmental issues [599, 600]. Hydrogen can be generated by different technologies such as steam reforming, water electrolysis, etc. [80, 324]. These studies showed that 90% of the available hydrogen gas in the market was produced by the steam methane reforming method and the remaining amount of hydrogen is produced by water electrolysis and coal gasification [601]. The decomposition of water vapour using DBD plasma is not considered as a hydrogen production energy efficient method [562]. However, hydrogen production using plasma technology has shown a lower cost compared to the water electrolysis method [532]. However, the hydrogen production from plasma offers low power requirement and it can be electronically controlled better than the other processes [593, 602]. The hydrogen production by plasma has been theoretically and experimentally investigated in previous studies [322, 333, 344, 531, 593]. The preliminary results of hydrogen production from water vapour by DBD plasma has been investigated [337]. The hydrogen production from water vapour plasmolysis has shown higher energy efficiency than previous studies [532, 562]. Furthermore, hydrogen can produce from plasma using a different feedstock such as water, methane and hydrogen sulfide [344, 531, 538, 562, 603-605]. The chemical conversion and synthesis analysis after applied the DBD plasma have been studied [606-609]. The decomposition of gases using DBD plasma can be operated at low cost: atmospheric pressure, low input gas temperature, and fast conversion [610-612]. Furthermore, the gas treatment by DBD plasma results in low energy efficiency due to plasma input power, additionally plasma electrodes and barriers [613]. However, the water vapour decomposition to their elements H_2 and O_2 gases using DBD plasma would increase with a high wall temperature. In the discharge zone of the DBD plasma, high-energy electrons can be generated in the discharge zone. The DBD plasma reaction efficiency is suggested to improve by adding a dilution gas such as Ar, He, and N_2 , it allows increasing the reaction opportunity between activated dilution molecules and the reactant molecules. Also, this method can be considered as a different way to get the plasma reaction performance [614-619]. In this work, a detailed study of the simulation and experimental analysis of hydrogen production from the Ar- H_2O mixture as a function in DBD plasma applied voltage is investigated. The effect of the dissociative attachment reaction (H^-) on Ar- H_2O decomposition kinetics mechanism was simulated. Argon is used as a dilution gas, the simulation and experimental results of

Chapter 4 Water vapour decomposition simulation

the effect of Ar flow rate on the produced H₂ concentration at different plasma voltage are compared. Also, the input water vapour temperature and flow rate effects on H₂ production are also investigated. Furthermore, the present work was compared to the previous results of water vapour plasmolysis at different reactor heating temperatures [337] with the current study results of dilution argon gas effect on hydrogen production.

4.2.1 Simulation model description

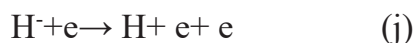
The simulation analysis of argon-water vapour plasmolysis is carried out by combining the water vapour plasmolysis reaction model and argon reactions [593,620]. Rehman et al [593] model is the basis model of this DBD simulation study, additionally same initial conditions are assumed like electron temperature (Te) of 3 eV. Moreover, the electron density in range of 1×10^{18} - $1 \times 10^{20} \text{ m}^{-3}$ was used in DBD plasma [621]. The dissociative attachment and dissociation reactions are selected in this simulation study. The simulated water vapour plasmolysis reaction model is shown in Table (4.9). The overall kinetic modeling of water vapour plasma has been investigated [344, 562]. Also, it has been reported that the dissociative attachment reactions producing negative radicals species (OH⁻, H⁻ and O⁻) because of their weak cross sections and electron energies of 6–12 eV [577]. Furthermore, the rates of negative ions production from water vapour plasmolysis are very small and less than 1%. The negative ions production from dissociative attachment reactions pathway of water vapour discharges were described as follow [577, 581]:



A mathematical model of the chemical reactions of water in the discharge channel has been described as the output hydrogen molecular and the stoichiometric radical's

Chapter 4 Water vapour decomposition simulation

generation of H_2 , O_2 , and H_2O_2 [576]. Furthermore, H_2O_2 is considered unstable molecule at the typical plasma conditions. However, it has been reported that H_2O_2 could be produced in low temperature water plasma especially if the process is carried out at supersonic flows [344]. Although, H_2O_2 radical has low predicted concentration and it could be neglected, but it is being discussed because the overall reaction mechanism kinetics process were affected with the reactions included H_2O_2 and the same were found for HO_2 , OH and H . Additionally, the following radicals have been shown by optical emission spectroscopy OH and H , while H_2 and H_2O_2 have been detected by chemical methods [587]. The non-thermal plasma processes are started including a high electric field, ultraviolet radiation and shock waves, and the formation of new reactive radicals such as hydrogen atom- H , hydroxyl- OH , and oxygen- O which are reacted with each other's and starting a chain of the chemical activity reactions [587]. It was reported that the initiation of water vapour dissociation pathway with the dissociative attachment reaction formed negative hydrogen ions (H^-) will participate to initiate reactions with other water molecules [593]. The simulation reaction mechanism is initiated with the dissociative attachment reaction producing negative H^- and OH radicals to combine with electron producing H radical [585];



The extra electron produced from electron detachment reaction will participate in starting a chain of water dissociation process reactions. In this study, the argon effect on hydrogen production from water vapour plasmolysis is investigated and compared with the experimental results. The simulation kinetic model has been carried out using COMSOL MultiphysicsTM reaction engineering laboratory (REL) [585]. It was seen that this package can provide an automatic sensing of stiff systems and an adaptive time-stepping algorithm with a tolerance of 10^{-6} [582]. Also, the simulation analysis is carried out with and without the dissociative attachment reaction to investigate the effect of (H^-) on the hydrogen production from the water vapour. Furthermore, the simulation and experimental results are compared at different plasma applied voltage. The plasma applied voltage is input to the simulation model as a function of plasma charge which is determined as a function of the plasma current and reaction time. The effect of the input water vapour flow rate and temperature on the hydrogen production are simulated and compared with experimental results.

Chapter 4 Water vapour decomposition simulation

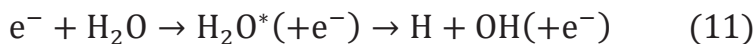
Table 4.9 Simulated reaction mechanism.

No.	Reaction	Type	Rate constant(K) [m ³ /mol-sec, m ⁶ /mol- sec]	Ref.
1	H ₂ O+e ⁻ → H+ OH +e ⁻	Dissociation reaction	9.978E+07	[541, 578]
2	H ₂ O+e ⁻ → H ⁻ +OH	Dissociative attachment	3.706E+07	[541, 583]
3	OH+OH→ H ₂ O ₂	Neutral-neutral reaction	1.02E+07	[578]
4	OH+ H ₂ O ₂ → H ₂ O+ HO ₂	Neutral-neutral reaction	1.02E+06	[578]
5	HO ₂ + HO ₂ → H ₂ O ₂ + O ₂	Surface reaction 1	9.64E+05	[578]
6	HO ₂ +H→ H ₂ + O ₂	Surface reaction 2	3.91E+07	[578]

The excitation and ionization reactions (7), (8) of plasma-Ar reactions can be described as follow [622-624]:



It is reported that these produced radicals interact with water vapour through the following reactions (9–11) [620],



4.2.2 Experimental setup and methods

A schematic diagram of the experimental setup is given in figure (4.21). The dielectric barrier discharge (DBD) Plasma is generated between high voltage and ground electrodes in the plate type reactor (PTR) reaction volume of 3.969 cm³ and in electrode gap distance of 4.5 mm. The sine wave frequency of 10 kHz is applied for plasma ignition at a high voltage range of 8–18 kV at DBD plasma power ranges of 82–120 W, respectively. A quartz glass part is used to insulate between both electrodes. The high voltage electrode is installed on the top center of the reactor over

Chapter 4 Water vapour decomposition simulation

the glass part. The ground electrode is connected into the base plate and the dissociation of water vapour occurred between both electrodes. The water vapour is produced by a steam generator at a temperature range of 523–623 K, pressure of 100 kPa, and flow rate in ranges of 0.075–0.125 mol/min. The distilled water was prepared and fed into the steam generator. The water vapour is injected combining with Ar gas inflow rates range of 0.01–0.025 mol/min. In this study, the PTR is not heated and the water vapour is mixed inside the steam generator and then fed into the reactor. In this experiment, the effect of Ar gas flow rates on the hydrogen production from water vapour plasmolysis is analyzed at different applied voltage. The outlet gases are separated in an ice trap. The feeding gas mixture was included water vapour and the dilution gas was Ar gas with a purity of 99.99%, which was flowed into the plasma discharge gap zone by the mass flow controller. The temperature of water vapour is settled using the steam generator device while the plasma applied voltage is controlled by a high voltage controller (variac). Furthermore, the gas samples are collected in a 0.5 mL syringe, and then the samples are analyzed using the single-phase gas chromatography (GC). The outlet gas concentrations were measured using GC model type of GC-2014S, SHIMADZU. Furthermore, the calibration of the GC is performed before starting the gas samples analysis using standard gas concentrations and the GC error is estimated within a range of $\pm 5\%$. It was reported that the H_2 generation studies have been successfully quantified by the single gas phase chromatography (GC) analysis [531, 538]. The measurements and the analysis of the outlet gas concentrations of all experimental conditions were repeated two times at the same conditions. The simulated hydrogen peak intensities concentrations are compared with the experimental GC results of Ar– H_2O mixture. The morphology and kinetics of He and Ar– H_2O using DBD plasma have been investigated [625], it was focused on the OH and H_2O_2 production using DBD plasma. The mixing process of Ar– H_2O is achieved inside the steam generator, after finishing the mixing process the mixture gas was sent to the PTR and the plasma ignition was initiated after 10 min. The total input gas mixture flow rate to the PTR was constantly kept according to all experimental conditions. The high purity argon was utilized and the flow rate was controlled by the mass flow controller. The DBD plasma ignition images of water vapour dissociation with and without argon gas are shown in figure (4.22). The images of the plasma applied voltage of 12 and 14 kV. This figure shows a uniform plasma ignition by combining argon gas with water vapour compared to the plasma ignition with water vapour only at the same plasma applied voltage. The concentration of the microdischarges was mostly found near to the high voltage electrode surface. Moreover, three current pulses of filament microdischarges were breakdown at each half cycle. However, the filamentary discharges are randomly generated along with the dielectric electrode surface. Also, it was found that plasma ignition is filled the PTR reaction volume with the filaments. It has been reported that filamentary

Chapter 4 Water vapour decomposition simulation

structure depending on the plasma ignition frequency [626]. They found that more filaments at a frequency of 10 kHz than at 1 kHz. This study focused on the hydrogen production from Ar-H₂O mixture theoretically and experimentally at different input water vapour temperature and plasma conditions. The addition of the dilution gas such as argon gas to the water vapour stream is suggested to improve the DBD plasma reaction efficiency.

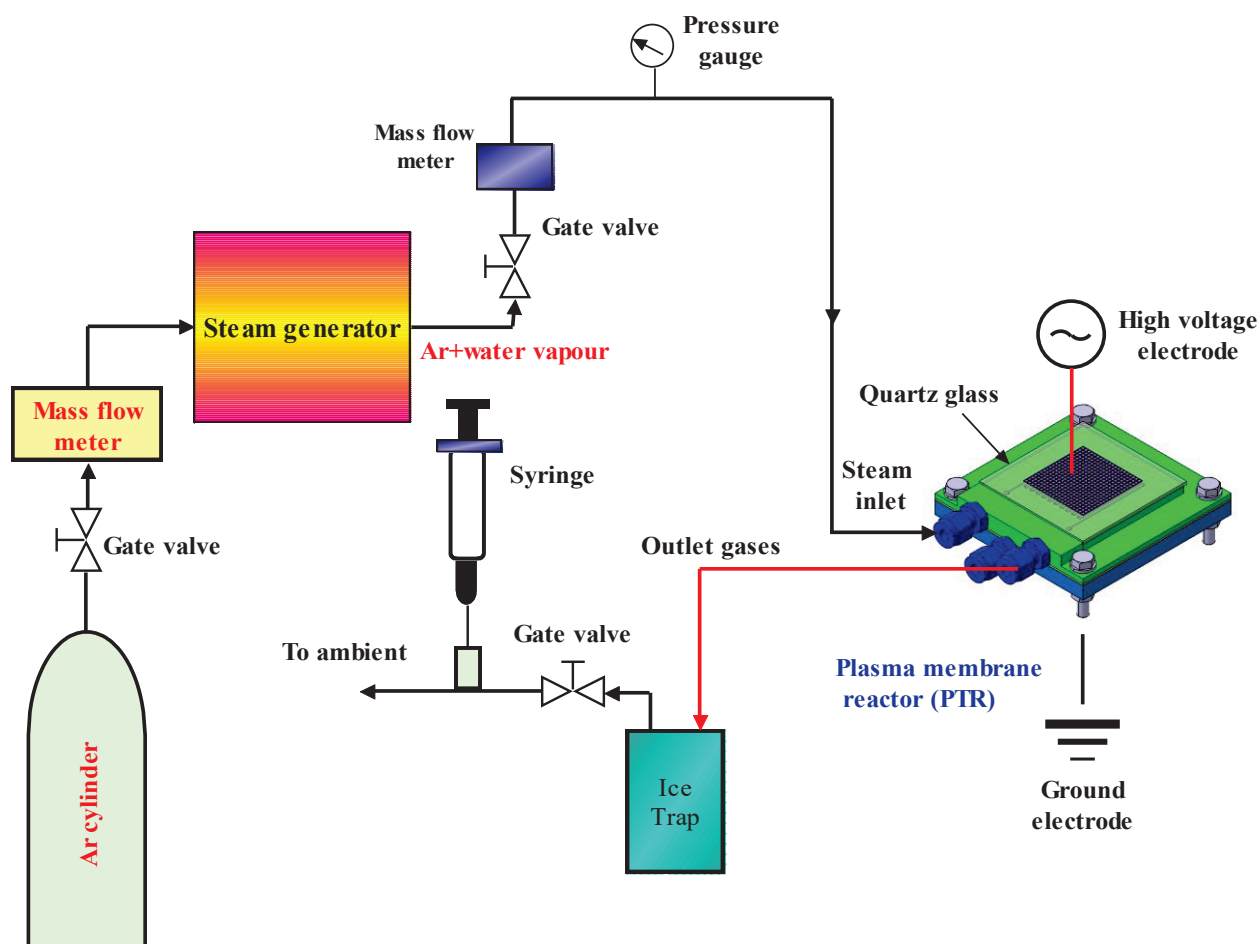


Fig. (4.21). Schematic diagram of the PTR experimental setup.

Chapter 4 Water vapour decomposition simulation

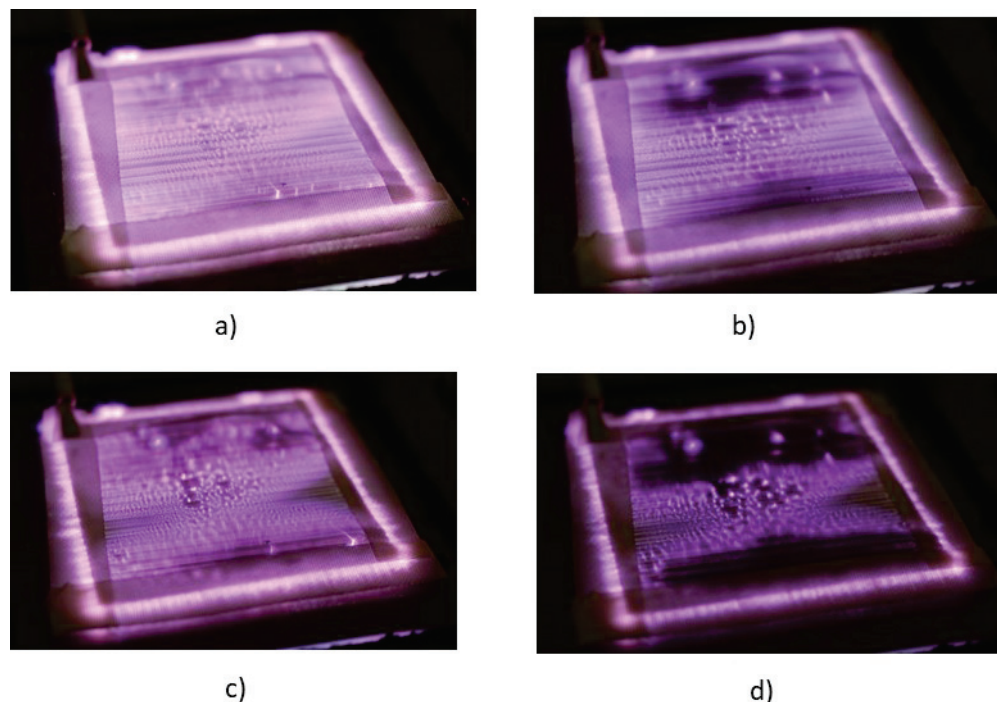


Fig. (4.22). Plasma ignition at different plasma voltage and with and without Ar gas: a) Water vapour +Ar at 14 kV, b) Water vapour +Ar at 12 kV, c) Water vapour only at 14 kV, and d) Water vapour only at 12 kV.

4.2.3 Results & discussions

4.2.3.1 The effect of Ar gas on H_2 production

In this simulation study, Argon gas is added to the water vapour stream reactions. The simulation has been carried out using the suggested model by Fahad et. al [593]. Also, the effect of the dissociative attachment reaction (H^- radical) on hydrogen production from water vapour plasmolysis was investigated. The experimental results of the effect of argon gas on the water vapour dissociation using DBD plasma at different plasma applied voltage are shown in figure (4.23). The water vapour was mixed with pure argon gas before injected into the PTR at argon flow rate in a range of 0.010–0.025 mol/min. Furthermore, the water vapour flow rate was constantly injected at 0.0755 mol/min for all experiments and the plasma input power range of 82–120 W at applied voltage range of 8–18 kV were utilized. From this figure, it was found that the hydrogen concentration increased with increasing the argon gas flow rate. Also, the concentration of hydrogen gas increased with the plasma applied voltage increased. It can be found that this method of the different levels of the input dilution argon gas changed the physics of the plasma discharge and improve the

Chapter 4 Water vapour decomposition simulation

efficiency of the plasma reaction; the dilution gas increased the reaction opportunity between activated dilution argon gas molecules and reactant molecules.

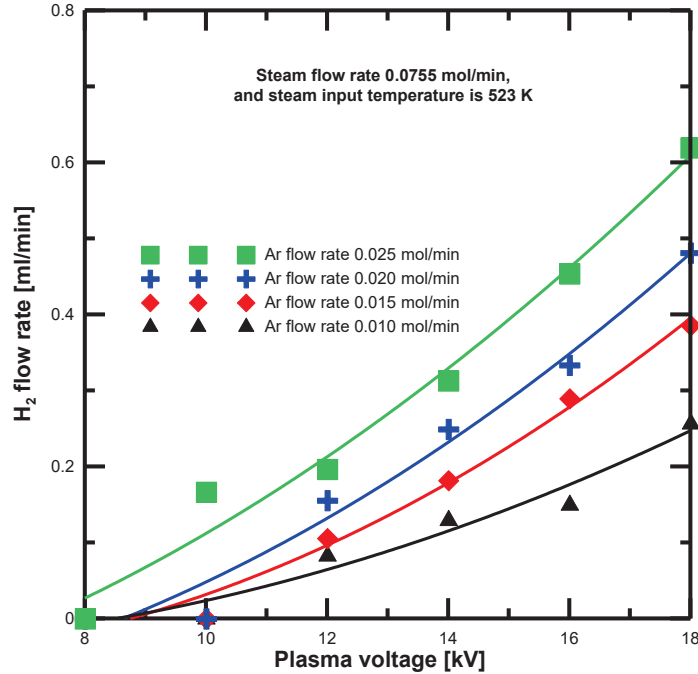


Fig. (4.23). Experimental results of the effect of Ar gas flow rate on the H₂ production from water vapour plasmolysis.

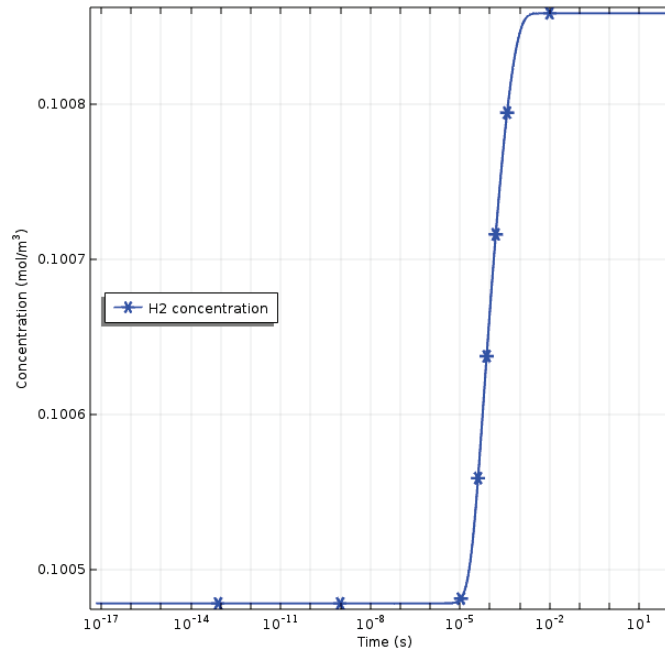
The Ar–H₂O simulation results of the reaction model with and without the dissociative attachment reaction are presented and also discussed in this section. The concentration results of H₂, H₂O, and H₂O₂ are compared for both models. The residence time in the PTR reactor could be set such that $\tau_{\text{reaction}} = \tau_{\text{residence}}$ by selecting a suitable combination of superficial velocity and characteristic length of reactor [626]. Figure (4.24) represents the hydrogen concentration with the plasma reaction time of both simulated models at the same input conditions. It was found that the hydrogen concentration of the simulated model with the dissociative attachment reaction was lower than that obtained from the simulated model without selecting the dissociative attachment reaction. It has been reported that the H₂ concentration produced from the water vapour dissociation pathway dropped by selecting of the dissociative attachment reaction [593]. Figure (4.25) indicates to the H₂O concentration results from both models. It was clear that the H₂O concentration reaches zero in the simulation model without H[•] radical while in the simulated model selecting the H[•] radical showed that the water vapour has a value as a reaction product. It was remarkable that the simulation model selecting the dissociative attachment reaction was more reliable to the experimental results due to some of the separated H₂ and O₂ gas were recombined and condensed inside the ice trap. The H₂O₂ production reaction was described in table

Chapter 4 Water vapour decomposition simulation

(4.9), while the destruction reactions of H_2O_2 can be described in table (4.10). The main source of H_2O_2 production in the absence of oxygen- O_2 was the recombination of the hydroxyl radicals- OH [628, 629]. The losses and destruction of H_2O_2 have been reported in four contributions: electron dissociation reactions, H_2O_2 removal through the gas flow, the diffusion to both electrodes, and H_2O_2 reactions with produced radicals such as OH , H , and O , [625], additionally the losses of H_2O_2 through the glass part has been registered much smaller than the loss due to the smaller area of the glass.

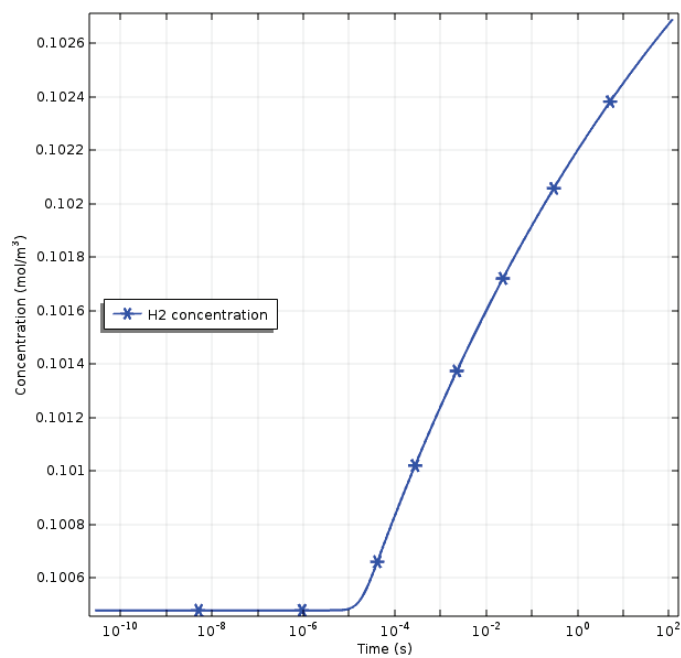
Table4.10 Destruction reactions for H_2O_2 , k rate coefficient $\text{m}^3.\text{s}^{-1}$, $\text{m}^6.\text{s}^{-1}$, and T_e electron temperature (eV).

No.	Reaction	Rate coefficient k	Ref
12	$\text{OH} + \text{H}_2\text{O}_2 \rightarrow \text{H}_2\text{O} + \text{HO}_2$	1.73×10^{-18}	[630]
13	$\text{H} + \text{H}_2\text{O}_2 \rightarrow \text{H}_2\text{O} + \text{OH}$	5.4×10^{-20}	[631]
14	$\text{H} + \text{H}_2\text{O}_2 \rightarrow \text{HO}_2 + \text{H}_2$	6.3×10^{-21}	[631]
15	$\text{O} + \text{H}_2\text{O}_2 \rightarrow \text{HO}_2 + \text{OH}$	2.2×10^{-21}	[630]
16	$\text{e} + \text{H}_2\text{O}_2 \rightarrow \text{H}_2\text{O} + \text{O}^-$	$1.57 \times 10^{-16} T_e^{-0.55}$	[632]
17	$\text{e} + \text{H}_2\text{O}_2 \rightarrow \text{OH} + \text{OH}^-$	$2.7 \times 10^{-16} T_e^{-0.5}$	[632]
18	$\text{e} + \text{H}_2\text{O}_2 \rightarrow 2\text{OH} + \text{e}$	$f(T_e)$	[633]
19	$\text{e} + \text{H}_2\text{O}_2 \rightarrow \text{H} + \text{HO}_2 + \text{e}$	$f(T_e)$	[633]



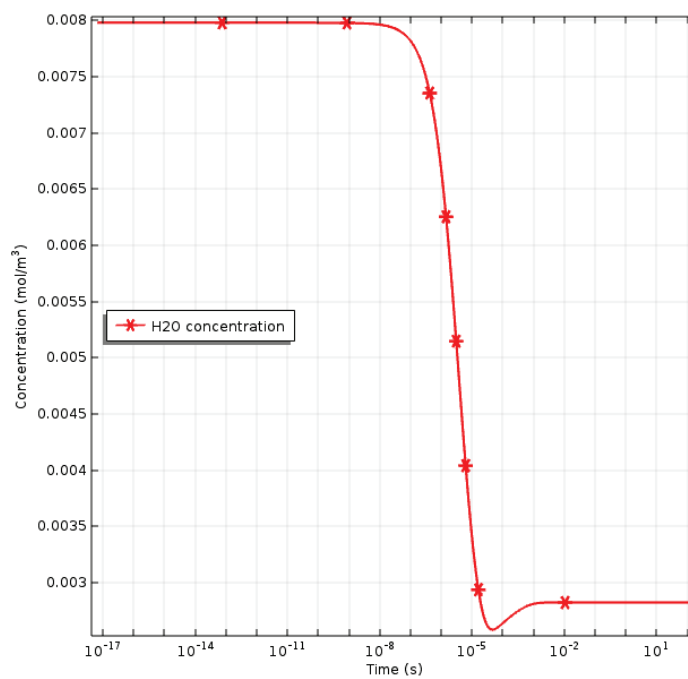
(a)

Chapter 4 Water vapour decomposition simulation



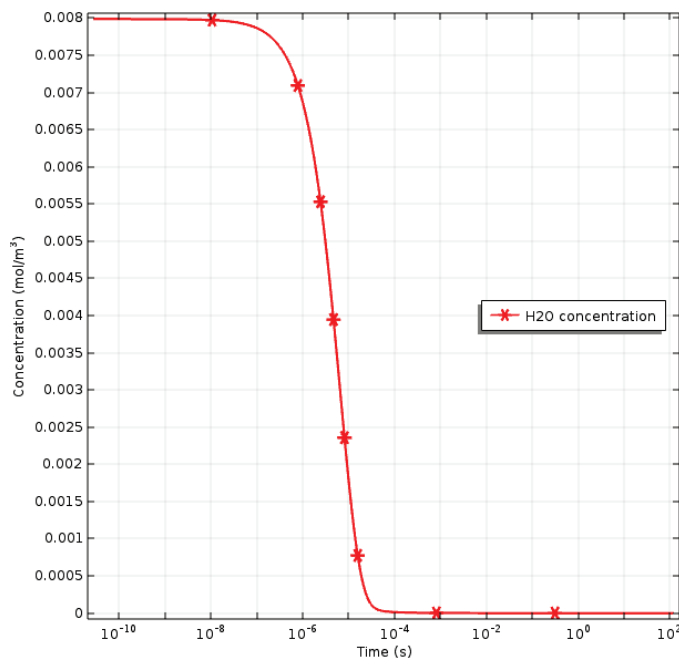
(b)

Fig. (4.24). Simulated Hydrogen concentration versus reaction time a) simulation model with H⁻ radical and b) Simulation model without H⁻ radical.



(a)

Chapter 4 Water vapour decomposition simulation



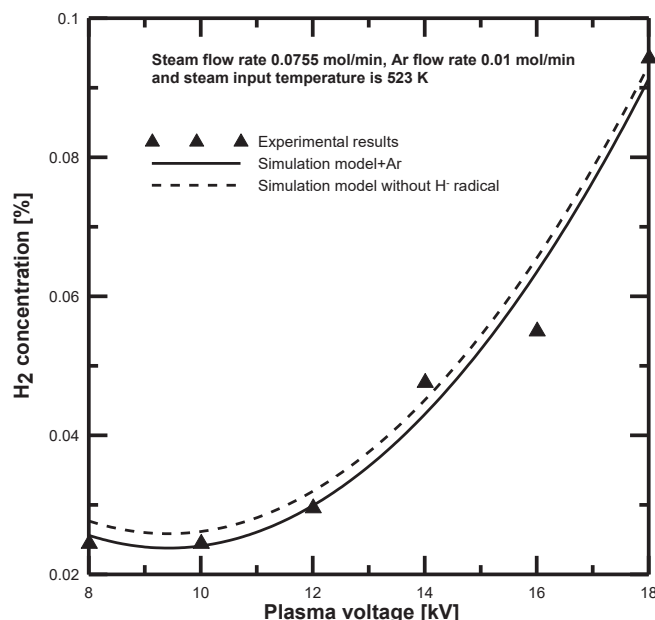
(b)

Fig. (4.25). Simulated H₂O concentration versus reaction time a) simulation model with H⁻ radical and b) Simulation model without H⁻ radical.

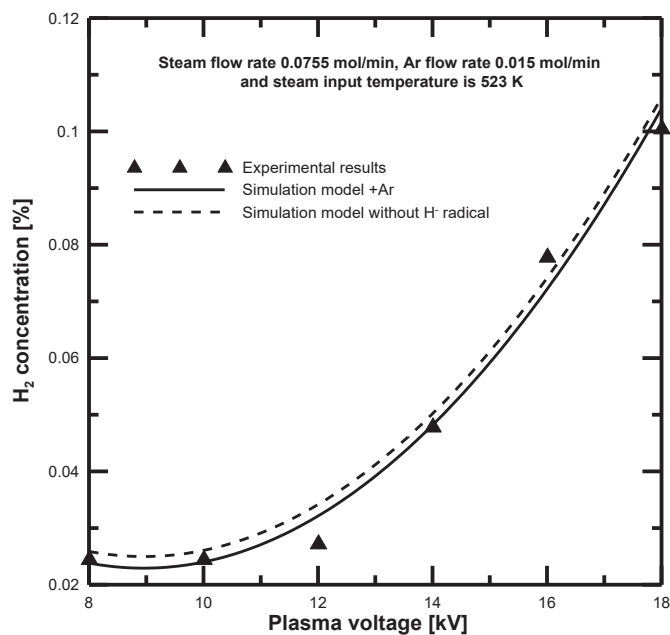
A comparison between simulation and experimental results of Ar-H₂O model with and without the dissociative attachment reaction (H⁻) was investigated at different argon gas flow rates. Figure (4.26) shows the hydrogen concentration results of the water vapour dissociation at different argon feeding flow rates in a range of 0.010–0.025 mol/min and a plasma input power range of 82–120 W were measured at applied voltage range of 8–18 kV. The feeding water vapour flow rate and temperature were remained constant at 0.0755 mol/min, 523 K, respectively for all Ar-H₂O experimental conditions. It was found that argon gas was revealed the hydrogen concentration results from water vapour by DBD plasma. Also, it was observed that the plasma applied voltage has a positive effect on the H₂ production from water vapour, the concentration of H₂ increased with the plasma voltage increased. Furthermore, the effect of the dissociative attachment reaction (H⁻) on the H₂ concentration results from Ar-H₂O simulation models was investigated by selecting and deselecting the dissociative attachment reaction in both models. It was found that the H₂ concentration results of the simulation model selecting the dissociative attachment reaction were more acceptable and near to the H₂ concentrations of the experimental results. These results were confirmed the results described before in this paper literature about the effect of the dissociative attachment reaction which decreased the produced hydrogen gas in water vapour plasma

Chapter 4 Water vapour decomposition simulation

dissociation [593]. Also, other electron impacts of water vapour breakdown pathways are not included in the current study such as dissociative ionization reaction, ionization reactions, and dissociative excitation because it has been reported that the concentrations of species with the plasma reaction time scale did not change.

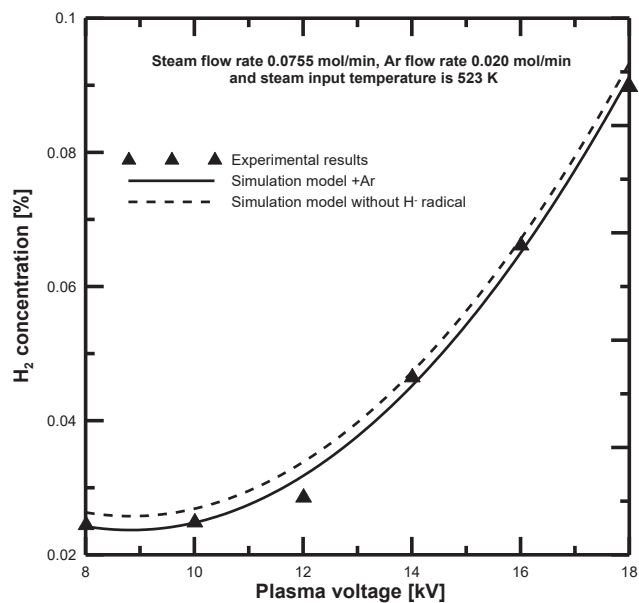


(a)

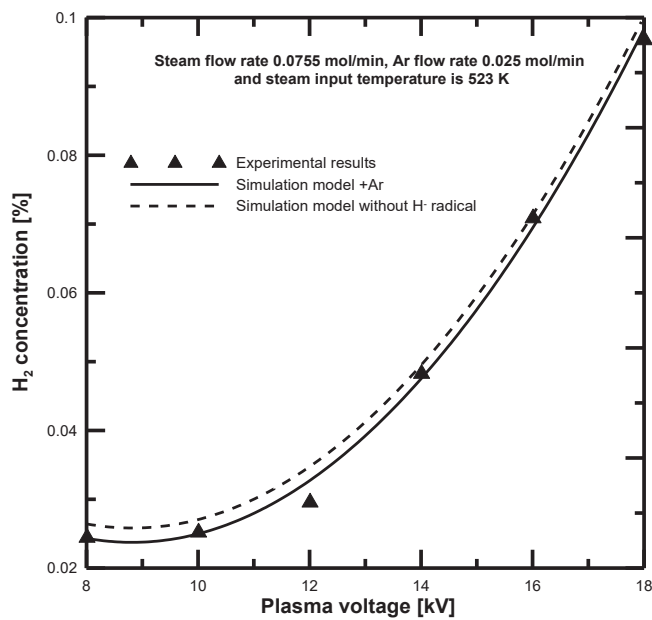


(b)

Chapter 4 Water vapour decomposition simulation



(c)



(d)

Fig. (4.26). Comparison between H₂ concentration results of both simulated models with experimental results are presented in a), b), c), and d).

Chapter 4 Water vapour decomposition simulation

4.2.3.2 The effect of input water vapour temperature and flow rate

The water vapour temperature was adjusted and controlled by the steam generator according to the experimental conditions. The steam generator temperature calibration accuracy was ± 0.5 °C. To clarify the water vapour temperature effect on the H₂ production from Ar-H₂O plasmolysis, the water vapor and argon gas feeding flow rates remained constant for all experimental conditions. The measurements are carried out at plasma applied voltage range of 8–18 kV and sinusoidal wave frequency of 10 kHz. Figure (4.27) presents the experimental results of the H₂ concentrations at different input water vapour temperatures versus the plasma applied voltage. It was found that the hydrogen production yield increased with the input gas temperature increased. The maximum obtained hydrogen concentration was at the highest feeding input water vapour temperature of 623 K. This figure is also evidence that the gas temperatures have a clear relation to increasing the concentration of the hydrogen production.

As discussed in the simulation results earlier, the simulation models were analyzed for the Ar-H₂O model with and without the selecting of the dissociative attachment reaction (H⁻). Figure (4.28) shows a comparison between the simulation and experimental results for the effect of feeding gas temperature at different plasma applied voltage. It was found that the results of the full simulation model included the dissociative attachment reaction (H⁻) have a lower H₂ concentration results than that obtained from the simulation model deselecting the dissociative attachment reaction. However, the concentration profiles trend of both models is found to be similar. Furthermore, the hydrogen concentration of the simulation model selecting the dissociative attachment reaction is more acceptable to experimental results than the other model for all comparisons of simulation and experimental results. The simulation results of both models showed that the feeding gas temperature has an important effect on the water vapour plasmolysis dissociation process. Also, it was found that the dissociation reaction and the dissociative attachment reaction to being an important starting reaction step in the argon-water vapour plasmolysis process [593].

The addition of the electron of the dissociative attachment reaction mechanism caused a significant decrease in the hydrogen concentration. It was observed from the simulation results that the concentration of produced H₂ to be the most affected species with the addition of negative hydrogen ions by selecting the dissociative attachment reaction. The second step of the negative hydrogen ion produced from the dissociative attachment reaction is converted by the ion electron detachment reaction as discussed in reaction (j).

Chapter 4 Water vapour decomposition simulation

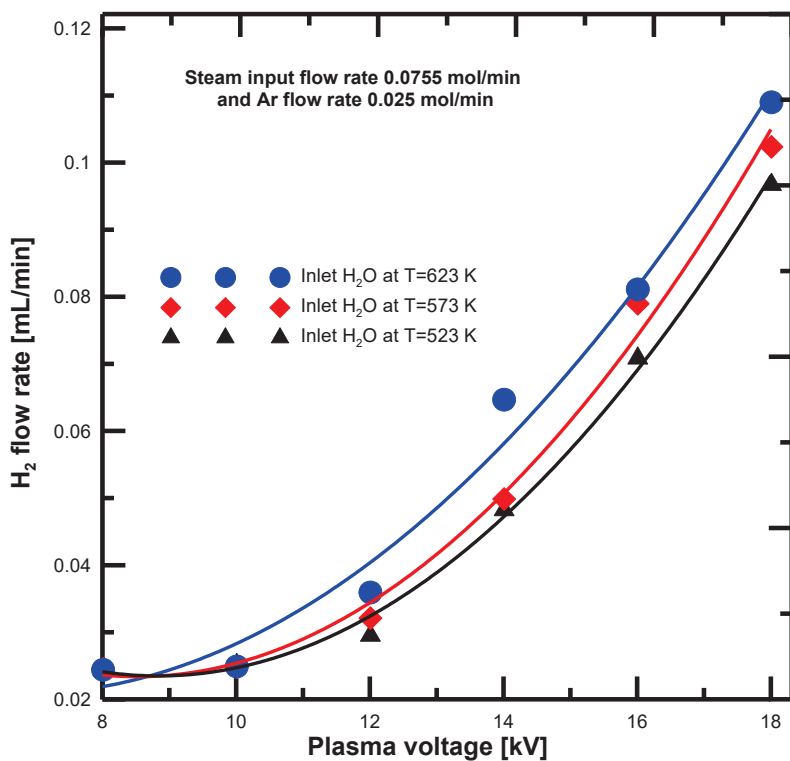
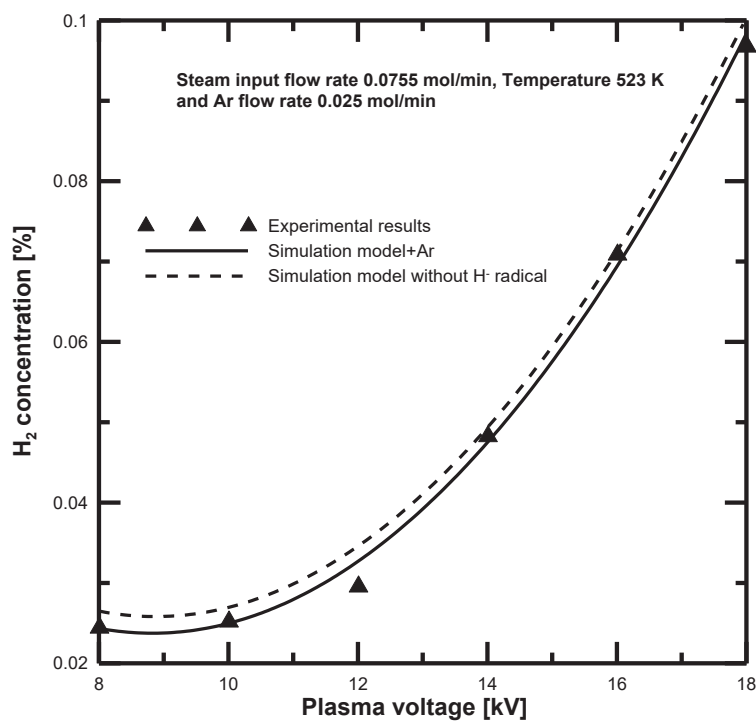
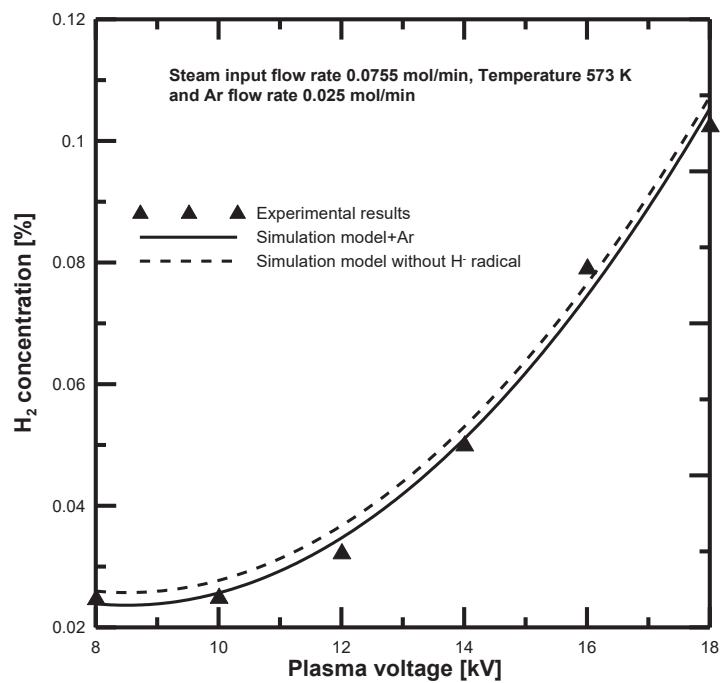


Fig. (4.27). Experimental results of the effect of input water vapour temperature on the H₂ production.

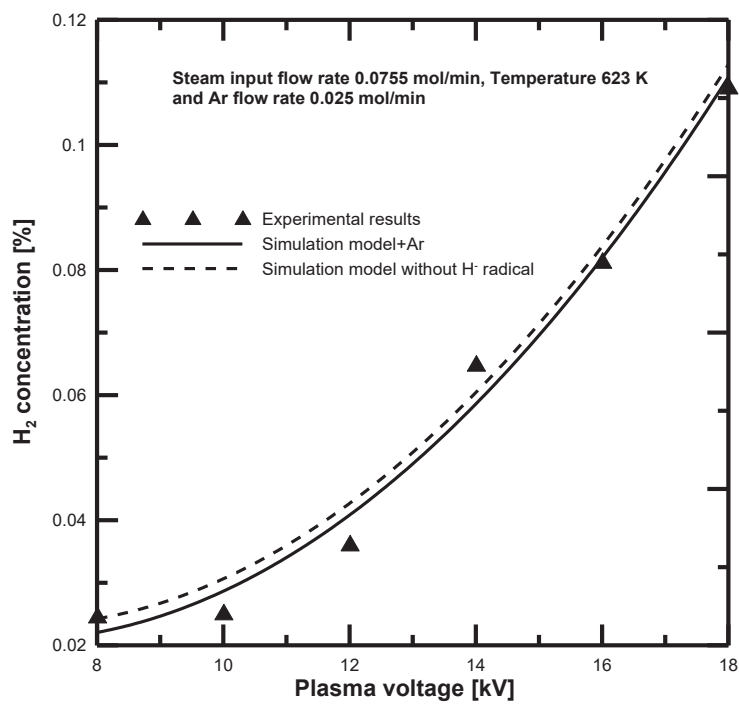


Chapter 4 Water vapour decomposition simulation

(a)



(b)



(c)

Chapter 4 Water vapour decomposition simulation

Fig. (4.28). The H₂ concentration results of both simulated models compared with experimental results of water vapour input temperature effect are presented in a), b), and c).

The dependence of hydrogen production on the water vapour feeding flow rate from Ar-H₂O plasmolysis was investigated. Figure (4.29) represents the H₂ concentration obtained from experimental results at different input water vapour flow rates versus plasma applied voltage. Different input water vapour flow rate was fed into the PTR at a temperature of 523 K and argon gas flow rate of 0.01 mol/min. The results indicated that the hydrogen concentrations increased with the feeding water vapour and plasma applied voltage increased. Moreover, the energy efficiency is considered an important parameter to evaluate the hydrogen production processes. The energy efficiency was defined as the ratio of the H₂ gained energy to the total amount of heat added as follow [539]:

$$\text{Energy efficiency}[\%] = \frac{\text{HHV} * \text{H}_2 \text{ output flow rate} [\text{W}]}{[\text{Plasma Power} + Q_{\text{add}} + \text{Condensation heat}] [\text{W}]} \times 100 \quad (9)$$

Where HHV is the hydrogen higher heating value, Q_{add} is the heat added to produce steam, and the condensation heat to get hydrogen and oxygen gas using ice trap. Figure (4.30) illustrates the energy efficiency of hydrogen production from Ar-water vapour mixture at different input plasma electric power and flow rates. It was found that the energy efficiency increased with the plasma input power and input flow rates. The maximum obtained results of energy efficiencies at high plasma input power were 0.0107%, 0.0253%, and 0.047% at Ar-H₂O flow rates of 0.075, 0.1, and 0.125 mol/min, respectively.

However, argon gas is added to the water vapour stream but the hydrogen concentration was still low. In the current study, the argon-water vapour mixture was injected into the reactor at the PTR temperature of 20 °C. To clarify the PTR heating effect and the addition of argon gas effect on the H₂ concentration produced from the water vapour plasmolysis, figure (4.31) shows a comparison between the experimental results of hydrogen production from the water vapour plasmolysis under the addition of the argon gas to the water vapour stream and pure water vapour at PTR temperature of 90 °C. The hydrogen production from water vapour plasmolysis were determined at plasma input power range of 82–120 W and applied voltage of 8–18 kV. It was found that the hydrogen concentration of water vapour only at PTR temperature of 90 °C was higher than that obtained from the argon-water vapour system. However, the addition of argon gas improved the H₂ concentration but was not similar to the PTR heating temperature which has a remarkable effect on the produced hydrogen gas from water vapour plasmolysis.

Chapter 4 Water vapour decomposition simulation

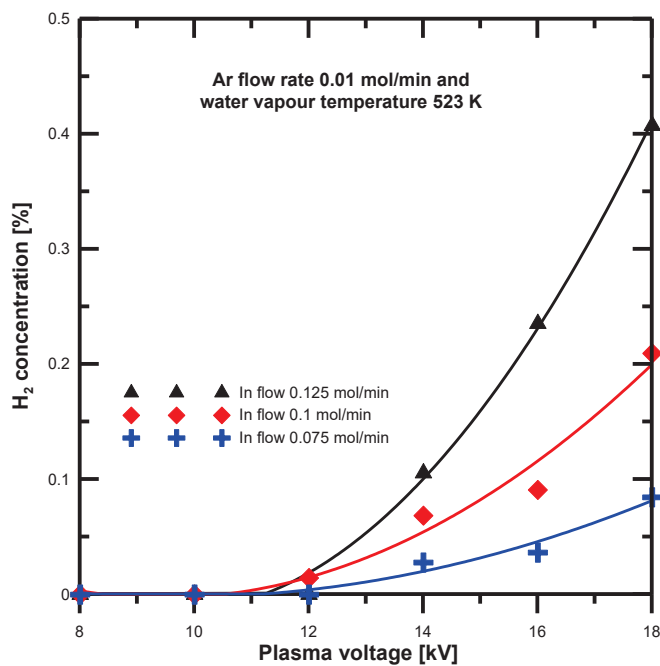


Fig. (4.29). Experimental results of the effect of input water vapour temperature on the H₂ production.

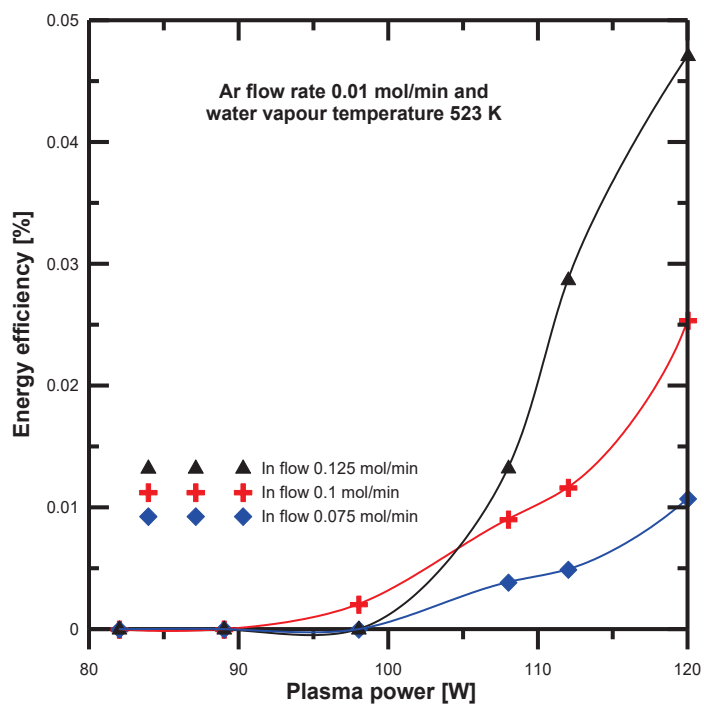


Fig. (4.30). Energy efficiency results at different input plasma power.

Chapter 4 Water vapour decomposition simulation

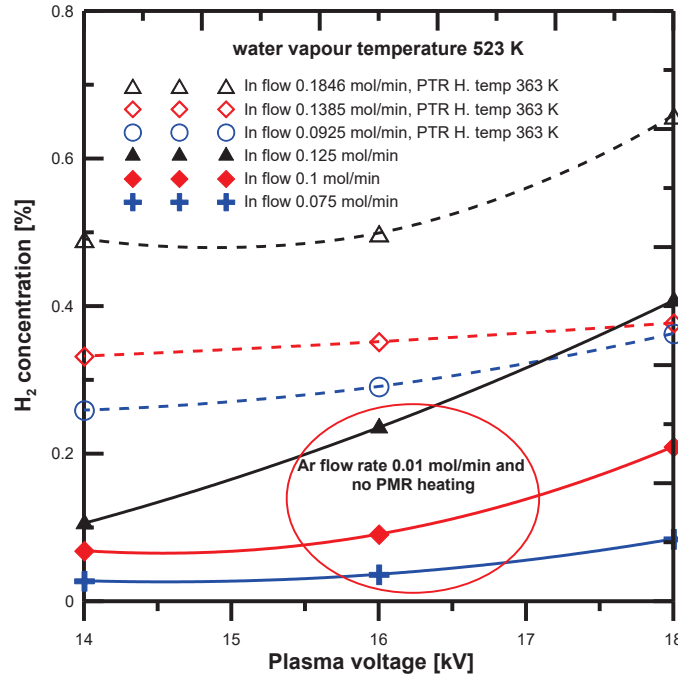


Fig. (4.31). Experimental results of the effect of input water vapour temperature on the H_2 production.

Conclusion

It was reported a simultaneous investigation of a theoretical and experimental analysis of hydrogen production from an atmospheric pressure argon-water vapour mixture as a function of DBD plasma applied voltage. The produced hydrogen concentration in Ar- H_2O increases with increasing argon flow rate and plasma voltage. Due to the importance of the dissociation reaction and the dissociative attachment of electrons, the simulation analysis was carried out by selecting and deselecting the dissociative attachment reaction (H^-). Also, it was found the H_2 concentration results of water vapour simulation model including the dissociative attachment reaction (H^-) that was nearly same as experimental results. This most likely due to the water vapour did not completely convert into H_2 and O_2 gas which was confirmed by H_2O and H_2O_2 concentration results of simulation models. The effect of the feeding water vapour temperature on the water vapour breakdown was investigated. It was found that the hydrogen concentration increased with the water vapour temperature increased. Also, a comparison between H_2 concentration results of simulation models with and without the dissociative attachment reaction as well as experimental results was investigated. Also, the water vapour feeding flow rate was found that has an important effect on the produced H_2 concentration. The hydrogen concentration increased with input gas and plasma voltage increased. To clarify the argon addition and reactor temperature effect

Chapter 4 Water vapour decomposition simulation

on H_2 production from water vapour plasmolysis, a comparison between H_2 concentration of experimental results of the water vapour plasmolysis under the addition of argon gas and pure water vapour at PTR temperature $90\text{ }^{\circ}\text{C}$. It was observed that the hydrogen concentration of pure water vapour at PTR temperature of $90\text{ }^{\circ}\text{C}$ has higher H_2 concentration values than that obtained from the Ar- H_2O system. However, the H_2 concentration improved by the addition of argon gas but it was not similar to the effect of the PTR heating temperature on the produced hydrogen gas from water vapour plasmolysis.

Chapter 4 Water vapour decomposition simulation

4.3 Comparative study between the simulation and experimental results of H₂ production from water vapour plasmolysis

Many substantial research efforts have been carried out to use hydrogen as an alternative energy carrier [599]. It is agreed with all environmental issues related to the usage of the conventional fuels such as exhaustion, pollution and climate change [600]. One of the great challenges faced the hydrogen production process is the combination between the energy sustainability and environmental protection. Different hydrogen economic studies have been investigated; it was found that the hydrogen economy offers two main advantages in terms of low greenhouse gases (GHGs) and used as an alternative fuel to reduce the consumption rate of fossil fuels [79, 594-598]. Different hydrogen production technologies have been investigated [80, 324]. Most of the available world hydrogen is produced by steam methane reforming process. It acts around 80-85 % of the total world hydrogen and the remaining is produced by water electrolysis and coal gasification methods [601]. Currently, methane is obviously considered the best choice of fossil fuels due to its availability and low GHGs emissions [634]. Also, hydrogen can be produced by the water electrolysis process which is considered a commercial method [583]. In addition, Hydrogen gas has been generated by thermochemical methods from the biomass process as a renewable and sustainable energy source [635]. Most of the hydrogen production technologies are directly or indirectly utilized fossil fuels, subsequently GHGs are emitted.

Water vapor plasmolysis is mostly considered as a clean hydrogen energy carrier which the hydrogen can be generated without any environmental impact. Plasma is generated using the electrical energy which transformed into electron kinetic energy then water molecules excitation and produce hydrogen and oxygen gas [337, 562]. The high productivity and efficiency is behind the continuous interest in hydrogen production using the non-thermal plasma or dielectric barrier discharge plasma (DBD plasma). Hydrogen production from water vapor using plasma has been viewed as a high expensive method, additionally; the efficiency has been registered value of 50 % compared with the conventional plasma reactors [333, 562]. Plasmolysis has the ability to produce hydrogen 1000 times more than the water electrolysis process due to the multiple excited species are produced by applying plasma, in addition, it was reported that the energy efficiency of the plasma chemical reaction is same as thermos-catalytic and electrolytic methods [80].

Different feed stocks have been utilized in plasma-chemical processes such as methanol, ethanol, kerosene, and water in liquid and vapor state [306, 310, 334, 336, 531, 543, 546, 547, 636]. The kinetic models of the hydrogen production from water

Chapter 4 Water vapour decomposition simulation

vapor using DBD plasma have been developed [593]. The hypothesis of this study is to simulate the hydrogen production from water vapor plasmolysis over a period of time that will lead to predict the chemical kinetics and compared it with the H_2 concentration of the experimental results under the same operating conditions. Two water vapor plasmolysis kinetic models are simulated for a cylindrical type reactor. The simulation analysis was carried out using non-thermal plasma at atmospheric pressure and incorporated with the initial species concentration. The effects of the dissociative attachment reaction on the simulation results of water vapor break down into hydrogen and oxygen gas were evaluated. The species concentrations at steady state were monitored for both simulation models. The hydrogen concentrations results were compared for both tested models and the H_2 concentration of experimental results. Also, the H_2 conversion rates of both models and experimental results were analyzed.

4.3.1 Simulation of hydrogen production

In this study, the concentrations of product gases of water vapor plasmolysis were simulated and investigated in a cylindrical type DBD plasma reactor using Reaction Engineering Lab of *COMSOL Multiphysics*TM. The complete reaction mechanism is shown in Table (4.11). The simulation analysis was carried out for the water vapor decomposition with several mechanisms including dissociative ion attachment and dissociation reaction but without ionization reaction. Also, the simulation is implemented by excluding the dissociative attachment reaction (H^-). The first model was excluded (reaction no (2)) in Table (4.11) to evaluate the effect of the dissociative attachment reaction (H^-) on the water vapor dissociation reaction mechanism pathway, while the second one used the full reaction mechanism in Table (4.11) including the dissociation reaction and the dissociative attachment reaction. However, it was reported that the dissociative attachment reaction (reaction (2)) was an important step for water vapor breakdown using plasma [593].

The experimental species concentrations data are utilized as input data to the simulation models analysis. In this reaction mechanism, water vapor is decomposed to generate hydrogen and oxygen molecules after a chain of reactions. The kinetics of H_2 formation from water vapor decomposition in a cylindrical type reactor was studied by applying DBD plasma. The water vapor density was determined at the water vapor temperature ranges of 250-350 °C using the ideal gas law. This simulation study results were compared with the experimental water vapor decomposition data and the pathway of reactions consists of six chemical reactions.

Chapter 4 Water vapour decomposition simulation

Table 4.11. Simulated reaction mechanism

No.	Reaction type	Type	Rate constant(K) [m ³ /mol-sec, m ⁶ /mol- sec]	Ref.
1	H ₂ O+e→ H+ OH +e	Dissociation reaction	9.978E+07	[541, 578]
2	H ₂ O+e→ H ⁻ +OH	Dissociative attachment	3.706E+07	[541, 583]
3	OH+OH→ H ₂ O ₂	Neutral-neutral reaction	1.02E+07	[578]
4	OH+ H ₂ O ₂ → H ₂ O+ HO ₂	Neutral-neutral reaction	1.02E+06	[578]
5	HO ₂ + HO ₂ → H ₂ O ₂ + O ₂	Surface reaction 1	9.64E+05	[578]
6	HO ₂ +H→ H ₂ + O ₂	Surface reaction 2	3.91E+07	[578]

Many studies have been carried out to model the water vapor decomposition using DBD plasma. The overall water vapor kinetic models and single type plasmachemical reactions like ionic collision and electronic for the water vapor have been investigated in different studies [80, 562, 577, 581]. A zero-dimensional model has been proposed for low density non-stationary discharge gas in water vapor by Avtaeva et al. [577]. The water vapor at very low pressure (133-150 kPa) have been used in their studies and the results showed that the most positive and negative species were H₃O⁺ and OH⁻ respectively. The effect of dissociative attachment reaction number (2) in table (4.11) included negative hydrogen a radical (H⁻) on the hydrogen production in cylindrical reactor was observed on the hydrogen formation kinetics. In the current study, two reaction mechanisms of water vapor dissociation are simulated for hydrogen production with and without the dissociative attachment reaction (H⁻). The simulation results are compared with the experimental hydrogen concentrations results.

The water vapor plasmolysis dissociation direct decomposition pathway can be expressed as follows [583]:

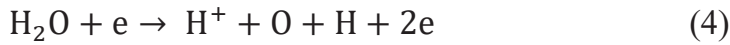


The primary species of water vapor decomposition are hydrogen and hydroxyl radicals [637]. The dissociation reaction of produced atomic hydrogen and hydroxyl radicals can be written as follows [587, 637, 638]:

Chapter 4 Water vapour decomposition simulation



The water vapor decomposition using DBD plasma is formed most of reactive species such as hydroxyl OH, H atoms, and oxygen atoms O^\cdot . It was associated that the primary chemical reaction produced species H and OH radicals, then these species react with each other to generate molecular products such as hydroperoxyl HO_2 [271]. The chemical reactions pathway included the negative species (OH^- , H^- , and O^-) of water vapor have also been reported [577,581]. Also, it was reported that the following reactions may happen in the water vapor plasmolysis but it has low probability and required a relative high energy [581], therefore, these reactions are not included in the current simulation studies.



The simulation reaction mechanism of water vapor plasmolysis by the dissociative attachment of electrons was included and water vapor dissociation is initiated with the dissociative attachment of an electron (H^-). In this simulation study, the effect of dissociative attachment reaction (H^-) was investigated on the water vapor decomposition using DBD plasma. The negative hydrogen radical (H^-) formed in the full reaction mechanism combines with the electron through electron detachment process as follows:



In the current simulation study, the reaction mechanism model was proposed and analyzed for both different mechanism pathways of the water vapor dissociation. The reaction kinetic models were implemented using Reaction Engineering Lab. (REL) in COMSOL MultiphysicsTM [585]. This package provides an automatic sensing of stiff systems and an adaptive time stepping algorithm with tolerance of 10^{-6} [582].

4.3.2 Initial boundary conditions

The initial concentration of water vapor was determined using the ideal gas law at the given water vapor temperature and atmospheric pressure. In this simulation study, water vapor and electrons are the only input reactants to the system. The initial number of electron density was set at 10^6 m^{-3} . Furthermore, it was found that the equilibrium electron density values for non-thermal (DBD) plasma vary in a range of (10^{18} - 10^{21} m^{-3}) [621, 639]. While it was experimentally reported that the lowest value

Chapter 4 Water vapour decomposition simulation

of electron density was 10^{17} m^{-3} [640]. The input plasma voltage ranges of 12-14 kV and pure water vapor flow rate of 0.0104 L/min were used at different water vapor temperatures range of 523-623 K. The hydrogen and oxygen gas species experimental concentrations data were set as input data.

4.3.3 Experimental method

In this study, pure water vapor was decomposed using DBD plasma in a cylindrical type reactor. The DBD plasma was generated between quartz glass and stainless steel surfaces at atmospheric pressure, while the discharge gap between surfaces was 1 mm. The water vapor plasmolysis experiment was carried out at a constant feeding flow rate of 0.0104 L/min, plasma applied voltage of 12-14 kV and temperature ranges of 250-350 °C. The outlet gas samples are taken after gas separated in the ice trap by using syringe then the hydrogen and oxygen concentrations are measured by gas chromatography (GC). The plasma reactor volume was 5.296 cm^3 . The hydrogen concentration was measured using gas chromatography (GC) model type of GC-2014S, SHIMADZU, in addition, the water vapor decomposition experiments were repeated two times. Furthermore, the GC error was estimated before starting the water plasmolysis experiments within $\pm 5\%$ by using standard gas concentrations. The water vapor was generated using the steam generator and the steam flow rate was controlled by mass flow controller while the pressure was monitored using the digital pressure gauges. Figure (4.32) represents the schematic diagram of the water vapor decomposition process in cylindrical type reactor. The discharge voltage was applied at frequency of 10 kHz. The decomposed gases were separated using the ice trap and the sample was collected using syringe. The current study aims to investigate the hydrogen production from water vapor using DBD plasma. The simulated hydrogen production experiments were carried out using different range of the operational parameters as mentioned above.

Chapter 4 Water vapour decomposition simulation

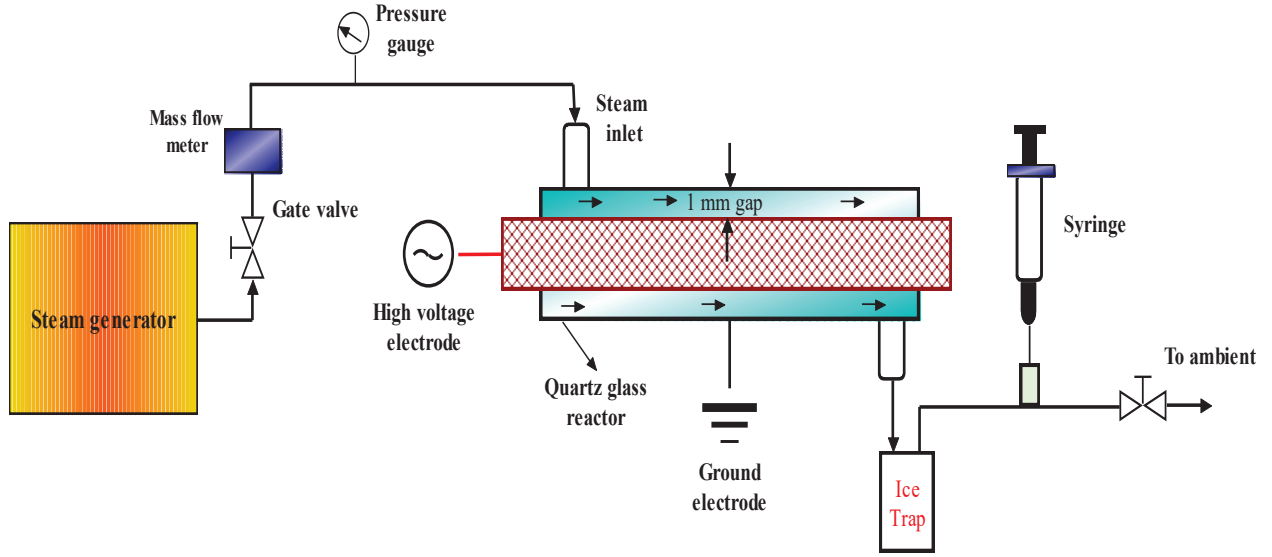


Fig 4. 32 Schematic diagram of hydrogen production using DBD plasma in a cylindrical type reactor.

4.3.4 Results and discussions

Figure (4.33) shows the plasma ignition test photos at plasma voltage range of 10-18 kV. The plasma ignition lighting is enhanced with the typical applied voltage increase. The total electrical power input to the DBD plasma is not the same as the total power consumption due to the lag of the voltage phase angle compared to the current phase angle [641]. The applied frequency of DBD plasma was adjusted at 10 kHz, the typical electric plasma power for one oscillation period can be determined as follows [642]:

$$P = VI \cos \varphi \quad (8)$$

$$I = \frac{V}{Z} \quad (9)$$

$$P = \frac{1}{2} \frac{V^2}{|Z|} \cos \varphi \quad (10)$$

Where the plasma voltage amplitude is V , the plasma current is I , Z is the impedance, and φ is the phase angle between voltage amplitude and current. Therefore, it was investigated that the power consumption in the DBD plasma is lower than the total plasma power utilized in the water vapor decomposition process. In addition, the total actual power consumed (P_{total}) can be calculated using the current (I_{peak}) and voltage (V_{peak}) peak values as follow [643]:

$$P_{total} = V_{peak} \times I_{peak} \quad (11)$$

Chapter 4 Water vapour decomposition simulation

The concentration of produced hydrogen gas with time was measured at different water vapor input temperatures and plasma applied voltage ranges of 12-14 kV. It was reported that the negative species (H^-) will combine due to their weak cross sections ($1-6 \times 10^{-18} \text{ cm}^2$ per molecule). Furthermore, the electron energies were in a range of 6-12 eV [581].

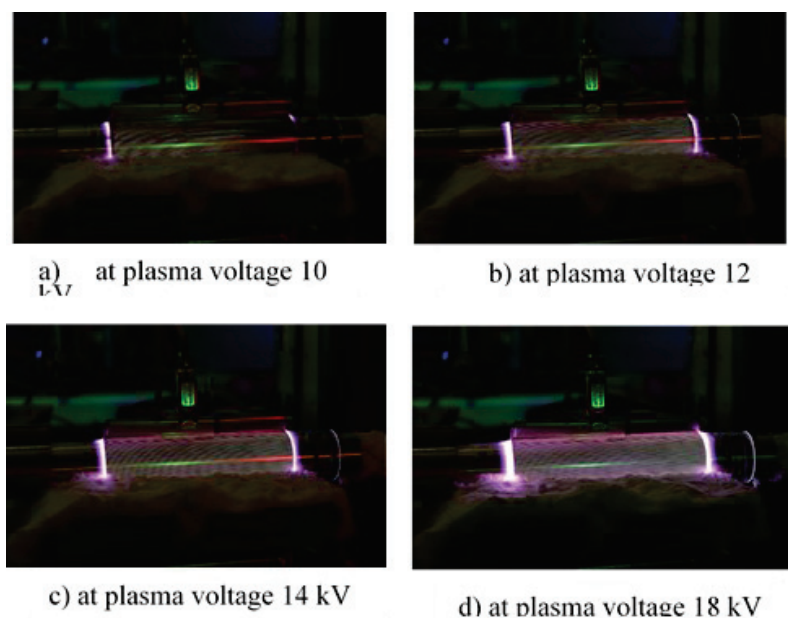


Fig 4.33 Steam decomposition at different plasma applied voltage.

4.3.5 Simulation model I (without dissociative attachment reaction)

The first simulation analysis was carried out without or by deselecting the dissociative attachment reaction. In this simulation model, the effect of dissociative attachment reaction on the concentration of hydrogen production from water vapor was analyzed by deselecting it from reaction scheme. The simulation results were used the experimental results data and the simulation analysis was carried out at the same operating conditions. The steady state concentration of the water vapor decomposition species without dissociative attachment reaction was introduced in [figure \(4.34\)](#). The input species concentrations data of this figure were taken from the experimental data, the experimental outlet hydrogen and oxygen concentrations were measured by GC were also used as a simulation input data. Atypical 99% of the concentrations of water vapor plasmolysis species are found such as H_2 , O_2 , OH , etc. at time scale 0.01s [588, 593]. The simulation result of steady state hydrogen gas concentration versus the evolution time is shown in [figure \(4.35\)](#). It was clear that the hydrogen concentration increases with the reaction time scale until reach to the steady state. It was found that the hydrogen concentration increased continuously with the

Chapter 4 Water vapour decomposition simulation

reaction time scale. Also, it was reported that the reaction of water vapor plasmolysis should be completed before the ions or gas particles reach to the reactor wall or to the electrode surfaces [582]. Also, different water vapor plasmolysis species spectra showed (H, OH, O etc.,) have been obtained [577, 588].

Figure (4.36) illustrates the water vapour concentration simulation results without the dissociative attachment reaction (H^-) over the time. It was clear from the simulation result that the total input water vapours are decomposed into their elements and the concentration of water vapour reach to zero. Although, some of the outlet hydrogen and oxygen gases are recombined in the ice trap by means experimental results showed a condensed water vapor inside the ice trap. Furthermore, this model results did not seem to be accurate because of the water vapour did not completely convert into hydrogen and oxygen in the real experiment. The outlet species concentrations of the experimental results at water vapor temperature of 523 K and plasma voltage of 12 kV are shown in figure (4.37). The results of the analyzed gas samples showed the concentration of the following species of (H_2 , O_2 , and N_2), in addition some of hydrogen and oxygen gas are recombined to compose water inside the ice trap.

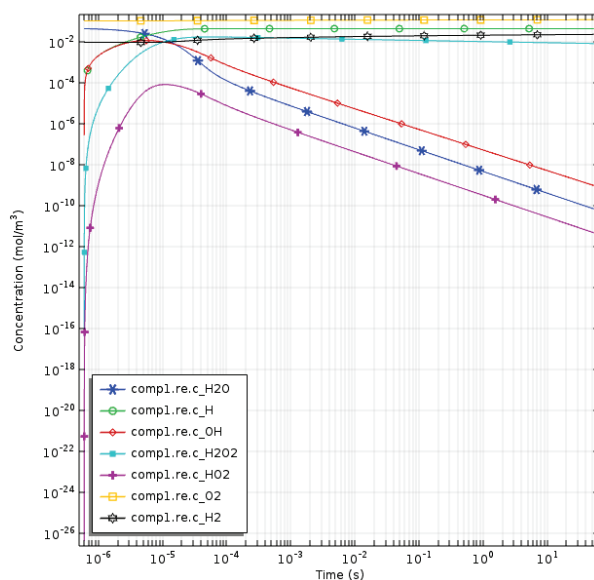


Fig 4. 34 Concentration of the outlet species versus the evolution time (Model I).

Chapter 4 Water vapour decomposition simulation

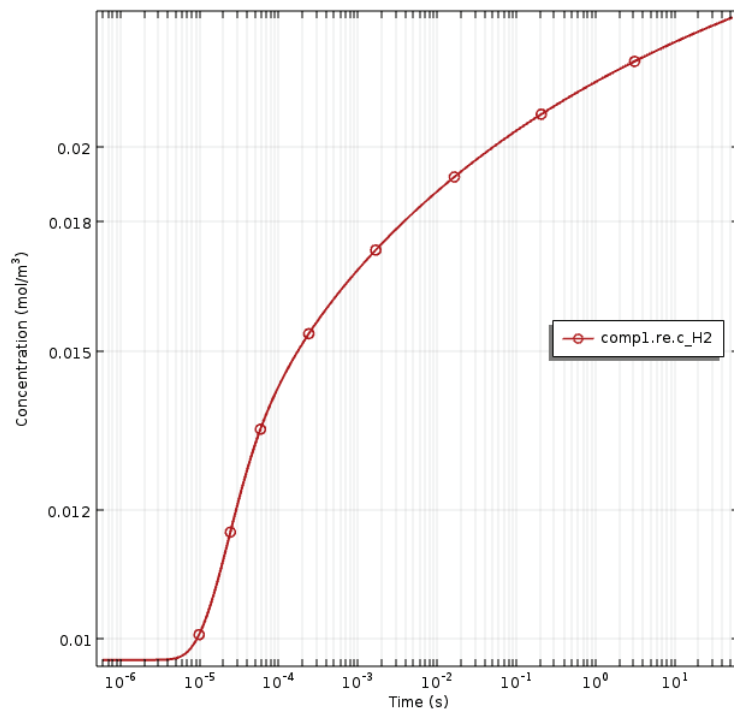


Fig 4. 35 H₂ profile concentration versus evolution time (Model I).

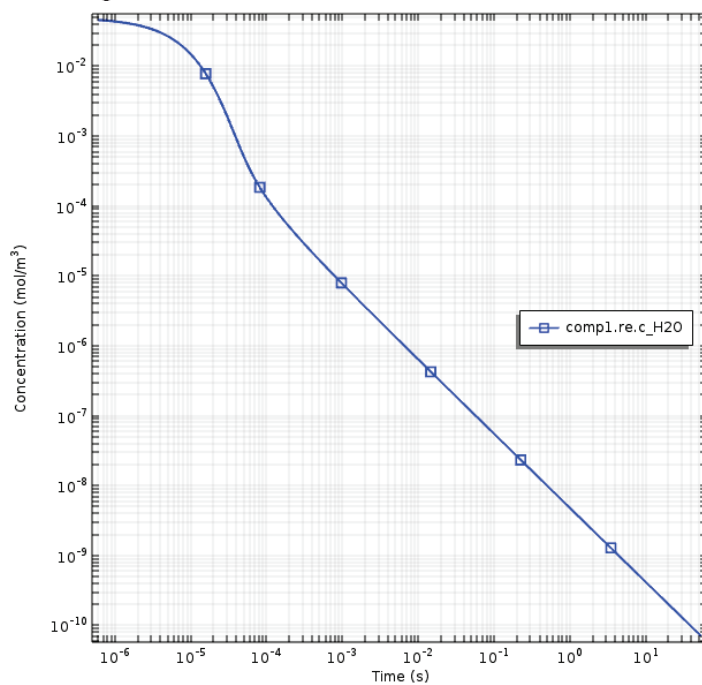


Fig 4. 36 H₂O profile concentrations versus evolution time (Model I).

Chapter 4 Water vapour decomposition simulation

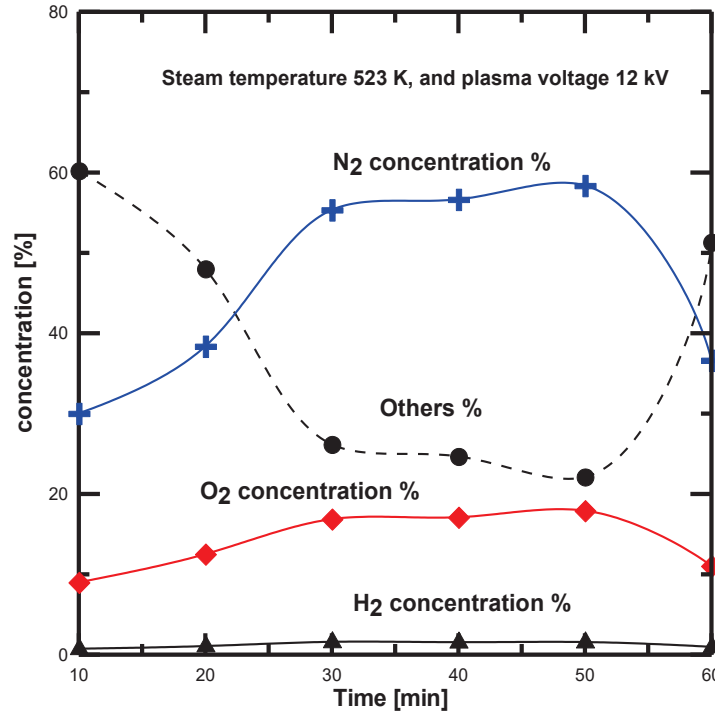


Fig 4. 37 Experimental results of outlet species concentrations of water vapor decomposition.

It was observed that the nitrogen gas concentration is included in the outlet species because of there are some of air content in the water vapour pathway line, also, it is possible that some of air was entered to syringe during the sample collections [588]. Furthermore, the hydrogen, oxygen, and nitrogen gas concentrations are typically showed the same profile trend. Additionally, it was found that the concentrations trend of H₂, O₂, and N₂ decreased at the end of the dissociation time due to more of produced H₂ and O₂ gas are recombined again to compose water molecules which resulted in the increasing of the concentration of the trend of others. To clarify the effect of water vapor decomposition deselecting the dissociative attachment reaction on the simulation results, a comparison between simulation and experimental results will discuss in the next section.

4.3.6 Comparison between theoretical and experimental results (Model I)

The simulation model of water vapor plasmolysis without dissociative attachment reaction (H⁻) (reaction (2)) was analyzed and compared with the water vapor decomposition experimental data. Figure (4.38) shows the effect of inlet water vapor temperature on the hydrogen production concentration over time at plasma applied voltage of 12 kV. The simulation results are obtained at different operating

Chapter 4 Water vapour decomposition simulation

temperatures, it was found that the hydrogen concentration increased with the inlet water vapor temperature at the same plasma applied voltage [337].

Furthermore, the hydrogen concentration of the simulation results without the dissociative attachment reaction was always showed that the concentration was higher than that obtained from the experimental results. As discussed before, the main reason of the decreasing of hydrogen concentration at the end of the dissociation time due to the recombination of H_2 and O_2 gas inside the ice trap, also, it was reported that some of the separated H_2 gas are still remained inside the ice trap.

Figure (4.39) describes the effect of inlet water vapor temperature at plasma applied voltage of 14 kV with time. It was found that the hydrogen concentration decreased with time but the hydrogen concentration values are higher than that obtained from plasma voltage 12 kV. The simulation and experimental results of H_2 concentration for low water vapor temperature of 523 K were higher than that obtained from high water vapor temperature due to the syringe sample collection error and the measurement procedures; it is possibly changed due to the change of the measurements accuracy and the separation procedure of the product gases.

The effect of plasma applied voltage on the hydrogen production from water vapor decomposition using DBD plasma and at constant temperature in ranges of 523-623 K are shown in figure (4.40a, b, c). It was found that the hydrogen concentration results of applied voltage 14 kV were higher than 12 kV at the same input temperature. Furthermore, this figure indicates that the simulation of H_2 concentration results at plasma voltage of 12 kV were higher than experimental results, while the concentration results at plasma voltage of 14 kV decreased with time scale and also are not same as the simulation results. The simulation results of hydrogen concentration at plasma applied voltage 12 kV were higher than experimental, these results were confirmed the results of deselecting the dissociative attachment (reaction no. (2) in table (4.11)) that investigated by Fahad et. al. [593]. The dissociative attachment reaction was found that has an important effect on the simulation results of the water vapor dissociation using DBD plasma and the concentration of hydrogen gas is higher than experimental values. From the analysis of simulation and experimental results, it was observed that the H_2 concentration results of the simulation model without the dissociative attachment reaction are higher than that obtained from the experimental results, also, the simulation trend profiles are changed according to the H_2 concentrations obtained from the water vapour dissociation experiments.

Chapter 4 Water vapour decomposition simulation

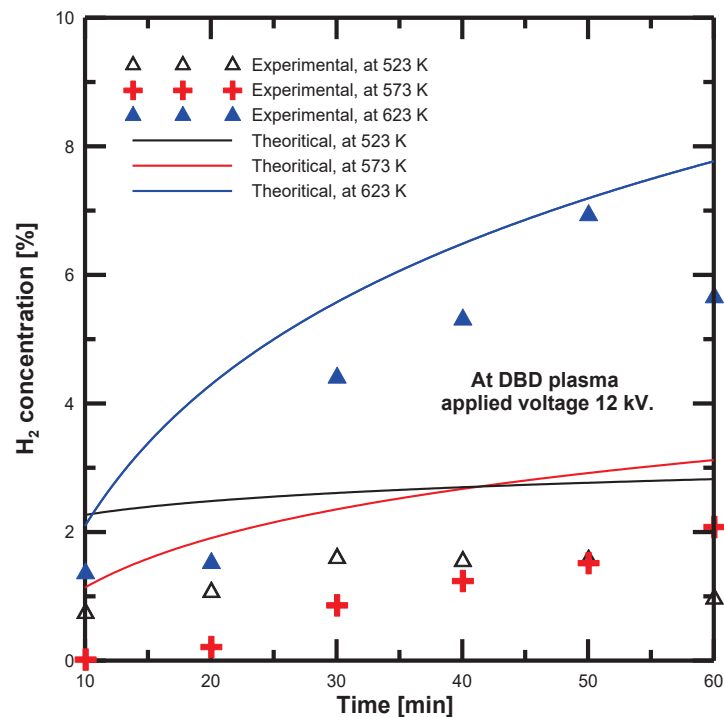


Fig 4. 38 Comparison between experimental and theoretical steam decomposition concentrations data at plasma voltage 12 kV.

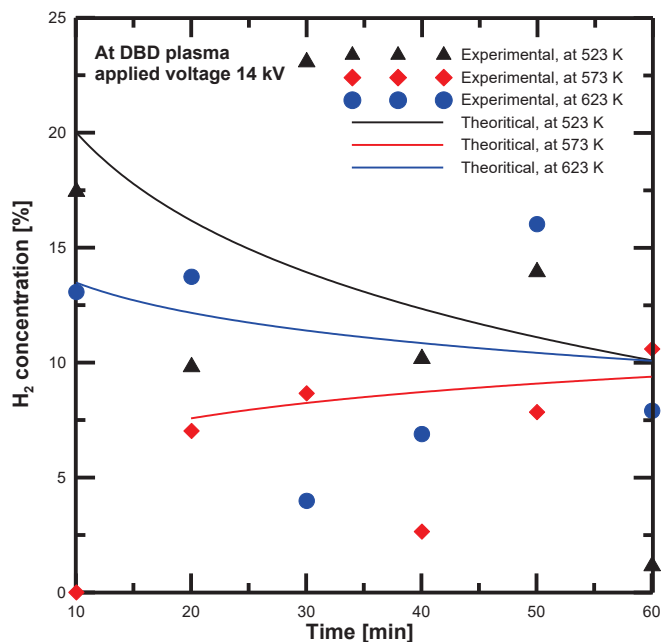
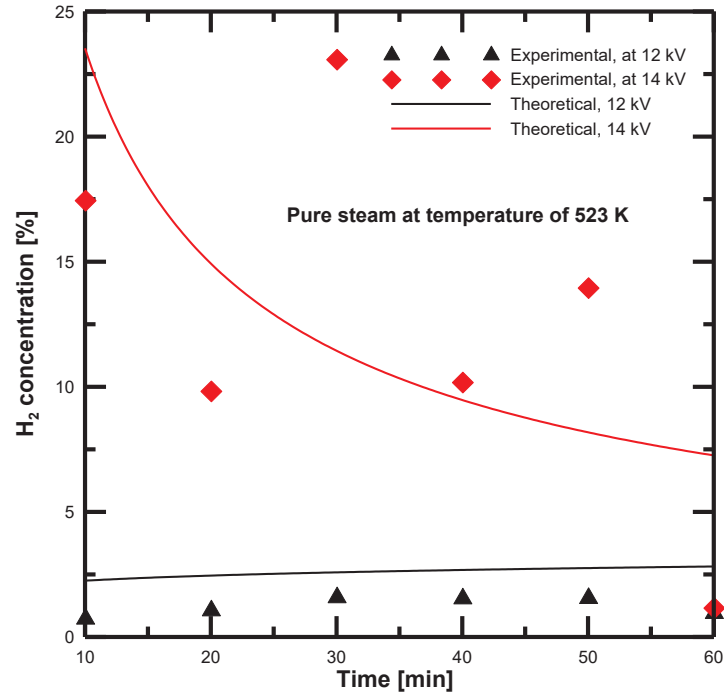
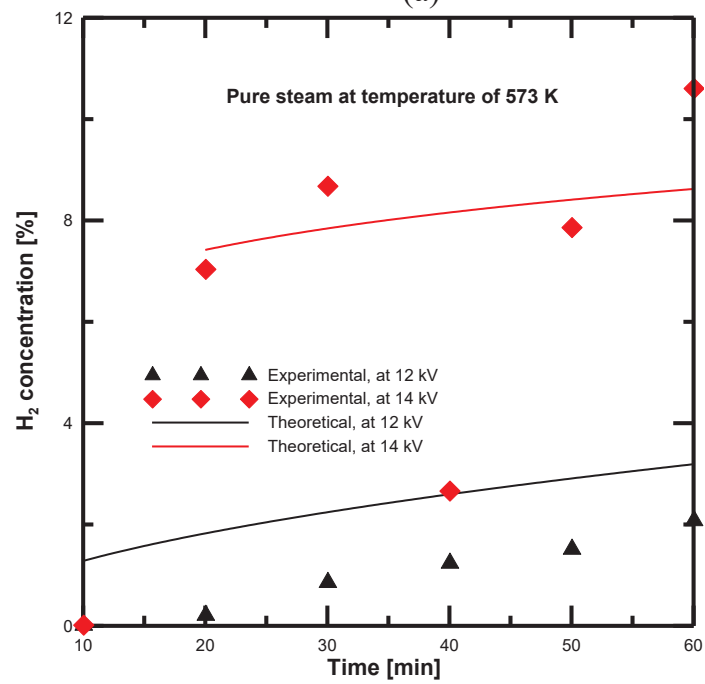


Fig 4. 39 Comparison between experimental and theoretical steam decomposition concentrations data at plasma voltage 14 kV.

Chapter 4 Water vapour decomposition simulation



(a)



(b)

Chapter 4 Water vapour decomposition simulation

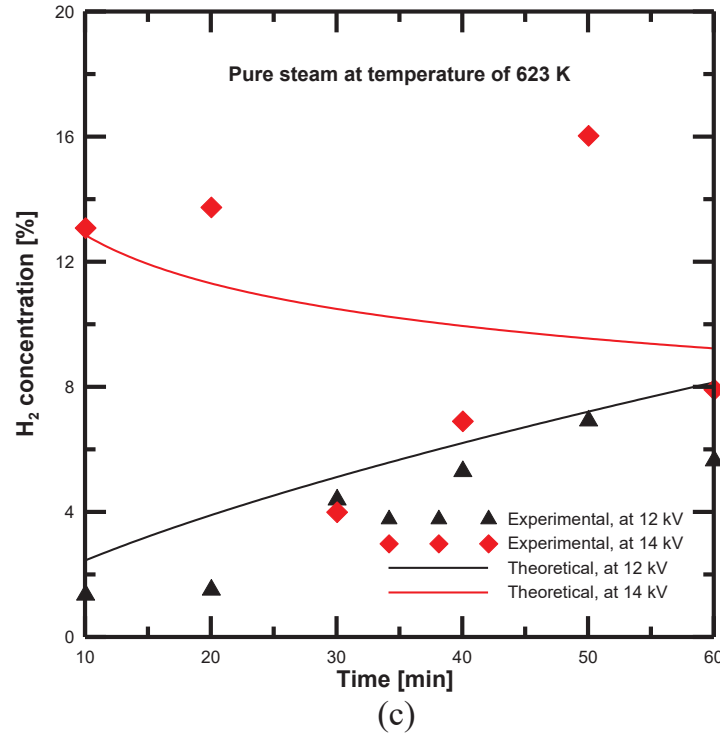


Fig 4. 40 Comparison between experimental and theoretical results of H₂ concentration at different input water vapor temperatures.

4.3.7 Theoretical analysis of water vapor decomposition using DBD plasma with dissociative attachment reaction

In this simulation model, the full reaction mechanism included the dissociative attachment reaction (H^-) was analyzed. The dissociative attachment reaction included H^- was utilized to break water vapor molecules by electron impact as a first step of chains of reactions. It could be stated that the hydrogen concentration value dropped by selecting the dissociative attachment reaction [593]. Additionally, it was reported that the dissociative ionization and dissociative excitation reactions have no effect on the kinetics as well as the species concentrations. Figure (4.41) shows the steady state concentration of the given full reaction mechanism species of H_2O , H , OH , H^- , H_2O_2 , HO_2 , O_2 and H_2 when the dissociative attachment reaction (H^-) was used. While e is expressed about the plasma discharge voltage at a frequency of 10 kHz. The concentration results of the species kinetic curves are based on a real water vapor decomposition case used in the simulation of water vapor decomposition without dissociative attachment reaction. Figure (4.42) indicates that the hydrogen concentration decreased from 0.025 to 0.01 moles/ m^3 , it was found that the dissociative attachment reaction is an important step in the water vapor dissociation

Chapter 4 Water vapour decomposition simulation

processes. Furthermore, the effect of dissociative attachment reaction (H^-) on hydrogen production from water vapor decomposition using DBD plasma was same as the simulation results obtained by Fahad et. al [593]. In addition, the simulation results of steady state water vapor concentration did not reach to zero as shown in figure (4.43). It was clear that some of water vapor are not converted into hydrogen and oxygen gas, these simulation result seems to be same as the real water vapor decomposition because of some of the water vapor was remained in the ice trap.

However, the concentration profile results of both simulation models are similar, but in the current simulation study, it was investigated the major products of these reaction mechanisms H_2 and O_2 . Further, the simulation and experimental results were compared in the next section.

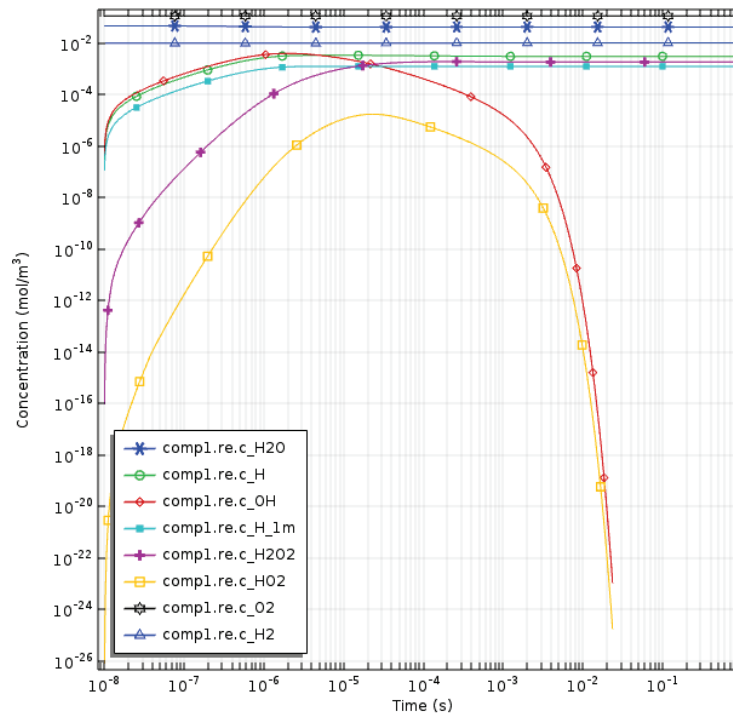


Fig 4. 41 Concentration profiles of the outlet species versus the evolution time with dissociative attachment reaction (H^-).

Chapter 4 Water vapour decomposition simulation

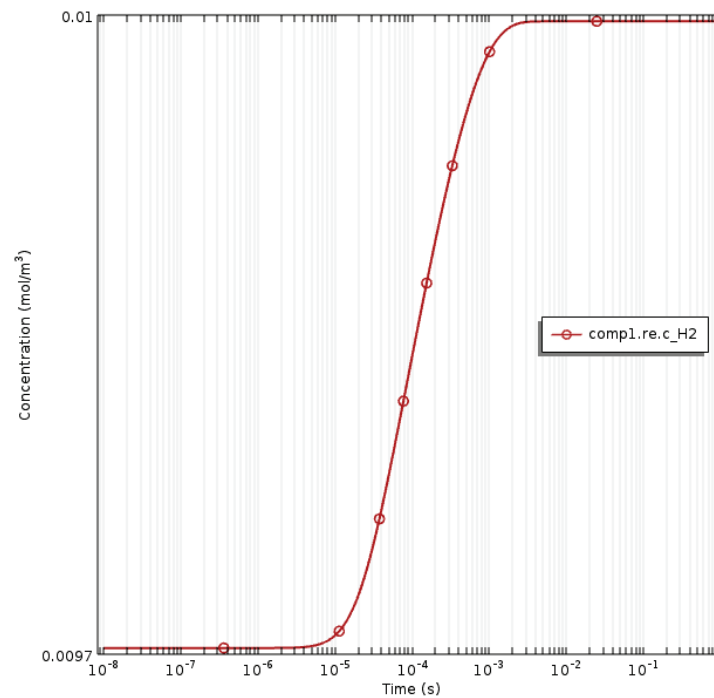


Fig 4. 42 H_2 concentration profile with dissociative attachment reaction (H^-).

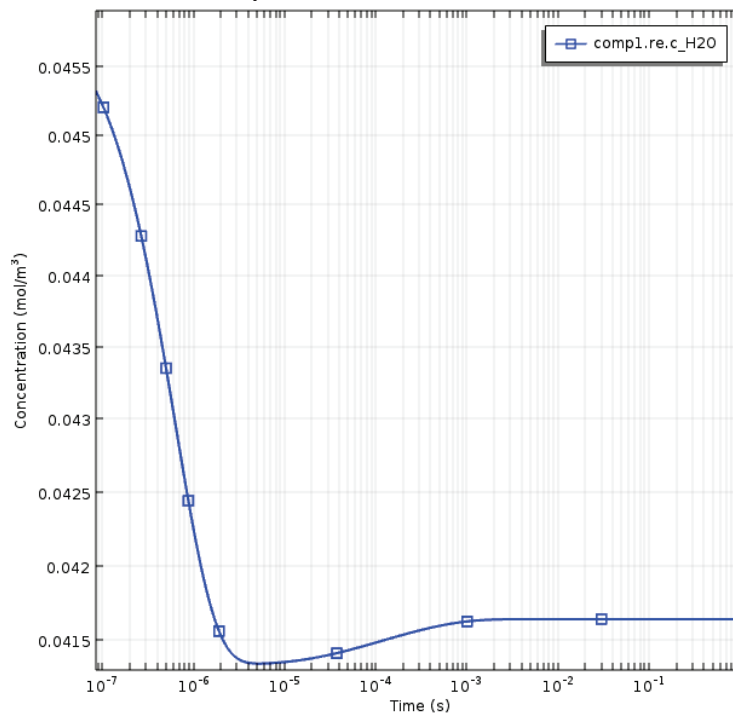


Fig 4. 43 H_2O concentration profile with dissociative attachment reaction (H^-).

Chapter 4 Water vapour decomposition simulation

4.3.8 Comparison between theoretical and experimental results (Model II)

Figure (4.44) presents theoretical and experimental results of the effect of inlet water vapor temperature on the hydrogen concentration at plasma applied voltage of 12 kV. Compared with the simulation analysis without the dissociative attachment reaction, it was found that the hydrogen concentrations values dropped in a range of 50-62 % by applying simulation analysis with dissociative attachment reaction. In addition, it was observed that the simulation results of hydrogen concentrations are nearly same as the experimental data due to add and start the water vapor breakdown with the dissociative attachment reaction. The hydrogen concentration results at different water vapor input temperatures and plasma applied voltage of 14 kV is shown in figure (4.45). The results of the simulation and experimental results seem to be same, however, the concentration trend was not similar in both plasma applied voltage for the simulation model with dissociative attachment reaction.

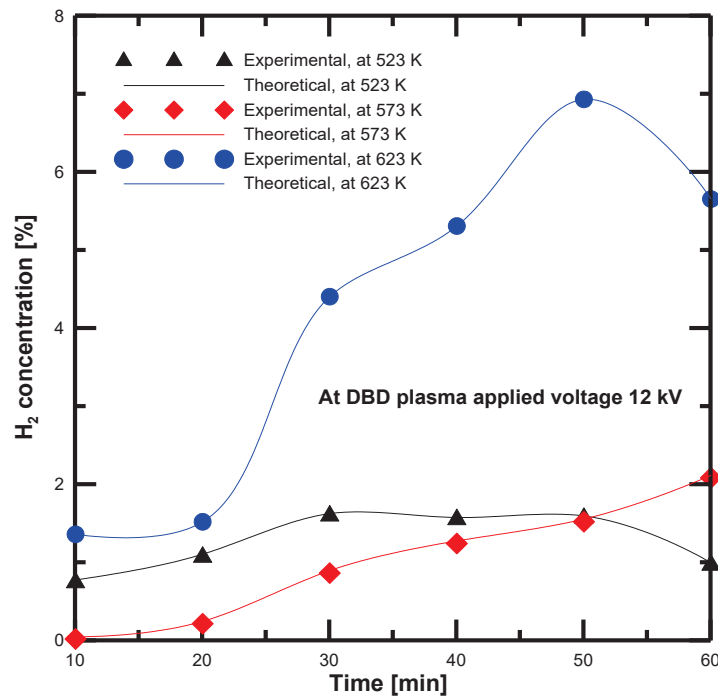


Fig 4. 44 Comparison between experimental and theoretical steam decomposition concentrations data at plasma voltage 12 kV.

Chapter 4 Water vapour decomposition simulation

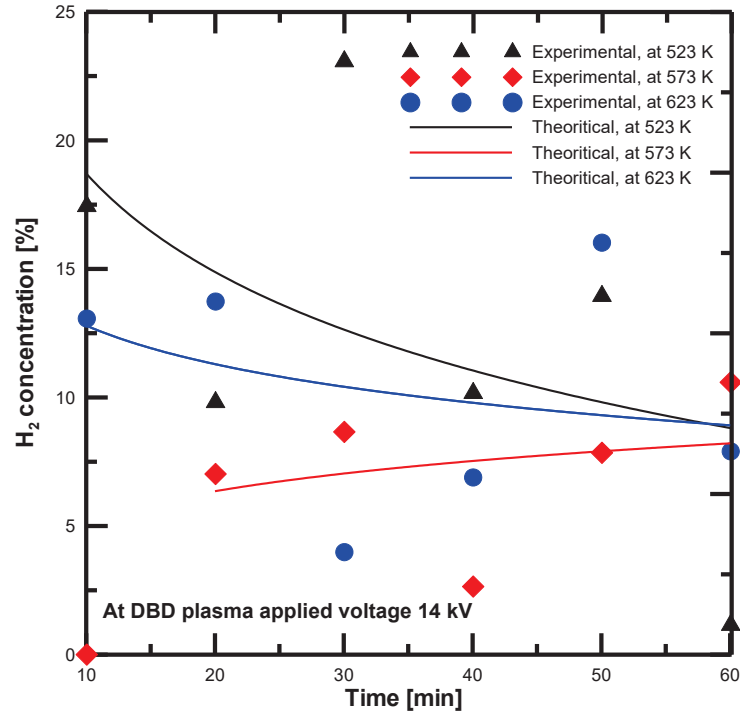
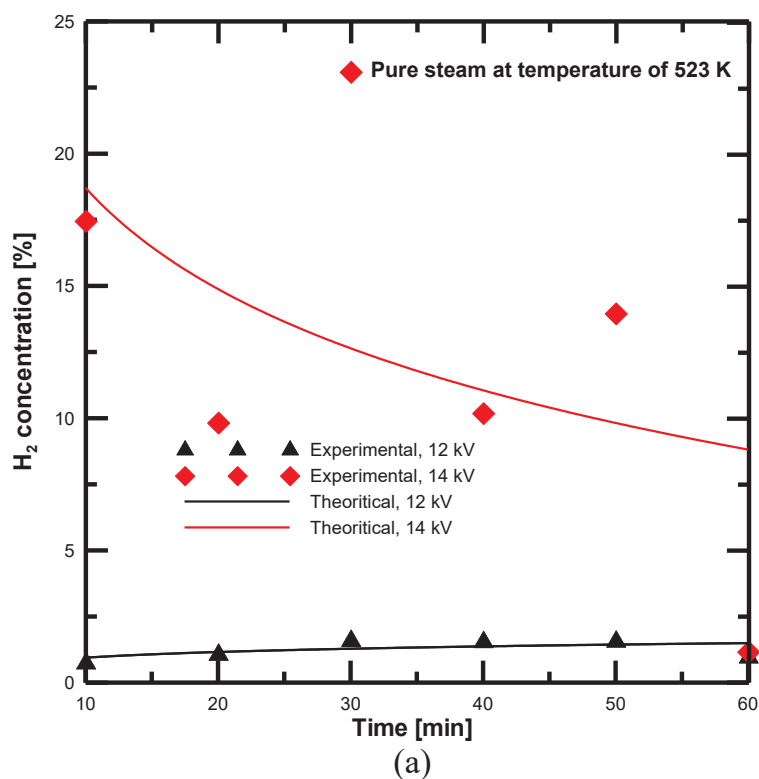


Fig 4. 45 Comparison between experimental and theoretical steam decomposition concentrations data at plasma voltage 14 kV.

Furthermore, it was found that the hydrogen concentrations of simulation model with dissociative attachment reaction at plasma voltage of 14 kV decreased from the simulation results obtained from simulation model without (H^-) radicals in a range of 10-16 %. The simulation results of hydrogen concentration obtained at plasma voltage 14 kV are not linearly changed with the water vapor input temperatures, while at plasma voltage 12 kV, the maximum obtained results of H_2 concentration at the highest input water vapor temperature. It is possibly changed due to sample collections during the experiment, some of hydrogen gas was not completely separated in the ice trap and some of separated hydrogen was remained inside the ice trap. To clarify the hydrogen concentration at different plasma voltage and at the same water vapor input temperature, [figure \(46a, b, c\)](#) shows the effect of plasma voltage on the hydrogen concentration of experimental and simulation results with dissociative attachment reaction versus the reaction revolution time. It was found that the simulation results of hydrogen concentration at plasma voltage 14 kV was higher than that obtained from 12 kV at the same input water vapor temperature. The simulation model with the dissociative attachment reaction (H^-) showed a good agreement with the water vapor experimental results, it was found that the dissociative attachment reaction to be an important step in water vapor decomposition using DBD plasma. Furthermore,

Chapter 4 Water vapour decomposition simulation

when the simulation was carried out with the dissociative attachment reaction mechanism (H^-), the hydrogen concentration dropped to be nearly same as the experimental results. Also, it was observed that the concentration of water molecules did not reach to zero, by means that some of the water vapor molecules are condensed inside the ice trap and did not convert into H_2 and O_2 gas.



Chapter 4 Water vapour decomposition simulation

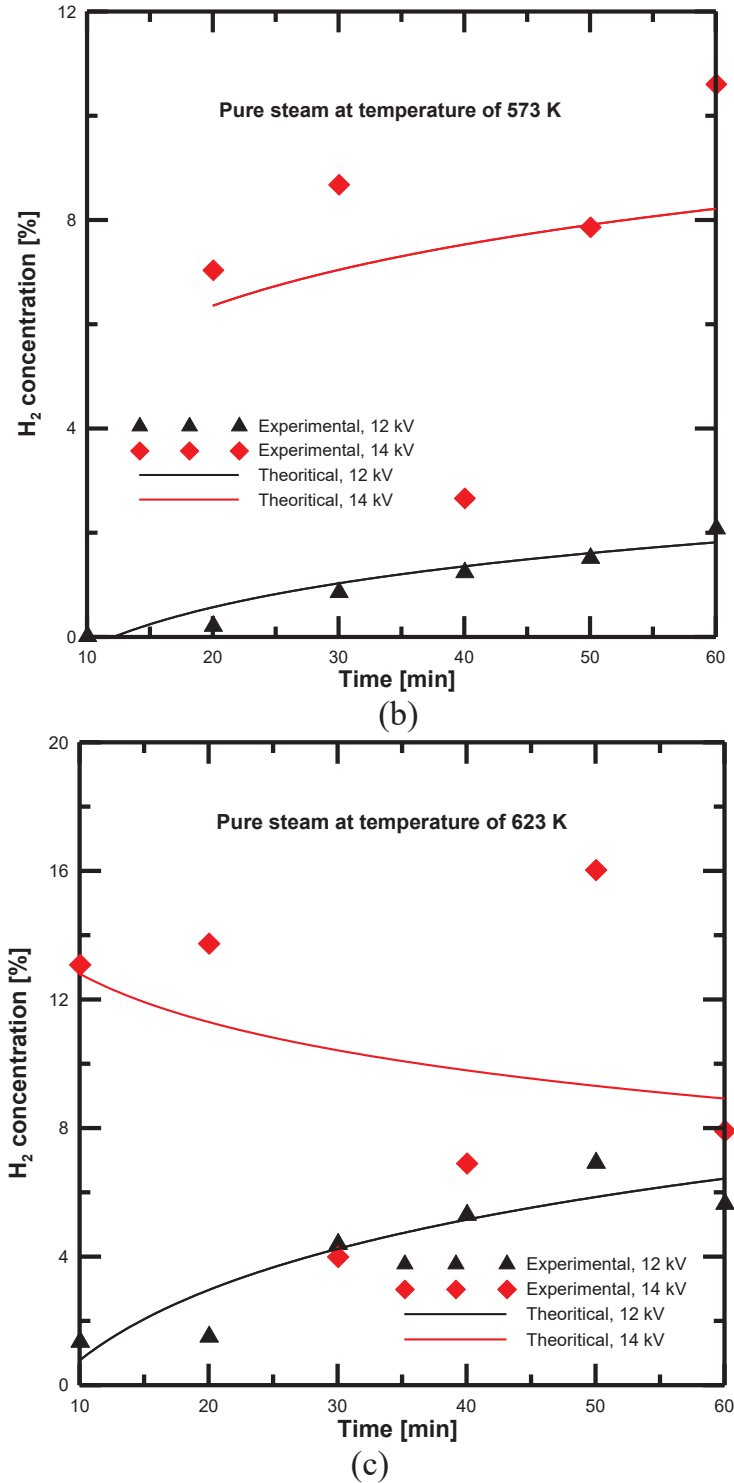


Fig 4. 46 Comparison between experimental and theoretical steam decomposition concentrations at steam temperature 623 K.

Chapter 4 Water vapour decomposition simulation

4.3.9 Comparison between both simulation models reaction mechanism results

The conversion rate of both simulation models has been evaluated and compared between the water vapor decomposition using DBD plasma experimental results. The conversion rate can be determined according to the following expression: *conversion rate [%] = (produced H₂ gas flow rate [mole/min]/water vapor input flow rate [mole/min]) × 100*. The water vapor was decomposed into their elements hydrogen and oxygen gas using DBD plasma. [Figure \(4.47\)](#) shows the conversion rate change of the hydrogen production from water vapor at different plasma voltage and at water vapor input temperature 523 K. The conversion rate of the simulation model with the dissociative attachment reaction showed good agreement with the conversion rate of the experimental results compared with the results of the simulation model without dissociative attachment reaction. The comparison between conversion rates of water vapor at input temperature of 573 K is presented in [figure \(4.48\)](#). The conversion rate of the simulation models result showed more hydrogen production concentration values than that obtained from the experimental concentration values. In both simulation models, it was found that the dissociative attachment reaction has an important effect as a first step of the water vapor dissociation process using plasma. Furthermore, it was observed that the conversion rate of input water vapor temperature 573 K was lower than the conversion rate of input water vapor temperatures of 523 and 623 K.

Chapter 4 Water vapour decomposition simulation

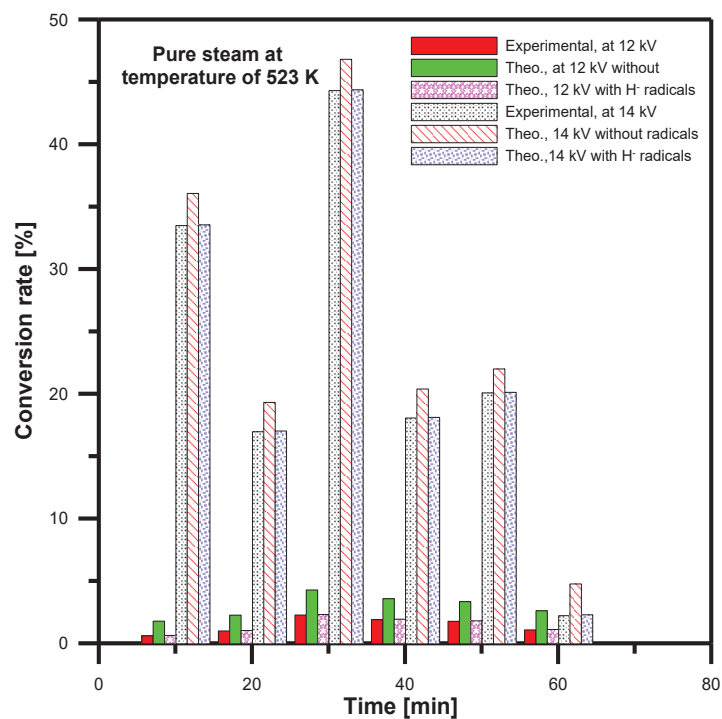


Fig 4. 47 Conversion rate *comparison* of both reaction mechanisms at temperature of 523 K and different plasma voltage.

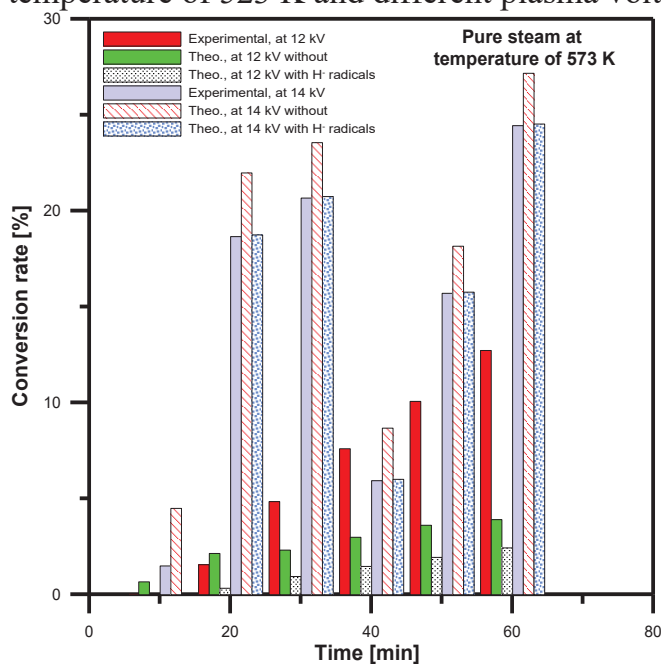


Fig 4. 48 Conversion rate *comparison* of both reaction mechanisms at temperature of 573 K and different plasma voltage.

Chapter 4 Water vapour decomposition simulation

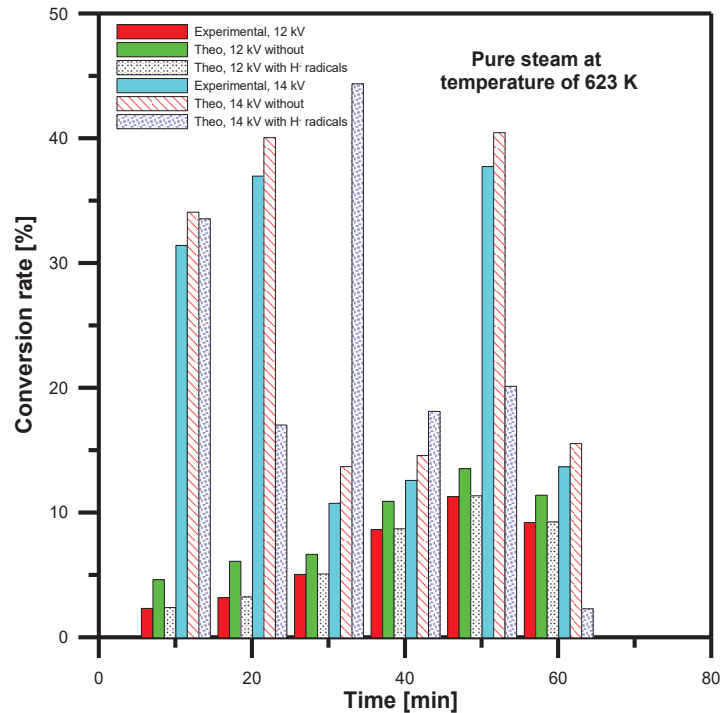


Fig 4. 49 Conversion rate *comparison* of both reaction mechanisms at temperature of 623 K and different plasma voltage.

In addition, the conversion rate of input water vapor at temperature of 623 K is shown in [figure \(4.49\)](#). The conversion rate results of the simulation model with dissociative attachment reaction seemed to be same in all water vapor input gas temperatures. Furthermore, it was found that the dissociation attachment reaction dominate the water vapor dissociation, in addition the hydrogen concentrations were dropped in both plasma applied voltages to be appeared same as the experimental results.

Conclusion

The simulation results showed that the dissociative attachment reaction and the dissociative reaction of electrons have an important effect on the water vapour breakdown processes. The simulation analysis showed that the hydrogen concentrations obtained from the simulation model with the dissociative attachment reaction were lower than those obtained from the simulation model deselecting the dissociative attachment reaction. The hydrogen concentration results of both models were compared with the experimental results. It was found that the hydrogen concentration results of the simulation model selecting the dissociative attachment reaction were nearly same as that obtained from the experimental results. It was observed that the concentration results dropped by the addition of H⁻ radical into the simulation model with the dissociative attachment reaction when used as a primary

Chapter 4 Water vapour decomposition simulation

reaction of electron water vapour plasmolysis. Furthermore, it was concluded that the dissociative attachment reaction included H^- radical controlled the hydrogen production from the detachment electron. The conversion rates were determined for the simulation models and the experimental results. The conversion rate results showed that the simulation model with the dissociative attachment reaction has introduced more acceptable data to the experimental results of the water vapour plasmolysis dissociation reactions pathway.

References

- [553] Xiao-Jun Yang. A new integral transform operator for solving the heat-diffusion problem, *Applied Mathematics Letters*, 64 (2017) 193–197.
- [554] Jian-Guo ZHANG. The Fourier-Yang integral transform for solving the 1-D heat diffusion equation. *THERMAL SCIENCE*: 2017, Vol. 21, Suppl. 1, pp. S63-S69.
- [555] Xiao-Jun YANG and Feng GAO. a new technology for solving diffusion and heat equations, *THERMAL SCIENCE*: Year 2017, Vol. 21, No. 1A, pp. 133-140.
- [556] Xiao-Jun YANG, Dumitru BALEANU, Mihailo P. LAZAREVI, and Milan S. CAJI. Fractal boundary value problems for integral and differential equations with local fractional operators, *THERMAL SCIENCE*: Year 2015, Vol. 19, No. 3, pp. 959-966.
- [557] Keidar, M., Beilis, I.: *Plasma Engineering: Applications from Aerospace to Bio and Nanotechnology*. Academic Press, Oxford(2013)
- [558] Sohbatzadeh, F., Colagar, A.H., Mirzanejhad, S., Mahmodi, S.: E. coli, P. aeruginosa, and B. cereus bacteria sterilization using afterglow of non-thermal plasma at atmospheric pressure. *Appl. Biochem. Biotechnol.* 160, 1978–1984 (2010)
- [559] Sohbatzadeh, F., Mirzanejhad, S., Ghasemi, M., Talebzadeh, M.: Characterization of a non-thermal plasma torch in streamer mode and its effect on polyvinyl chloride and silicone rubber surfaces. *J. Electrostat.* 71, 875–881 (2013)
- [560] Fridman, G., Gutsol, A., Shekhter, A.B., Vasilets, V.N., Fridman, A.: *Plasma Processes Polym.* 5(6), 503–533 (2008)
- [561] Roth, J.R.: *Industrial Plasma Engineering: Volume 2-Applications to Nonthermal Plasma Processing*. CRC Press, Boca Raton (2001).
- [562] Bockris JOM, Dandapani B, Cocke D, Ghoroghchian J. On the splitting of water. *International Journal of Hydrogen Energy* 1985; 10(3):179-201.
- [563] For the spectroscopic observation of water, see P. F. Bernath, *Phys. Chem. Chem. Phys.* 4, 1501 ~2002.
- [564] F. W. Taylor, *Rep. Prog. Phys.* 65, 1 ~2002.
- [565] X. Xie and M. J. Mumma, *Astrophys. J.* 386, 720 ~1992.
- [566] IAEA-TECDOC-799, *Atomic and Molecular Data for Radiotherapy and Radiation Research* ~International Atomic Energy Agency, 1995.
- [567] G. P. Karwasz, R. S. Brusa, and A. Zecca, *Rivista Nuovo Cimento* 24, No. 1 ~2001.
- [568] T. Shirai, T. Tabata, and H. Tawara, *Atomic Data Nucl. Data Tables* 79, 143 ~2001.
- [569] M. Hayashi, *Bibliography of Electron and Photon Cross Sections with Atoms and Molecules*, in *20th Century–Water Vapour–NIFS-Data-81* ~National Institute for Fusion Science, Oroshi-cho, Toki, Japan, 2003.

- [570] Y. Itikawa, editor, *Photon and Electron Interactions with Atoms, Molecules and Ions*, Landolt-Boörnstein, Volume I/17, Subvolume C ~Springer, New York, 2003.
- [571] Y. Itikawa, N. Mason. Cross Sections for Electron Collisions with Water Molecules. *J. Phys. Chem. Ref. Data*, 2005, 34(1), 1-22.
- [572] Gadkari, S., Tu, X., Gu, S.: Fluid model for a partially packed dielectric barrier discharge plasma reactor. *Phys. Plasmas* 24, 093510 (2017)
- [573] Pan, J., Li, L., Chen, B., Song, Y., Zhao, Y., Xiu, X.: Numerical simulation of evolution features of the atmospheric-pressure CF₄ plasma generated by the pulsed dielectric barrier discharge. *Eur. Phys. J. D* 70, 136 (2016)
- [574] Abidat, R., Rebiai, S., Benterrouche, L.: Numerical simulation of atmospheric dielectric barrier discharge in helium gas using COMSOL Multiphysics. In: *Systems and Control (ICSC)*, 2013 3rd International Conference on (pp. 134–139). IEEE (2013)
- [575] Golubovskii, Y.B., Maiorov, V.A., Behnke, J., Behnke, J.F.: Modelling of the homogeneous barrier discharge in helium at atmospheric pressure. *J. Phys. D* 36, 39 (2002).
- [576] Mededovic S, Finney WC, Locke BR. Electrical discharges in mixtures of light and heavy water. *Plasma Processes and Polymers* 2008; 5(1):76-83.
- [577] Avtaeva S, General A, Kel'man V. Kinetic model for low density non-stationary gas discharge in water vapour. *Journal of Physics D: Applied Physics* 2010;43:315201.
- [578] Sobacchi M, Saveliev A, Fridman A, Kennedy LA, Ahmed S, Krause T. Experimental assessment of a combined plasma/catalytic system for hydrogen production via partial oxidation of hydrocarbon fuels. *International Journal of Hydrogen Energy* 2002;27(6):635-42.
- [579] S. G. Lias, "Ionization Energy Evaluation" in *NIST Chemistry WebBook*, NIST Standard Reference Database Number 69, edited by P. J. Linstrom and W. G. Mallard ~National Institute of Standards and Technology, Gaithersburg, MD, 2001. <http://webbook.nist.gov>.
- [580] B. Ruscic *et al.*, *J. Phys. Chem. A* **106**, 2727 ~2002.
- [581] Dolan T. Electron and ion collisions with water vapour. *Journal of Physics D: Applied Physics* 1993; 26:4.
- [582] Lozano-Parada JH, Zimmerman WB. The role of kinetics in the design of plasma microreactors. *Chemical Engineering Science* 2010;65 (17):4925-30.
- [583] Šingliar M. Solar energy using for hydrogen production. *Petroleum & Coal* 2007; 49(2):40-7.
- [584] Lieberman, M.A., Lichtenberg, A.J.: *Principles of Plasma Discharges and Materials Processing*. John Wiley, Hoboken (2005)
- [585] Zimmerman WBJ. Multiphysics modeling with finite element methods, series on stability, vibration and control of systems, series A, vol. 18. London: World Scientific Publishing Company; 2006.
- [586] J. Schutten, F. J. de Heer, H. R. Moustafa, A. J. H. Boerboom, and J. Kistemaker. Gross- and Partial-Ionization Cross Sections for Electrons on Water Vapor in the Energy Range 0.1-20 keV. *The Journal of Chemical Physics*, 1966, 44(10), 3924-28.

- [587] Lukes P, Clupek M, Babicky V, Simek M, Tothova I, Janda V, et al. Role of solution conductivity in the electron impact dissociation of H₂O induced by plasma processes in the pulsed corona discharge in water. HAKONE XI, 11th international symposium on high pressure, low temperature plasma chemistry, contributed papers, Ole'ron Island; 2008.
- [588] Shih KY, Locke BR. Optical and electrical diagnostics of the effects of conductivity on liquid phase electrical discharge. IEEE Transactions on Plasma Science 2010; 99:1-10.
- [589] H. Cho, Y. S. Park, H. Tanaka, and S. J. Buckman. Measurements of elastic electron scattering by water vapour extended to backward angles. J. Phys. B: At. Mol. Opt. Phys. 37 (2004) 625–634.
- [590] M. Yousfi and M. D. Benabdessadok. Boltzmann equation analysis of electron-molecule collision cross sections in water vapor and ammonia. J. Appl. Phys. 80 (1996), 6619 -30.
- [591] H. C. Straub, B. G. Lindsay, K. A. Smith, and R. F. Stebbings. Absolute partial cross sections for electron-impact ionization of H₂O and D₂O from threshold to 1000 eV. J. Chem. Phys. 108 (1998), 109- 116.
- [592] M. V. V. S. Rao, I. Iga, and S. K. Srivastava. Ionization cross-sections for the production of positive ions from H:O by electron impact. J. Geophys. Res. 100 (1995), 421-425.
- [593] Rehman F, Lozano-Parada JH, Zimmerman WB. A kinetic model for H₂ production by plasmolysis of water vapours at atmospheric pressure in a dielectric barrier discharge microchannel reactor. Int J Hydrogen Energy 2012; 37:17678-90.
- [594] I. Dincer. Technical, environmental and exergetic aspects of hydrogen energy systems. Int J of Hydrogen Energy 2002; 27: 265–285.
- [595] L. Barreto, A. Makihira, K. Riahi. The hydrogen economy in the 21st century: a sustainable development scenario. Int J of Hydrogen Energy 2003; 28: 267–284.
- [596] A. Midilli, I. Dincer. Key strategies of hydrogen energy systems for sustainability. Int J of Hydrogen Energy 2007; 32: 511 – 524.
- [597] J.O. Abe, A.P.I. Popoola, E. Ajenifuja, O.M. Popoola. Hydrogen energy, economy and storage: Review and recommendation. Int J of hydrogen energy 2019; 44: 15072 -86.
- [598] The Forever Fuel, The Story of Hydrogen, *Peter Hoffman*, 1st edition, Taylor & Francis group, eBook, 2019.
- [599] Gupta NM. Factors affecting the efficiency of a water splitting photo catalyst: a perspective. Renew Sust Energy Rev 2016; 71:585-601.
- [600] Dubey PK, Tripathi P, Tiwari RS, Sinha ASK, Srivastava ON. Synthesis of reduced graphene oxide/TiO₂ nanoparticle composite systems and its application in hydrogen production. Int J Hydrogen Energy 2014; 39:16282-92.
- [601] Simpson AP, Lutz AE. Exergy analysis of hydrogen production via steam methane reforming. International Journal of Hydrogen Energy 2007; 32(18):4811-20.

- [602] Zimmerman WB. Electrochemical microfluidics. *Chem Eng Sci* 2011; 66:1412-25.
- [603] John S, Hamann JC, Muknahallipatna SS, Legowski S, Ackerman JF, Argyle MD. Energy efficiency of hydrogen sulfide decomposition in a pulsed corona discharge reactor. *Chem Eng Sci* 2009; 64:4826-34.
- [604] Zhao G-B, John S, Zhang J-J, Hamann JC, Muknahallipatna SS, Legowski S, et al. Production of hydrogen and sulfur from hydrogen sulfide in a nonthermal-plasma pulsed corona discharge reactor. *Chem Eng Sci* 2007; 62:2216-27.
- [605] Zhao G-B, John S, Zhang J-J, Wang L, Muknahallipatna S, Hamann JC, et al. Methane conversion in pulsed corona discharge reactors. *Chem Eng J* 2006; 125:67-79.
- [606] Nozaki T, Goujard V, Yuzawa S, Moriyama S, Agiral A and Okazaki K. Selective conversion of methane to synthetic fuels using dielectric barrier discharge contacting liquid film, 2011 *J. Phys. D: Appl. Phys.* 44 274010.
- [607] Aghamir F, Matin N, Jalili A, Esfarayeni M, Khodagholi M and Ahmadi R. Conversion of methane to methanol in an ac dielectric barrier discharge, 2004 *Plasma Sources Sci. Technol.* **13** 707–11.
- [608] Dilecce G and De Benedictis S. Laser diagnostics of high-pressure discharges: laser induced fluorescence detection of OH in He/Ar–H₂O dielectric barrier discharges, 2011 *Plasma Phys. Control. Fusion* **53** 124006.
- [609] Dilecce G, Ambrico P, Simek M and De Benedictis S. LIF diagnostics of hydroxyl radical in atmospheric pressure He-H₂O dielectric barrier discharges, 2012 *Chem. Phys.* **398** 142–7.
- [610] M. B. Chang and H. M. Lee. Abatement of perfluorocarbons with combined plasma catalysis in atmospheric-pressure environment, *Catal. Today*, 2004, 89, 109- 115.
- [611] M. B. Chang and J.-S. Chang. Abatement of PFCs from Semiconductor Manufacturing Processes by Nonthermal Plasma Technologies: A Critical Review, *Ind. Eng. Chem. Res.*, 2006, 45, 4101-4109.
- [612] M. S. Gandhi and Y. S. Mok. Decomposition of trifluoromethane in a dielectric barrier discharge non-thermal plasma reactor, *J. Environ. Sci.*, 2012, 24, 1234- 1239.
- [613] T. Nozaki, Y. Miyazaki, Y. Unno and K. Okazaki. Energy distribution and heat transfer mechanisms in atmospheric pressure non-equilibrium plasmas, *J. Phys. D: Appl. Phys.*, 2001, 34, 3383-90.
- [614] N. R. Pinhão, A. Janeco and J. B. Branco. Influence of Helium on the Conversion of Methane and Carbon dioxide in a Dielectric Barrier Discharge, *Plasma Chem. Plasma Process.*, 2011, 31, 427-439.

- [615] V. Goujard, J. M. Tatibouet and C. Batiot Dupeyrat. Carbon Dioxide Reforming of Methane Using a Dielectric Barrier Discharge Reactor: Effect of Helium Dilution and Kinetic Model, *Plasma Chem. Plasma Process*, 2011, 31, 315-325.
- [616] D. B. Nguyen and W. G. Lee. Analysis of helium addition for enhancement of reactivity between CH₄ and CO₂ in atmospheric pressure plasma, *J. Ind. Eng. Chem.*, 2015, 32, 187-194.
- [617] M. Ramakers, I. Michielsens, R. Aerts, V. Meynen and A. Bogaerts. Effect of Argon or Helium on the CO₂ Conversion in a Dielectric Barrier Discharge, *Plasma Process. Polym.* 2015, 12, 755-763.
- [618] A. Ozkan, T. Dufour, G. Arnoult, P. De Keyzer, A. Bogaerts and F. Reniers. CO₂–CH₄ conversion and syngas formation at atmospheric pressure using a multi-electrode dielectric barrier discharge, *J. CO₂ Util.*, 2015, 9, 74-81.
- [619] R. Snoeckx, S. Heijckers, K. Van Wesenbeeck, S. Lenaerts and A. Bogaerts. CO₂ conversion in a dielectric barrier discharge plasma: N₂ in the mix as a helping hand or problematic impurity? , *Energy & Environmental Science*, 2015, 1-16.
- [620] M. Varne, G.R. Dey, T. N. Das. Evaluation of optimum conditions for hydrogen generation in argon-water vapor dielectric barrier discharge. *International Journal of Hydrogen Energy*, 2016; 41, 22769-774.
- [621] Nehra V, Kumar A, Dwivedi H. Atmospheric non-thermal plasma sources. *International Journal of Engineering (IJE)* 2008; 2(1):53.
- [622] Dey GR, Das TN. Yields of hydrogen and hydrogen peroxide from argon-water vapor in dielectric barrier discharge. *Plasma Chem Plasma Process* 2016; 36:523-34.
- [623] Takechi K, Lieberman MA. Effect of Ar addition to O₂ plasma in an inductively coupled, traveling wave driven, large area plasma source: O₂/Ar mixture plasma modeling and photoresist etching. *J Appl Phys* 2001; 90:3205-11.
- [624] Kogelschatz U. Dielectric-barrier discharges: their history, discharge physics, and industrial applications. *Plasma Chem Plasma Process* 2003; 23:1-46.
- [625] Y. Du, G. Nayak, G. Oinuma, Z. Peng, P. J Bruggeman. Effect of water vapor on plasma morphology, OH and H₂O₂ production in He and Ar atmospheric pressure dielectric barrier discharges. *J. Phys. D: Appl. Phys.* **50** (2017) 145201–11.
- [626] M. D. Campanell, J. N. Larid, T. Provost, S. W. Vasquez, and S. J. Zweben, “Measurements of the motion of filaments in a plasma ball,” *Phys. Plasmas* 17, 053507 (2010).
- [627] Butterworth T. Effect of volumetric flow rate on decontamination efficiency of a microplasma ozonation system. Sheffield: The University of Sheffield; 2010.

- [628] Locke B and Shih K. Review of the methods to form hydrogen peroxide in electrical discharge plasma with liquid water. *Plasma Sources Sci. Technol.* 20 (2011) 034006–21.
- [629] Liu D, Bruggeman P, Iza F, Rong M and Kong M. Global model of low-temperature atmospheric-pressure He + H₂O plasmas. *Plasma Sources Sci. Technol.* 19 (2010) 025018–40.
- [630] Atkinson R, Baulch D, Cox R, Hampson R, Kerr J, Rossi M and Troe J. Evaluated Kinetic and Photochemical Data for Atmospheric Chemistry: Supplement VI. IUPAC Subcommittee on Gas Kinetic Data Evaluation for Atmospheric Chemistry. *J. Phys. Chem. Ref. Data*, 1997, 26, 1329–499.
- [631] Baulch D, Cobos C, Cox R, Esser C, Frank P, Just T, Kerr J, Pilling M, Troe J, Walker R and Warnatz J. Evaluated Kinetic Data for Combustion Modelling. *J. Phys. Chem. Ref. Data*, 1992, 21, 411–734.
- [632] Nandi D, Krishnakumar E, Rosa A, Schmidt W and Illenberger E. Dissociative electron attachment to H₂O₂: a very effective source for OH and OH[−] generation. *Chem. Phys. Lett.* 2003, 373, 454–9.
- [633] Soloshenko I, Tsiolko V, Khomich V, Bazhenov V, Ryabtsev A, Schedrin A and Mikhno I. Features of sterilization using low-pressure DC-discharge hydrogen-peroxide plasma. *IEEE Trans. Plasma Sci.* 2002, 30, 1440–4.
- [634] Stefanidis GD, Vlachos DG. Intensification of steam reforming of natural gas: choosing combustible fuel and reforming catalyst. *Chemical Engineering Science* 2010; 65(1): 398-404.
- [635] Guoxin H, Hao H, Yanhong L. Hydrogen-rich gas production from pyrolysis of biomass in an auto generated steam atmosphere. *Energy & Fuels* 2009; 23(3):1748-53.
- [636] Rico VJ, Cotrino J, Gallardo V, Sarmiento B, Brey JJ, Gonza'lez- ElipseAR. Hybrid catalytic-DBD plasma reactor for the production of hydrogen and preferential CO oxidation (CO-PROX) at reduced temperatures. *Chemical Communications* 2009; 41:6192-4.
- [637] Medodovic S, Locke B. Primary chemical reactions in pulsed electrical discharge channels in water. *Journal of Physics D: Applied Physics* 2009; 42:049801.
- [638] Shirafuji T, Morita T, Sakai O, Tachibana K. Enhancement of OH production rate in plasma on water by mixing Ar. *Proceedings of the international symposium on plasma on plasma chemistry, Bochum, Germany; 2009.*
- [639] Zhang Y, Wen XH, Yang WH. Excitation temperatures of atmospheric argon in dielectric barrier discharges. *Plasma Sources Science and Technology* 2007; 16:441.
- [640] Abdul-Majeed WS, Parada JHL, Zimmerman WB. Optimization of a miniaturized DBD plasma chip for mercury detection in water samples. *Analytical and Bioanalytical Chemistry* 2011; 401(9):2713-22.

- [641] Zito JC, Arnold DP, Durscher RJ, Roy S. Investigation of impedance characteristics and power delivery for dielectric barrier discharge plasma actuators. In: 48th AIAA aerospace sciences meeting; 2010.
- [642] Kostov K, Honda R, Alves L, Kayama M. Characteristics of dielectric barrier discharge reactor for material treatment. *Braz J Phys* 2009; 39:322-5.
- [643] F. Rehman, Y. Liu, W. B.J. Zimmerman. The role of chemical kinetics in using O₃ generation as proxy for hydrogen production from water vapour plasmolysis. *Int J Hydrogen Energy* 2016;41,6180-92.

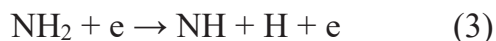
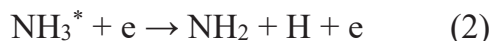
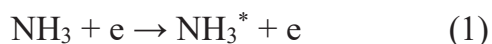
Chapter 5. H₂ Production from ammonia gas

Chapter 5 H₂ Production from ammonia gas

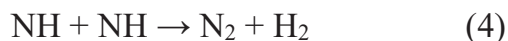
5.1 Introduction

Hydrogen is often considered as an attractive alternative fuel to overcome the environmental issues. Hydrogen is a clean energy source and can be utilized in portable energy applications with water as the combustion by-product [644]. It can be produced by different renewable energy sources. However, the hydrogen economy is still limited due to the hydrogen storage inability in a safe and economical manner [645]. Hydrogen gas demands are recently growing which motivated the scientific researchers to improve hydrogen production technologies [80, 324, 337, 338, 646, 647]. The DBD plasma can create excited and reactive species, which means that high electrons energy are generated allowing them to interact with the catalyst materials at milder temperatures and pressures. The synergistic between catalyst materials and plasma species have been studied to improve the decomposition process of different molecules such as steam reforming of methane, [648] dry reforming of hydrocarbons, [649–653], pollutant decomposition [649, 650], etc.

It has been reported the optical emission spectroscopy (OES) of NH₃ decomposition by dielectric barrier discharge plasma (DBD), it has been found that the OES of NH₃ was dominated by the band of the electronic excited NH₃^{*} molecule, in range of 563.5–567 nm [654–657]. The decomposition of NH₃ gas by DBD plasma could be mainly achieved by the NH₃^{*} species due to the other species weak band intensities of N₂^{*}, NH^{*}, H^{*}.



It was reported that ammonia decomposition by DBD plasma mainly activated to produce NH₃^{*} species, then activated by an electron to generate NH₂ and NH species. The hydrogen and nitrogen gas can be generated from NH species through the following reaction [655],



5.2 Zirconia material effect on H₂ production from ammonia-argon base gas in plasma plate type reactor

In this study, we report the hydrogen production measurements from ammonia decomposition of DBD plasma-assisted catalysis on zirconia (ZrO₂) as well as plasma-only

Chapter 5. H₂ Production from ammonia gas

reactions to assess hydrogen production through DBD plasma process and distinguish between plasma-only and catalyst material surface contributions. The hydrogen concentrations at different input ammonia-argon base concentrations of 0.5% and 2% are determined. Furthermore, the effect of residence time on hydrogen production is also evaluated. The energy efficiency and output hydrogen flow rates of plasma-assisted zirconia catalytic material is compared.

5.2.1 Experimental setup

In this experiment, ammonia-argon base gas was fed at atmospheric pressure into the plate type reactor in a range of 0.1-1.0 L/min and plasma applied voltage ranges of 12-18 kV. The hydrogen production from Ammonia gas concentrations of 0.5% and 2% were monitored. The plasma plate reactor was filled with catalyst material type of zirconia materials, Table (5.1) shows zirconia material characteristics. While the DBD plasma was ignited in the electrode gap distance of 4.5 mm. Figure (5.1) shows the schematic diagram of plasma-catalyst assisted for hydrogen production from ammonia gas. Ammonia gas was fed into the plate reactor and was controlled by the mass flow controller. The decomposed gas samples were taken using a syringe and then analyzed by the gas phase chromatography (GC). Also, the hydrogen concentration measurements were carried out for the plate reactor with and without adding zirconia catalytic material to evaluate the catalyst material effect on ammonia decomposition into H₂ and N₂ gas.

Table 5.1 Characteristics of zirconia catalyst material.

Diameter (mm)	Density (g/mL)	Relative static permittivity (at 10 kHz)	Mass (g)	Volume (L)
1	6.07	20-24	36	0.00593

Chapter 5. H₂ Production from ammonia gas

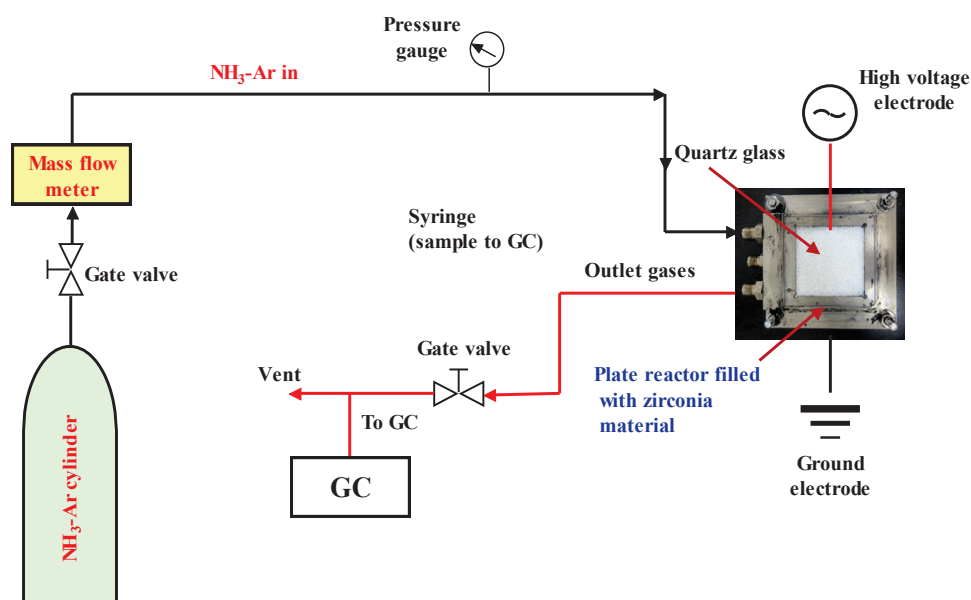


Fig 5. 1 Schematic diagram of Experimental setup.

5.2.2 Results & discussions

5.2.2.1 effect on H₂ production from 0.5% NH₃-Ar base gas

Ammonia gas is an important hydrogen energy carrier, additionally, ammonia has no environmental impact because ammonia is carbon-free. Ammonia gas is decomposed by non-thermal plasma or atmospheric to produce hydrogen and nitrogen gas. Zirconia (ZrO₂) catalytic material is used to enhance hydrogen production from ammonia gas. The most interesting observations have been registered where the DBD plasma reactor is filled with the spherical beads of a high dielectric material such as ZrO₂, it can enhance the electric fields at the points of contact between the beads will lead to getting higher concentrations of excited species [658, 659]. Also, it has been reported that the nature of catalyst surface can have an effect on the electric field, and irregularities such as surface roughness or the presence of surface pores can make variations in the electric field and some of the local regions of field intensification can become a high-energy electrons source [660]. The decomposed gases were analyzed by gas phase chromatography (GC), while the outlet gases are collected using a syringe. The conversion rate is determined according to the following expression: $\text{conversion rate [\%]} = \frac{\text{H}_2 \text{ concentration [\%]}}{(\text{NH}_3 \text{ concentration [\%]} \times 1.5)} \times 100$.

Figure (5.2) demonstrates the H₂ conversion rate of ammonia gas at different plasma applied voltage and input ammonia flow rates. It was found that the conversion rate increased with plasma voltage at all ammonia input flow rates. Also, the maximum conversion rates of 66.85 %, 33.66%, 26.47% were obtained at ammonia input flow rate of 0.1, 0.5, 1 L/min and plasma voltage of 18 kV, respectively. Furthermore, it was

Chapter 5. H₂ Production from ammonia gas

observed that the GC chemical species results included H₂, N₂, O₂ and unreacted ammonia gas. Moreover, there is a positive contribution of the zirconia packing material on the conversion obtained, because of the plasma electric field enhancement at the contact points, but a negative contribution due to the lower residence time of the high ammonia gas flow rates.

Figure (5.3) shows the hydrogen concentration at different energy density and feeding ammonia flow rates. The energy density (E_d) is calculated according to the following relation: $E_d = ((1000 \times P)/v) \times t$, where P is the input power [W], v is the reactor volume [cm^3], and ammonia decomposition residence time [s]. It was found that the hydrogen concentration increased with the energy density increased. Also, it was observed that the maximum obtained hydrogen concentration was 0.499% at ammonia input flow rate of 0.1 L/min and energy density of 69.6 J/cm³. It was clear that the best results were obtained at low NH₃ input flow rate due to high energy density. Figure (5.4) shows the residence time effect on hydrogen production from ammonia decomposition at DBD plasma applied voltage of 18 kV. It was clear that residence time was an important factor for ammonia decomposition into hydrogen and nitrogen gas which appeared with increasing ammonia input flow rate. It can be concluded that residence time has a negative effect on the hydrogen production from ammonia decomposition by DBD plasma influencing the retention time which changes the electric field distribution and plasma reactivity.

5.2.2.2 Zirconia effect on H₂ production from 2% NH₃-Ar base gas

To understand ammonia decomposition using plasma-catalysts, it is important to ammonia decomposition reaction mechanism which is initiated by the adsorption of ammonia molecules onto the active site surface. These adsorbed ammonia molecules undergo successive N–H bond cleavage, releasing hydrogen atoms that can combine to form molecular hydrogen [661]. Neyts and Bal [662] have recently investigated that the catalytic material addition to a plasma discharge can improve the plasma electric field influencing the species retention time at the catalyst material surface and increasing the surface reactivity. Moreover, the catalyst materials will yield more electrical energy when materials of higher dielectric constant are used resulting in the formation of more electrons of higher energy which increased the ionized and excited species. In this work, the effect of the ammonia feeding gas concentration on hydrogen production was investigated. Also, zirconia catalytic material was utilized to fill the plasma plate reactor type. Ammonia–argon base gas with a concentration of 2% was fed into the reactor at 0.1 L/min and atmospheric plasma voltage range of 12–18 kV.

Chapter 5. H₂ Production from ammonia gas

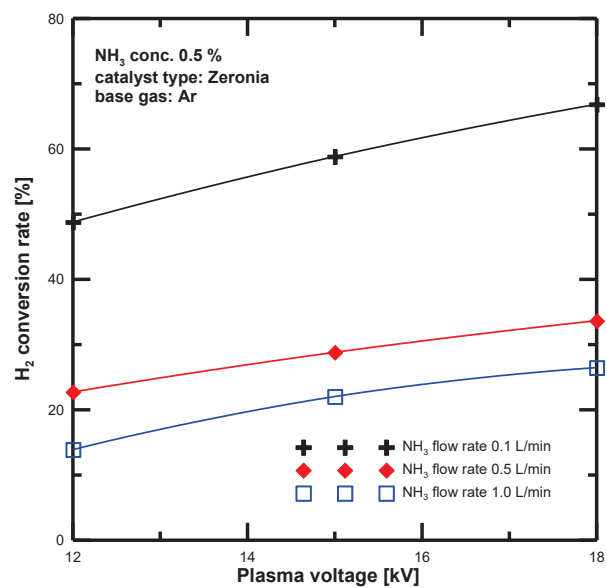


Fig 5. 2 The effect of plasma voltage on H₂ conversion at different NH₃ flow rates.

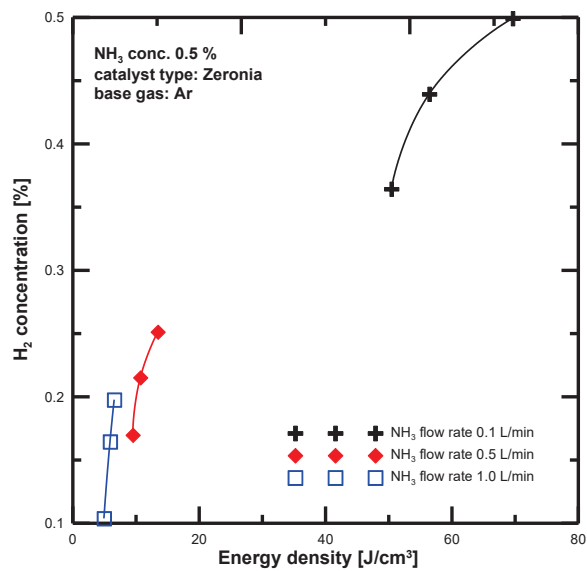


Fig 5. 3 Energy density effect on H₂ concentration at different NH₃ flow rates.

Chapter 5. H₂ Production from ammonia gas

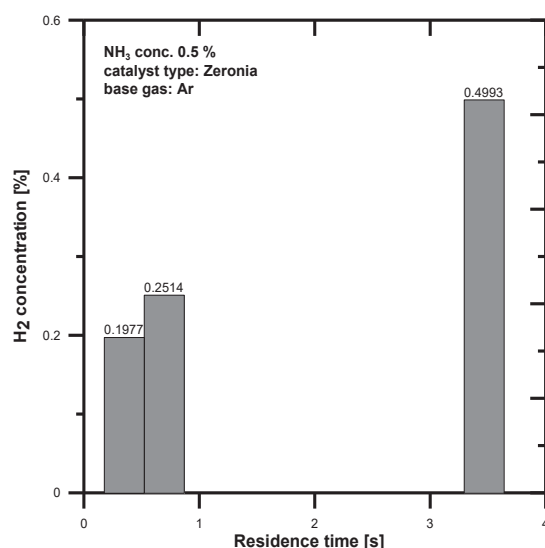


Fig 5. 4 Residence time effect on hydrogen concentration at plasma voltage of 18 kV. Also, this experiment is carried out without catalyst materials to declare zirconia catalytic material effect on the hydrogen production from ammonia-Ar gas base at different plasma applied voltage. Ammonia-Ar base experiment was carried out with and without filling the plate reactor with zirconia catalytic material. Figure (5.5) illustrates the hydrogen conversion rate results of both experiments with and without adding zirconia catalytic material. It was found that H₂ conversion rate increased with the plasma applied voltage increased. Also, the conversion rate results of ammonia decomposition experiment with adding zirconia catalytic material have higher values than ammonia decomposition experiment without catalyst material. It can be concluded that zirconia material can be utilized to enhance ammonia decomposition using DBD plasma. To clarify the catalytic material effect on H₂ production from ammonia gas, the hydrogen concentration versus the energy density is shown in figure (5.6). It was observed that the hydrogen concentration enhanced by the addition of zirconia catalytic material to the ammonia decomposition system by DBD plasma. It was clear that the ammonia gas molecules are absorbed by zirconia material active surface producing higher electron energy.

Chapter 5. H₂ Production from ammonia gas

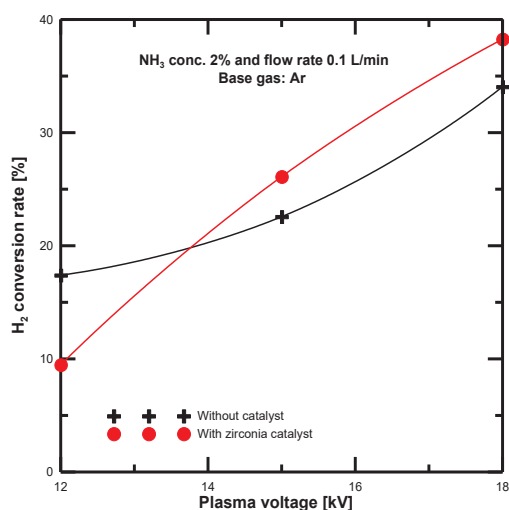


Fig 5. 5 Comparison of zirconia catalyst effect on H₂ conversion rate from 2% NH₃.

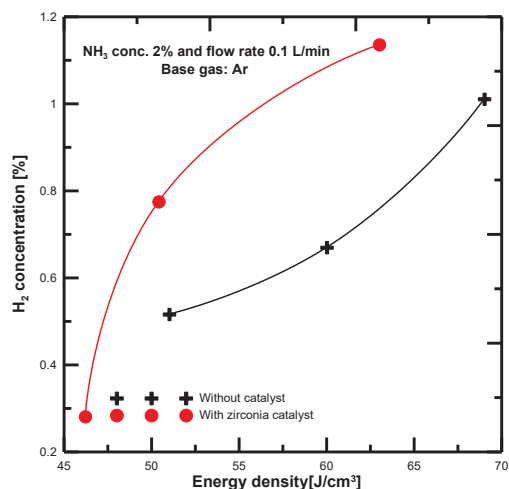


Fig 5. 6 Comparison of H₂ concentrations with and without zirconia catalyst at different energy density.

5.2.2.3 Evaluation of ammonia-Ar base gas decomposition by DBD plasma

To assess the decomposition process of the ammonia-Ar gas base at different concentrations by the DBD plasma, the hydrogen flow rate was determined at an input flow rate of 0.1 L/min and at different input electric power. A comparison between the hydrogen flow rates results of ammonia input concentrations of 0.5 & 2% was described in figure (5.7). It was found that the hydrogen flow rate increased with the input power for both ammonia input concentrations. However, the hydrogen flow rate results of the ammonia input concentration of 2% were higher than lower input ammonia concentration at different input electric power. In addition to the catalyst effect on ammonia decomposition by DBD plasma, it can be concluded that the hydrogen production will also depend on the plasma

Chapter 5. H₂ Production from ammonia gas

input power. The energy efficiency of the DBD ammonia decomposition process will also depend on the catalyst material structural features such as its morphology, porosity, and chemical activity as well as plasma nature. Figure (5.8) compares the energy efficiency results of both ammonia experiment concentrations at different electric power. It was clear that energy efficiency increased with increasing plasma input power. Furthermore, it was found that the maximum energy efficiency obtained at NH₃ concentration of 2% was 0.1948 % while at 0.5% NH₃ concentration was 0.084%.

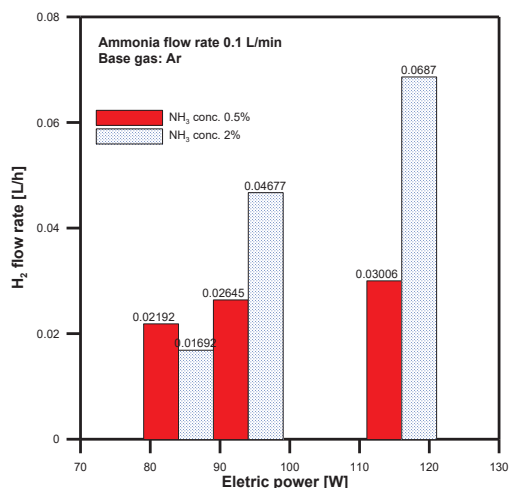


Fig 5. 7 Comparison between H₂ flow rate results of different ammonia input concentrations.

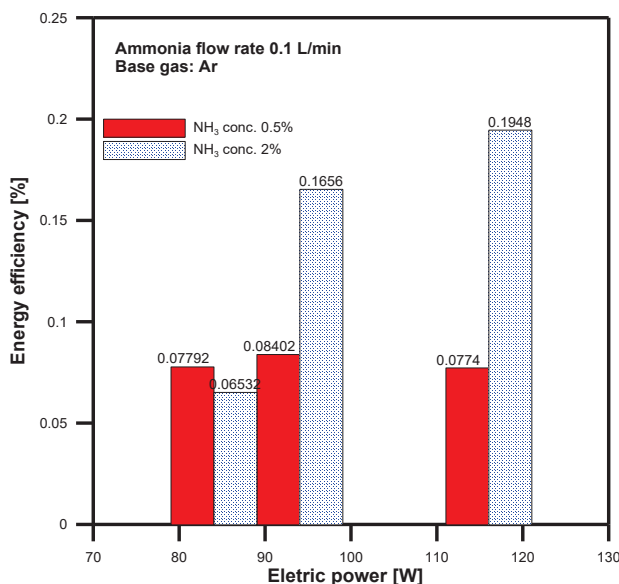


Fig 5. 8 Comparison of energy efficiency results at different plasma input power.

Chapter 5. H₂ Production from ammonia gas

Conclusion

Ammonia-argon base gas was decomposed into hydrogen and nitrogen gas by DBD plasma at different ammonia-argon gas base concentrations of 0.5% and 2% were investigated. The effect of zirconia catalyst material on ammonia decomposition was studied. It was found that the NH₃ conversion rate was significantly increased when DBD plasma was combined with the catalyst. Furthermore, it was observed that the energy density has a positive effect on the produced hydrogen gas concentrations of both ammonia concentrations experiments. Additionally, it was clear that hydrogen concentration increased with ammonia decomposition reaction time or residence time increase. The NH₃ conversion and hydrogen concentration obtained by plasma-catalyst mode from ammonia concentration of 2% were much higher than those obtained using plasma only. Also, it was compared the hydrogen concentration results at different input energy density for NH₃ decomposition with and without zirconia catalyst. It was found that the hydrogen concentration of plasma-catalyst system was much higher than plasma only system. An evaluation of plasma-catalyst system was developed to compare different ammonia input concentrations. In general, adding zirconia catalytic material into the ammonia decomposition process by DBD plasma will affect the physical and electrical properties of the gas discharge which causes some modification to the produced hydrogen and nitrogen gases of the plasma-catalytic processes. The energy efficiency results of both ammonia concentrations experiments were compared. It was seen that the maximum energy efficiency obtained at NH₃ concentration of 2% was 0.1948 % while at 0.5% NH₃ concentration was 0.084%.

5.3 Ruthenium and Soda glass effect on NH₃ decomposition

Hydrogen fuel is the best solution to tackle the CO_x and NO_x emission to the environment from the traditional fossil fuels [663]. The hydrogen combustion has registered more enthalpy (142 MJ/kg) than other fuels [80]. Hydrogen is mostly available in water and gaseous hydrocarbon fuels. Numerous studies have been reviewed the hydrogen production technologies [80, 324]. Thus, more energy is consumed to generate hydrogen fuel from steam reforming, water splitting, etc. Further, the preliminary results of the hydrogen production from water vapour decomposition by dielectric barrier discharge plasma (DBD) have been experimentally demonstrated [337].

Ammonia has more advantages than the other hydrogen energy carriers; Table (5.2) compares between the fuel's characteristics for hydrogen energy storage [664]. Ammonia has a higher gravimetric density than the other fuels; in addition to the stored energy cost per volume of ammonia is three times lower than of hydrogen fuel [665]. Therefore, ammonia can be typically used as an eco-friendly energy carrier due to the combustion products are only water and nitrogen [666]. Ammonia decomposition process has been

Chapter 5. H₂ Production from ammonia gas

delivered a CO_x-free hydrogen fuel for fuel cells and the electric vehicles applications [517].

Ammonia gas can be decomposed by thermal heating and plasma. Hydrogen production from thermal catalytic ammonia decomposition has been investigated [511]. The DBD plasma is considered a specific plasma type of AC discharge; it can be ignited at atmospheric pressure and provides good thermodynamics non-equilibrium plasma. Furthermore, it has been reported that the catalyst-plasma can activate and produce a variety of molecules such as methane (CH₄), and Ammonia (NH₃) to generate the desired products [667–669]. The supported catalyst materials such as Ru, Ni, Fe, and Ir have been commonly used in the hydrogen production processes. Moreover, ruthenium (Ru) is presented the most highly active transition metals [670]. Ruthenium material is always supported using metal oxides like Al₂O₃ and MgO.

The plasma-catalytic ammonia decomposition has been enhanced the hydrogen production process [368]. Ammonia gas can be produced from syngas by Haber-Bosh process. Also, Christensen et al. [671] have been suggested to convert fossil fuels into ammonia gas and then utilized as a clean fuel in the remote applications. Further, ammonia can be thermally decomposed into N₂ and H₂ at a temperature range of 350–400 °C [672]. The hydrogen production from ammonia is a more attractive process compared with the methane reforming process because there is no CO_x emission, no water for steam reforming, and the poisoning of PEM electrodes is completely eliminated because there is no CO production. Ammonia can be decomposed by thermal heating and electrolysis processes [673]. Moreover, the hydrogen production from ammonia is a cost-effective, more reliable, and environmentally friendly than the other hydrogen production techniques.

Various catalytic ammonia decomposition reactor configurations have been reviewed [491]. The most common catalytic reactors type was the packed-bed reactors, but these reactors cannot meet the scale up requirements [492]. Hence, more considerable researches have been delivered to develop more efficient reactor with low residence time and high responsiveness [493, 494]. The microreactor technologies can provide a specific activation area and more efficient hydrogen transport [495]. The combining between plasma and catalyst is enhanced the ammonia decomposition process due to the ignition of plasma raise the reactor temperature and leads to more catalyst activation [667].

Chapter 5. H₂ Production from ammonia gas

The current study aims to report the effect of ruthenium and soda glass catalyst materials on the hydrogen production from ammonia decomposition using the plasma-catalytic reactor. The hydrogen concentrations result from ammonia gas using ruthenium (Ru/Al₂O₃) and soda glass (SiO₂) as catalyst materials are experimentally investigated. Low ammonia gas concentration of 0.5% is injected into the plate microreactor at ambient conditions, while the dielectric barrier discharge plasma (DBD) type is ignited. The conversion rate results are determined for the both plasma-catalyst systems. Further, the hydrogen conversion rate and the energy efficiency of both experiments are compared to assess the plasma-catalyst system effect on the ammonia decomposition process.

Table 5. 2 Comparison between ammonia and other fuels for hydrogen storage [664].

Fuel/storage	Pressure (bar)	Density (kg/m ³)	HHV (MJ/kg)	Energy density (GJ/m ³)	Specific volumetric cost (\$/m ³)	Specific energetic cost (\$/GJ)
Gasoline (C ₈ H ₁₈ /liquid tank)	1	736	46.7	34.4	1000	29.1
CH ₄ /integrated storage system	250	188	55.5	10.4	400	38.3
LPG	14	288	48.9	19	542	28.5
Methanol	1	749	15.2	11.4	693	60.9
Hydrogen/metal hydrides	14	25	142	3.5	125	35.2
Ammonia/pressurized tank	10	603	22.5	13.5	181	13.3
Ammonia/metal amines	1	610	17.1	10.4	183	17.5

5.3.1 Experimental

Ammonia-argon gas concentration of 0.5% was fed into the plasma-catalytic plate microreactor at atmospheric pressure in a range of 0.1-1.0 L/min. The DBD plasma type was ignited at a sinusoidal frequency of 10 kHz and applied voltage range of 12-20 kV. The DBD plasma can produce a good reactive plasma area at the ambient temperature with low power consumption and too short response time [361]. The effects of two different catalyst material types of ruthenium-aluminum (Ru/Al₂O₃), and soda glass (SiO₂) on the ammonia decomposition were investigated. Figure (5.9) shows the schematic diagram of the ammonia decomposition experimental setup by DBD plasma in the catalytic

Chapter 5. H₂ Production from ammonia gas

microreactor. Mass flow controller was used to control the ammonia feeding gas, while the gas pressure was adjusted by pressure regulator. Thermocouples K-type was conducted to monitor the temperature change across the ammonia decomposition process. The atmospheric pressure or the DBD plasma was generated in the gap distance of 4.5 mm between the high voltage and the ground electrodes. The glass quartz plate thickness of 2 mm was utilized as the dielectric barrier, while the high voltage electrode was connected into the top of the reactor (mesh copper plate). The stainless steel material was used in the manufacturing of the reactor parts. The concentration of the hydrogen gas was analyzed using the gas chromatography (GC) model type of (GC-2014S, SHIMADZU). The catalyst material was installed inside the reactor gap; Table (5.3) presents the characteristics of the catalytic materials utilized in this study. Moreover, the DBD plasma effect on the decomposition process was investigated. Figure (5.10) describes the ammonia gas conversion by the DBD plasma in the existence of the catalyst materials. This figure declares the ammonia decomposition process under the DBD plasma and catalytic material effect. It has been reported that the hydrogen production from ammonia decomposition enhanced with the temperature increased [674]. The ammonia decomposition processes would be enhanced by combining plasma and catalyst materials. Ammonia decomposition using Ru-particle size range of 2–7 nm has been reported [675, 676].

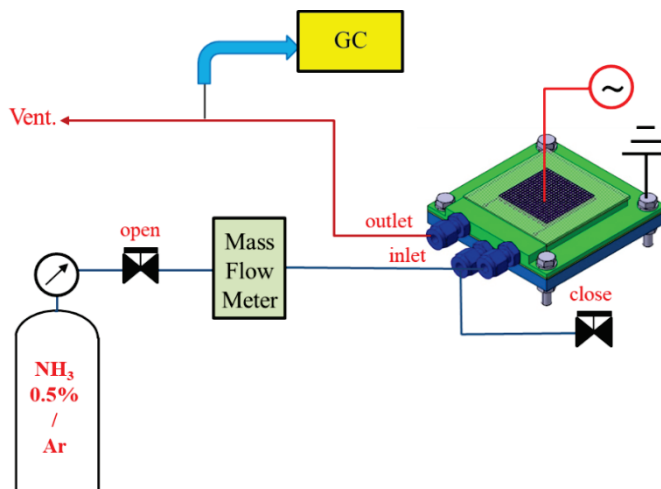


Fig 5. 9 The experimental setup Schematic diagram.

Chapter 5. H₂ Production from ammonia gas

Table 5. 3 Characteristics of the catalyst materials.

	Main component	Particle diameter	Density	Relative permittivity
	—	mm	g/cm ³	—
Ruthenium	Ru/Al ₂ O ₃	1.0		
Soda glass	SiO ₂ (70%)	1.0	2.5	6.0

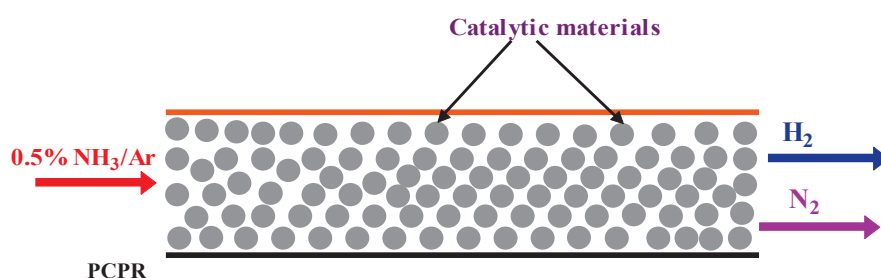


Fig 5. 10 Schematic presenting ammonia decomposition into H₂ and N₂ gas in the plasma catalytic plate reactor.

5.3.2 Results & discussions

Experimental analysis of ammonia decomposition under atmospheric pressure plasma assisted with two different catalyst materials was carried out comparing the produced H₂ gas concentrations and the hydrogen conversion rates. The performance of the catalytic materials was determined as a function of plasma applied voltage and inlet ammonia gas flow rate. It has been reported that the plasma ignition is accompanied with the reactor temperature increase [511]. The resulting plasma heat would enhance the catalyst material activation and improve the NH₃ decomposition process. Figure (5.11) compares the surface temperatures at obtained from ammonia decomposition process at different applied plasma voltage. It was found that the surface temperature increased with the plasma applied voltage increased. Also, it was noted that the surface temperature increased with the plasma ignition time. The hydrogen production from ammonia decomposition using both catalytic materials will discuss in details in the next section.

Chapter 5. H₂ Production from ammonia gas

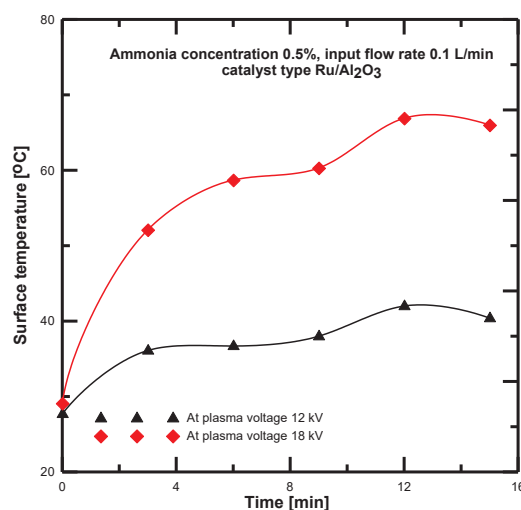


Fig 5. 11 Comparison of surface temperature obtained with the Ru catalyst at different plasma voltage.

Ruthenium-Aluminum catalyst effect on Ammonia decomposition

The performance of the hydrogen production from ammonia decomposition by DBD plasma assisted with the Ru/Al₂O₃ catalyst. The microreactor gap was filled with the Ru catalyst material with a particle size diameter of 1 mm. Figure (5.12) shows the assembled reactor with the Ru catalyst material, in addition to the reactor plasma ignition photo. It was clear that the DBD plasma was uniformly ignited. The hydrogen concentrations were measured at different input ammonia gas flow rate and at different plasma voltage. Figure (5.13) shows the hydrogen concentration results at different input ammonia gas flow rates with Ru-catalyst material. The Ru/Al₂O₃ catalyst shows the highest hydrogen concentrations and reaction rates with increasing the plasma applied voltage. It is indicated that the Ru catalyst effect raised with the input ammonia flow rate increased. Ammonia gas decomposition with supporting the ruthenium particles were registered an important effect as a function of the plasma voltage to enhance the hydrogen production from ammonia gas. Ammonia decomposition using a catalytic membrane reactor (Ru) at pressure range of (3-5 bar) and temperature ranges of (350-450°C) has been described [511]. Ruthenium materials have been showed that a highly activation to NH₃ decomposition.

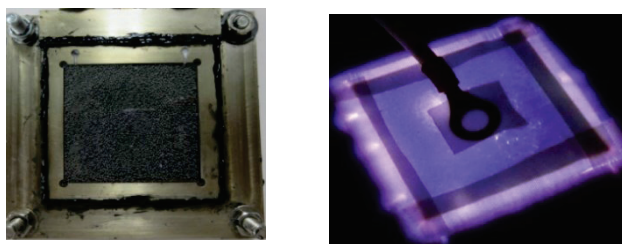


Fig 5. 12 Photographs of the PCPR complete assembly with Ru and under plasma ignition.

Chapter 5. H₂ Production from ammonia gas

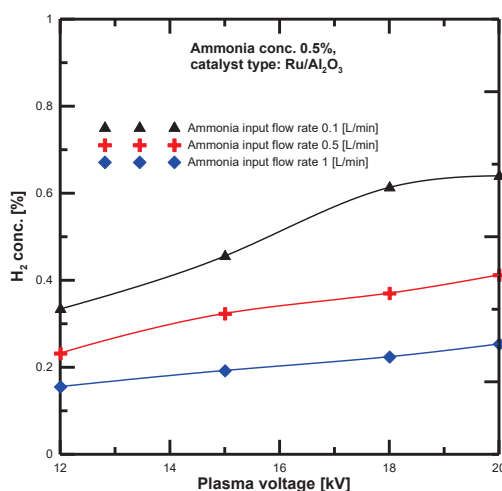


Fig 5.13 Comparison of H₂ concentration results at different input ammonia flow rates with assistance of Ru/Al₂O₃ catalyst.

To clarify ammonia decomposition with supporting of the Ru catalyst, the conversion rate was calculated as a function of the H₂ gas concentration as follows: $conversion\ rate\ [\%] = \frac{H_2\ concentration\ [\%]}{(NH_3\ concentration\ [\%] \times 3/2)} \times 100$. Figure (5.14) shows the conversion rate of the catalytic activity of ammonia decomposition at different plasma voltage and NH₃ input flow rate. The atmospheric pressure or DBD plasma was ignited at applied voltage range of 12-20 kV and plasma power range of 56-90 W, respectively. It was found that the conversion rate increased with the plasma voltage due to the resulting temperature increased with the plasma applied voltage increase which raised the effect of the support material and lead to more Ru particles activation. The maximum obtained conversion rate was 85.65% at plasma voltage of 20 kV and NH₃ flow rate of 0.1 L/min. It has been reported that the Ru-catalyst materials have a high sensitive structure and activity to ammonia decomposition because of its electronic properties that desorbed N diatoms [375, 677]. Furthermore, the smaller Ru particle size (<0.8nm) will lead to high activation [675].

Chapter 5. H₂ Production from ammonia gas

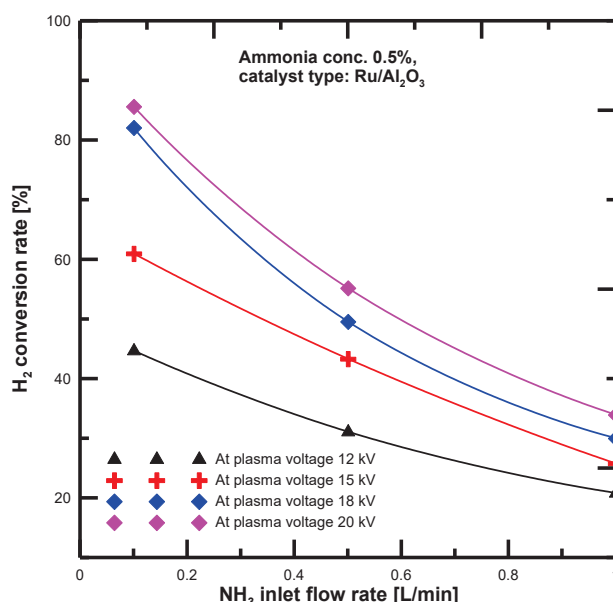


Fig 5. 14 Comparison of ammonia decomposition with the Ru catalytic activity at different NH₃ inlet flow rates.

Soda glass (SiO₂) catalyst effect on ammonia decomposition

Different catalyst materials characterization studies have been investigated using chemisorption are failed because of the activation surface area of the catalytic materials and its loading are limited [678]. Soda glass (SiO₂) catalyst materials with particle diameter of 1 mm are prepared. Ammonia gas was fed into the reactor at NH₃ concentration of 0.5% and flow rate range of 0.1-1 L/min. The microreactor is filled with the soda glass material then reassembled and the plasma ignition is shown in figure (5.15). The plasma ignition photo was taken at plasma voltage of 14 kV and NH₃ gas flow rate of 0.1 L/min. The plasma-catalyst can enhance the hydrogen production from ammonia decomposition because it will combine between the plasma and catalyst material advantages [667]. Furthermore, the resulting heat from the plasma ignition is revealed the catalytic material activation. This study focuses on the low ammonia concentration (0.5%) decomposition using different using different catalyst materials under the DBD plasma ignition at different applied plasma voltage. Soda glass (SiO₂) material has several advantages such as low material cost, high durability, and high chemical stability. Hence, it can be used as a highly activated catalyst materials. Figure (5.16) demonstrates the plot of the hydrogen concentration versus the plasma voltage at different ammonia gas flow rates. The hydrogen concentration results are increased with the DBD plasma voltage at all NH₃ feeding flow rates. Moreover, the maximum H₂ concentration results are obtained at low NH₃ feeding flow rate (0.1 L/min) because of its high energy density and larger residence time. The hydrogen production from ammonia gas decomposition was appeared to be an excellent choice to cover the fuel cells market needs from H₂ gas due to the hydrogen production from ammonia gas is a CO_x-free [679]. Figure (5.17) illustrates the hydrogen conversion

Chapter 5. H₂ Production from ammonia gas

rate of NH₃ decomposition under plasma-catalyst at different DBD plasma applied voltage. The soda glass material activation is enhanced with the plasma voltage that leads to larger NH₃ conversion rate. It was clear that the supported catalytic materials play an important role for ammonia decomposition process using DBD plasma. The conversion rate of ammonia decomposition supported by soda glass catalyst was 84.39, 54.66, and 29.79% at 0.1, 0.5, and 1 L/min, respectively. The conversion rate results of NH₃ decomposition by DBD plasma supported by soda glass showed a higher conversion rate than that obtained from heating-supported by soda glass material (conversion rate 70% at temperature of 923K) [670]. The influence of the Ru/Al₂O₃ catalytic materials on the ammonia decomposition conversion rate is greater than SiO₂ materials under the DBD plasma effect. Similar results have been obtained by Vannice and co-workers from the ammonia decomposition supported by Ru and SiO₂ materials [680].

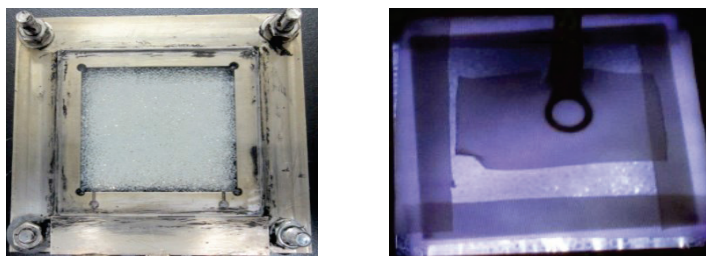


Fig 5. 15 The PCPR full assembly with soda glass and plasma ignition photos.

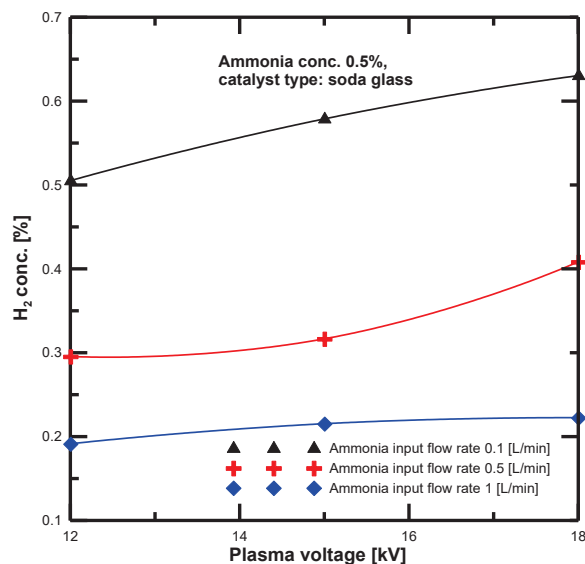


Fig 5. 16 Comparison of H₂ concentration results at different ammonia flow rates with assistance of SiO₂ catalyst.

Chapter 5. H₂ Production from ammonia gas

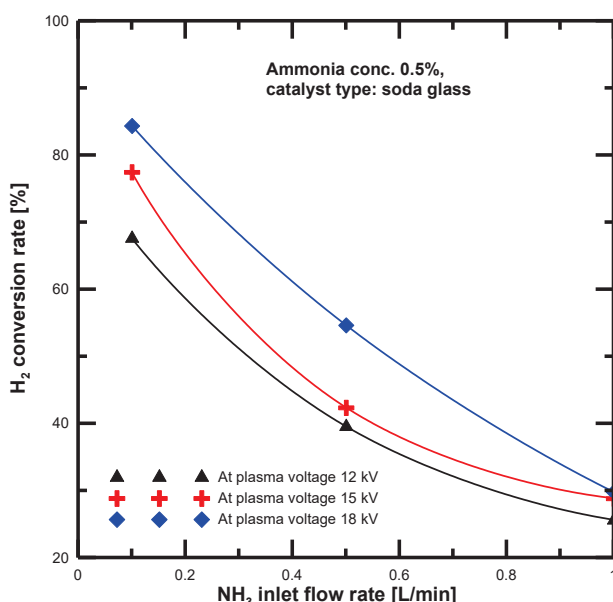


Fig 5. 17 Comparison of ammonia decomposition with the SiO₂ catalytic activity at different NH₃ inlet flow rates.

5.3.3 Assessment of the catalyst effect on the hydrogen production from ammonia decomposition by DBD plasma

The combination of the catalytic materials with the DBD plasma type is considered a promising method to generate high hydrogen concentration compared with applying plasma or catalyst alone. In this paper section, an assessment between the plasma-catalyst systems was developed for hydrogen production from low ammonia concentration decomposition. Figure (5.18) compares the conversion rate results of the plasma-catalyst ammonia decomposition systems. The Ru/Al₂O₃ catalyst showed the highest conversion rate results compared with the other plasma-catalyst systems. These results are similarly same as the previous literature survey results that the Ru-catalyst has the highest influence on the plasma-catalyst system. Whereas, the soda glass as a catalyst material also showed a high conversion rate under the DBD plasma effect. The maximum conversion rate of the plasma-catalyst system using SiO₂ was 84.39%, while the Ru/Al₂O₃ catalytic system was registered 85.65%. On the other hand, Ru-catalyst has been used in ammonia decomposition under heating process to increase the H₂ recovery to 35% [511]. Therefore, several researches have been developed using Ru/Al₂O₃ to decrease the process cost and combining between ruthenium and alumina properties can maximize the hydrogen production from NH₃ decomposition [681, 682].

Chapter 5. H₂ Production from ammonia gas

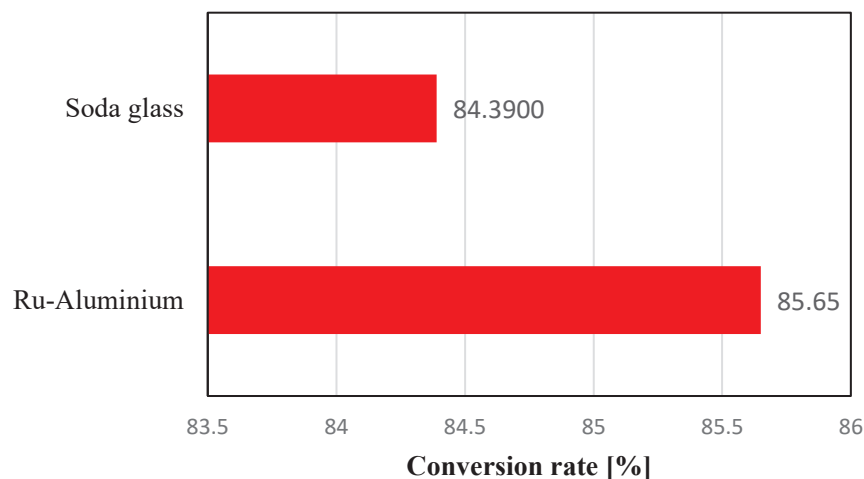


Fig 5. 18. Comparison of ammonia decomposition conversion rate results at different catalyst material types.

The energy efficiency of the ammonia decomposition can be determined according to the following equation:

$$\text{Energy efficiency}[\%] = \frac{\text{HHV} * \text{H}_2 \text{ flow rate}[\text{W}]}{\text{The total power consumption} [\text{W}]} \times 100$$

Figure (5.19) compares the energy efficiency plot of Ru/Al₂O₃ and SiO₂ experiments at different plasma applied voltage. It was found that the energy efficiency of the ruthenium plasma catalyst material has higher values than that obtained from SiO₂-plasma experiment. By applying plasma, it will lead to a high catalyst dispersion and more active surface area. It was observed that the activated catalyst is enhanced the ammonia decomposition by DBD plasma. The main difference between thermal ammonia decomposition and plasma decomposition is the operating pressure, plasma-catalyst system operates at atmospheric pressure. It can be concluded that the catalyst material is enhanced the NH₃ decomposition process using DBD plasma due to the formation of microdischarges and the electric field surface enhancement.

Chapter 5. H₂ Production from ammonia gas

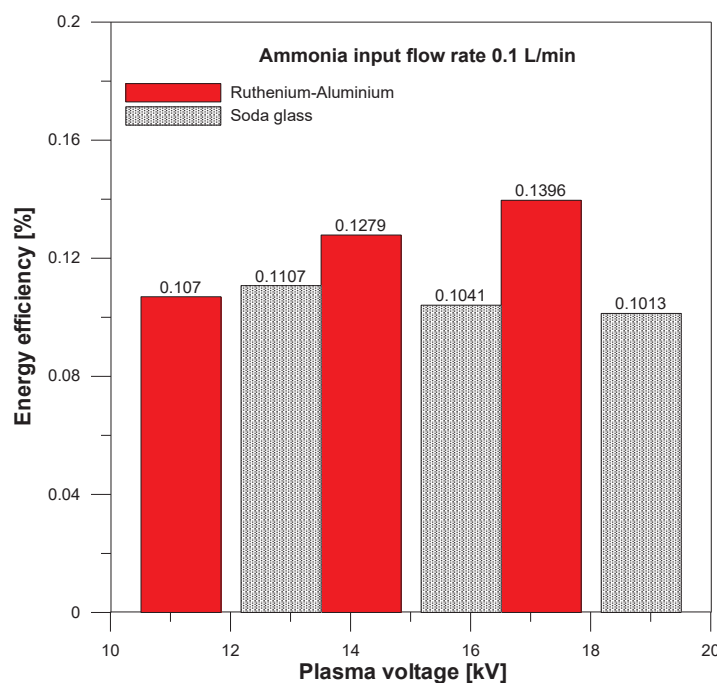


Fig5. 19 Comparison of ammonia decomposition energy efficiency results at different plasma voltage.

Conclusion

Hydrogen production from ammonia gas decomposition by DBD plasma using Ru/Al₂O₃ and SiO₂ as a catalytic material was evaluated. Low NH₃/Ar gas base concentration of 0.5% was investigated at a flow rates of 0.1-1 L/min, while the DBD plasma was ignited at applied voltage range of 12-20 kV. The soda glass material (SiO₂) is used due to its advantages like inexpensive material cost and high durability. The results are compared with the Ru/Al₂O₃ catalyst material results. It was found that ruthenium catalyst material is the most activation catalyst material, additionally, the maximum conversion rate results of Ru-catalyst, SiO₂ are 85.65, and 84.39%, respectively. Furthermore, the combining between plasma and catalyst materials is enhanced the ammonia decomposition process. By applying plasma leads to more activated catalyst material surface area and leads to more hydrogen production. Also, the energy efficiency of the Ru/Al₂O₃ catalyst showed a higher result than that obtained from SiO₂ material. Moreover, it was found that the the combining between plasma and catalyst material in NH₃ decomposition is a promising technology especially it works at atmospheric pressure. The resulting heat from plasma is enhanced the hydrogen production from ammonia decomposition. Finally, soda glass can be utilized in the NH₃ decomposition process with a high conversion rate and at low cost, but more studies are still required to investigate the durability in ammonia decomposition.

Chapter 5. H₂ Production from ammonia gas

5.4 Alumina thickness effect on low concentration ammonia

Numerous efforts have been investigated to develop the hydrogen energy carriers for delivery and storage [683, 684]. Hydrogen fuel can be generated from methanol and ammonia with high energy density [685, 686]. Furthermore, different hydrogen production technology studies have been investigated [80, 324]. Preliminary results have been introduced for water vapour decomposition by dielectric barrier discharge plasma (DBD) [337]. It has been reported that the (DBD) plasma-assisted with the catalytic materials can activate and transform a variety of molecules such as methane (CH₄), Ammonia (NH₃), and organic pollutants, to generate the desired products [667–669]. Among the hydrogen energy carrier, ammonia gas has the highest gravimetric density (17.7 wt %) and hydrogen contents. Also, the decomposition process of ammonia gas is carbon-free by means of no need to manage the CO_x species [517]. Different ammonia decomposition processes have been presented to deliver pure hydrogen gas without environmental impact. Ammonia decomposition with catalytic materials has been developed a higher hydrogen production yield [368]. The transition catalyst materials including Ru, Ni, and Fe are commonly used in the NH₃ decomposition process [370]. Ruthenium (Ru) catalyst materials have been registered the highest activation results, while Ni is sometimes used due to the ruthenium material cost is high [27]. Hence, Ru materials are supported by metal oxides such as Al₂O₃, and MgO. Ammonia gas can be decomposed into H₂ and N₂ gas by the thermal decomposition and DBD plasma [368, 511]. The combining between plasma and catalyst material is enhanced and accelerates the H₂ production from NH₃ gas [668]. The catalyst material grain size is considered an important parameter in NH₃ activation and decomposition processes [687]. The objective of the current study was to investigate the effect of alumina materials (Al₂O₃) thickness on a low concentration NH₃ decomposition by DBD plasma. Alumina. Alumina is used as a catalyst material at different diameters size 1 mm, 2 mm. Comparisons between the hydrogen concentrations, conversion rate, and the energy efficiencies are developed to elucidate the highest reactor operating conditions.

5.4.1 Experimental

In this experiment, 0.5% ammonia-argon gas was fed into the fixed bed plasma catalytic plate type reactor at atmospheric pressure in a range of 0.1–1.0 L/min. The dielectric barrier discharge plasma (DBD) was applied at the sinusoidal frequency of 10 kHz and voltage range of 12–18 kV. The atmospheric pressure or the DBD plasmas is considered a specific plasma type which can provide a good thermodynamics non-equilibrium, easy to use, and DBD plasma is effective in the gases chemical and physical processes [536]. Furthermore, the DBD plasma has the ability to produce a highly reactive plasma at room temperature with low power consumption at atmospheric pressure condition and very short response time [361]. The effects of alumina material grain size diameters of 1 mm, and 2 mm on ammonia decomposition were tested. The hydrogen production from Ammonia gas

Chapter 5. H₂ Production from ammonia gas

concentration of 0.5% was monitored at different input gas flow rate. Figure (5.20) shows the schematic diagram of the ammonia decomposition by DBD plasma in the catalytic reactor. The ammonia feeding gas flow rate was controlled by the mass flow controller and ammonia gas pressure was adjusted by pressure regulator. Thermocouples K-type were conducted to monitor the temperature change across the ammonia decomposition process. The atmospheric pressure or the dielectric barrier discharge plasma was generated in the gap distance of 4.5 mm between the high voltage electrode and the ground electrode. The glass quartz plate thickness of 2 mm was utilized as the dielectric barrier, while the high voltage electrode was connected into the top of the catalytic reactor (mesh copper plate). The stainless-steel material was used in the manufacturing of the reactor parts. The produced gas samples were taken using a syringe. The concentrations of the hydrogen and nitrogen gas were analyzed by the gas chromatography (GC) model type of GC-2014S, SHIMADZU. The GC accuracy was determined in range of $\pm 5\%$ using the standard gas concentrations. The plasma catalytic plate reactor was filled with catalyst materials; Table (5.4) shows the characteristics of the alumina catalytic materials. The DBD plasma effect on the decomposition process was investigated. The catalyst materials are prepared and installed inside the fixed bed reactor. It was reported that ammonia decomposition reaction activity increased with temperature increased [674]. Ammonia gas is decomposed by the DBD plasma according to the following reaction:



The NH₃ decomposition was estimated from the H₂ and N₂ concentration measurements. The catalyst materials are considered an important parameter influencing ammonia decomposition process.

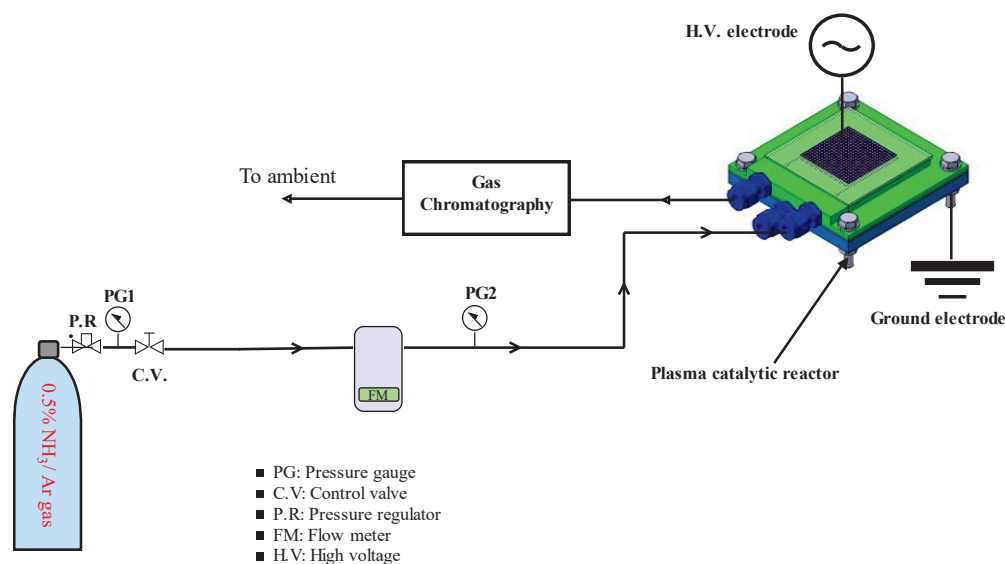


Fig 5. 20 The schematic diagram of ammonia decomposition experimental setup.

Chapter 5. H₂ Production from ammonia gas

Table 5. 4 Characteristics of the catalyst materials.

	Main component	Particle diameter	Density	Relative permittivity
	—	mm	g/cm ³	—
Alumina (type-1)	Al ₂ O ₃ (99.5%)	1.0	3.8	10.0
Alumina (type-2)	Al ₂ O ₃ (99.5%)	2.0	3.8	10.0

5.4.2 Results & discussions

Alumina (Al₂O₃) is considered a basic catalytic material support because of its strength, chemical inertness, and hardness is high. Alumina as a catalyst material can possess a larger surface area which results in its high surface activation for the decomposition process. In this paper section, two different alumina particle diameter size materials (1mm, 2mm) were tested. Figure (5.21) shows the reactor assembly and the plasma ignition photos of both materials. The plasma ignition photos are taken at plasma voltage of 18 kV. Low ammonia gas concentration (0.5%) was fed into the reactor at different gas flow rates. Ammonia is decomposed under the DBD plasma voltage ranges of 12-18 kV. The plasma-catalyst system has been reported a higher H₂ production rate than that obtained from plasma only or catalyst only experiments.

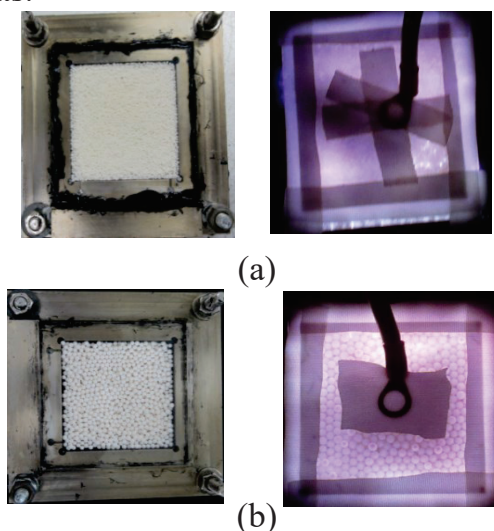


Fig 5. 21 The catalytic reactor full assembly with Alumina photos: a) Al₂O₃ particle size 1 mm b) Al₂O₃ particle size 2 mm.

Chapter 5. H₂ Production from ammonia gas

Alumina material is usually utilized as a metal support material combining with materials such as (Ru, Ni, and Ir). It is expected that the combining between plasma and the alumina catalyst would enhance the hydrogen production from ammonia decomposition. Figure (5.22) compares the hydrogen concentration results from ammonia decomposition by plasma-alumina catalyst at different ammonia feeding flow rates and plasma voltage. It was found that the hydrogen concentration results of Al₂O₃ particle size diameter 1 mm are higher than Al₂O₃ particle size diameter of 2 mm. The activation surface area of catalyst material depends on the particle size, therefore the ammonia decomposition using small alumina particle diameter showed the highest H₂ concentration results. In the DBD plasma type, High-electron energy can be generated inside the plasma-catalyst discharge zone [670]. Low concentration ammonia is decomposed at atmospheric pressure and ambient temperature through the impact reaction of electrons. Therefore, the ammonia gas can be decomposed at low operation cost. Furthermore, the combination between the DBD plasma and the heterogeneous catalyst materials is revealed the produced hydrogen gas from ammonia decomposition. Figure (5.23) demonstrates the H₂ conversion rate plot at different NH₃ input flow rates and plasma applied voltage. Alumina is utilized as a catalyst material with different particle sizes in two different NH₃ decomposition experiments. The catalyst material particle size showed an important effect on the conversion of NH₃ gas. It was found that the conversion rate results of smaller Al₂O₃ particle size (1 mm) are higher than Al₂O₃ (2 mm) because of the smaller alumina particle size has the highest activation surface area. Moreover, the resulting heat from the applied plasma is activated the catalyst contact surface area in the plasma discharge zone that leads to increase the hydrogen production from ammonia decomposition. Furthermore, the addition of Ar, He, and N₂ gas can also improve the DBD plasma reaction efficiency because that allows the activated Ar dilution gas reacts with the reactant molecules. The DBD plasma reaction enhanced the catalyst dispersion and leads to a large activation surface area [369-371]. Also, the plasma-catalyst system can be carried out at lower operation temperatures that reduce the catalyst sintering and agglomeration. Furthermore, one of the most important function of combining plasma and catalyst is to prevent the coke formation. The combination of the catalytic materials with the DBD plasma type is considered a promising method to produce a higher hydrogen concentration compared with the plasma or catalyst only. The assessment of the plasma-catalyst systems was developed for hydrogen production from low ammonia concentration decomposition.

Figure (5.24) compares the energy efficiency results of the plasma-catalyst ammonia decomposition systems. The energy efficiency can be determined according to the following equation:

$$\text{Energy efficiency}[\%] = \frac{\text{HHV} * \text{H}_2 \text{ outlet flow rate}[\text{W}]}{\text{The total energy consumption} [\text{W}]} \times 100$$

The energy efficiency result of NH₃ feeding flow rates of 0.1 and 0.5 L/min of alumina 2 mm was higher than that obtained from alumina 1 mm due to the total power consumption

Chapter 5. H₂ Production from ammonia gas

is high. The activation surface area of catalytic material is an important factor influencing the H₂ production from ammonia decomposition by DBD plasma. It was observed that alumina catalyst material has the ability to activate and enhance the H₂ production from ammonia decomposition.

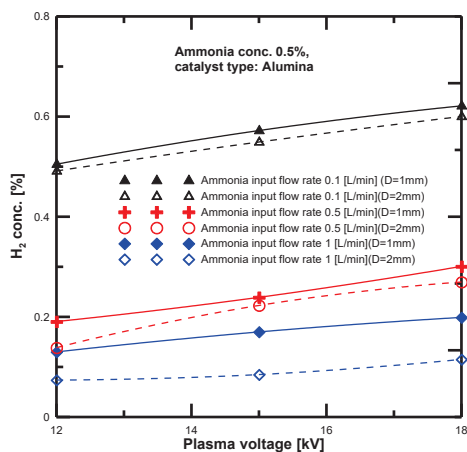


Fig 5. 22 Hydrogen concentration results at different plasma voltage.

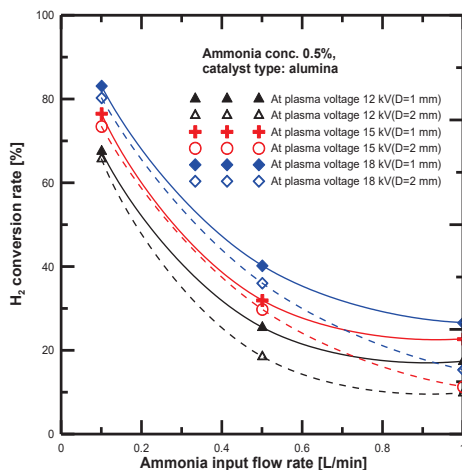


Fig 5. 23 Comparison of hydrogen conversion rate results at different NH₃ flow rates.

Chapter 5. H₂ Production from ammonia gas

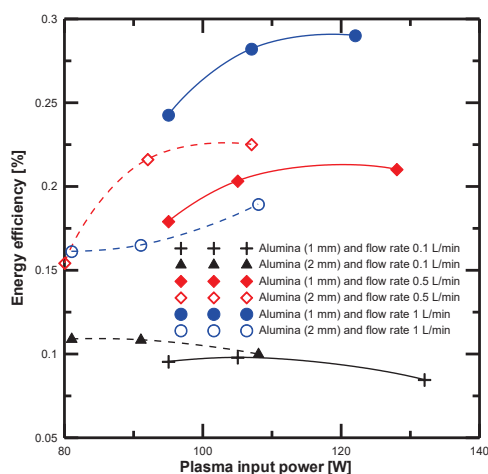


Fig 5. 24 Comparison of ammonia decomposition conversion rate results at different catalyst material types.

Conclusion

Hydrogen production from catalytic ammonia decomposition is considered a viable route to generate carbon-free hydrogen gas for fuel cells. The effect of the alumina particle size diameter of 1 mm and 2 mm on the plasma-catalyst ammonia decomposition process was investigated. The hydrogen concentration and the conversion rate were determined at different feeding ammonia flow rates and applied plasma voltage. It was found that the hydrogen concentration results of a low Al_2O_3 particle size diameter of 1 mm were higher than particle size 2 mm. The ammonia decomposition conversion rate of alumina particle diameter 1 mm was found to be greater than alumina particle size 2 mm, additionally the maximum conversion rate results were 83.19, 80.35% at Al_2O_3 particle size 1 mm, and 2 mm, respectively. Further, the energy efficiency of alumina catalytic ammonia decomposition by DBD plasma was decreased with the plasma input power increase. It can be concluded that the alumina catalytic material particle size diameter was an important factor affecting the activation of ammonia decomposition processes.

5.5 Energy and exergy analysis of thermal ammonia decomposition

Exergy or the second law efficiency is increasingly played an important role in design optimization and problem modeling and formulation in most of the recent engineering thermodynamics studies. Thermodynamics, entropy generation, and exergy analysis methods are mostly applied in the modern engineering systems [688-690]. These engineering tools lead to the best use of energy resources: energy transformations and power production devices. Also, energy is a thermodynamic analysis tool and is a property

Chapter 5. H₂ Production from ammonia gas

of the system; the energy total amount doesn't change during interactions [691]. The second law of thermodynamics showed that the quality of the energy used by the system as well as the quantity. The analysis of the second law of thermodynamics based on exergy and entropy concepts. Hence, the second law elaborates on the quality of energy and its relation to the surrounding. The quality term is named as "Exergy", different equivalent names were found from our literature review such as available energy, availability, work capability, etc. Exergy can be defined as the maximum available work can be produced by the system as it becomes at equilibrium state with its surrounding. The exergy analysis is obtained as a function of entropy relations. Entropy is expressed about the system irreversibility, it allows us to investigate the progress of non-equilibrium process [692]. Exergy is destroyed and cannot be converted due to system irreversibility. The exergy analysis is established through the interfaces between thermodynamics, heat transfer, and fluid mechanics. Various studies have presented the relationship between global warming and greenhouse gases (GHG). Most of the GHG was emitted from fossil fuel combustion and industrial applications [324, 693, 694]. Hydrogen fuel is considered the best solution to overcome all environmental issues related to conventional fuels. Many efforts have been investigated to develop new alternative methods for hydrogen carrier and storage [683, 684].

Hydrogen production from ammonia decomposition has more advantages than the other hydrogen carriers such as ammonia gas is a Cox-free H₂ carrier, and it has a higher gravimetric density 17.7 wt% than methanol 12.8 wt% [511, 517]. Hydrogen can produce from ammonia by plasma and thermal decomposition processes [517, 368]. The life-cycle assessment of renewable ammonia and its environmental impact has been investigated [695]. The hydrogen production from ammonia decomposition is an energy-intensive process, the thermal decomposition reaction of ammonia gas into hydrogen and nitrogen gas can be written as follow:



Catalytic materials are used to enhance the ammonia decomposition process including Ru, Ni, Fe materials [670]. Ruthenium catalytic materials have a high activation impact on the decomposition process of ammonia gas [681, 682]. Different reactors configurations and types have been utilized in the decomposition process of ammonia [491]. The most common reactor type used in ammonia decomposition is the packed bed reactor, but the scaling-up process showed some deficiencies and it cannot meet the distributed power system requirements [492]. Therefore, more effort is required to provide more efficient reactors with good residence time and heat transfer [493, 494]. Furthermore, more advanced analysis of the current system such as exergy or second law analysis leads to improve the system performance and design concepts [696].

Chapter 5. H₂ Production from ammonia gas

The exergy analysis has been utilized to optimize ammonia gas production processes [697]. Also, the exergy analysis information of thermal ammonia decomposition is typically important to develop the future process design [698]. In this paper, the exergy or the second law efficiency analysis is introduced for hydrogen production from the thermal ammonia decomposition in catalytic cylindrical type reactor. Ruthenium catalytic material (Ru-Al₂O₃) is used to improve the dissociation process of ammonia gas. The energy and exergy analysis is determined at different reactor temperatures. The feeding pressure effect on the decomposition process is evaluated. Moreover, the entropy generation and exergy destroyed are determined as well as the energy and exergy results are compared.

5.5.1 Methodology

The exergy analysis can be regarded as an advanced tool for analyzing the energy conversion processes. The thermodynamic inefficiencies and irreversibility of the system design can be identified by the exergy tool. Furthermore, it can help the user to get the best decision for system improvement [699, 700]. The specific exergy can be determined from the physical and chemical exergy terms as follows [701]:

$$Ex = Ex_{ph} + Ex_{ch} \quad (2)$$

While the physical exergy (Ex_{ph}) is calculated from the following equation:

$$Ex_{ph} = (h - h_0) - T_0(s - s_0) \quad (3)$$

The chemical exergy of the gaseous mixture is determined from the following relation [702]:

$$Ex_{ch} = RT_0 \ln \frac{P_0}{P_p} \quad (4)$$

Where, R is the universal gas constant. The difference between the total exergy input and exergy output is named the exergy destruction.

$$Ex_{dest} = Ex_{in} - Ex_{out} \quad (5)$$

The exergy efficiency is formulated in different ways and it can be defined as the ratio of the total exergy output to total exergy inputs [703], as follows:

$$\eta_{II} = \eta_{ex} = \frac{Ex_{out}}{Ex_{in}} = 1 - \frac{Ex_{dest}}{Ex_{in}} \quad (6)$$

The entropy concept is depending on the equilibrium state and reversible process in the classical thermodynamics [704]. The entropy generation term measures the irreversibility

Chapter 5. H₂ Production from ammonia gas

or the non-equilibrium process. All irreversible processes are accompanied by the increasing of entropy, hence the entropy generation is identified as the inequalities and irreversibility of the system. The entropy generation can be determined from the following relation [705]:

$$S_g = \int_{t_1}^{t_2} \dot{S}_g dt \quad (7)$$

While the entropy generation number (N_s) is defined as the ratio between the exergy destroyed to the total exergy input. This relation showed that the more exergy destroyed the more entropy generation.

$$N_s = \frac{Ex_{dest}}{Ex_{in}} \quad (8)$$

Hence the exergy efficiency can be rewritten as follows:

$$\eta_{II} = 1 - N_s \quad (9)$$

The previous equation shows that the second law efficiency improved, and the system performance will enhance by minimizing the entropy generation number. From the previous discussion, it is clear that the second law of thermodynamics revolves around exergy and entropy concepts.

5.5.2 System description

In this study, a cylindrical type reactor filled with ruthenium catalytic material was used in the thermal decomposition of ammonia gas. Figure (5.25) shows the experimental setup of the ammonia decomposition system. The Ammonia gas was fed into the reactor at a concentration of 100% and a flow rate of 1.7 L/min. Ammonia feeding gas pressure was controlled in a range of 0-300 kPa. Ru-Al₂O₃ catalyst material diameter of 1 mm was mounted inside the reactor cylinder. Ruthenium has been reported that ruthenium material has the highest activation results of the ammonia decomposition process [675, 676]. The catalytic cylindrical reactor diameter and length are 1.6 cm and length 30 cm, respectively. The reactor was heated at a temperature range of 473-773 K using the digital electric heating furnace. The feeding gas flow rate and pressure were controlled by the mass flow controller and pressure regulator. The decomposed hydrogen gas concentration was measured using the hydrogen gas analyzer. The glass wool material was revolved around the reactor to prevent heat loss.

Chapter 5. H₂ Production from ammonia gas

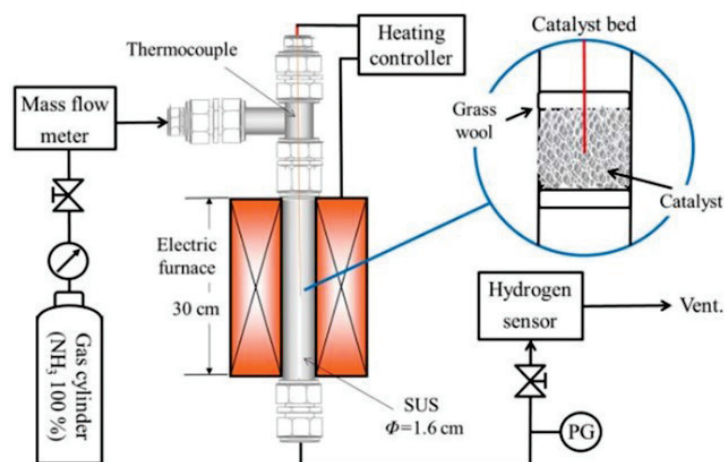


Fig 5. 25 Schematic diagram of catalytic thermal ammonia decomposition.

5.5.3 Results & discussion

Thermodynamics analysis alone is an unambiguous answer to the maximum output energy from the system. Therefore, the exergy analysis or the second law of thermodynamics can provide the best answer to the energy quality or the maximum available work from the system “exergy” [689]. In the exergy analysis of the actual system, the exergy is destroyed and the entropy generation is generated due to the system irreversibility. Hence, the exergy destroyed is proportional to the entropy generation or the entropy generation number (N_s). The feeding pressure effect on NH_3 decomposition was investigated. Figure (5.26) shows the maximum conversion rate results at a heating temperature of 773 K. It has been reported that the increase in ammonia decomposition feeding gas pressure is unfavorable [511]. The results of this study are confirmed that the maximum conversion rate was obtained at low ammonia gas feeding pressure. The conversion rate of NH_3 gas reaches to 100% at feeding pressure 0 kPa (gauge pressure) and the conversion rate decreased with the feeding pressure increased. The performance of the ammonia decomposition system can be defined by energy efficiency. Figure (5.27) demonstrates the energy efficiency results at different heating temperatures and feeding pressure. The energy efficiency results of the feeding gas pressure 0 kPa (gauge) were higher than those obtained at the other feeding gas pressures. Also, it was found that the energy efficiency revealed with the heating temperature increased. The maximum obtained energy efficiencies were 73.5, 71.9, 65.9, and 64.8% at feeding gauge pressure 0, 100, 200, 300 kPa.

The energy and exergy analysis of the ammonia decomposition system can provide the system design parameter modification to enhance the system efficiency. Different parameters influence the hydrogen production from ammonia decomposition such as feeding gas pressure reactor configuration and heat transfer. The irreversibility degree or

Chapter 5. H₂ Production from ammonia gas

non-equilibrium can be determined by the classical thermodynamics analysis or the second law of thermodynamics. The exergy destroyed is defined as the difference between the total exergy input and the total exergy output.

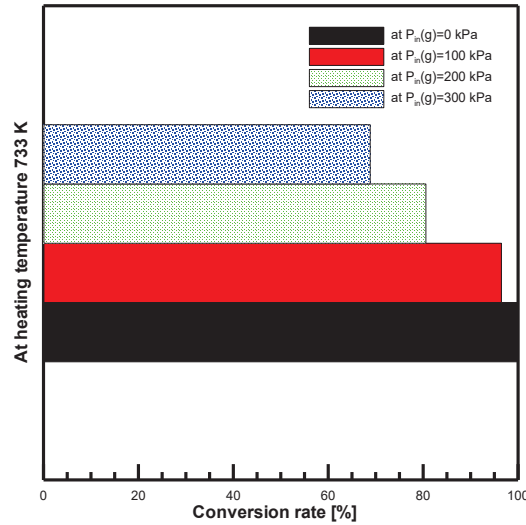


Fig 5. 26 The maximum conversion rate% from the catalytic NH₃ decomposition system at 773 K.

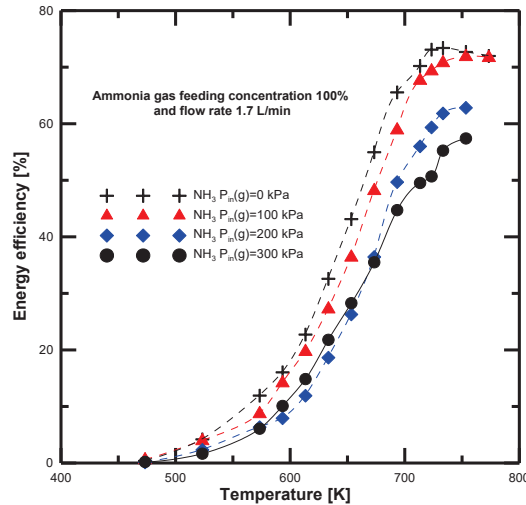


Fig 5. 27 Energy efficiency analysis at different heating temperature.

Figure (5.28) shows the exergy destroyed or the exergy destruction rate plot at different reactor temperatures and feeding pressures. The exergy destroyed increased with the reactor heating temperature as well as the ammonia feeding gas pressure. It was clear that the hydrogen production from the ammonia decomposition system is subjected to the dissipative process non-equilibrium. The energy quality of the ammonia decomposition system can be expressed by applying the second law of thermodynamics. Figure (5.29)

Chapter 5. H₂ Production from ammonia gas

presents the exergy efficiency at different reactor heating temperatures and pressures. The maximum obtained exergy efficiency was 13.34% at feeding gauge pressure 0 kPa and reactor temperature of 773 K. Furthermore, the entropy generation concept can express about the non-equilibrium of the decomposition process. Moreover, the entropy generation number (Ns) in these modern thermodynamics showed the degree of irreversibility. Figure (5.30) shows the change of the entropy generation number (Ns) with the exergy efficiency at NH₃ feeding gauge pressure 0 kPa. It was observed that the entropy generation number or the irreversibility degree decreased with the second law or exergy efficiency increased. The entropy generation number quantity is related to the process non-equilibrium or irreversibility. Therefore, the authors suggest renaming the entropy generation number (Ns) to be the irreversibility degree (I_d) using the same relation in equation (8). The irreversibility degree (I_d) is a concise concept and can be defined as the resulting entropy quantity due to system non-equilibrium.

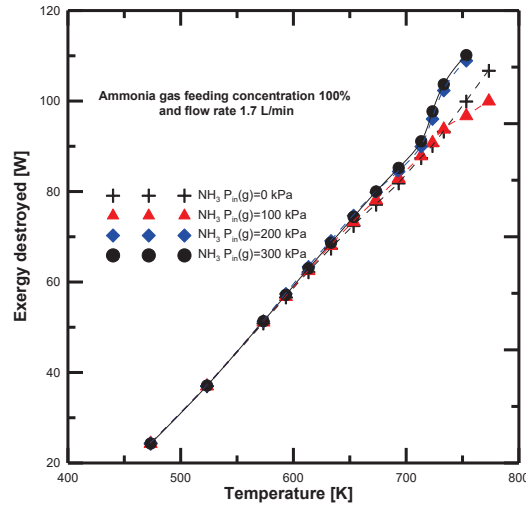


Fig 5. 28 Exergy destroyed analysis at different heating temperature

Chapter 5. H₂ Production from ammonia gas

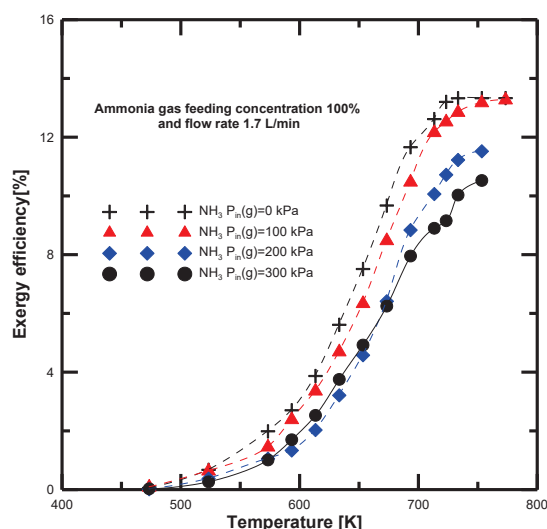


Fig 5. 29 Exergy efficiency results at different NH₃ feeding pressures and temperatures.

Recently, the exergy concept has been used in a different context to improve the conversion system [706]. Exergy analysis describes the energy quality and it helps to estimate the most efficient condition of the decomposition system. Different parameters are influenced by the hydrogen production from the ammonia decomposition process such as reactor temperature, feeding pressure, reactor design and configuration, and heat and mass transfer. A comparison between the energy and second law efficiency was delivered to investigate the energy quality. Figure (5.31) compares the energy and exergy efficiency of the optimum or ambient conditions of the hydrogen production from ammonia gas. It was observed that the second law efficiency result was lower than the energy efficiency, it means that the exergy was destroyed. It was clear how real the H₂ production from the catalytic ammonia decomposition system, it was related to the entropy generation. Hence, the analysis showed that a more energy efficient system is needed. These results represent how far the real ammonia decomposition system deviates from its equilibrium state.

Chapter 5. H₂ Production from ammonia gas

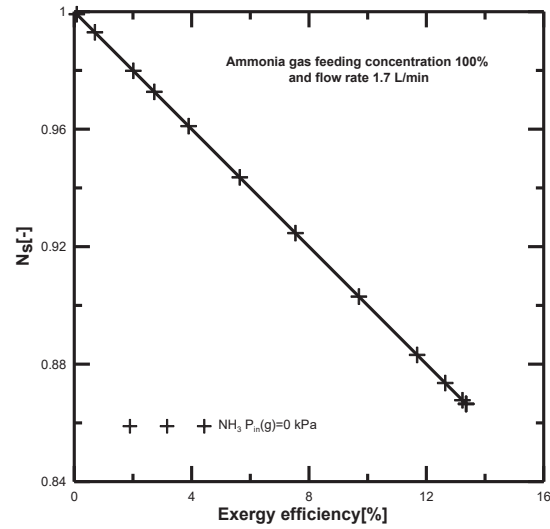


Fig 5. 30 Entropy generation number results at NH₃ feeding pressure 0 kPa (gauge pressure).

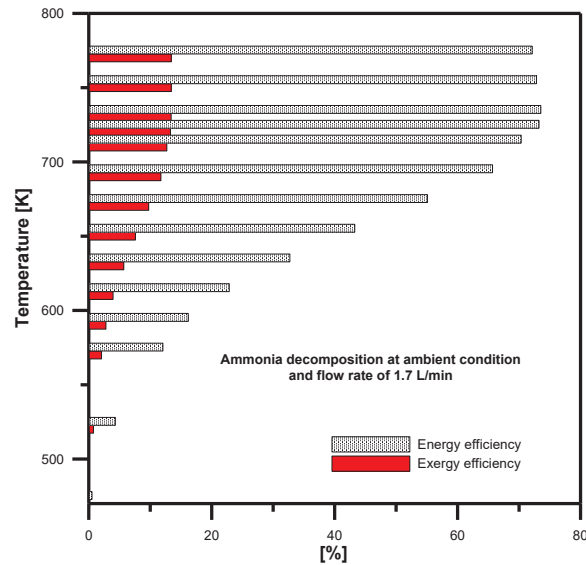


Fig 5. 31 Comparison between energy and exergy efficiency results.

Conclusion

In the present study, the energy and exergy concepts are used to analyze the hydrogen production from the ammonia decomposition system. Moreover, the entropy generation is analyzed to provide the quantity of non-equilibrium of the decomposition process. The entropy generation number (N_s) is renamed to be the irreversibility degree (I_d). The irreversibility degree (I_d) is more concise and express about the system non-equilibrium

Chapter 5. H₂ Production from ammonia gas

with its environment. Furthermore, the exergy destruction is determined. The feeding pressure effect on 100% ammonia concentration decomposition is investigated at different reactor heating temperature range of 473-773 K. The conversion rate% results proved that the increase of ammonia feeding gas pressure is unfavorable [11], because of the maximum result is obtained at 0 kPa gauge pressure. It was found that the maximum energy efficiencies are 73.5, 71.9, 65.9, and 64.8% at feeding gauge pressure 0, 100, 200, 300 kPa, respectively. The exergy destruction increased with the reactor temperature increased. Moreover, the irreversibility degree (I_d) was decreased by improving the exergy efficiency, the maximum exergy efficiency is 13.34% at ammonia gas feeding pressure of 0 kPa. The exergy analysis can describe the inefficiencies of the current system and the exergy efficiency can be enhanced by improving the system design parameters. A comparison between energy and exergy efficiency showed how the real ammonia decomposition process deviates from its environment.

5.6 Energy and exergy analysis of NH₃ decomposition by DBD plasma

Energy is required for all human needs; fossil fuels are mostly used as the main energy source in different energy applications. It was found that the global energy usage distributions were estimated as follows: fossil fuels 80%, renewable energy 14% and nuclear power 6% [707]. A high amount of greenhouse gases are emitted from fossil fuels combustion which has a high environmental impact. Therefore, clean energy becomes an essential need to decrease the continuous growth of greenhouse gases. Hydrogen gas is considered the cleanest energy carrier which can produce from different production technologies [324]. Most of the available hydrogen gas in the market is produced from the steam reforming process [80, 438]. The main disadvantage of this method is the reaction product contents which are included the carbon dioxide, which is a greenhouse gas. The most practical method of hydrogen production methods is the electrolysis method. The electrolysis method energy efficiency can reach higher than 70%, but the cost of the required electricity is too high [708]. The integrated renewable energy source such as wind power, solar energy, and hydropower can be used to provide the required electricity [709, 710]. The energy content of hydrogen is registered 2.5 times compared with conventional fuels [348]. It can be considered that the hydrogen fuel as the future energy carrier, on the other hand, different economic studies have been developed to investigate the hydrogen production technologies cost. Currently, it was investigated that the cost of hydrogen production technologies is still high [349]. The technical performance of 19 selected hydrogen production methods has been comparatively evaluated [350]. The results showed that the reforming method using fossil fuels has the highest energy values and the lowest energy value was the hydrogen production by the photonic (solar) production method.

Chapter 5. H₂ Production from ammonia gas

Ammonia is considered the most pure hydrogen energy carrier source, it is an inexpensive fuel [80]. Pure ammonia gas is registered a higher energy density (8.9 kW.h.kg⁻¹) than methanol (6.2 kW.h, kg⁻¹) [711]. Ammonia is decomposed into hydrogen and nitrogen gas in a single reaction step without any carbon monoxide or sulfur products, additionally, the leakage can simply detect due to its strong odor [712]. Pure hydrogen gas was generated from a plasma catalytic membrane reactor using the Pd-Cu membrane with an energy efficiency of 28.5% [368]. The analysis of the ammonia decomposition reactor to generate hydrogen for fuel cell applications has been investigated [713]. Further, the performance assessment of hydrogen and ammonia combustion using various fuels for power generators have been analyzed [442]. Furthermore, it was found that hydrogen can produce from steam decomposition using DBD plasma has been preliminarily investigated [337].

Hydrogen gas is separated using a palladium-based membrane; the recent advances of hydrogen purification in membrane technology for hydrogen were investigated [443]. Currently, membrane technologies are considered the most promising process because of their cost-effectiveness, low energy consumption, and the operation is easy [448]. Different hydrogen permeation studies have been developed [346, 445-447, 714]. It was shown that the hydrogen permeation through the Pd-Cu membrane improved by applying plasma. A comparison between the exergy efficiency of hydrogen production methods from renewable energy sources has been developed [715]. It was showed that the liquefaction process has very energy-intensive and required a lot of exergy.

In this study, the performance of energy and exergy analyses of three hydrogen production methods from ammonia decomposition using DBD plasma were experimentally evaluated. The cylindrical type reactor (PMR) was only utilized as a first ammonia decomposition system. Additionally, the pre-catalytic reactor (CR) is added to the second system and filled with the catalytic material. In the third system, the effect of zeolite material type (SA-600A) on the hydrogen separation in PMR was investigated. The energy and exergy efficiency have been determined at different ammonia input flow rates for all ammonia decomposition systems. The sustainability index and the depletion factor were analyzed to clarify the influence of the irreversibilities or the exergy destruction rate on exergy efficiency. A comparison between energy and exergy efficiency of all systems was developed, additionally, the maximum hydrogen production rate % and the depletion factor have been compared.

5.6.1 Thermodynamics and exergy analyses

In the current study, a comparative assessment of three different hydrogen production methods from ammonia decomposition using DBD plasma in the cylindrical type reactor (PMR). The hydrogen is separated using palladium-copper membrane-type Pd60%-Cu40% and is installed inside the PMR. The thermodynamics analysis has been carried out based on the inlet and outlet conditions of the system, energy and second law efficiency or

Chapter 5. H₂ Production from ammonia gas

exergy efficiency are determined and compared for the hydrogen separation from ammonia decomposition systems. Exergy can be defined as the available work from an energy source. The maximum obtainable work from the system when matter or energy such as thermal energy reach to thermodynamic equilibrium. Exergy is a measurement term can be expressed how the system deviates from the equilibrium state with its environment. The exergy concept is incorporated the qualitative and quantitative properties of energy. The second law efficiency or exergy efficiency has measured the performance of a system relative to the performance under reversible conditions for the same dead state.

The entropy generation is expressed about the irreversibility phenomenon which leads to the exergy destruction and caused an increase of energy consumption whatever the energy source. The objective of exergy analysis is to determine the imperfections of thermodynamics or the exergy losses and to evaluate the causes of the exergy losses. The second law efficiency can lead to thermodynamic improvements of the process [716]. The assumption of hydrogen production systems from ammonia decomposition can be listed as follow:

- The decomposed ammonia gas is evaluated at atmospheric pressure (100 kPa) and ambient temperature (27 °C).
- The plasma type is dielectric barrier discharge (DBD).
- The hydrogen gas is separated using the Pd-Cu40% membrane with a thickness of 20 μm .
- The ammonia decomposition systems operate at a steady state.
- The potential and kinetic energy are neglected throughout the systems.

The general steady state of the mass balance equation can be expressed as follows:

$$\sum \dot{m}_{in} = \sum \dot{m}_{out} \quad (1)$$

Where, \dot{m} is the mass flow rate, the subscripts in and out are inlet and outlet, respectively. Also, the energy balance can be expressed as follows:

$$\sum \dot{E}_{in} = \sum \dot{E}_{out} \quad (2)$$

$$\dot{E}_{kin,in} + \dot{E}_{pot,in} + \dot{Q} + \sum \dot{m}_{in} h_{in} = \dot{E}_{kin,out} + \dot{E}_{pot,out} + \dot{W} + \sum \dot{m}_{out} h_{out} \quad (3)$$

Where \dot{E}_{in} is the total inlet energy transfer rate, \dot{E}_{out} is the total outlet energy transfer rate, \dot{Q} denotes the net input heat, \dot{W} is the rate of work output, and h is the specific enthalpy [717]. In this study the changes in the potential and kinetic energies are neglected, therefore eqn (3) can be written as follows:

$$\dot{Q} + \sum \dot{m}_{in} h_{in} = \dot{W} + \sum \dot{m}_{out} h_{out} \quad (4)$$

From the previous equation, it was seen that the total energy input of the system is equal to the total energy output. The energy efficiency of the system can be written as:

Chapter 5. H₂ Production from ammonia gas

$$\eta_{en} = \frac{\sum \dot{E}_{out}}{\sum \dot{E}_{in}} \quad (5)$$

The exergy and the general second law formulation is given as [701],

$$\sum \dot{X}_{in} - \sum \dot{X}_{out} = \sum \dot{X}_{dest} \quad (6)$$

Also, it can be written as follows:

$$\sum \left(\left(1 - \frac{T_0}{T_p} \right) \dot{Q}_p - \dot{W} \right) + \sum \dot{m}_{in}(X_{in} + X_{ch,in}) - \sum \dot{m}_{out}(X_{out} + X_{ch,out}) = \sum \dot{X}_{dest} \quad (7)$$

Where the input flow exergy is given by the following equation:

$$X_{in} = h_{in} - h_{out} - T_0(s_i - s_0) \quad (8)$$

Where T_0 is the ambient temperature, X_{ch} is the chemical exergy of the species gas, X_{dest} is the exergy destroyed, \dot{Q}_p denotes the total heat transfer rate at temperature T_p , and location p , \dot{W} is the work done rate, s is the specific entropy and the subscript zero indicates the properties at ambient temperature and atmospheric pressure [718].

The chemical exergy of gaseous species can be expressed as follows [702]:

$$\dot{E}_{ch} = \dot{m}RT_0 \ln \frac{P_0}{P_p} \quad (9)$$

Where, R is the universal gas constant. Second law efficiency or Exergy efficiency is formulated in different ways and it can be defined as the ratio of the all exergy output as useful exergy to all exergy inputs [703]. The exergetic efficiency is given by the following relation:

$$\eta_{II} = \eta_{ex} = \frac{\dot{X}_{out}}{\dot{X}_{in}} \quad (10)$$

This relation showed that the exergetic efficiency will be improved and reach to the maximum value when the system irreversibility or the exergy loss is minimized [719]. The exergy analysis becomes an important tool to evaluate and predict the thermodynamics process imperfection. The analysis results of exergy can be used to improve the thermodynamic process under consideration [720-725]. Furthermore, the sustainability index is determined to recognize the system performance and its improvement opportunities. The sustainability index indicates how the system in the real life and supports to improve the current status of the system for more efficient use and it can be formulated as follows [726]:

$$SI = \frac{1}{1 - \eta_{ex}} \quad (11)$$

Or

Chapter 5. H₂ Production from ammonia gas

$$SI = \frac{1}{Dp} \quad (12)$$

The depletion factor (D_p) can be determined as the ratio of the exergy destruction rate to the exergy input rate of the system.

$$Dp = \frac{\dot{X}_{dest}}{\dot{X}_{in}} \quad (13)$$

The exergy analysis of hydrogen production from ammonia decomposition using DBD plasma is studied for three different ammonia decomposition systems. The cylindrical type reactor is used and DBD plasma type is applied at different ammonia flow rates. The energy and exergy efficiency are determined and compared for three ammonia decomposition systems.

5.6.2 Results & discussion

Exergy analysis of H₂ production from NH₃ decomposition in PMR only

Ammonia is considered an important energy carrier gas which can utilize to produce high purity hydrogen gas. Ammonia can be decomposed into their constituent's hydrogen and nitrogen gas using DBD plasma. In the plasma membrane reactor (PMR) experiment, ammonia gas is decomposed using DBD plasma and the hydrogen gas is separated using the Pd60%-Cu40% membrane with a thickness of 20μm. The driving force of the hydrogen permeation is produced by using a vacuum pump which will generate a pressure difference between the inlet and permeable side. The hydrogen concentration at the permeate side of PMR is determined using the H₂ gas analyzer. The ammonia gas input flow rate is controlled using the mass flow meter, while the pressure at the inlet and permeate sides are registered by digital pressure gauges. The exergy analysis of the ammonia decomposition using DBD plasma in plasma membrane reactor (PMR) is determined. The exergy analysis of PMR only is based on the process shown in figure (5.32). Ammonia is decomposed into hydrogen and nitrogen gas according to the following reaction [727],



This reaction is carried out at atmospheric pressure using DBD plasma without using the catalytic materials. The reaction rate can be represented as follows [727]:

$$r_{\text{NH}_3} = k_0 \exp\left(-\frac{E_a}{RT}\right) P_{\text{NH}_3} \quad (15)$$

Where r_{NH_3} the ammonia reaction rate, k_0 is the frequency factor, E is the activation energy, P_{NH_3} is the partial pressure of ammonia, and T is the reactor temperature.

Chapter 5. H₂ Production from ammonia gas

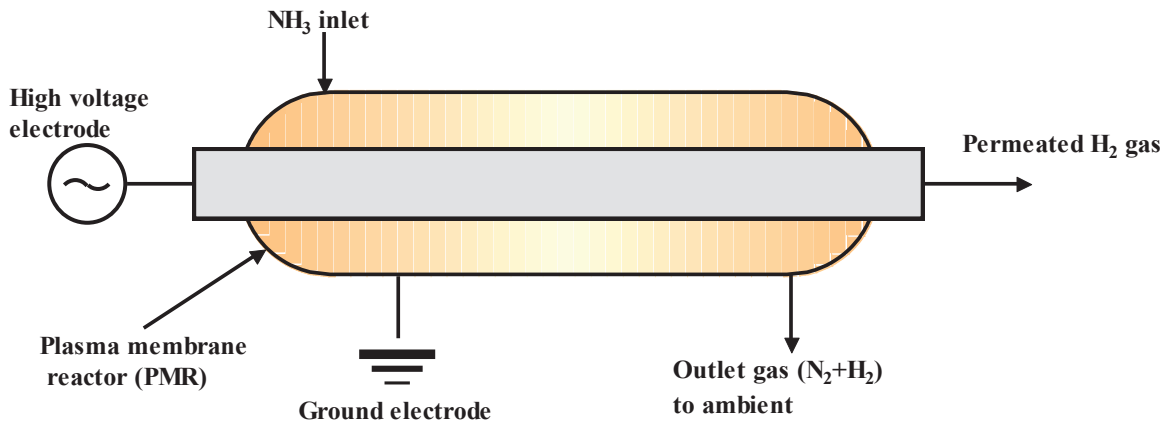


Fig 5. 32 Schematic diagram of NH₃ decomposition using PMR only.

The ammonia gas kinetic parameters used in the energy and exergy efficiency calculation is listed in Table (5.5).

Table 5. 5 Ammonia gas kinetic and reactor parameters.

Parameter	Value
Frequency factor, k_0	$1.33 \times 10^{11} \text{ mol. M}^{-3} \cdot \text{s}^{-1} \cdot \text{Pa}^{-1}$
Activation energy, E_a	$1.9 \times 10^5 \text{ J. mol}^{-1}$
Catalyst	2 % Ru/Al ₂ O ₃
Catalyst particle diameter, D_p	0.00031— 0.00072 m
CR internal diameter	16 mm
CR reaction temp.	450 °C
NH ₃ concentration of supply gas	100%
Specific heat of ammonia, $C_{p_{\text{NH}_3}}$	$19.99 + 49.77T - 15.37T^2 + 1.92T^3 + 0.18/T^2$ kJ.kmol ⁻¹ .K ⁻¹
Specific heat of hydrogen, $C_{p_{\text{H}_2}}$	$26.09 + 8.21T - 1.97T^2 + 0.159T^3 + 0.04/T^2$ kJ.kmol ⁻¹ .K ⁻¹
Specific heat of nitrogen, $C_{p_{\text{N}_2}}$	$33.06 - 11.36T + 11.43T^2 - 2.77T^3 - 0.15/T^2$ kJ.kmol ⁻¹ .K ⁻¹

The hydrogen production or the permeation rate percent of hydrogen production from ammonia gas decomposition using PMR only is shown in figure (5.33). The hydrogen production rate can be calculated by the following relation:

$$H_2 \text{ production (permeation) rate [\%]} = \frac{\text{Permeated } H_2 \text{ flow rate } \left[\frac{L}{\text{min}} \right]}{\text{Input ammonia gas flow rate } \left[\frac{L}{\text{min}} \right]} \times 100$$

(16)

Chapter 5. H₂ Production from ammonia gas

It was seen that the hydrogen production rate increased at low ammonia input flow rates and the maximum obtained permeated H₂ gas flow rate was 1.8 L/h. The total energy inputs to the PMR experiment are concluded in the plasma power and pump power. The energy efficiency is calculated according to the following relation:

$$\eta_{en} = \frac{\dot{m}_{H_2} \times HHV}{\dot{m}_{NH_3} \times LHV + (\text{plasma power} + \text{pump power})} \quad (17)$$

Where the higher heating of hydrogen gas is HHV and LHV is the lower heating value of input ammonia gas. A comparison between the energy and exergy efficiency of the PMR experiment is presented in figure (5.34). It was clear that the obtained energy efficiency is higher than the exergy efficiency of the PMR experiment due to the process irreversibility. Furthermore, the sustainability index (SI) and the depletion factor (Dp) is determined and is shown in figure (5.35).

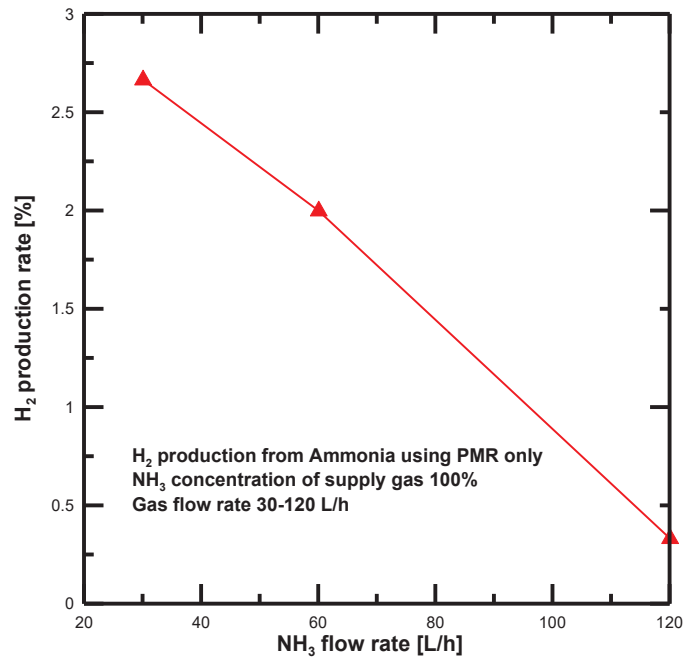


Fig 5.33 Hydrogen production rate from ammonia decomposition using DBD plasma in PMR only.

Chapter 5. H₂ Production from ammonia gas

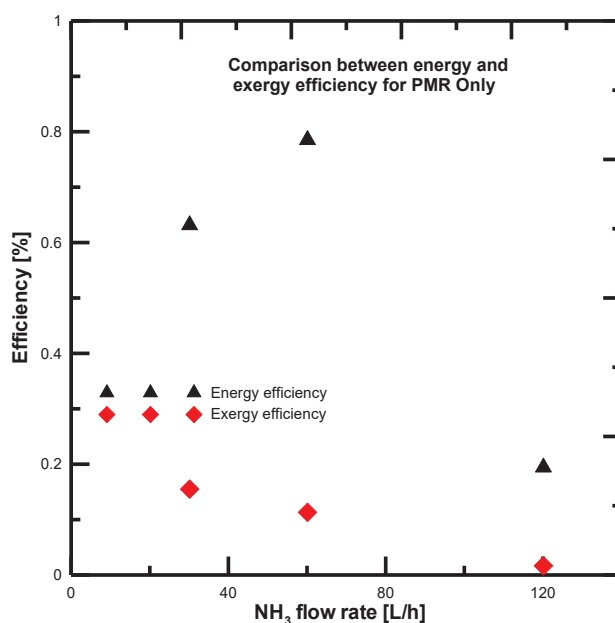


Fig 5.34 Comparison between energy and exergy efficiency of ammonia decomposition in PMR only.

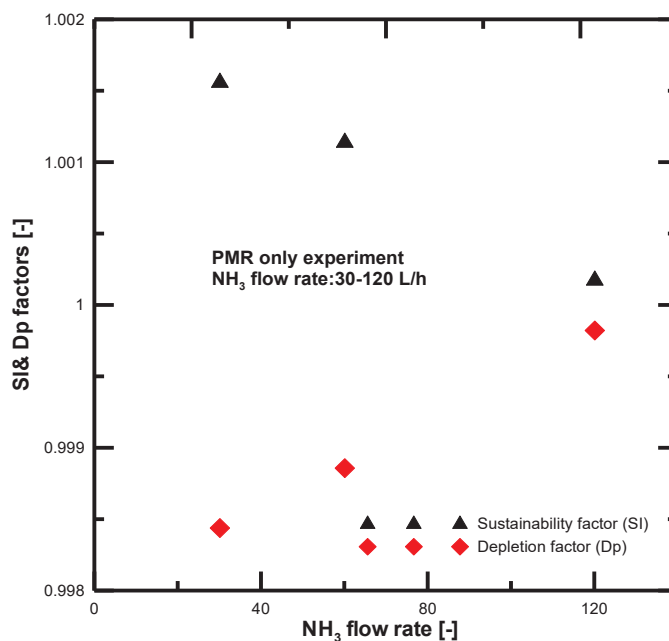


Fig 5.35 Comparison between DP & QF of ammonia decomposition in PMR only.

The most interesting result of this comparison is the decreasing of sustainability factor with ammonia flow rate increase while the depletion factor increased, it means that the exergy destruction rate increased with the ammonia input flow rate increased.

Exergy analysis of H₂ production from NH₃ gas in PMR and pre-catalytic reactor

Chapter 5. H₂ Production from ammonia gas

This ammonia decomposition system is mainly composed of two reactors, the pre-catalytic (CR) and the PMR reactors. Firstly, ammonia gas flows through the CR and then passes into the PMR, the main objective of the pre-catalytic reactor is added to decompose ammonia into H₂ and N₂ gases. Figure (5.36) shows the schematic diagram of hydrogen production from ammonia decomposition using the CR-PMR system. In this ammonia decomposition system, the pre-catalytic reactor (CR) is utilized and installed before the PMR. The temperature of the pre-catalytic reactor is raised to 450 °C and is filled with the catalytic material type of 2% Ru/Al₂O₃. In pre-reactor, Ammonia gas is decomposed into hydrogen and nitrogen gas at the settled high heating temperature. The hydrogen gas analyzer is used to measure the hydrogen gas concentration. The inlet and permeate pressures are monitored by the digital pressure gauges, while the vacuum pump is used to produce the permeation driving force. Additionally, the hydrogen production rate percent versus the ammonia gas input flow rate is shown in figure (5.37).

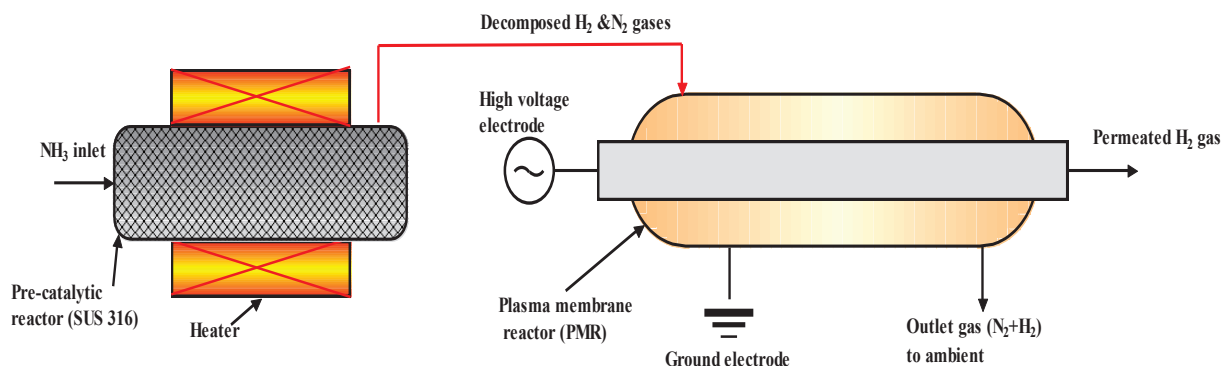


Fig 5.36 Schematic diagram of NH₃ decomposition using CR-PMR system.

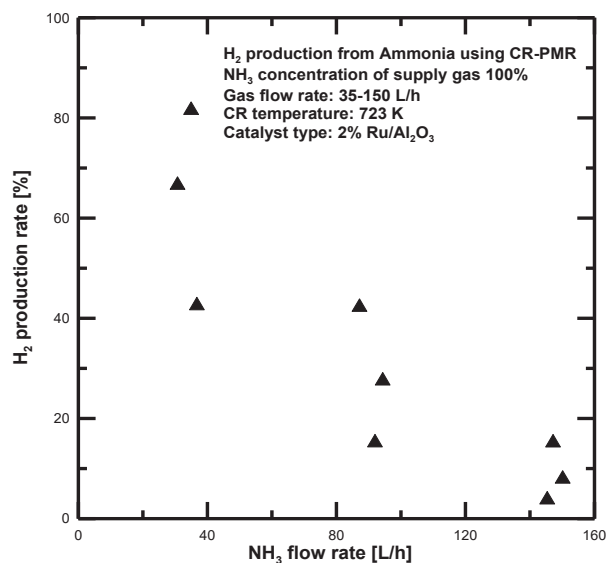


Fig 5.37. Hydrogen production rate from ammonia in CR and PMR.

Chapter 5. H₂ Production from ammonia gas

It was seen that the hydrogen production rate increased to reach the maximum value of 55.2 L/h by adding the pre-catalytic reactor which ammonia gas is decomposed into hydrogen and nitrogen gas before the PMR. The energy efficiency is determined according to the following equation:

$$\eta_{en} = \frac{\dot{m}_{H_2} \times HHV}{\dot{m}_{NH_3} \times LHV + (\text{plasma power} + \text{heating power} + \text{pump power})} \quad [18]$$

Figure (5.38) shows the comparison between the exergy and energy efficiency of CR-PMR system. The energy efficiency of ammonia decomposition using CR-PMR system is raised to be 16.1% compared with the PMR only system, additionally the exergy efficiency increased to reach 4.91%. It was clear the effect of adding the pre-catalytic reactor on the hydrogen production from ammonia decomposition using DBD plasma. The exergy analysis of CR-PMR system showed that the ammonia decomposition system still has a high irreversibility and exergy destruction rate is still high. The exergy destruction compared to the exergy input rate can be expressed by the sustainability index and the depletion factor (Dp) which is shown in figure (5.39).

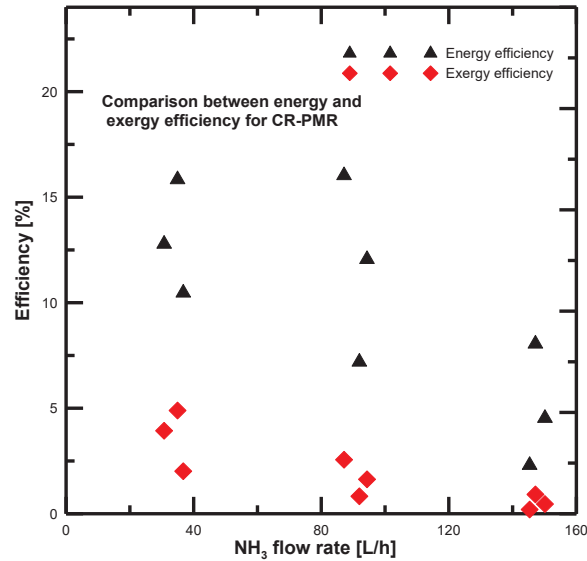


Fig 5.38 Comparison between energy and exergy efficiency of ammonia decomposition in CR-PMR.

Chapter 5. H₂ Production from ammonia gas

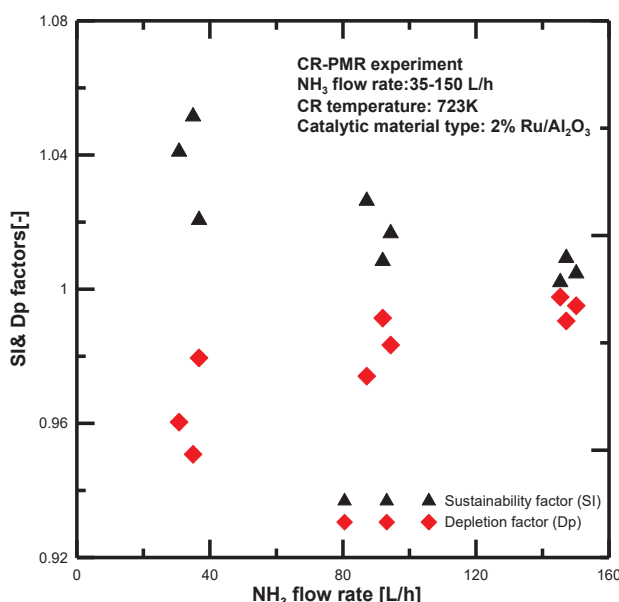


Fig 5.39 Comparison between DP & QF of ammonia decomposition in CR-PMR.

5.6.3 Exergy analysis of H₂ production from NH₃ gas in PMR with zeolite and pre-catalytic reactor

Atypical schematic diagram of the ammonia decomposition in a CR and PMR with zeolite material is shown in figure (5.40). In this ammonia decomposition system, the PMR is filled with zeolite material type of SA-600A with particle diameter of 1.5 mm, additionally the CR is also filled with 2% Ru/Al₂O₃ same as the previous ammonia decomposition system. Hydrogen gas only is permeated through the Pd-Cu40% membrane thickness of 20 μ m and the hydrogen gas analyzer is installed at the permeate side to measure the concentration of H₂ gas.

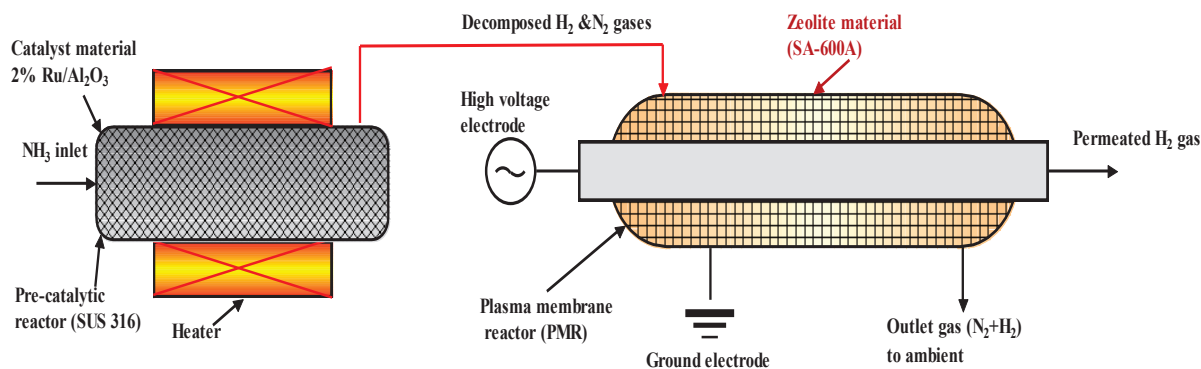


Fig 5. 40 Typical schematic diagram of NH₃ decomposition using CR-PMR with zeolite material.

Chapter 5. H₂ Production from ammonia gas

In addition to DBD plasma, the zeolite materials are added in the PMR to improve the hydrogen separation in the PMR, subsequently the H₂ permeation through the Pd-Cu40% membrane. The pre-catalytic reactor temperature is raised to 450 °C and the ammonia gas is decomposed into hydrogen and nitrogen gas. The hydrogen gas concentration is measured before the PMR reactor by the H₂ gas analyzer. The hydrogen and nitrogen gas concentrations are 75%, 25%, respectively. It was found in the CR-PMR system that ammonia gas is directly decomposed into hydrogen and nitrogen gas in pre-catalyst reactor. Figure (5.41) presents the hydrogen production rate at different ammonia gas input flow rates. The permeated hydrogen flow rate in CR-PMR with zeolite increased to reach to 192 L/h compared to the PMR and CR-PMR systems. Also, the hydrogen production rate increased to 96.6% by adding the zeolite material type of SA-600A. In the PMR system, the hydrogen permeation through the Pd-Cu40% membrane increased by adding the zeolite materials compared with other systems. The energy and exergy efficiency versus different ammonia input flow rates are shown in figure (5.42). It was clear that the CR-PMR with zeolite material has a great impact on the energy and exergy efficiency, the energy and exergy efficiency increased to reach the maximum values of 44.1%, 6.35%, respectively.

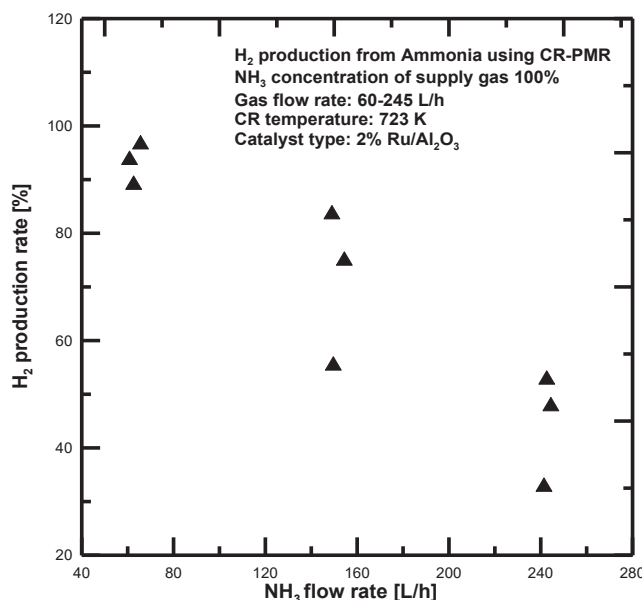


Fig 5.41 Hydrogen production rate from ammonia decomposition using DBD plasma in CR-PMR with zeolite.

Chapter 5. H₂ Production from ammonia gas

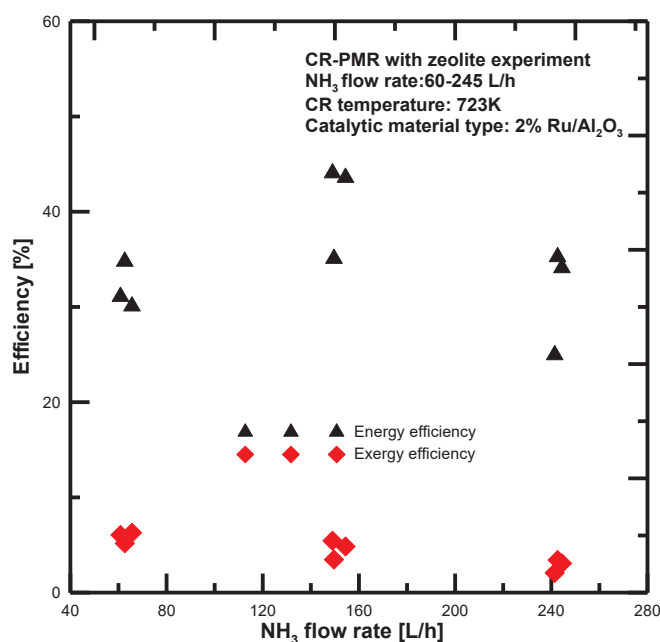


Fig 5.42 Comparison between energy and exergy efficiency of ammonia decomposition in CR-PMR.

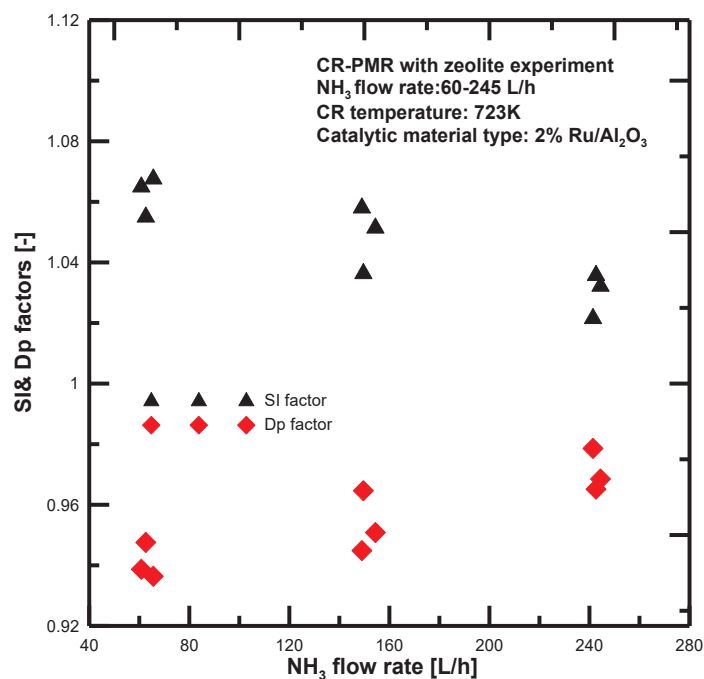


Fig 5.43 Comparison between SI & Dp of ammonia decomposition in CR-PMR with zeolite.

To clarify the ammonia decomposition using the CR-PMR with zeolite system, the sustainability index and the depletion factor are determined. Figure (5.43) represents the sustainability index and the depletion factor versus different ammonia input flow rates. It

Chapter 5. H₂ Production from ammonia gas

was seen that the depletion factor increased with ammonia input flow rate increased by means the exergy destruction rate increased. Moreover, the sustainability factor is decreased with the ammonia input flow rate increased which means that the exergy efficiency decreased.

The evaluation of the energy and exergy efficiency of all hydrogen production from ammonia decomposition systems using DBD plasma are compared in this paper section. Comparisons between the energy efficiency of three ammonia decomposition systems are shown in figure (5.44). It was clear that the energy efficiency improved by adding the pre-catalytic reactor before the plasma membrane reactor. Also, the energy efficiency of the CR-PMR with zeolite system is higher than that obtained from PMR and CR-PMR systems. The influence of adding zeolite material (SA-600A) in PMR is appeared in the hydrogen production rate and the energy efficiency. The comparison of exergy analysis of ammonia decomposition systems using DBD plasma at different ammonia input flow rates is shown in figure (5.45). This figure shows that the exergy efficiencies of modified systems did not increase too much due to the irreversibility's and exergy destruction rate were so high. The exergy efficiency isn't influenced too much more by adding the catalyst materials in the CR-PMR with zeolite system due to the exergy input rate is still high compared to the exergy output rate from the system. The catalyst material effect is found in the amount hydrogen production from the system. The depletion factor analysis of all systems is given in figure (5.46). It is considered that the depletion factor is an important parameter to evaluate the exergy destruction rate of ammonia decomposition systems. It was clear from this figure that the depletion factor of PMR system is higher than the other both modified systems. Additionally, it was seen the depletion factor of all systems increased with the ammonia gas input increased.

To clarify the effect of catalyst materials on the hydrogen production rate from ammonia decomposition systems using DBD plasma, a comparison between the maximum permeation rate percent values of all systems are presented in figure (5.47). This figure indicates that the hydrogen permeation rate raised from 2.66%, 81.6 to be 96.6% in PMR, CR-PMR and CR-PMR with zeolite systems, respectively. The hydrogen production from PMR system is increased by adding the CR, ammonia is decomposed at high temperature in CR to hydrogen and nitrogen gas before entering the PMR. Additionally, the hydrogen permeation rate percent is improved by filling the PMR with zeolite material type SA-600A.

Chapter 5. H₂ Production from ammonia gas

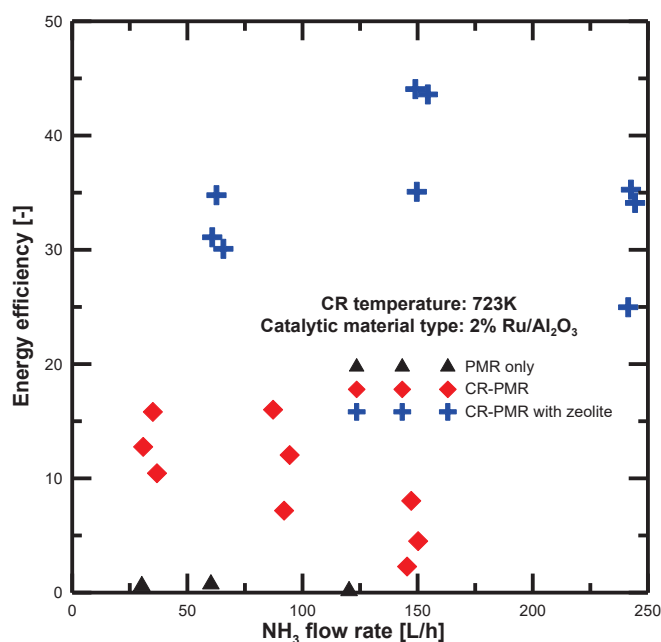


Fig 5.44 Comparison between energy efficiency of ammonia decomposition systems using DBD plasma.

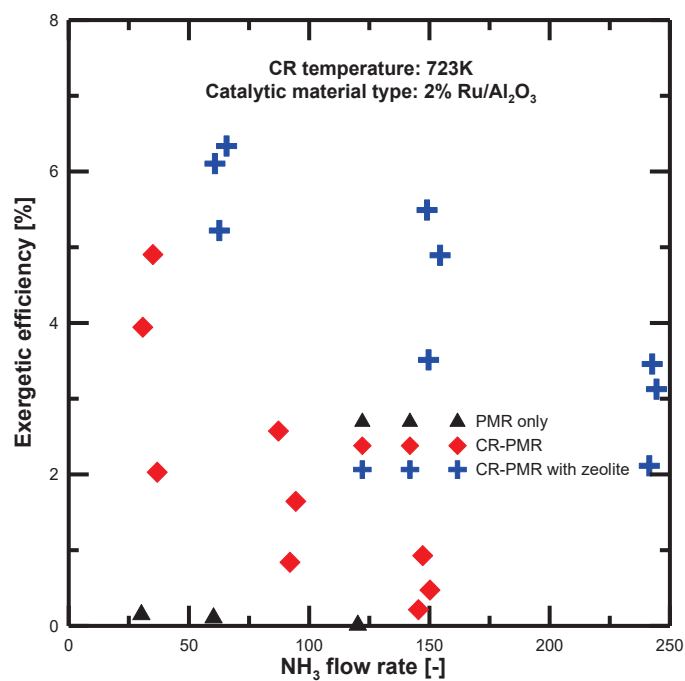


Fig 5.45 Comparison between exergetic efficiency of ammonia decomposition systems using DBD plasma.

Chapter 5. H₂ Production from ammonia gas

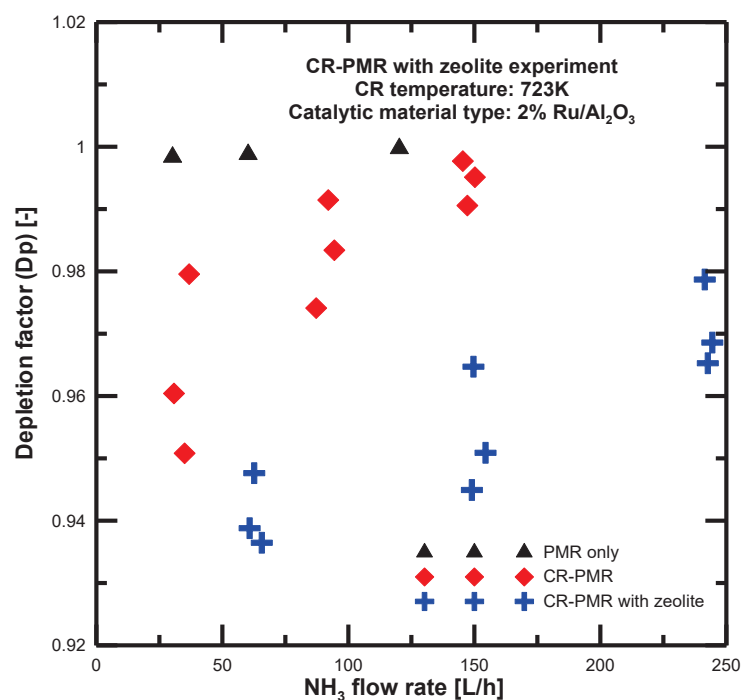


Fig 5.46 Comparison between depletion factors of ammonia decomposition systems using DBD plasma.

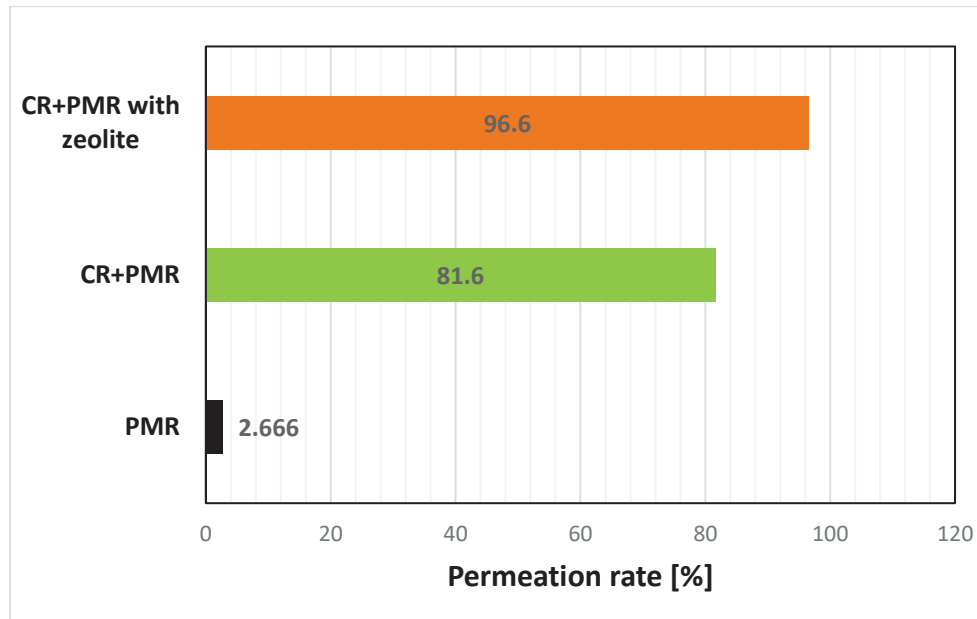


Fig 5.47 Comparison between permeation rate percent of ammonia decomposition systems using DBD plasma.

Chapter 5. H₂ Production from ammonia gas

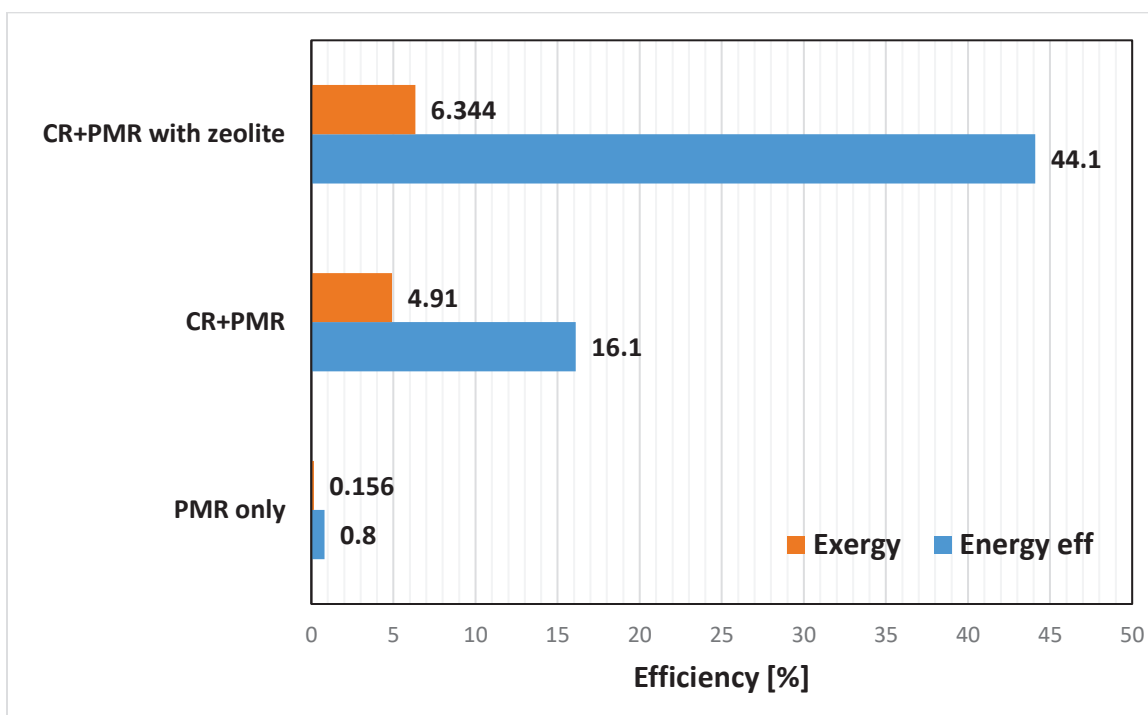


Fig 5.48 Comparison between the maximum energy and exergy efficiency of ammonia decomposition systems.

Figure (5.48) shows a comparison between the maximum obtained values of the energy and exergy efficiencies of all ammonia decomposition systems. It was clear that the energy efficiency is always higher than the exergy efficiency in all systems due to the systems irreversibilities which appeared in high values of exergy destruction rate. The maximum exergy efficiency is obtained from the CR-PMR with zeolite was 6.344% and the maximum energy efficiency was 44.1%.

Conclusion

The energy and exergy analysis of hydrogen production from ammonia using DBD plasma was performed for three ammonia decomposition systems. The ammonia decomposition reactor systems were analyzed at different ammonia input flow rates, additionally, the energy and exergy efficiency are comparatively assessed for all ammonia decomposition systems. The DBD plasma type is applied to the PMR and the hydrogen gas was separated using the Pd-Cu40% membrane with thickness of 20 μ m. It was shown that the ammonia decomposition in CR-PMR with zeolite system has the highest energy and exergy efficiency values. However, the results of hydrogen production rate from ammonia decomposition in PMR only was lower than other systems. It was found that the hydrogen production, energy and exergy efficiency increased due to adding the pre-catalytic reactor to the PMR system. The CR temperature was heated to 450 °C and was filled with the

Chapter 5. H₂ Production from ammonia gas

catalyst material of 2%Ru/Al₂O₃. It was noted that ammonia gas was decomposed into hydrogen and nitrogen gases due to the CR high temperature and the catalyst material effect on the ammonia decomposition process, additionally the hydrogen gas concentration was monitored by H₂ gas analyzer before entering to the PMR. Furthermore, the zeolite material type of SA-600A was added to the PMR to improve the hydrogen permeation rate percent through Pd-Cu40% membrane that in the CR-PMR with zeolite system. It was observed that the maximum hydrogen permeation rate were 2.66, 81.6 and 96.6% in PMR, CR-PMR and CR-PMR with zeolite, respectively. The energy and exergy efficiencies of ammonia decomposition systems were compared, it was found that the energy efficiency increased by adding the CR to the system. In contrast, the exergy efficiencies of all ammonia decomposition systems were low due to the systems irreversibilities compared to the energy efficiencies values. The maximum obtained energy efficiencies values were 0.8, 16.1, 44.1%, while the maximum exergy efficiencies values were 0.156, 4.91, and 6.344% that for PMR, CR-PMR, and CR-PMR with zeolite systems, respectively. It can be concluded that the exergy destruction rate of all ammonia decomposition systems were still too high although using the modified ammonia decomposition systems. The sustainability index and depletion factor were determined for all systems, it was observed that the depletion factor increased with ammonia input flow rates increased while the sustainability index decreased at the same input ammonia flow rates. Additionally, it was found that the depletion factor of PMR system were higher than CR-PMR and CR-PMR with zeolite systems, respectively.

5.7 Hydrogen Production and Heat Transfer Distributions of Ammonia Decomposition in an Atmospheric Pressure Plasma Plate Reactor

5.7.1 Introduction

Ammonia gas is considered an important hydrogen energy carrier and can deliver CO_x-free hydrogen for different applications, such as fuel cells [517]. In recent decades, different studies have evaluated hydrogen storage [9]. Fossil fuels and renewable energy sources are the most used methods to produce hydrogen and include coal, natural gas, biomass, hydropower, geothermal, solar, and wind energy [324]. Methods of hydrogen production from fossil fuel and biomass resources have been extensively investigated, such as steam, partial oxidation, autothermal, plasma, aqueous phase, and pyrolysis methods [728].

A number of renewable energy projects have applied a methodology to evaluate the effectiveness of instruments to increase energy efficiency to 45% by 2030 [729]. Most of the available hydrogen in the market is produced by steam reforming and water electrolysis. The energy balance of experimental and theoretical catalytic steam reforming reactions has been investigated [326]. Steam methane reforming has been performed over a mixed Ni/MgAl+CrFe₃O₄ catalyst [327]. Hydrogen production vapor has been investigated using

Chapter 5. H₂ Production from ammonia gas

dielectric barrier discharge plasma (DBD) from different materials such as ammonia, hydrocarbons, water vapor, and biomass fuels.

A nonlinear autoregressive model was used to predict the syngas temperature and composition of biomass gasification during plant operation with different operating conditions [730]. Non-thermal plasma was used to assist the decomposition of benzene as a tar analogue [365]. Gliding arc non-thermal plasma has also been used to generate H₂ and H₂O₂ [531]. Preliminary results have been investigated for hydrogen production from water vapor [337]. A kinetic model has been provided for hydrogen production from water vapor plasmolysis at atmospheric pressure in a dielectric barrier discharge micro-channel reactor [364].

Recently, the development of dielectric barrier discharge (DBD) plasma at atmospheric pressure has increased [731]. DBD plasma involves a specific type of AC discharge at atmospheric pressure. It provides non-equilibrium plasma with good thermodynamics. DBD plasma is mostly effective in chemical and physical processes of gases [536]. The main advantages of DBD plasma are its ability to produce highly reactive plasma at room temperature with low electric power consumption and a short time response [361]. However, recent DBD plasma applications have had unfavorable temperature increases due to the use of modern reactors and operation at higher frequency.

DBD plasma has been applied in several applications, such as pollutant removal [732], biomedical applications [733], surface treatment [734], and flow control [735]. The heat generated by atmospheric-pressure or non-equilibrium DBD plasma often causes energy waste. Therefore, most of the plasma applications use an external cooling circuit. The resulting temperature rise from plasma is significantly affected by various chemical and electronic processes. To have better operating conditions, the plasma temperature must be controlled appropriately. Several attempts have been made to understand the heat transfer mechanism. Plasma diagnostics, computer modeling, and detailed experimental analyses have been developed to recognize local temperatures [736].

Atmospheric-pressure DBD plasma can be characterized as weakly ionized plasma with properties resembling transient high-pressure glow discharge properties. Due to the presence of a dielectric barrier material, the energy input into the plasma system is limited. However, the gas temperature of the DBD plasma in practical applications has increased, and the plasma reaction fields strongly depends on the plasma properties and external cooling conditions.

Several studies on the heat transfer across plasma reactors have been developed [613]. The reactor heating temperature effect on the steam decomposition using DBD plasma has been investigated [737]. The heat transfer mechanism characteristics in methane-DBD plasma have been investigated [738]. A numerical simulation has been used to analyze the momentum and heat transfer of Ar gas in a needle-to-plane dielectric barrier discharge reactor [739]. DBD plasma ignition obviously generates non-uniform Joule heating.

Chapter 5. H₂ Production from ammonia gas

Therefore, more information is needed about the heat transfer characteristics in atmospheric-pressure or DBD plasma to optimize them for plasmas applications.

The current study reports on the hydrogen production and heat transfer distribution across a plasma plate type reactor (PPR) using 0.5% ammonia-argon as a base gas. The effects of the electrode gap distance and residence time on the ammonia decomposition were investigated. The heat transfer distributions across the PPR were analyzed at different voltages, and the total heat transfer rate and overall heat transfer coefficient were determined at different operating conditions. The energy efficiency results of reactor experiments were also compared.

5.7.2 Experimental

Ammonia-argon base gas with a concentration of 0.5% was decomposed into hydrogen and nitrogen gas by DBD in PPR at atmospheric pressure. Figure 5.49 shows a diagram of the experimental setup. Ammonia gas was fed into the electrode gap distance of the PPR between both electrodes. Quartz glass was used as a dielectric with a thickness of 2 mm. A high-voltage electrode was connected to a copper mesh, which had a thickness of 0.25 mm. A metal plate (SUS 316) was used as the ground electrode and connected to an oscilloscope.

The plasma was generated using a power source with a 10-kHz sinusoidal voltage of 12—18 kV. The DBD plasma was produced with a discharge area of 45 mm × 45 mm. Measurements were taken for two different electrode gap distances of 4.5 mm and 1 mm. The decomposed gases were collected from the outlet reactor port using a syringe. The collected samples were analyzed using gas phase chromatography (GC; GC-2014S, SHIMADZU). The GC device was calibrated, and the error was estimated to be within ±5%. The input power was determined by a power meter, and the temperature was measured using K-type thermocouples connected at different PPR points. The feed gas was controlled by a mass flow controller (MFC).

Chapter 5. H₂ Production from ammonia gas

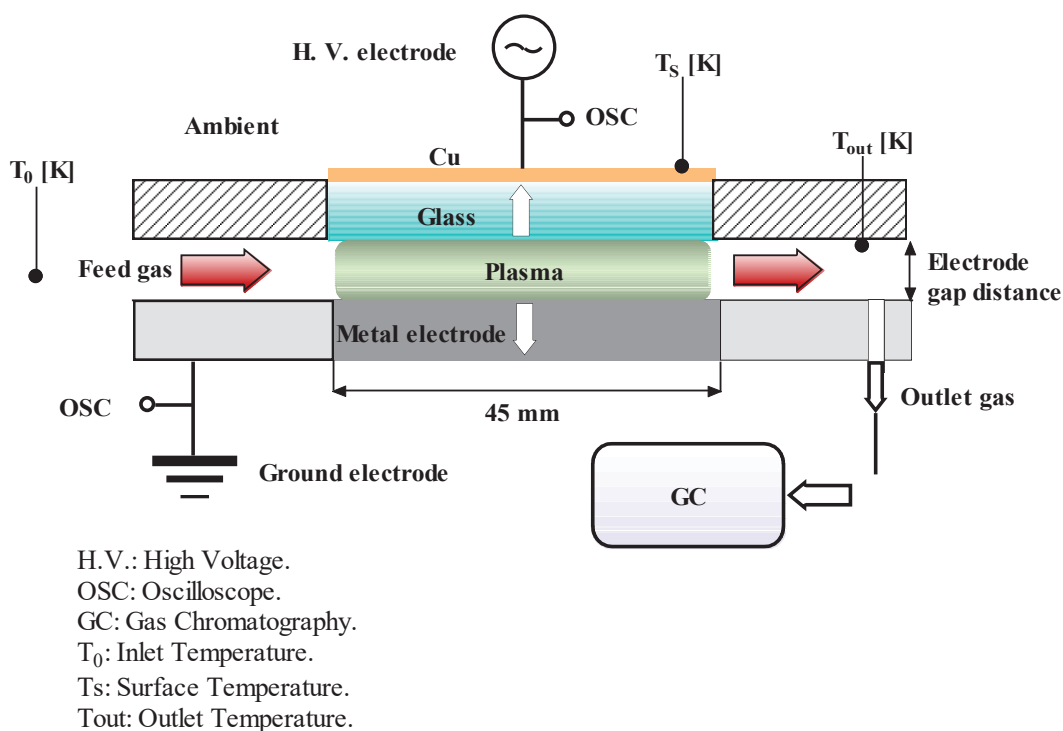


Fig. 5.49 Experimental setup.

Figure 5.50 shows a photo of the PPR assembly photo without plasma and at plasma ignition. The gas inlet, outlet, and PPR surface temperatures were measured by K-type thermocouples. Ammonia gas was fed into the PPR discharge gap at 0.1–1 L/min at atmospheric pressure (100 kPa) and ambient temperature. The plasma discharge power was determined at different voltages using the power meter. The DBD plasma was generated in the discharge gap between the high-voltage electrode and the ground electrode. The energy distributions across the ground electrode, high-voltage electrode, and heat loss are discussed.

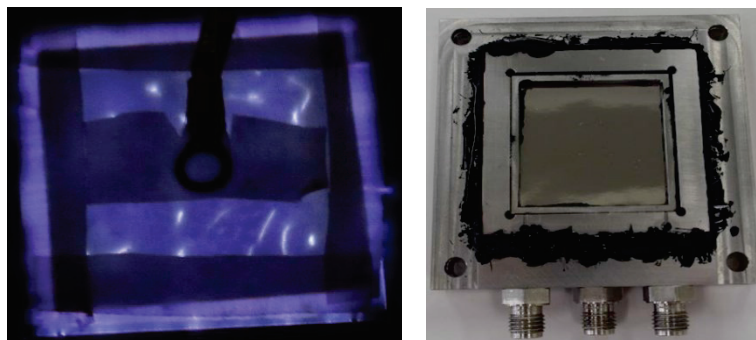


Fig. 5.50 Plasma plate reactor photos.

Chapter 5. H₂ Production from ammonia gas

5.7.3 Energy distribution

The energy equation for heat transfer by conduction of macroscopic expression is [613]:

$$\rho C_{Pg} u \frac{\partial T}{\partial x} = \lambda \left(\frac{\partial^2 T}{\partial x^2} + \frac{\partial^2 T}{\partial y^2} \right) + G \quad (1)$$

where x is the gas flow direction [m], y is the perpendicular direction to flow [m], G is the heat generation rate per unit volume [$\text{W} \cdot \text{m}^{-3}$], T is the gas temperature [K], u is the gas velocity [$\text{m} \cdot \text{s}^{-1}$], ρC_{Pg} is the heat capacity of the feeding ammonia gas [$\text{J} \cdot \text{m}^{-3} \cdot \text{K}^{-1}$], and λ is the thermal conductivity [$\text{W} \cdot \text{m}^{-1} \cdot \text{K}^{-1}$]. The heat conduction equation has been used by many studies for modeling in DBD plasma analysis [735]. Uniform heat generation has been produced by micro discharges.

Figure 5.51 shows the heat transfer resistances across the reactor. This figure shows the heat flow from the plasma discharge gap to the high-voltage electrode. The total heat transfer rate can be determined with the following equation [551]:

$$dQ = U (T_g - T_a) dA \quad [\text{W}] \quad (2)$$

where U is the overall heat transfer coefficient [$\text{W}/\text{m}^2 \cdot \text{K}$], A is the total heat transfer area [m^2], T_g is the gas temperature, and T_a is the PPR's surrounding temperature [K]. The convection heat transfer from the inner plasma to the dielectric glass is obtained based on the gas input conditions. The conduction heat transfer resistances through the metal and dielectric electrodes are calculated according to equation (1).

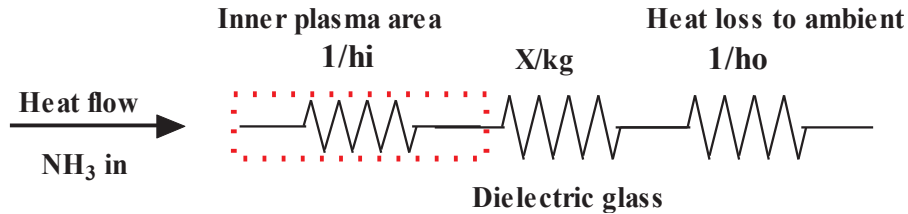


Fig. 5.51 Heat transfer resistances from inner plasma to high-voltage electrode direction.

The heat loss resistance from the high-voltage electrode surface to atmosphere was determined using Churchill and Chu's [552] Nusselt number relation:

$$Nu = 0.68 + \frac{0.670 Ra^{1/4}}{[1 + (0.492 / Pr)^{9/16}]^{4/9}} \quad (3)$$

where Pr is the Prandtl number, and Ra is the Rayleigh number ($Ra = Gr Pr$). The Grashof number was estimated from the following relation:

$$Gr = \frac{g \beta (T_s - T_a) L^3}{\nu^2} \quad (4)$$

Chapter 5. H₂ Production from ammonia gas

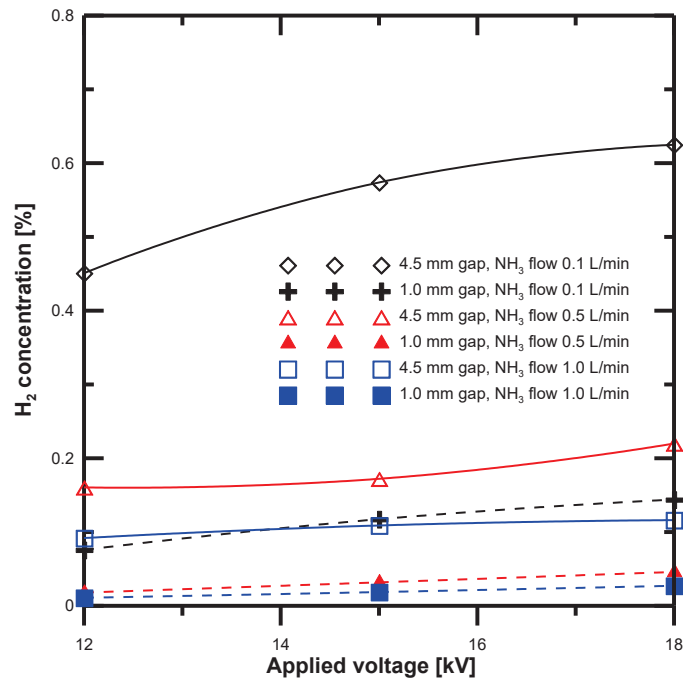
where β [K⁻¹] is the thermal expansion coefficient, ν [m²/s] is the kinematic viscosity, L [m] is the gap length, g is gravitational acceleration, and T_s and T_a [K] are the reactor-surface and ambient temperatures, respectively. The external heat transfer coefficient can be obtained from the Nusselt number relation, $Nu = h_o L / k_{airj}$.

5.7.4 RESULTS AND DISCUSSION

Ammonia as an energy carrier contains more hydrogen than other liquids. Atmospheric-pressure plasma is characterized as a weak plasma due to the limited energy fed into the plasma system. The effects of the electrode gap distance at different NH₃ flow rates were examined, and the heat transfer distribution was determined for both electrode gap distances.

5.7.4.1 Electrode gap distance effect

Figure 5.52 demonstrates the H₂ concentration obtained at different flow rates and electrode gap distances. The H₂ concentration at a gap distance of 4.5 mm was higher than that at 1 mm at all flow rates. The concentration of the H₂ also increased with the voltage. To clarify the effect of the gap distance, the produced H₂ flow rate was compared between ammonia gas flow rates of 0.1 and 1 L/min. The H₂ gas flow rate was determined based on GC concentration analysis. Figure 5.53 shows the results. The hydrogen flow rate at a gap distance of 4.5 mm was higher than that at 1 mm.



Chapter 5. H₂ Production from ammonia gas

Fig. 5.52 Comparison of hydrogen concentration at different discharge gap distances.

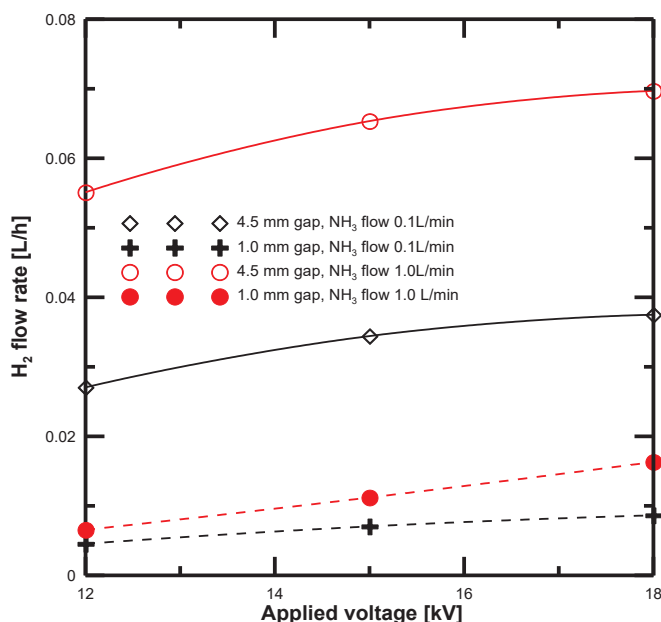


Fig. 5.53 H₂ flow rate versus voltage at different discharge gap distances.

It was clear that the ammonia decomposition was improved with increasing gap distance. The residence time of ammonia decomposition can be determined based on the feed gas flow rate and the electrode gap distance. The ammonia conversion rate was calculated according to the following relation:

$$\text{NH}_3 \text{ conversion rate [\%]} = \text{H}_2 \text{ conc [\%]} / ([\text{NH}_3]_0 \text{ conc.} \times 1.5) \times 100 \quad (5)$$

where H₂ conc is the produced hydrogen gas concentration at the PPR exit, and [NH₃]₀ is the initial ammonia concentration.

Figure 5.54 shows the conversion rate of ammonia at different plasma voltages and residence times with a gap distance of 4.5 mm. The conversion rate increased with the residence time and reached a maximum value of 83.65% at a voltage of 18 kV and NH₃ input flow rate of 0.1 L/min. Similarly, the conversion rate of ammonia decomposition with a gap distance of 1 mm is shown in figure 5.55, where the conversion rate shows the same trend. The maximum rate was 19.28% at 18 kV and 0.1 L/min. It is obvious that the conversion rate values are lower than those at 4.5 mm due to the lower residence time and ammonia reaction time at a gap distance of 1 mm.

Chapter 5. H₂ Production from ammonia gas

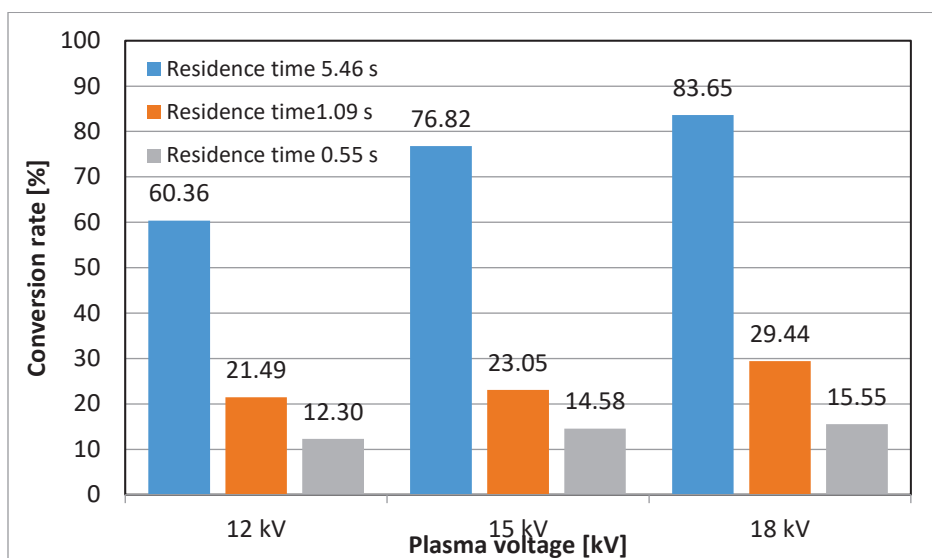


Fig. 5.54 NH₃ conversion rate versus residence time in PPR with electrode gap of 4.5 mm.

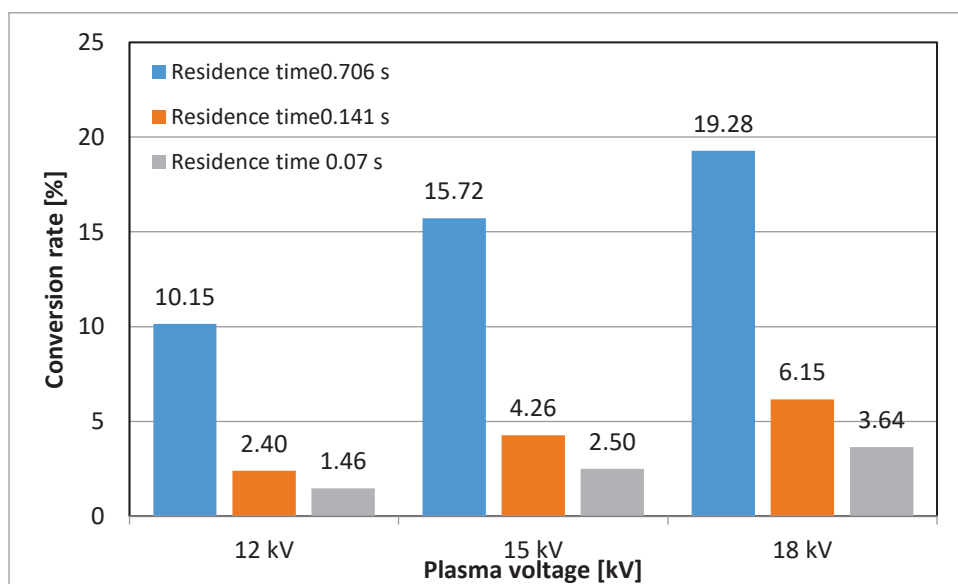


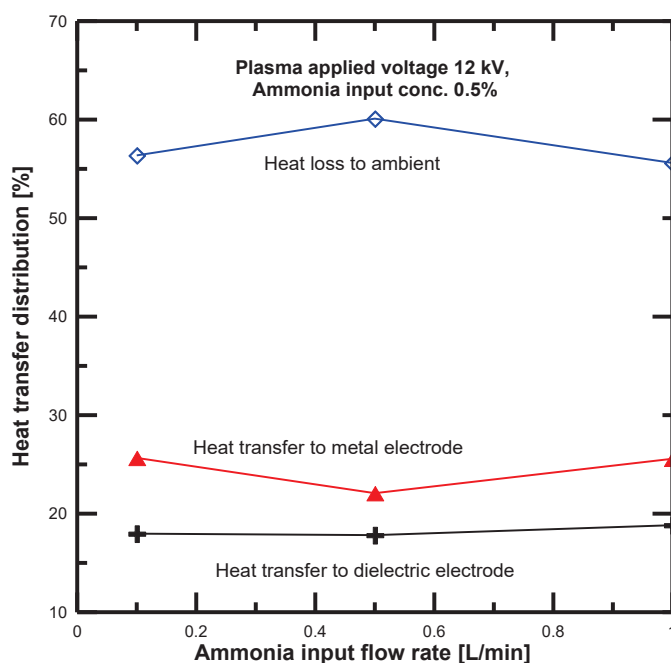
Fig. 5.55 NH₃ conversion rate versus residence time in PPR with electrode gap of 1 mm.

Chapter 5. H₂ Production from ammonia gas

5.7.4.2 Heat transfer distribution analysis

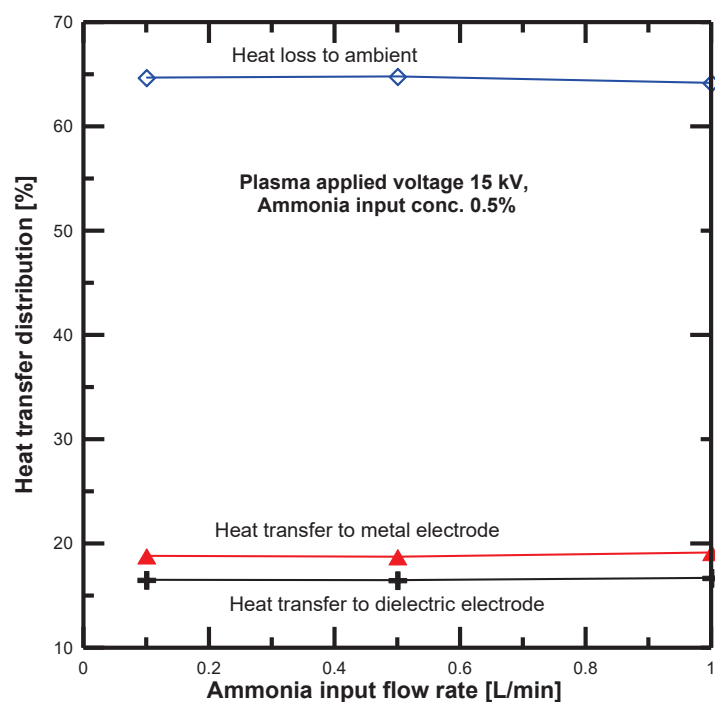
Figure 5.56 compares the heat transfer distribution across the dielectric, metal electrodes, and heat loss to the atmosphere at 12 kV. These results were determined based on the energy distribution equations discussed in the previous section. 80% of the DBD plasma input power was transferred as heat to both electrodes [552], around 65% was transferred to the dielectric electrode, and 15% was transferred to the metal or ground electrode. This is due to the micro discharge concentration spreading on the dielectric glass electrode's surface in a much larger area than the filament diameter.

Figure 5.57 shows the heat transfer distribution to the dielectric electrode at different voltages and NH₃ input flow rates. The heat transfer distribution at 12 kV was higher than at 15 kV and 18 kV. The variation of the heat transfer distribution of the dielectric electrodes was slightly decreased at low ammonia flow rate, and the amount is related to the enthalpy gained by the ammonia feed gas. Secondary electron emissions deliver more ionization, which leads to higher metal electrode heating than that of the dielectric electrode.

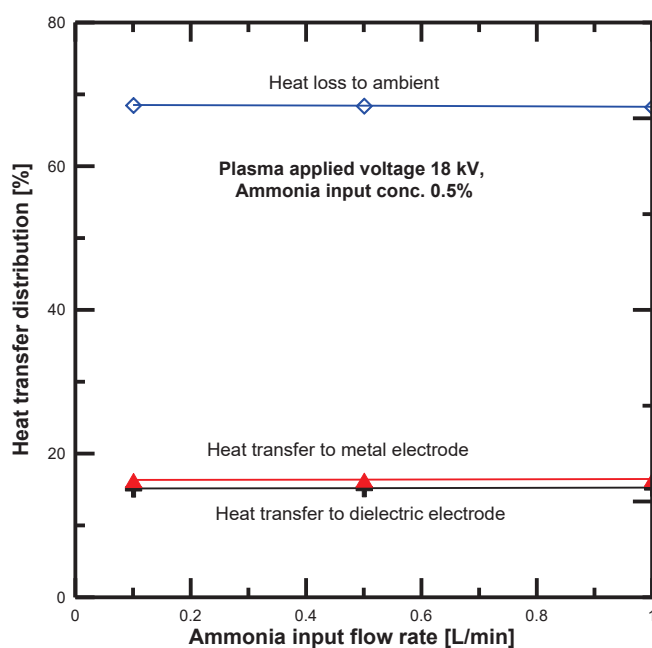


(a)

Chapter 5. H₂ Production from ammonia gas



(b)



(c)

Fig. 5.56 Heat transfer distribution in PPR with electrode gap distance of 4.5 mm: (a) plasma voltage 12 kV, (b) plasma voltage 15 kV, (c) plasma voltage 18 kV.

Chapter 5. H₂ Production from ammonia gas

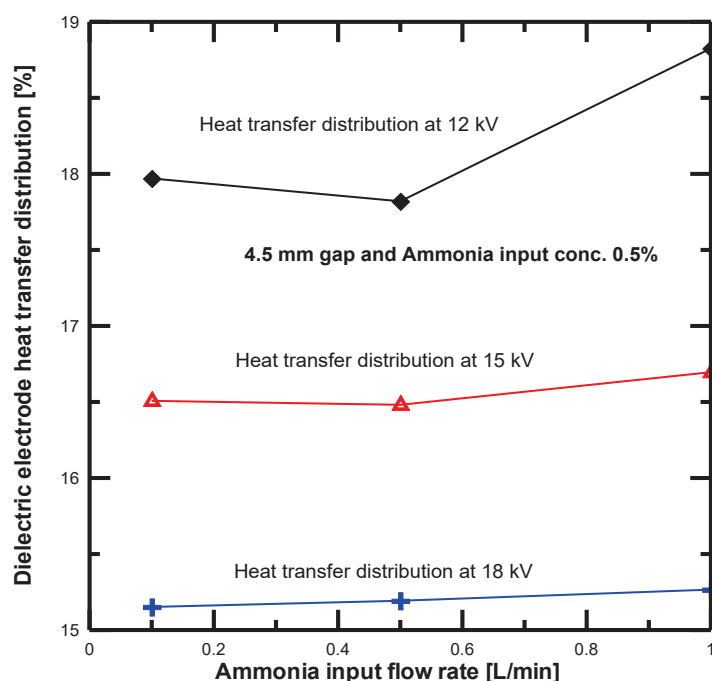


Fig. 5.57 Dielectric electrode heat transfer distribution.

Figure 5.58 compares the heat transfer distribution of the metal electrode at different voltages. The heat transfer distribution increased with ammonia input flow rate at 15 and 18 kV. The heat transfer distribution was clearly decreased at an NH₃ flow rate of 0.5 L/min and 12 kV. It has been reported that the heat transfer mechanism is not affected by the feed gas' physical properties but is influenced by changes in the plasma structure [613].

Additionally, the heat transfer distribution of the metal electrode was higher than that obtained from the dielectric electrode. The total heat transfer rate at different input flow rates and voltages is shown in figure 5.59. It is clear from this figure that the total heat transfer rate at 18 kV was much higher than at 15 kV and 18 kV. Most of the plasma heat was transferred to the high-voltage electrode direction due to the concentration of micro discharges at the electrode surface. Furthermore, the DBD plasma heat transfer mechanism was not affected by the changes of the feed gas' physical properties, while the ammonia's decomposition behavior using DBD plasma was obviously changed.

Figure 5.60 presents the overall heat transfer coefficient at different input flow rates and plasma voltages. It is clear that the overall heat transfer coefficient increased with the voltage. Furthermore, the overall heat transfer coefficient at the ammonia flow rate of 1 L/min was higher than at 0.5 and 0.1 L/min. Conversely, the overall heat transfer coefficient at the high ammonia flow rate exceeded those of the lower ones, while the conversion rate results at the same ammonia flow rate were lower.

Chapter 5. H₂ Production from ammonia gas

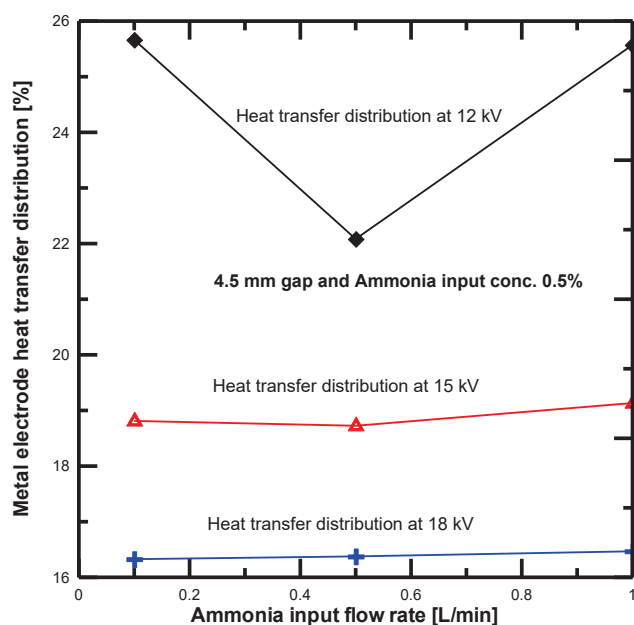


Fig. 5.58 Metal electrode heat transfer distribution.

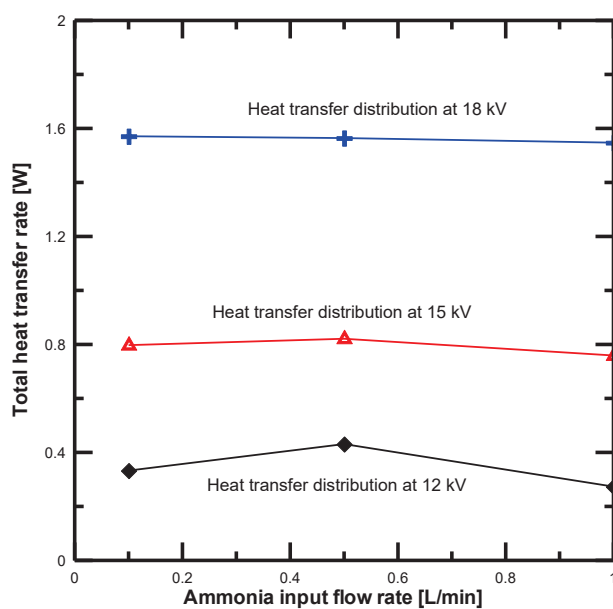


Fig. 5.59 Total heat transfer rate distribution at different plasma voltages.

Chapter 5. H₂ Production from ammonia gas

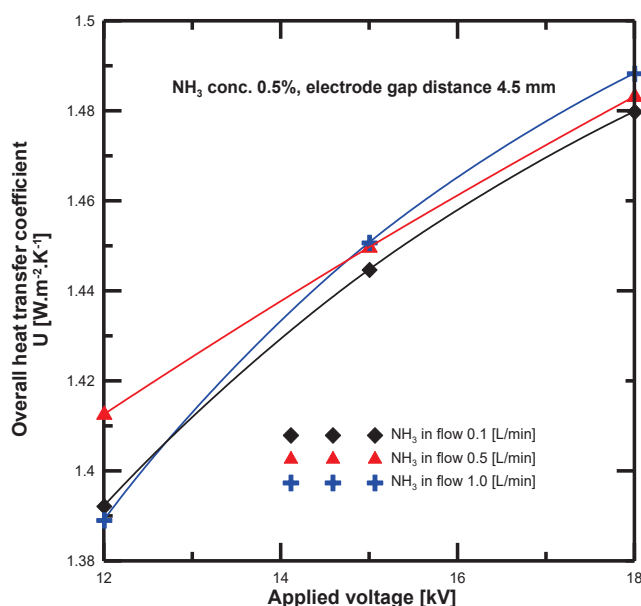


Fig. 5.60 Overall heat transfer coefficient at different NH₃ flow rates.

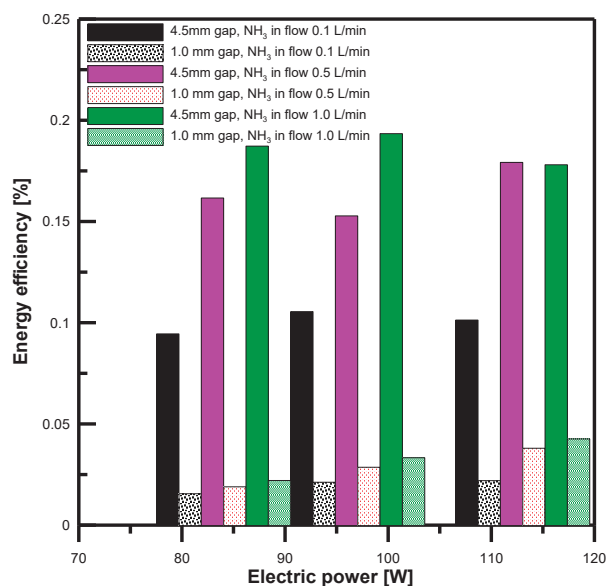


Fig. 5.61 Comparison of energy efficiency versus input electric power.

Figure 5.61 compares the energy efficiency of both reactors with different electrode gap distances and electric power. It is clear that the energy efficiency was higher at a gap distance of 4.5 mm than at 1 mm. The maximum energy efficiencies at 4.5 mm with input flow rates of 1, 0.5, and 0.1 L/min were 0.1936%, 0.178%, and 0.1057%, respectively. The maximum energy efficiencies at 1 mm with ammonia input flow rates of 1, 0.5, and 0.1 L/min were 0.0428%, 0.038% and 0.022%, respectively.

Chapter 5. H₂ Production from ammonia gas

Conclusion

In this study, ammonia-argon base gas was decomposed into hydrogen and nitrogen gas by atmospheric-pressure DBD plasma. Ammonia gas was fed into PPRs with electrode gap distances of 1 mm and 4.5 mm. The hydrogen production was affected by the electrode gap distance. The hydrogen concentration and flow rate at a gap distance of 4.5 mm results were much higher than at 1 mm.

The effect of the residence time on the hydrogen conversion was also investigated. The maximum conversion rates at 4.5 mm and 1 mm were 83% and 19.29%, respectively. The heat transfer distribution of metal, dielectric electrodes, and heat loss to the atmosphere were determined at different voltages, and most of the heat generation was transferred to the dielectric electrode surface due to the concentration of micro discharges near the high-voltage electrode. The heat transfer mechanism was not affected by the ammonia physical properties, while the ammonia decomposition by the DBD plasma was obviously changed.

The energy efficiency of NH₃ decomposition was determined at different input power. The maximum obtained energy efficiencies with an NH₃ concentration of 5% and gap distance of 4.5 mm were 0.1936%, 0.178%, and 0.1057% at ammonia input flow rates of 1, 0.5, and 0.1 L/min, respectively. Those at a gap distance of 1 mm were 0.0428%, 0.038%, and 0.022%, respectively.

References

- [644] Yin SF, Xu BQ, Zhou XP, Au CT (2004) Appl Catal A Gen 277:1–9.
- [645] Hill A, Torrente L (2014) Murciano. Int J Hydrog Energy 39:7646–7654.
- [646] Rosen, M. A.; Scott, D. S. Comparative efficiency assessment for a range of hydrogen production processes. *Int. J. Hydrogen Energy* 1998, 23, 631–640.
- [647] Shiga, H.; Shinda, K.; Hagiwara, K.; Tsutsumi, A.; Sakurai, M.; Yoshida, K.; Balgen, E. Large scale hydrogen production from biogas. *Int. J. Hydrogen Energy* 1998, 23, 631–640.
- [648] Nozaki, T.; Okazaki, K. Non-thermal plasma catalysis of methane: Principles, energy efficiency, and applications. *Catal. Today* 2013, 211, 29–38.
- [649] Allah, Z. A.; Whitehead, J. C. Plasma-catalytic dry reforming of methane in an atmospheric pressure AC gliding arc discharge. *Catal. Today* 2015, 256, 76–79.
- [650] Gallon, H. J.; Tu, X.; Whitehead, J. C. Effects of Reactor Packing Materials on H₂ Production by CO₂ Reforming of CH₄ in a Dielectric Barrier Discharge. *Plasma Processes Polym.* 2012, 9, 90–97.
- [651] Tu, X.; Gallon, H. J.; Twigg, M. V.; Gorry, P. A.; Whitehead, J. C. Dry reforming of methane over a Ni/Al₂O₃ catalyst in a coaxial dielectric barrier discharge reactor. *J. Phys. D: Appl. Phys.* 2011, 44 (27), 274007–274007.
- [652] Tu, X.; Whitehead, J. C. Plasma-catalytic dry reforming of methane in an atmospheric dielectric barrier discharge: Understanding the synergistic effect at low temperature. *Appl. Catal., B* 2012, 125, 439–448.
- [653] Kim, J.; Abbott, M. S.; Go, D. B.; Hicks, J. C. Enhancing C–H Bond Activation of Methane via Temperature-Controlled, Catalyst–Plasma Interactions. *ACS Energy Lett.* 2016, 1 (4), 94–99.
- [654] Watson, J. K. G., & Majewski, W. A. (1986). Assignment of the schuster band of ammonia. *Journal of Molecular Spectroscopy*, 115, 82–87.
- [655] Agostino, R., Cramarossa, F., Benedictis, S. D., & Ferraro, G. (1981). Kinetic and spectroscopic analysis of NH₃ decomposition under R.F. plasma at moderate pressure. *Plasma Chemistry and Plasma Processing*, 1, 19–35.
- [656] Cicala, G., De Tommaso, E., Raino, A. C., Lebedev, Y. A., & Shakhmatov, V. A. (2009). Study of positive column of glow discharge in nitrogen by optical emission spectroscopy and numerical simulation. *Plasma Sources Science and Technology*, 18, 025032.

- [657] Nicholas, J. E., Spiers, A. I., & Martin, N. A. (1986). Kinetics and mechanism in the decomposition of NH_3 in a radio-frequency pulse discharge. *Plasma Chemistry and Plasma Processing*, 6, 39–51.
- [658] Zhang, Y., Wang, H., Jiang, W., & Bogaerts, A. (2015). Two-dimensional particle-in cell/ Monte Carlo simulations of a packed-bed dielectric barrier discharge in air at atmospheric pressure. *New Journal of Physics*, 17, 083056.
- [659] Koen Van, L., & Annemie, B. (2016). Fluid modelling of a packed bed dielectric barrier discharge plasma reactor. *Plasma Sources Science and Technology*, 25, 015002.
- [660] Butterworth, T., Elder, R., & Allen, R. (2016). Effects of particle size on CO_2 reduction and discharge characteristics in a packed bed plasma reactor. *Chemical Engineering Journal*, 293, 55–67.
- [661] Hansgen DA, Vlachos DG, Chen JG (2010) *Nat Chem* 2:484–489.
- [662] Neyts, E. C., & Bal, K. M. (2017). Effect of electric fields on plasma catalytic hydrocarbon oxidation from atomistic simulations. *Plasma Processes and Polymers*, 14, 1600158.
- [663] L. Schlapbach, A. Züttel, Hydrogen-storage materials for mobile applications. *Nature*, 414 (2001) 353-358.
- [664] C. Zamfirescu, I. Dincer, Using ammonia as a sustainable fuel. *Journal of Power Sources*, 185 (2008) 459-465.
- [665] D.A. Kramer, US Geological Survey, Mineral and Commodities Summaries, January 2007.
- [666] G. Strickland, Ammonia as a hydrogen energy storage medium, in *Proceedings of the 5th Annual Thermal Storage Meeting*, Paper 8010555-2, 10th October 1980, McLean, VA, USA.
- [667] Neyts, E. C.; Ostrikov, K.; Sunkara, M. K.; Bogaerts, A. Plasma Catalysis: Synergistic Effects at the Nanoscale. *Chem. Rev.* 2015, 115 (24), 13408–13446.
- [668] Whitehead, J. C. Plasma–catalysis: the known knowns, the known unknowns and the unknown unknowns. *J. Phys. D: Appl. Phys.* 2016, 49 (24), 243001–243001.
- [669] Mehta, P.; Barboun, P.; Go, D. B.; Hicks, J. C.; Schneider, W. F. Catalysis Enabled by Plasma Activation of Strong Chemical Bonds: A Review. *ACS Energy Lett.* 2019, 4 (5), 263.
- [670] Choudhary, T.; Sivadinarayana, C.; Goodman, D. Catalytic ammonia decomposition: CO_x -free hydrogen production for fuel cell applications. *Catal. Lett.* 2001, 72, 197–201.

- [671] C.H. Christensen, T. Johannessen, R.Z. Sorensen, J.K. Norskov, *Catal. Today* 111(2006) 140–144.
- [672] S.F. Yin, Q.H. Zhang, B.Q. Xu, W.X. Zhu, F.C. Ng, C.T. Au, *J.Catal.* 224 (2004)
- [673] F. Vitse, M. Cooper, G.G. Botte, *J. Power Sources* 142 (2005) 18–26.
- [674] R. Atsumi, R. Noda, H. Takagi, L. Vecchione, A. D. Carlo, Z. D. Prete, K. Kuramoto. Ammonia decomposition activity over Ni/SiO₂ catalysts with different pore diameters. *Int. J. Hydrogen Energy*, 2014, 39, 13954–61.
- [675] Li, X.-K.; Ji, W.-J.; Zhao, J.; Wang, S.-J.; Au, C.-T. Ammonia decomposition over Ru and Ni catalysts supported on fumed SiO₂, MCM-41, and SBA-15. *J. Catal.* 2005, 236, 181–189.
- [676] Karim, A. M.; Prasad, V.; Mpourmpakis, G.; Lonergan, W. W.; Frenkel, A. I.; Chen, J. G.; Vlachos, D. G. Correlating particle size and shape of supported Ru/ γ -Al₂O₃ catalysts with NH₃ decomposition activity. *J. Am. Chem. Soc.* 2009, 131, 12230–12239.
- [677] Yin, S.; Xu, B.; Zhou, X.; Au, C. A mini-review on ammonia decomposition catalysts for on-site generation of hydrogen for fuel cell applications. *Appl. Catal., A* 2004, 277, 1–9.
- [678] Shen, X.; Garces, L.-J.; Ding, Y.; Laubernds, K.; Zerger, R. P.; Aindow, M.; Neth, E. J.; Suib, S. L. Behavior of H₂ chemisorption on Ru/TiO₂ surface and its application in evaluation of Ru particle sizes compared with TEM and XRD analyses. *Appl. Catal., A* 2008, 335, 187–195.
- [679] A.J. Appleby and F.R. Foulkes, *Fuel Cell Handbook* (Van Nostrand Reinhold, New York, 1989).
- [680] M.C.J. Bradford, P.E. Fanning and M.A. Vannice, *J. Catal.* 172 (1997) 479.
- [681] Hill, A. K.; Torrente-Murciano, L. Low temperature H₂ production from ammonia using ruthenium-based catalysts: Synergetic effect of promoter and support. *Appl. Catal., B* 2015, 172, 129–135.
- [682] Mukherjee, S.; Devaguptapu, S. V.; Sviripa, A.; Lund, C. R.; Wu, G. Low-temperature ammonia decomposition catalysts for hydrogen generation. *Appl. Catal., B* 2018, 226, 162–181.
- [683] Jena, P. Materials for hydrogen storage: Past, present, and future. *J. Phys. Chem. Lett.* 2011, 2, 206–211.
- [684] Eberle, U.; Felderhoff, M.; Schuth, F. Chemical and physical solutions for hydrogen storage. *Angew. Chem., Int. Ed.* 2009, 48, 6608–6630.
- [685] Sordakis, K.; Tang, C. H.; Vogt, L. K.; Junge, H.; Dyson, P. J.; Beller, M.; Laurenczy, G. Homogeneous catalysis for sustainable hydrogen storage in formic acid and alcohols. *Chem. Rev.* 2018, 118, 372–433.

- [686] Klerke, A.; Christensen, C. H.; Nørskov, J. K.; Vegge, T. Ammonia for hydrogen storage: Challenges and opportunities. *J. Mater. Chem.* 2008, 18, 2304–2310.
- [687] Israni, S. H.; Harold, M. P. Methanol steam reforming in single fiber packed bed Pd–Ag membrane reactor: experiments and modeling. *J. Membr. Sci.* 2011, 369, 375–387.
- [688] Moran M. J. and Sciubba. E. Exergetic analysis: principles and practice. *J. Eng. Gas Turbines Power*, 1994, Vol 116, 285-290.
- [689] Stecco S. and Moran M. J., eds., 1990, *A future for Energy*, Pergamon, Oxford, UK.
- [690] Valero, A. and Tsatsaronis, G., eds., 1992, ECOS '92, *Proc. Int. Symp. Efficiency, Costs, Optimization and Simulation of Energy Systems, Zaragoza, Spain*, ASME Press, New York.
- [691] Dincer I, Cengel YA. Energy, entropy and exergy concepts and their roles in thermal engineering, *Entropy* 2001; 3: 116-49.
- [692] Gallavotti G. Entropy, thermostats and chaotic hypothesis. *Chaos* 2006; 16:384-9.
- [693] Pachauri, R. K.; Allen, M. R.; Barros, V. R.; Broome, J.; Cramer, W.; Christ, R.; van Ypersele, J.-P. Climate change 2014 synthesis report. Contribution of working groups I, II, and III to the fifth assessment report of the Intergovernmental Panel on Climate Change; IPCC: Geneva, Switzerland, 2014.
- [694] Lackner, K. S.; Brennan, S.; Matter, J. M.; Park, A.-H. A.; Wright, A.; Van Der Zwaan, B. The urgency of the development of CO₂ capture from ambient air. *Proc. Natl. Acad. Sci. U. S. A.* 2012, 109, 13156–13162.
- [695] Bicer, Y.; Dincer, I. Life cycle environmental impact assessments and comparisons of alternative fuels for clean vehicles. *Resour. Conserv. Recy.* 2018, 132, 141–157.
- [696] Bejan A, Tsatsaronis G, Moran MJ. Thermal design and optimization. Wiley; 1996.
- [697] Sorin MV, Brodyansky VM. A method for thermodynamic optimization e I. theory and application to an ammonia-synthesis plant. *Energy* 1992; 17(11): 1019-31.
- [698] M. Penkuhn, G. Tsatsaronis. Comparison of different ammonia synthesis loop configurations with the aid of advanced exergy analysis. *Energy* 137 (2017) 854-864.
- [699] Szargut J, Morris DR, Steward FR. Exergy analysis of thermal, chemical and metallurgical processes. Hemisphere Publishing; 1988.

- [700] Tsatsaronis G. Definitions and nomenclature in exergy analysis and exergoeconomics. *Energy* 2007; 32(4):249e53. <http://dx.doi.org/10.1016/j.energy.2006.07.002>.
- [701] Pavelka M, Klika V, Vagner P, Marsík F. Generalization of exergy analysis. *Appl Energy* 2015; 137:158-72.
- [702] J. Szargut, D. R. Morris and F. R. Steward, *Exergy Analysis of Thermal and Metallurgical Processes*, Hemisphere Publishing Corporation, 1988.
- [703] W. Van Gool, *Energy Policy: Fairly Tales and Factualities*, in O.D.D. Soares et al. *Innovation and Technology—Strategies and Policies*, Kluwer, Dordrecht, 1997, pp. 93–105.
- [704] Lucia U. Mathematical consequences and Gyarmatis principal in Rational Thermodynamics. *Nuovo Cimento* 1995, B110 (10): 1227-35.
- [705] Sama DA. The use of the second law of thermodynamics in process design. *J Energy Resour Technol* 1995; 117 (3):179e85.
- [706] Hammond G. Engineering sustainability: thermodynamics, energy systems, and the environment. *International Journal of Energy Research* 2004; 28:613–39.
- [707] M. A. K. Lodhi, Helio-hydro and helio-thermal production of hydrogen, *Int. J. Hydrogen Energy*, 2004, 29(11), 1099–1113.
- [708] F. Barbir, PEM electrolysis for production of hydrogen from renewable energy sources, *Sol. Energy*, 2005, 78(5), 661–669.
- [709] E. P. Da Silva, et al., Analysis of hydrogen production from combined photovoltaics, wind energy and secondary hydroelectricity supply in Brazil, *Sol. Energy*, 2005, 78, 670–677.
- [710] C. Koroneos and D. Rovas, A solar thermal power system in the city of Thessalonica with the use of the pinch method for entropy minimisation, *Int. J. Exergy*, 2007, 4(2), 134–150.
- [711] K. Gardner, *Portable Fuel Cells for Military Applications*, Washington, DC, 2001.
- [712] A. Wojcik, H. Middleton, I. Damopoulos, J. Van Herle, Ammonia as a fuel in solid oxide fuel cells, *J. Power Sources* 118 (2003) 342–348.
- [713] V. Alagharu, S. Palanki, K. N. West. Analysis of ammonia decomposition reactor to generate hydrogen for fuel cell applications. *J. of Power Sources*, 2010, 195, 829-833.
- [714] M. El-Shafie, S. Kambara, Y. Hayakawa. A comparison between GDP and PDP experiments of hydrogen permeation through 15µm Pd60-Cu40% membrane

thickness in a micro channel plate type reactor. *Fusion Engineering and Design*, 2019, 149, 111320-27.

[715] K. Christopher and R. Dimitrios. A review on exergy comparison of hydrogen production methods from renewable energy sources. *Energy Environ. Sci.*, 2012, 5,6640-51.

[716] J. Szargut, D. R. Morris and F. R. Steward, *Exergy Analysis of Thermal, Chemical, and Metallurgical Processes*, Hemisphere Publishing Corporation, 1988, ISBN 0-89116-574-6.

[717] F. Balkan, N. Colak and A. Hepbasli, Performance evaluation of a triple-effect evaporator with forward feed using exergy analysis, *Int. J. Energy Res.*, 2005, 29, 455–470.

[718] R. L. Cornelissen, *Thermodynamics and Sustainable Development: The Use of Exergy Analysis and the Reduction of Irreversibility*, PhD thesis, University of Twente, The Netherlands, 1997.

[719] G. P. Hammond and A. J. Stapleton, *Exergy Analysis of the United Kingdom Energy System*, in *The Paper Presented at the Institute of Mechanical Engineers*, 2001, vol. 215, no. 2, pp. 141–162.

[720] C. Koroneos, T. Spachos and N. Mousiopoulos, Exergy analysis of renewable energy sources, *Renewable Energy*, 2003, 28(2), 295– 310.

[721] G. Wall, *Exergetics, Exergy Ecology Democracy*, Molndal, 1998.

[722] Hans Dieter Baehr, assiduity K N Pattas, *Thermodynamics: Introduction in Fundamental and in Technical Applications*, Giahoudis-Giapoulis, Thessaloniki, 1978.

[723] F. Goran and O. Per, Exergies of natural resources in life-cycle assessment and other applications, *Energy*, 1997, 22(9), 923– 931.

[724] W. A. Amos, *Costs of Storing and Transporting Hydrogen*, National Laboratory Renewable Energy, 1998, NREL/TP-570-25106.

[725] G. Beccali, M. Cellura and M. Mistretta, New exergy criterion in the multi\criteria context: a life cycle assessment of two plaster products, *Energy Convers. Manage.* 2003, 44, 2821–2838.

[726] Dincer, I., Rosen, M.A., 2013. *Exergy: Energy, Environment and Sustainable Development*, second ed. Elsevier, NY.

[727] A.S. Chellappa, C.M. Fischer, W.J. Thomson, Ammonia decomposition kinetics over Ni-Pt/Al₂O₃ for PEM fuel cell applications, *Appl. Catal. A: Gen.* 227 (2002) 231–240.

- [728] Bassani, A., Previtali, D., Pirola, C., Bozzano, G., Colombo, S., Manenti, F., Mitigating Carbon Dioxide Impact of Industrial Steam Methane Reformers by Acid Gas to Syngas Technology: Technical and Environmental Feasibility, *J. sustain. dev. energy water environ. syst.*, 8(1), pp 71-87, 2020.
- [729] dos Anjos, M. M., Tenenwurcel, D. R., Santos, L. A. O., Ferreira, W. R., Costa, A. L., Pereira, E. M. D., Low Carbon Transition through Renewables Sources – An Overview of the Renewable Energy Program in the State of Minas Gerais, *J. sustain. dev. energy water environ. syst.*, 8(2), pp 252-267, 2020.
- [730] Mikulandrić, R., Böhning, D., Lončar, D., Modelling of Temperature and Syngas Composition in a Fixed Bed Biomass Gasifier using Nonlinear Autoregressive Networks, *J. sustain. dev. energy water environ. syst.*, 8(1), pp 145-161, 2020.
- [731] U. Kogelschatz, *IEEE Trans. Plasma Sci.* 30, 1400 (1987).
- [732] J. Van Durme, J. Dewulf, C. Leys, and H. Van Langenhove, *Appl. Catal. B- Environ.* 78, 324 (2008).
- [733] F. Iza, G. J. Kim, S. M. Lee, J. K. Lee, J. L. Walsh, Y. T. Zhang, and M. G. Kong, *Plasma Process. Polym.* 5, 322 (2010).
- [734] G. Borcia, C. A. Anderson, and N. M. D. Brown, *Plasma Sources Sci. Technol.* 12, 335 (2003).
- [735] T. C. Corke, C. L. Enloe, and S. P. Wilkinson, *Annu. Rev. Fluid Mech.* 42, 505 (2009).
- [736] Eliasson B, Hirth M and Kogelschatz U 1987 *J. Phys. D: Appl. Phys.* 20 1421–7.
- [737] M. El-Shafie, S. Kambara, Y. Hayakawa. Study of the Reactor Temperature Effect on H₂ Production from Steam Decomposition Using DBD Plasma. *Energy Reports* 6S2 (2020) pp. 45-51.
- [738] Massines F, Rabehi A, Decomps P, Gadri R B, Segur P and Mayoux C 1998 *J. Appl. Phys.* 83 (6) 2950–7.
- [739] Sen Li, Fan Gu, Bo Tang, Tingting Ma, and Xiaobing Wang. Numerical analysis of the momentum and heat transfer in an atmospheric pressure dielectric barrier discharge. *AIP Advances*, 9, 035219 (2019).

